Topologically close-packed phase prediction in Ni-based superalloys: phenomenological structure maps and bond-order potential theory

Bernhard Seiser
St. Edmund Hall, University of Oxford

Supervisors:
Prof. D.G. Pettifor, Dr. A.N. Kolmogorov
Prof. R. Drautz

Thesis submitted for the degree of
Doctor of Philosophy
at the
University of Oxford
Michaelmas term, 2011

Contents

Abstract

Single crystal nickel-based superalloys are used in modern gas turbines because of their remarkable resistance to creep deformation at elevated temperatures, which is ensured by the addition of significant amounts of refractory elements. Too high concentrations of refractory elements can lead to the formation of topologically-close packed (TCP) phases during exposure to conditions of high temperature and stress which result in the degradation of the creep resistance. The traditional methods for predicting the occurrence of TCP phases in Ni-based superalloys have been based on the PHACOMP and newPHACOMP methodologies which are well-known to fail with respect to new generations of alloys. In this work a novel two-dimensional structure map ($\bar{N}$, $\overline{\Delta V/V}$) for TCP phases where $\bar{N}$ is the valence-electron count and $\overline{\Delta V/V}$ is a composition-dependent size factor. This map is found to separate the experimental data on the TCP phases of binary, ternary and multi-component TCP phases into well-defined regions corresponding to different structure types such as A15, σ, χ, δ, P, R, μ, and Laves. In particular, increasing size factor separates the A15, σ and χ phases from the δ, P, R, μ phases. The structure map is then also used in conjunction with CALPHAD computations of σ phase stability to show that the predictive power of newPHACOMP for the seven component Ni-Co-Cr-Ta-W-Re-Al system is indeed not ideal.

In order to gain a microscopic understanding of the observed structural trends, namely the differences between the two groups of TCP structures with increasing $\overline{\Delta V/V}$ and the trend from A15 to σ to χ with increasing $\bar{N}$, the electronic structure is coarse-grained from density functional theory (DFT) to tight-binding to bond-order potentials (BOPs). First, DFT is used to calculate the structural energy differences across the elemental $4d$ and $5d$ transition metal series and the heats of formation of the binary alloys Mo-Re, Mo-Ru, Nb-Re, and Nb-Ru. These calculations show that the valence electron concentration stabilizes A15, σ and χ but destablizes μ and Laves phases. The latter are shown to be stabilized instead by relative size difference. Second, a simple canonical TB model in combination with the structural energy difference theorem is found to qualitatively reproduce the energy differences predicted by the elemental DFT calculations. The structural energy difference theorem rationalizes the importance of the size factor for the stability of the μ and Laves binary phases as observed in the structure map and DFT heats of formation. Finally, analytic BOP theory is employed to identify the structural origins of the energy differences between TCP structure-types that lead to the trends found within the two-dimensional structure map.

Acknowledgements

For the successful completion of this thesis work I wish to deeply thank my advisors, David Pettifor, Ralf Drautz and Aleksey Kolmogorov for their support, guidance and continuous encouragements. In particular I would like to thank David for his endless patience throughout my stay in Oxford and for his deep insights in this research field which has been of great value for me. It would not have been possible to do this work without his valuable input.

A special thanks also goes to Thomas Hammerschmidt for his valuable contributions to this work and for always having a fridge full of exotic beer. I would also like to thank all collaboration partners in the Alloys By Design consortium, in particular, Roger Reed, Nils Warnken, Cathie Rae and Allesandro Mottura.

Many thanks go to the people in the MML for their permanent readiness for discussion, help and cheering me up at difficult times. In particular I need to thank John Drain for his support and helpful comments throughout the writing process. I would also like to acknowledge the help I received from Michael Ford, Roxana Margine and Ting Qin. Moreover, I am much indebted to all the people in the AM and IT departments at ICAMS for making my stays in Bochum intersting and enjoyable.

This project was generously funded by the Engineering and Physical Sciences Research Council (EPSRC). I would also like to thank my college, St. Edmund Hall, and the Materials department for providing additional funding that allowed me to attend conferences.

Most of all I would like to thank all my family who, as always, has provided me endless love and support throughout my DPhil.

Publications

List of publications that are relevant for this thesis:

- **Modelling topologically close-packed phases in superalloys: Valence-dependent bond-order potentials based on ab-initio calculations**
  T. Hammerschmidt, B. Seiser, R. Drautz and D. G. Pettifor.
  Superalloys 2008, eds R. C. Reed et al., 847-853, (2008)

- **TCP phase predictions in Ni-based superalloys: structure maps revisited**
  B. Seiser, R. Drautz and D. G. Pettifor.
  Acta Materialia, 59, 749-763, (2011)

- **Theory of structural trends within 4d and 5d transition metal topologically close-packed phases**
  B. Seiser, T. Hammerschmidt, A. N. Kolmogorov, R. Drautz and D. G. Pettifor.
  Physical Review B, 83, 224116-224133, (2011)

Chapter 1

Introduction

Since the 1940s nickel-based superalloys have been used as materials for blades in gas turbines and jet engines due to their excellent mechanical strength, corrosion and oxidation resistance and their ability to withstand creep deformation at temperatures above 70% of the melting temperature. Modern superalloys are very complex, consisting of up to 12 different elements, and have compositions specifically tailored to achieve the desired properties. The resistance to creep deformation at elevated temperatures is ensured by the addition of significant amounts of refractory elements. On exposure to high temperature and stress, too high concentrations of refractory elements lead to the formation of topologically-close packed (TCP) phases which results in the degradation of the creep resistance. In addition to being found in multi-component systems, TCP phases, like the well-known A15, σ, P, R, δ, μ, M and the Laves (C14, C15, and C36) phases, are also frequently found in compounds with fewer constituents, such as binary, ternary and quaternary alloys. Although all TCP phases have a relatively high and uniform packing density of atoms and are all characterised by the same structural features, their crystal structures, stoichiometries, and stability can be very different. Investigations into the controlling factors of the stability of individual TCP phases in binary, ternary and quaternary alloys have led to the development of methods, such as the PHACOMP and NewPHACOMP methodologies, that aim to predict the occurrence of TCP phases in nickel-based

superalloys. These models either interpolate knowledge about mechanical properties and phase stability extracted from known multi-component systems or extrapolate data from binary and ternary systems. In general, most of these methods do quite well in interpolating data but, because the theory which underlies them lacks a physical grounding, predictions can be inaccurate.

With the aim of basing the design of new superalloys on theoretical analysis and computer models, rather than on empiricism and trial-and-error testing, materials scientists and engineers from universities and leading gas turbine manufacturers in the UK have formed the EPSRC-funded collaboration 'Alloys by Design: A materials modelling approach'. This project addresses the challenge of bridging the gap from electronic up to continuum scale modelling. The goal of the multi-scale modelling approach is to carry out numerical modelling work at various scales such that the knowledge gained from finer length scale simulations can be used at coarser length scales in order to provide a fundamental physical description for each level in the modelling hierarchy. Working at both different length and time scales is crucial because most materials phenomena are manifestations of processes that are operative over several time and length scales. Hence, in order to get a complete understanding of the behaviour of nickel-based superalloys, not only with respect to TCP phase formation, the simulations will have to span the electronic, atomistic, microstructural and continuum scales. As shown in Fig. 1.1, this will include length scales ranging from the subnanometre level up to centimetres, and time scales from picoseconds to hours.

The result of this multi-scale modelling approach will lead to guidelines for the design of improved superalloy compositions. The desired characteristics of the target superalloys are not only lower development and materials costs and castability but also superior mechanical properties, such as microstructural stability, oxidation and creep resistance. As part of this research consortium, this thesis aims to establish a deeper physical understanding of the stability of TCP phases as an important first step towards the development of tools that allow for a more successful prediction of TCP formation in Ni-base

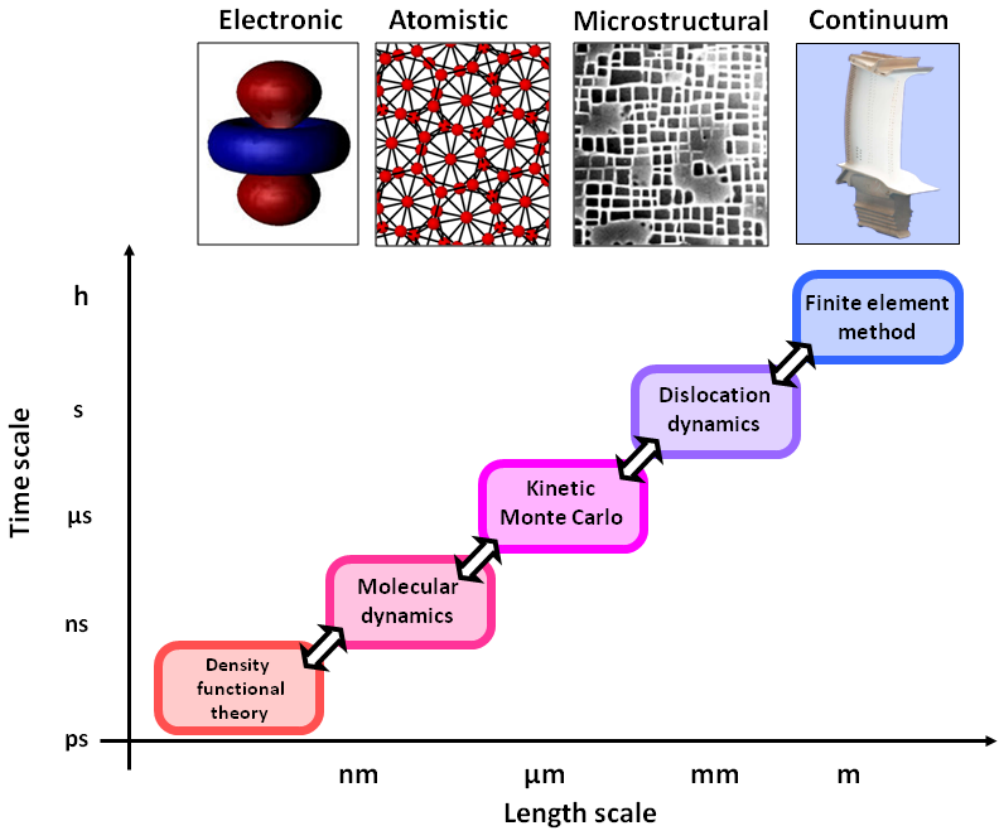

Figure 1.1: The hierarchies in multiscale materials modelling [1].

superalloys. The main focus of this thesis is on the influence of the two most important factors, the valence electron concentration and the atomic size difference, on the stability of individual TCP phases. For this purpose both empirical methods, phenomenological two-dimensional structure maps, and theoretical methods, analytic bond-order potentials, are employed as follows.

Firstly, in chapter 3, we propose a novel phenomenological two-dimensional structure map ($\bar{N}$,$\overline{\Delta V/V}$) where $\bar{N}$ is the average electron concentration and $\overline{\Delta V/V}$ is a composition dependent size-factor difference. The two structure map co-ordinates allow us to carry out a comprehensive study of the occurrence of binary, ternary and multi-component TCP phases without being restricted to a particular stoichiometry or structure type as in the existing literature. We discuss the trends which are observed within the new structure map using the experimental data for binary alloys and explain the relation

between regions demarcating different TCP structure types. Detailed investigations of ternary phase diagrams and multi-component systems show that TCP phases, regardless of the number of constituents, are located in the same regions of the structure map that are favoured by the binary compounds of the same structure type. Thus, the structure map allows us to test the mainly utilised methods, CALPHAD and NewPHACOMP, in predicting the susceptibility of nickel-based superalloys to TCP phase formation. An assessment of CALPHAD and NewPHACOMP methods based on our structure map to this procedure is described in detail in chapter 4.

Secondly, in chapters 5 and 6, the relationship between different modelling methods is examined by coarse-graining the electronic structure from density-functional theory (DFT) through a tight-binding (TB) model to an analytic bond-order potential (BOP). The analytic BOPs are then used to provide insight into the microscopic origin of the structural trends within TCP phases which are observed within our two-dimensional structure map, in particular the separation of A15, σ and χ from μ and Laves with increasing size factor difference, $\overline{\Delta V/V}$, and the trend from A15 $\rightarrow \sigma \rightarrow \chi$ with increasing valence electron concentration, $\bar{N}$. Chapter 5 presents DFT structural energy difference curves for the elemental $4d$ and $5d$ transition metal series and DFT heats of formation curves for a set of binary systems. The elemental DFT calculations provide the quantitative benchmark for the energy differences between the various structure-types across the elemental $4d$ and $5d$ transition metal series. A simple canonical TB model in combination with the structural energy difference theorem is found to qualitatively reproduce the energy differences predicted by DFT. The structural energy difference theorem rationalizes the importance of the size factor for the stability of the μ and Laves binary phases as observed in the structure map and DFT heats of formation. Finally, in chapter 6, analytic BOP theory is employed to identify the structural origins of the energetic differences between TCP structure-types that lead to the trends found within the two-dimensional structure map.

In the following, nickel-based superalloys will be introduced and their development, ap-

plications and fabrication summarized. The description of the origin of their outstanding properties leads directly to a detailed discussion of the TCP phases which addresses their most important characteristics. The main methods which are commercially utilised for alloy design, and in particular those used to control TCP phase formation, are explained.

Chapter 2

Topologically close-packed phases in Ni-based superalloys

2.1 Nickel-based superalloys

A superalloy, or a high-performance alloy, is a complex metallic alloy that exhibits excellent mechanical strength and creep resistance at high temperatures, good surface stability, and corrosion and oxidation resistance. Superalloys are usually based on nickel, cobalt, or nickel-iron and they consist of various combinations of lesser amounts of Mo, W, Al, Ti, Ta, Nb, Re, Ru, Hf, C and B. Nickel is an ideal base alloying element for very demanding applications, such as mobile land-based power units and aircraft applications, because of its high melting point of 1453°C and its ability to dissolve other metals, which can be used to improve high temperature creep resistance, fatigue life, phase stability, as well as oxidation and corrosion resistance [2].

2.1.1 Application and fabrication

The first engines built in the 1940s worked at turbine entry temperatures of about 700°C and were, compared to modern standards, very inefficient. Over the past 60 years, enormous effort has been made to increase engine efficiency by developing materials capable of

withstanding higher temperatures for much longer periods of time. Modern gas turbines for jet propulsion engines, like the Rolls-Royce Trent 800, operate at turbine entry temperatures above 1700°C. As shown in Fig. 2.1, nickel-based superalloys are used where the highest temperatures occur, namely in the combustion chamber, the last few compressor stages before the combustion chamber and, more importantly, in the turbine stages. In these high-pressure regions the temperature of the gas steam is about 2300°C, causing the surface of turbine blades to reach up to and beyond 1700°C, which is the current upper limit of temperature which nickel-based superalloys can withstand [3]. The ability to operate at such high gas steam temperatures and the enormous resultant increases in efficiency have been achieved by innovations in processing and blade design and via improvements in alloy composition.

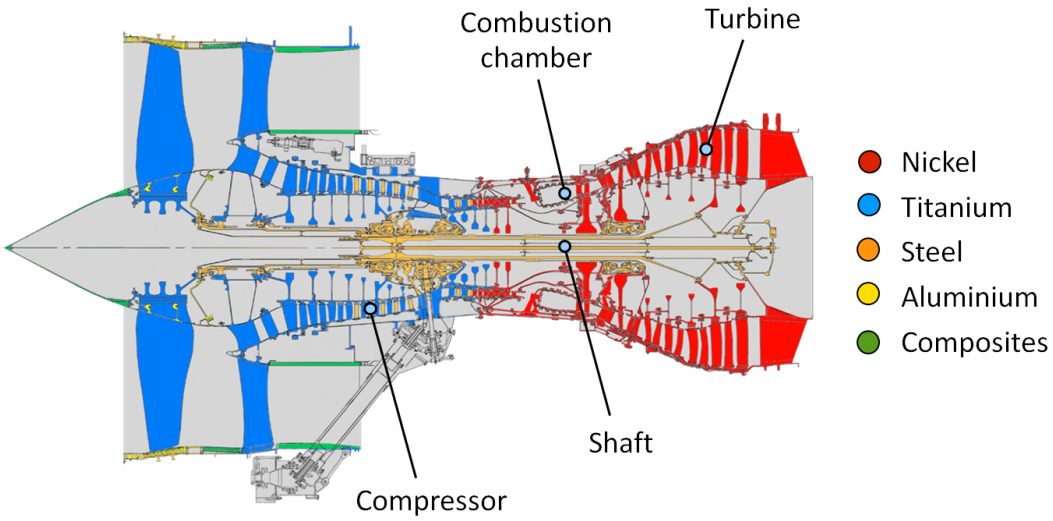

Figure 2.1: The Rolls-Royce Trent 800 engine showing the extensive use of nickel-based superalloys in the combustor and turbine sections [3]. (Image adapted from Rolls-Royce [4])

The first nickel-based superalloys were wrought alloys which were later replaced by conventionally cast alloys. Further improvement involved the introduction of directional solidification which produced columnar microstructures rather than an equiaxed grain

structure: blades cast with directional solidification showed much better creep behaviour than their predecessors [3]. Contemporary blades are cast using the single crystal method and, as a result, have no grain boundaries. This technique is better than conventional casting because the alloys can be heat treated at higher temperatures. This is due to the reduction of grain boundary strengthening elements such as boron and carbon which decrease the melting temperature of the alloy [3]. Hence, single crystal alloys show less microsegregation and eutectic content and have, therefore, improved fatigue properties. In addition to improvements in casting methods, changes in the design of the turbine blades have contributed to increases in efficiency. Turbine blades with special cooling channels allow gas steam temperatures above the melting temperature of pure nickel. Moreover, significant progress has also been achieved by optimising the chemistry of nickel-based single crystal superalloys [5].

The general trends in composition across the generations of nickel-based superalloys are given in Tab. 2.1. It shows that later generations contain more rhenium and tungsten because at the end of the 1970s it was found that these refractory elements, in particular rhenium, markedly improve the creep resistance of nickel-based superalloys [6]. Alloy designers refer to this improvement as the rhenium-effect. As a result, over the past few decades the rhenium content of single-crystal superalloys has been steadily increased until the average content of rhenium in nickel superalloys reached its limit at around 6 wt.%. The amount of rhenium that can be added is limited for two reasons: firstly, due to its low availability relative to the demand for it, rhenium is among the most expensive industrial metals; secondly, too large concentrations of refractory elements can lead to the formation of detrimental topologically-close packed phases. In order to solve the latter problem attention is now being focused on replacing rhenium with ruthenium (as shown in Tab. 2.1), because it has been suggested that ruthenium has the effect of reducing the susceptibility to the precipitation TCP phases, albeit for reasons which are not well understood [7].

Alloy name	PWA 1480	CMSX-4	TMS 75	TMS 138	TMS 162
Generation	1^{st}	2^{nd}	3^{rd}	4^{th}	5^{th}
Creep performance [°C]	1010	1050	1070	1100	1110
Element	Alloy composition (wt.%)				
Ni	bal.	bal.	bal.	bal.	bal.
Co	5.0	9.6	12.0	5.9	5.8
Cr	10.0	6.5	3.0	2.9	2.9
Mo	0.0	0.6	2.0	2.9	3.9
W	4.0	6.4	6.0	5.9	5.8
Re	0.0	3.0	5.0	4.9	4.9
Al	5.0	5.6	6.0	5.9	5.8
Ti	1.5	1.0	0.0	0.0	0.0
Ta	12.0	6.5	6.0	5.6	5.6
Hf	0.0	0.1	0.1	0.1	0.09
Ru	0.0	0.0	0.0	2.0	6.0

Table 2.1: The compositions of common cast nickel-based superalloys [3]. The creep performance is indicated by the highest temperature at which rupture occurs in more than 1000 h at 137 MPa (see Fig. 1.17 in [3]). The balance (bal.) is nickel.

2.1.2 Influence of the microstructure on the mechanical properties

The outstanding properties of nickel-based superalloys are derived mainly from the existence of ordered γ' domains ($L1_2$ structure) in a disordered γ matrix phase, with all the atoms occupying the sites of an underlying fcc lattice forming a single crystal [3]. Figure 2.2 shows typical γ' precipitates in a γ matrix (dark channels) of a nickel-based superalloy. The elements Al, Ti, Nb, V and Ta prefer to segregate to the γ' phase [3]. In contrast, Co, Fe, Cr, Ru, Mo, and Re prefer to segregate to the γ phase. Moreover, W may partition in both γ and γ' [3]. The proportion of the latter elements should be high in order to keep the fraction of γ phase as small as possible since creep deformation on the microscale occurs mainly in the γ channels lying between γ' precipitates. Hence, one would assume that the optimum microstructure would consist of pure γ' without any γ but it has been shown that the creep performance is best when the fraction of γ' is about 65% [8]. Alloys with larger γ' fractions have worse creep resistance due to a change

in the rafting direction as a result the inhomogeneous microstructure [8]. Moreover, the composition of the alloy must be appropriately chosen in order to control the lattice misfit between γ' and γ. If the lattice misfit is too large, then the γ/γ' interfacial energy might cause γ' coarsening which leads to a loss of coherency [9].

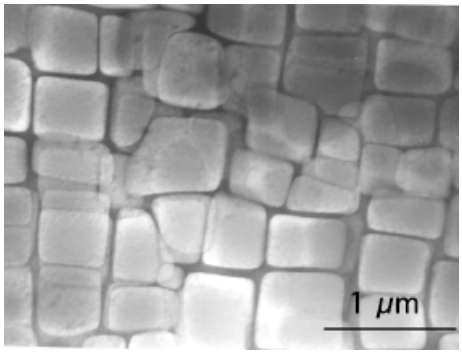

Figure 2.2: A transmission electron micrograph showing large fractions of γ' precipitates (brighter cuboidal structures) in a γ matrix (dark channels) [10].

If carbon is added to superalloys at levels of up to 0.2 wt.% it tends to form carbides with refractory elements such as Ti, Ta, and Hf [11]. This is desirable for disk applications where the carbides are present at the grain boundaries because they lead to an increase in rupture strength at high temperatures and can prevent grain boundary sliding. Besides their strengthening effect on grain boundaries, carbides formed in the matrix can also reinforce the alloy. Moreover, carbides have the benefit of linking elements that during service would otherwise promote phase instabilities and consequently the formation of detrimental phases [12]. However, Liu et al. [13] showed that the amount and distribution of carbides has to be carefully controlled because carbides can provide crack initiation sites which can eventually lead to fracture. Furthermore, they worsen creep properties when present in single-crystal blade alloys.

Apart from the phases described so far, superalloys can also contain topologically close-packed (TCP) phases such as the σ, χ, μ, δ, P, R and Laves phases [11]. In nickel-based superalloys these phases usually form at high temperatures (above 800°C [14]) and cause mechanical properties to deteriorate [15, 16]. TCP phases contain high concentrations

of creep-strengthening elements and usually precipitate from the γ phase. In general, they have plate-like or needle-like shapes [17], although block-like shapes, found to be less detrimental, have also been observed [18]. Due to their brittleness [19] at low temperatures and high strain rates, TCP phases act as barriers to moving dislocations and therefore can cause crack initiation. Even more important is the effect of the TCP phases on the mechanical strength of the alloy: during their precipitation, the TCP phases deplete the γ/γ' structures of refractory metals, thereby causing a considerable decrease in solid solution strengthening. Although several different TCP phases have been observed in superalloys, the influence of each individual phase on mechanical properties has not been studied in detail. Probably the most important, and consequently best studied, phase is the σ phase (see Fig. 2.3). It is commonly the first TCP phase to form and provides nucleation points for other TCP phases [14]. The σ phase is a physically hard, mostly plate-like phase. Precipitates of the μ phase are needle-like or plate-like [19] and affect the creep strength by disturbing the regularity of the γ/γ' microstructure and consequently softening the alloy [20]. However, precipitates of the μ phase play only a minor role in the progress of crack initiation. This observation also holds for the Laves phases, C14, C15 and C36, although it has been shown that a high proportion of Laves phases in superalloys can lead to a decrease in tensile ductility and a deterioration of creep properties.

Despite the variation in their deleterious effects, all TCP phases observed in superalloys share a number of characteristics which allow them to be treated as one class of structures. Fortunately, TCP phases do not only form in multi-component systems such as nickel-base superalloys but they occur as intermetallic phases found in unary, binary and ternary systems. This gives us the opportunity to build up an understanding of TCP phase stability in multi-component systems by starting from materials which are less complex. The most important characteristics of TCP phases will be discussed in the following section.

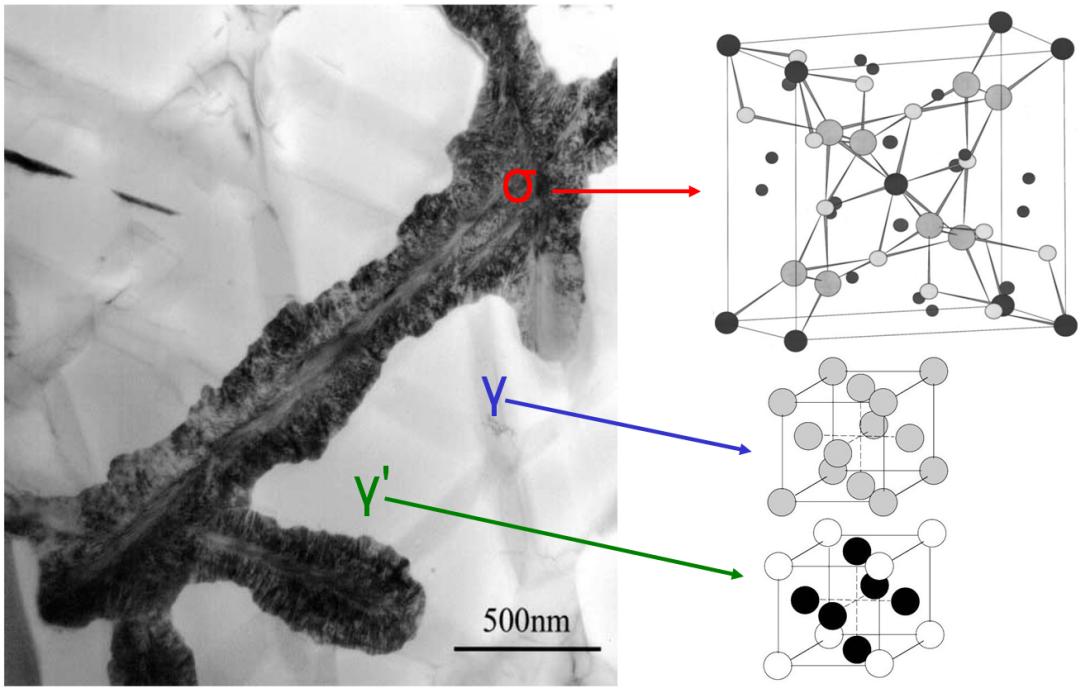

Figure 2.3: Left: A scanning electron micrograph showing the σ phase precipitating from the γ phase (dark channels) and spreading into the γ' [14]. Right: Schematic illustrations of the crystal structure of σ (top), γ (middle) and γ' (bottom). Images from [21].

2.2 Topologically close-packed phases

Over the past decades many papers discussing TCP phases have been published, however, most studies address specific aspects of TCP phase formation of only a certain type of TCP phase. The only comprehensive work on TCP phases as a class of structures was published by Sinha [22] in 1972. In this paper, Sinha not only discusses the characteristic topology of TCP phases in detail but also accounts for the essential features of the structures in terms of, for example, alloy physics and alloy chemistry and tries to understand the stability mechanisms. The most important characteristics and unique topological features of TCP phases discussed in this paper together with more recent findings that are relevant for this work are discussed in this section.

2.2.1 Topology

TCP phases were first characterised by Frank and Kasper [23, 24] who showed that a number of complex phases can be represented as packings of hard spheres of different radii. The basic stacking units are the co-ordination polyhedra (Fig. 2.4) which have exclusively triangular faces. The most important polyhedron is the 5-fold symmetric icosahedron, Z12, where 12 refers to the co-ordination number Z of the atom at the centre of the polyhedron. Z12 polyhedra are found in all TCP phase where they are combined with more highly co-ordinated Frank-Kasper polyhedra namely, Z14, Z15 and Z16. Such polyhedra can be sub-divided into a number of tetrahedral groupings of four atoms each. Regular tetrahedra are found only when the polyhedra are icosahedra, i.e. when they have a co-ordination number of 12. Thus, all of the interstices of such a structure are at the centre of a tetrahedron. Tetrahedral interstices represent the smallest possible voids between spheres of moderate size difference [22]. Hence, Beattie and Hagel [25] termed these structures topologically close-packed phases.

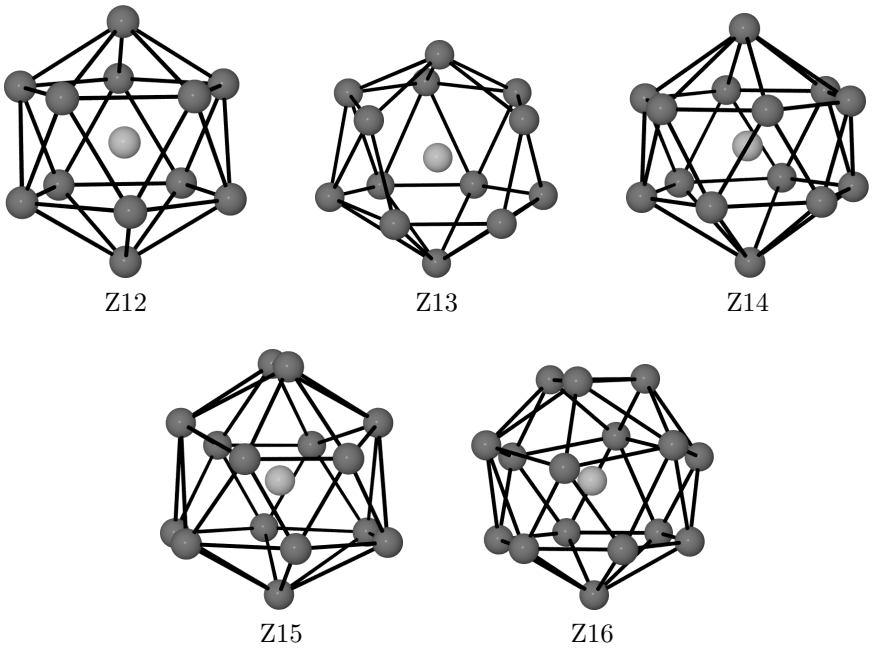

Figure 2.4: The Frank-Kasper co-ordination polyhedra Z12, Z14, Z15 and Z16 including the Z13 co-ordination polyhedra of the χ phase.

In practice, the co-ordination polyhedra distort in order to fill space completely or conform to the translational periodicity of the lattice. This is demonstrated in Fig. 2.5 for the simplest two TCP structure-types, A15 and C15, which have no internal degrees of freedom. Importantly, it shows that for the Z12 co-ordination polyhedra half of the neighbouring atoms of the C15 polyhedron are located much closer to the central atom as compared to the equidistantly distributed neighbours of the A15 phase. This difference in the degree of distortion is reflected not only in dissimilar bond lengths as shown in Fig. 2.5 but also in different bond angles. Kasper's investigations on the nearest-neighbour distances of hard sphere packings indicated that atoms should occupy the sites from lowest to highest co-ordination with increasing atomic size [26]. This is generally observed amongst the TCP phases but there are exceptions [27]. Table 2.2 summarises the different Frank-Kasper co-ordination polyhedra for the most common TCP phases, namely A15, σ, χ, P, R, δ, μ, M and the Laves phases. Three polytypes of the Laves phases are observed: the cubic C15-$MgCu_2$, the hexagonal C14-$MgZn_2$, and the dihexagonal C36-$MgNi_2$ structure. These polytypes are related to each other in that their co-ordination polyhedra and basic unit layers are identical, while the stacking sequence of the layers is different. Note that the χ phase is strictly speaking not a member of the topologically close-packed family of structures because it contains atoms with co-ordination shells that are made up of 13 neighbours (Z13 co-ordination polyhedra) which have non-triangular faces. However, studies indicate that the same principles hold for the χ phase as for the TCP phases [22]. The structure types shown in Table 2.2 are ranked according to their fraction of 12-fold sites, f_{12}, as per the last column.

The Frank-Kasper polyhedra can be generated from hexagonal close-packed layers by the systematic omission of certain atoms in the close-packed layers. The resulting layers are the so-called Kagome nets. These nets can be stacked in several ways, and the resulting structures can be analyzed in terms of the stacking sequence which greatly simplifies the classification of the TCP structures. The advantage of the layer description

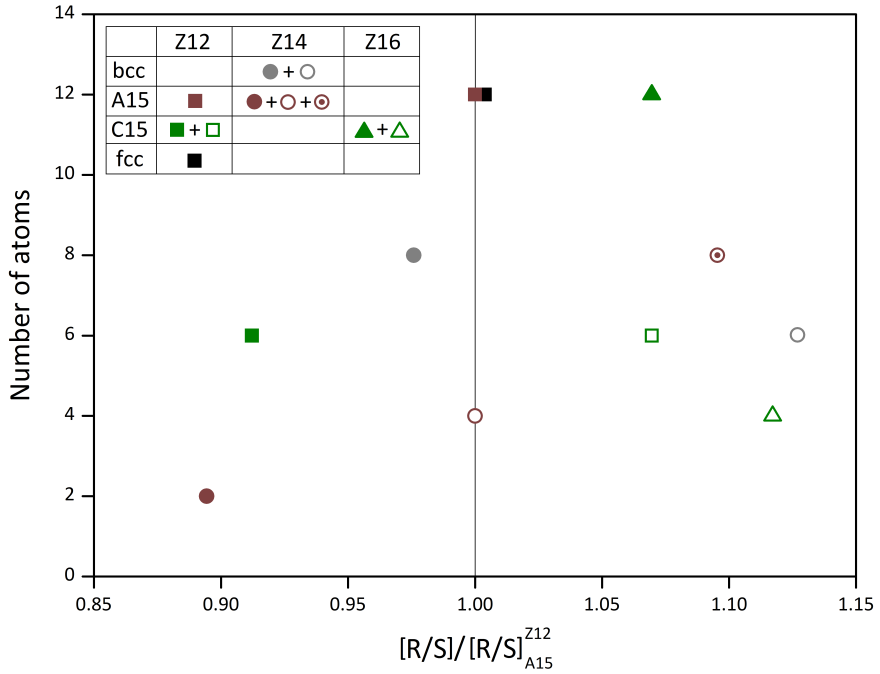

Figure 2.5: The number of neighbours for the individual co-ordination polyhedra Z12 (squares), Z14 (circles) and Z16 (triangles) of fcc (black), bcc (grey), A15 (brown) and C15 (green) versus the normalised distance. The distances, R, are normalised by the corresponding Wigner-Seitz radius, S, of each structure. First, second and third nearest-neighbours are indicated with full, empty and dotted symbols, respectively.

is its more intuitive two-dimensional nature, as compared to the stacking of co-ordination polyhedra. However, these two descriptions are not mutually contradictory since layers are just projections, in a certain direction, of co-ordination polyhedra stacked together. These layers allow us to explain the slip characteristics of TCP phases by considering the high degree of close-packed planar stacking compared to fcc, bcc and hcp structures.

Shoemaker and Shoemaker [28], as well as Andersson [29], suggested an alternative classification of TCP phases in terms of elementary units. These units, like parallelograms, are composed of antiprisms. The TCP phases can then be treated as a hierarchy of structures from simple to complex where higher order structures are built from lower order structures. A very good overview of the classification in terms of elementary units is given by Kuo et al. [30]. In their paper, TCP phases are classified into three groups,

Structure	Atoms in basis	Neq. sites	Co-ordination polyhedra Z12	Z13	Z14	Z15	Z16	$\langle Z \rangle$	f_{12}
fcc/hcp	1/2	1/2	(1)	0	0	0	0	12.00	1.00
C14	12	3	8	0	0	0	4	13.33	0.67
C15	24	2	16	0	0	0	8	13.33	0.67
C36	24	5	16	0	0	0	8	13.33	0.67
M	52	11	28	0	8	8	8	13.36	0.54
μ	13	5	7	0	2	2	2	13.39	0.54
R	53	11	27	0	12	6	8	13.39	0.51
δ	56	14	24	0	20	8	4	13.43	0.43
P	56	12	24	0	20	8	4	13.43	0.43
χ	58	4	24	24	0	0	10	13.10	0.41
σ	30	5	10	0	16	4	0	13.47	0.33
A15	8	2	2	0	6	0	0	13.50	0.25
bcc	1	1	0	0	(1)	0	0	14.00	0.00

Table 2.2: The co-ordination polyhedra of the most common TCP phases. The third column gives the number of non-equivalent (neq.) sites. The co-ordination polyhedra of fcc, hcp and bcc are also given (the 12- and 14-fold co-ordination polyhedra are given in parenthesis since they are not the true Z12 and Z14 Frank-Kasper polyhedra). $\langle Z \rangle$ is the average co-ordination number. Structures are ranked from the lowest to highest fraction of 12-fold polyhedra, f_{12}.

the hexagonal antiprisms, the pentagonal antiprisms and the hexagonal-pentagonal antiprisms. The first group contains all structures with elementary structural units Cr_3Si and Zr_4Al_3, i.e. all the structures which are related to σ. This group also contains the A15 phase. Pentagonal antiprisms are elementary structural units of Laves phases related structures. They include the Laves, μ and M phases. The structure of the P phase has mixed hexagonal and pentagonal antiprisms and belongs to the last class that also includes R and δ. Unfortunately, the χ phase cannot be allocated to one of the groups as the χ phase does not belong to the family of TCP structures as was discussed above.

2.2.2 Factors controlling TCP phase stability

Pioneering work in the understanding of factors controlling the stability of intermetallic phases was carried out during the first half of the 20th century by Häag, Pauling, Laves and, in particular, Hume-Rothery. In the 1920's, Hume-Rothery distinguished the factors

which influence compound formation and which control alloying behaviour. Based on the investigation of Cu, Ag and Au alloys, he claimed that a connection between the formation of a specific structurally complex alloy phase in a certain composition range, atomic size, crystal structure and a particular concentration of valence electrons exists. Since the publication of Hume-Rothery's important findings, many studies investigating the stability of transition metal alloys with respect to the three factors have been carried out. In the following, the relevant studies related to TCP phase formation are discussed.

Valence electron concentration

In 1948, Sully and Heal, by comparing σ phases in Co-Cr and Cr-Fe, were the first to realise that the valence electron concentration strongly affects the stability range of the σ phase [31]. In the early 1950s discoveries of TCP phases in other binary and ternary systems allowed Beck and his collaborators to investigate the formation of these TCP phases in terms of the valence electron concentration in more detail [32–34]. However, rather than working with the number of valence electrons N, Beck et al. chose to work with the number of holes in the d-band, N_h, as per Pauling's work on electron-hole theory from 1938 [35].

Pauling combined theory and experimental observations in order to provide a coherent explanation for the magnetic properties of the first long-period transition elements (Cr, Mn, Fe, Co and Ni). He found that it is a characteristic of transition elements that the $3d$ orbitals, which should host 10 electrons (5 electrons per spin), remains only partially-filled due to hybridization with 4s and 4p orbitals. This led Pauling to the interpretation that the five d-orbitals of each spin could be divided into 2.44 non-bonding and 2.56 bonding orbitals. Moreover, he assumed that for Cr 5.78 hybrid *spd* electrons (from a total of 6 electrons) are bonding, which leaves 0.22 electrons added to the $3d$ non-bonding orbitals. As a result, for Cr there are $2 \times 2.44 = 4.88$ holes in the d-shell, or an electron hole number of 4.66 (4.88 - 0.22). Extending this to Mn, Fe, Co and Ni, and assuming that the number of *spd*-bonding electrons remains constant at 5.78 with a linear increase in

non-bonding electrons, gives electron vacancy numbers of 3.66 for Mn, 2.66 for Fe, 1.66 for Co, and 0.66 for Ni. The magnetic moments predicted with this model for Ni, Co and Fe are in close agreement with experimental results at zero temperature. In general, the electron vacancy numbers N_h are extended to elements other than Cr, Mn, Fe, Co and Ni by assuming that vacancy numbers are constant within a periodic group. This approach was criticised by Hume-Rothery [36] who pointed out that the compressibility of Cr, Mo and W are significantly different, meaning that the bond strengths are different and hence that the effective valence should also change within a periodic group. In addition, several studies of ternary systems lend additional support to a composition dependency of N_h values [32, 37]. From the study of these simple systems it is clear that the N_h values are also dependent on composition and are not the same as for the first period.

Nevertheless, for simplicity, it was common practice to assume almost constant vacancy numbers within a periodic group. A possible set of electron hole numbers for transition elements based on Pauling's original predictions are listed in Tab. 2.3.

Period	Group				
	VI	VII	VIII	IX	X
4	Cr, 4.66	Mn, 3.66	Fe, 2.22*	Co, 1.71*	Ni, 0.61*
5	Mo, 4.66	Tc, 3.66	Ru, 2.66	Rh, 1.66	Pd, 0.66
6	W, 4.66	Re, 3.66	Os, 2.66	Ir, 1.66	Pt, 0.66

Table 2.3: Electron hole numbers N_h for transition elements used by Beck et al. to determine the range over which TCP phases such as σ, P, R, δ and μ are stable [32–34]. The numbers marked with * are determined by magnetic mismatch measurements. All other values are extrapolations and estimates of Pauling's predictions.

Beck and his collaborators used these values to calculate the average hole number $\bar{N}_h$ of an alloy from the sum of the hole number of the constituents weighted by their atomic concentration in the alloy. $\bar{N}_h$ was applied to characterise the range over which TCP phases such as σ, P, R, δ and μ are stable. It was found that, in general, all studied TCP structures predominantly occur in preferred $\bar{N}_h$ ranges in binary and ternary alloys. Although there is a considerable overlap between the preferred valence electron ranges for

the individual TCP phases, whenever some of these phases co-exist, a certain sequence of occurrence with respect to the valence electron concentration is retained. From their study of binary alloys of $4d$ and $5d$ transition elements, Haworth and Hume-Rothery were the first to find that the following succession of phases exists with increasing valence electron concentration [38]:

$$\text{bcc} \rightarrow \text{TCP}(\text{A15} \rightarrow \sigma \rightarrow \chi) \rightarrow \text{hcp} \rightarrow \text{fcc}.$$

There is a similar trend in the phase sequence given by f_{12} for bcc, A15, σ, χ, hcp and fcc (see Tab. 2.2). Thus, it is tempting to relate the structural stability of the phases to the number of 12-fold sites in the unit cell, as suggested by Berne et al. [39]. In chapter 6 we will investigate whether the structural trend bcc $\rightarrow$ A15 $\rightarrow \sigma \rightarrow \chi \rightarrow$ hcp $\rightarrow$ fcc can indeed be explained by the percentage of icosahedral sites.

Difference in atomic size

The valence electron concentration cannot fully explain cases where the electron hole condition is fulfilled but no TCP phases are formed. Nor can it explain the existence of TCP phases such as the Friauf-Laves phases because these are formed over a wide range of concentrations below 8 electrons. Laves [40], for the Friauf-Laves phases, and Duwez [41], for the σ phase, showed that the difference in atomic size of the constituent elements is also of significant importance for the stability of TCP phases. A comprehensive investigation into the influence of size difference on the stability of TCP phases was carried out by Watson and Bennett [42]. They studied the ratio of the equilibrium atomic volume of the A and B transition metal elements, V_A/V_B, in A-B binary alloys and found that specific ranges of V_A/V_B can be associated with specific TCP structure-types.

Electronegativity

The third factor thought to affect the stability of TCP phases is the electronegativity difference. Although many studies investigating the influence of electronegativity on the structural stability of a variety of intermetallic compounds have been carried out, literature focusing on TCP phases related to electronegativity is rare and also inconclusive. Sinha [22] only addresses this topic in a short comment about the observation that most A-B binary TCP phases involve the combination in which A belongs to a group towards the left of group VII in the periodic table and B lies in groups to the right of this column. A theoretical tight-binding study on the stability of 2:1 stoichiometric binary transition metal compounds [43], which showed that the Laves phases can be separated into their correct domains from the $CuAl_2$ (C16) and $MoSi_2$ ($C11_b$) phases by the two co-ordinates of valence electron concentration and size-factor difference, demonstrated that the electronegativity difference plays only a minor role for the stability.

2.3 TCP phase prediction

After the discovery of the σ phase in the IN-100 nickel alloy and the observation of its ability to significantly degrade creep rupture properties [44], considerable efforts were made to try to understand the occurrence of TCP phases, so that their formation could be suppressed. Originally, the occurrence of the σ phase was controlled by modifying the alloy composition, based on the traditional Edisonian approach, but later the optimisation process also utilised information provided by modelling techniques which predicted the tendency of austenitic alloys to precipitate TCP phases. These methods are based on the understanding of the factors controlling the stability of TCP phases which had been gathered from studies of binary, ternary and quaternary TCP phases as discussed in the previous section.

In the following subsections, the main commercially utilised methods for alloy design, and in particular those used to control TCP phase formation, will be discussed. The first

method, PHACOMP, an acronym for PHAse COMPutation [45], was the most commonly used method until the beginning of the 1990s [18]. Since the development of PHACOMP in the mid 1960s, many more methods have been proposed, with the most important being NewPHACOMP. In parallel, a more general approach to materials modelling was introduced by the CALPHAD group in the late 1960s. Their goal was to establish sophisticated thermodynamic database systems that allow a consistent description of phase diagrams to predict stable phases, as well as their respective thermodynamic properties, in regions where no experimental information exists.

2.3.1 PHACOMP-like methods

In 1964, Boesch and Slaney [46] used Rideout and Beck's [32] concept of the average number of holes was described in Sec. 2.2.2 to predict the presence of σ phases in complex commercial Ni and Co-based superalloys. This approach became known as PHACOMP. The method evaluated the average number of holes based on the composition of the γ matrix as it was assumed that TCP phases form exclusively within the γ phase. Therefore $\bar{N}_h$ is calculated by

$$\bar{N}_h = \sum_i c_i N_{h,i}, \tag{2.1}$$

where c_i is the atomic fraction of element i in the γ phase and $N_{h,i}$ is its corresponding electron vacancy number as given in Tab. 2.3. Boesch and Slaney argued that values of $\bar{N}_h$ greater than a critical electron vacancy number concentration are an indication of possible TCP phase formation during long-term service of an alloy in the critical temperature range. The limit of stability of the γ phase is reached when $\bar{N}_h > \bar{N}_h^{crit} \approx 2.45 - 2.50$. In the early days of PHACOMP, the γ composition was estimated from the overall alloy composition based on empirical observations of the formation of secondary phases like γ', borides and carbides, as explained in detail by Sims [18]. In order to get the correct residual composition of the γ phase by discarding the composition of all secondary phases from the whole alloy, all phases must be known exactly, otherwise the application of the

PHACOMP method will lead to unsatisfactory results [47]. Hence, nowadays, PHACOMP calculations are usually accompanied by phase diagram calculations like CALPHAD to provide more accurate results for the composition of γ and γ' [48].

In Sec.2.2.2 one problem of PHACOMP has already been highlighted, namely the uncertainty of elemental N_h values and the fact that the values neither show any electronegativity dependence nor change with atomic size. According to Morinaga [49], this lack of physical footing is the reason why PHACOMP is poor in describing the precipitation of the μ phase. Moreover, for some new alloy compositions which contain elements with unknown N_h values, PHACOMP was not applicable without adjusting the parameters [18]. However, more concerning is the threshold, $\bar{N}_h^{crit}$, because it is found to be dependent on the particular alloy system and TCP structure type [18]. Thus, in practice it must be revised for each individual alloy. Moreover, as the threshold is temperature-independent, PHACOMP also does not give any information about the temperature range where σ may be stable [50].

NewPHACOMP and similar approaches

In 1984, the poor performance of PHACOMP, in particular in describing the precipitation of the μ phase, led Morinaga's group to propose a similar one-parameter method called NewPHACOMP [49], or the '*d*-electrons concept' [51], which aimed to predict the occurrence of TCP phases such as σ, μ and Laves. In their first paper, Morinaga and Yukawa retain the original PHACOMP concept of a single-valued function determining the tendency of the γ phase to form TCP phases. However, the number of electron holes, N_h, which is the important parameter in the PHACOMP method, is dropped in NewPHACOMP. Instead, a parameter Md, which is an average energy level of *d*-orbitals of the alloying transition metals, was introduced, and used to treat the phase stability in austenitic alloys. The average Md, which is the compositional value for an alloy, analogous

to the average electron vacancy number, $\bar{N}_h$, is defined as:

$$\bar{Md}_\gamma = \sum_i c_i Md_i, \tag{2.2}$$

where c_i is the atomic fraction of element i and Md_i is the value of Md for each element constituting the γ phase. Note that it has long been argued that if the assumption that TCP phases form exclusively within the γ phase is correct, as studies have indicated that they can also form from the γ/γ' interface [14]. More recent studies by Yukawa [51], Zang [52] and Caron [53] have investigated the relation between the average value of Md parameters calculated from the estimated γ matrix composition $\bar{Md}_\gamma$ and from the total composition, $\bar{Md}_{alloy}$. Caron's study showed that there is almost a linear relation between $\bar{Md}_\gamma$ and $\bar{Md}_{alloy}$ which indicates that the study of both parameters does not affect the predictability of this method. This conclusion will be verified in chapter 4.

Md values for individual elements are obtained on the basis of theoretical calculations of electronic structures using the discrete variational-$X\alpha$ cluster method [54]. This molecular orbital method is based on the Hartree-Fock-Slater approximation which is used to calculate the electronic structure of Ni_3Al and a cluster model for a transition metal M added to Ni_3Al. By adding M to Ni_3Al, new eigenstates appear above the Fermi level E_F due to the d-orbitals of the additive element. The average of the energy levels of the d-orbitals for an alloying element is defined as Md. The values of Md for various transition metals and Cu, Al and Si, where the zero level was set to the Fermi level of Ni_3Al, are listed in Tab. 2.4. The Md values for non-transition metal elements were determined empirically to be 1.9 eV. Figure 2.6 shows the relation between Md and N_h values. It shows that the Md values only differ significantly from the N_h values for the late $3d$ transition metals. This variation in the Md values closely resembles that proposed independently by Watson and Bennett in the same year as Morinaga et al. proposed the NewPHACOMP method [42]. They plotted the stability ranges of the non-Laves TCP phases of binary transition metal alloys as a function of the average d-band hole count,

$\bar{N}_h$, observing that the TCP phases are stable over a considerable range of $\bar{N}_h$. They suggested an effective number of holes N_h^{eff}, as shown in Fig. 4 of [42], which were chosen such that all the TCP phases were associated within the narrowest possible range of $\bar{N}_h^{eff}$. Like Morinaga they found that the values for the late $3d$ transition metals deviate from the linearity of N_h, reflecting the influence of atomic size and magnetism.

Element		Md [eV]	Element		Md [eV]
	Ti	2.271		Zr	2.944
	V	1.543	$4d$	Nb	2.117
	Cr	1.142		Mo	1.550
	Mn	0.957		Hf	3.020
$3d$	Fe	0.858	$5d$	Ta	2.224
	Co	0.777		W	1.655
	Ni	0.717		Re	1.267
	Cu	0.615		Al	1.900
				Si	1.900

Table 2.4: A list of Md numbers for various elements used for NewPHACOMP calculations [49].

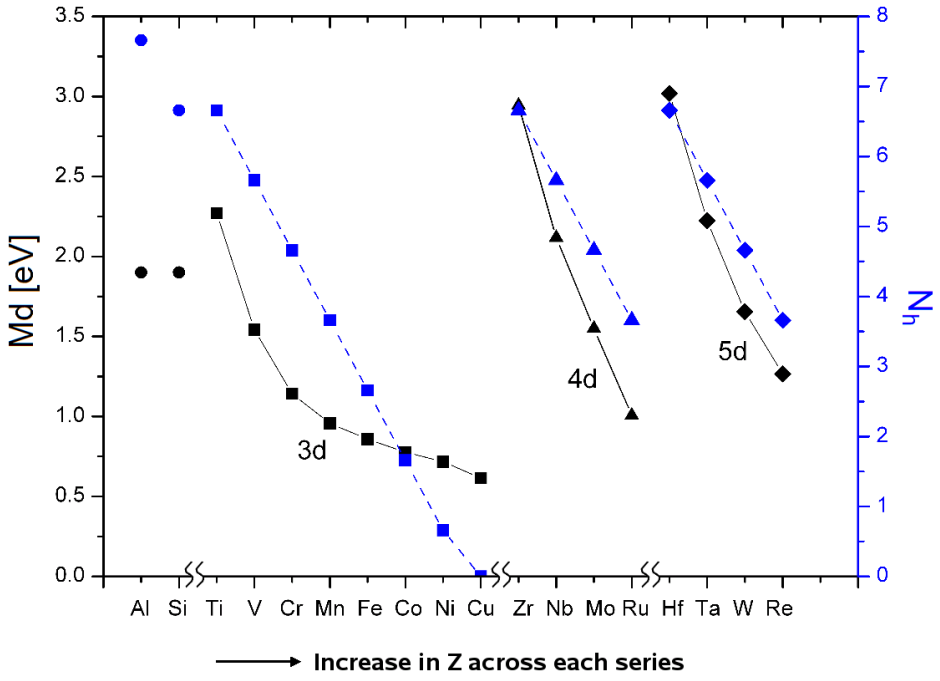

Figure 2.6: N_h (blue, dashed line) and Md values (black, solid line) for transition elements used in PHACOMP and NewPHACOMP calculations, respectively.

As in the case of the PHACOMP method, an alloy is predicted to be prone to the precipitation of TCP phases when the Md_γ value becomes larger than a critical value dependent on the phase type. However, unlike in the PHACOMP method the evaluation of a variety of phase diagrams for different ternary systems at various temperatures led to a description of the temperature dependence of the critical value $\bar{Md}^{crit}$ value for the σ phase,

$$\bar{Md}^{crit}(T) = 6.25 \times 10^{-5} \times T + 0.834, \tag{2.3}$$

where, T is the temperature in Kelvin. This temperature dependence implies that alloys which are σ-free at low temperatures stay σ-free at higher temperatures because the critical value increases with temperature whereas the composition of the γ phase with its elementary Md values does not change as it is assumed by Morinaga [49]. However, recent experimental studies, carried out by Rae and Reed [14], have shown that this temperature dependence which was originally obtained from ternary systems, is not valid for multi-component systems. They observed that two second-generation superalloys, RR2073 and RR2075, do not form σ phases at an annealing temperature of 800°C. σ phases are, however, formed at 950°C and maintain stability at temperatures of 1050°C. Moreover, it is well known that the microstructure of the superalloys and the composition of the γ phases vary with temperature [2, 3, 11]. This leads to the conclusion that the time/temperature-dependence of $\bar{Md}^{crit}$ should be revised. Besides this discrepancy, NewPHACOMP has proved to be more suitable in the search for σ- and μ-free alloy compositions than its predecessor PHACOMP. However, like PHACOMP, due to its semi-empirical nature, there are still a number of questions concerning the applicability and theoretical justification of NewPHACOMP.

In the original paper of NewPHACOMP, Morinaga et al. [49] also indicated that the ionicity and the bond order which show the strength of ionic and covalent bonds between elements in alloys can be very useful in understanding mechanical properties. This led to the development of advanced NewPHACOMP models [55] which also include the bond

order Bo values obtained from DV-$X\alpha$ calculations. By calculating $\bar{Bo}$ which follows the same procedure as the calculation of $\bar{Md}$, Matsugi et al. [56] plotted $\bar{Md}$ and $\bar{Bo}$ values of commercial cast single crystal alloys in a ($\bar{Md}$, $\bar{Bo}$) plane, and showed that successful cast alloys tend to cluster closely in the ($\bar{Md}$, $\bar{Bo}$) plane. This area is the target region for the design of high-performance superalloys. While Md represents chemical properties such as phase stability, the new parameter Bo is related in some way to the strength of the alloy [57]. Therefore, the purpose of Bo is to predict mechanical properties but Bo does not help to improve the prediction of σ phase formation.

2.3.2 CALPHAD

In the CALPHAD (CALculation of PHAse Diagrams) method, thermodynamic parameters determined on the basis of a variety of experimental data (such as phase boundaries, activities, specific heats or enthalpies) are used to parameterize an expression for the Gibbs free energy, G, for each phase [48,58,59]. Once the Gibbs free energy is parameterized, the stable phases in the phase diagram may be obtained by minimising the Gibbs free energy. Moreover, one may derive other quantities from it in the following way:

$$S = \frac{dG}{dT}\Big|_P, \qquad H = G + TS, \qquad V = \frac{dG}{dP}\Big|_T, \qquad C_P = -T\left(\frac{d^2G}{dT^2}\right)\Big|_P . \tag{2.4}$$

If more than one phase is stable within a system, the thermodynamic properties of that system depend on the properties of the individual phases. They contribute to the total Gibbs free energy as

$$G = \sum G^{(i)} n^{(i)}, \tag{2.5}$$

where $n^{(i)}$ is phase fraction and $G^{(i)}$ the Gibbs energy of phase i. CALPHAD employs a number of models and approximations to describe the temperature, pressure and concentration dependence of the free energy functions so that the Gibbs free energy of a phase

can be written as

$$G^{(i)} = G_T^{(i)}(T,x) + G_P^{(i)}(P,T,x) + G_m^{(i)}(T_C,\beta_0,T,x), \tag{2.6}$$

where $G_T(T,x)$ is the contribution to the Gibbs free energy from temperature, T, and the composition, x, $G_P(P,T,x)$ is the contribution of the pressure, P, and $G_m(T_C,\beta_0,T,x)$ is the magnetic contribution of the Curie temperature, T_C, and the average magnetic moment per atom, β_0. For the description of the temperature dependence it is common to use a power series representation for pure substances such as pure elements or compounds. A common form is

$$G_T(T,x) = a + bT + cT\ln(T) + \sum d_n T^n, \tag{2.7}$$

where a, b, c and d_n are composition-dependent coefficients. This expression is only valid for temperatures above the Debye temperature. There also exist expressions for the pressure and magnetism dependence, but at normal pressures, contributions to the Gibbs energy due to pressure are neglected. For multi-component systems the Gibbs energy is written as a sum of three contributions:

$$G = G_0 + G_{ideal} + G_{xs}. \tag{2.8}$$

The first term G_0 corresponds to the Gibbs energy of the pure elements in the given phase, the second term, G_{ideal}, is the Gibbs free energy contribution due to the entropy of mixing of an ideal solution. The last term G_{xs} is the excess term of mixing, the difference between G and $G_0 + G_{ideal}$. Commonly used models for the calculation of G_{xs} include those for stoichiometric phases, regular solution type models for disordered phases, and sublattice models for ordered phases having a range of solubility or exhibiting an order/disorder transformation [48].

In CALPHAD the coefficients of the Gibbs energy functions are determined from experimental data for each system. In order to obtain an optimized set of coefficients, it

is desirable to take into account all types of experimental data starting from unary and binary systems and then extrapolating to ternaries and multi-component alloys. In recent years increasing emphasis has been placed on supplementing experimental databases with data from ab-initio calculations, such as structural energies and elastic and magnetic properties. An excellent review by Turchi et al. [60] discusses present phenomenological methodologies for successfully casting ab-initio results in a CALPHAD formalism for the subsequent prediction of thermodynamic properties of multi-component alloys [61]. It has also been indicated that an enrichment of databases with more and more first-principles data is, alone, not very helpful. Instead, fundamental information like relevant electronic parameters for electron phases (e.g. TCP phases) gained from first-principle calculations are required to improve the robustness and the predictive capability of CALPHAD.

In most of the literature (e.g. [48], [62] and [63]) CALPHAD is considered to be a successful tool that can provide predictions close to experimental measurements. However, most authors neglect to mention that CALPHAD's success mainly depends on the reliability of its thermodynamic database [59]. Given this, it is somewhat peculiar that most authors do not publish information about their database or, in general, the information which is included for their predictions. This makes it difficult to give a critical overview of the robustness of CALPHAD. For example, Saunders et al. [50] impressively demonstrate the capability of a newly developed database to predict not only TCP phase formation but also its potential to describe phenomena which cannot be understood with PHACOMP-like approaches, such as the effect of Re on TCP phase formation. Yet, in the description of the database, the set of multi-component systems against which the database is evaluated is not mentioned. Another example, which highlights the difficulty in drawing meaningful conclusions, is a paper by Rae and Reed [14] where Saunder's work is cited. They list CALPHAD calculations and the experimental results of TCP phase formation in 6 superalloys. Surprisingly, no superalloy is correctly predicted by CALPHAD in the temperature range that is investigated. Therefore, even if the authors' aim is neither to question nor support the robustness of CALPHAD, it significantly ques-

tions its applicability. Of course, however, it should be noted that it is not clear if citing Saunder's work implies that they used the same database.

A general review of the use of CALPHAD for nickel-based superalloy design was published by Zhao and Henry [64]. They compare the thermodynamic predictions using CALPHAD with experimental observations. The conclusion is that thermodynamic calculations do a reasonably good job in predicting the stability of γ' and a less satisfactory job for TCP phases, in particular for μ and P phases. The reason for the less accurate prediction in the case of μ and P phases is that they are poorly described within the thermodynamic database, as less experimental data for μ and P phases has been available for the validation of the database, in comparison to the well studied and more ubiquitous σ phase. A test series, including several different superalloys and TCP phases, shows that even with a state-of-the-art database, CALPHAD fails to predict 6 out of 12 experimental observations of TCP phases. Their main explanation for this disappointing result is that the limit of the target region for achieving optimum strength while avoiding TCP phase formation, namely the γ/γ' boundary, is not well defined. This is due to the fact that the thermodynamic stability of TCP phases is not well assessed in current nickel databases as a direct consequence of insufficient experimental phase diagram data for TCP phases. However, the authors maintain that CALPHAD can be used to indicate trends while also making clear that their lack of confidence in the predicted amounts and stability temperatures of TCP phases. This may be due to the general problem that thermodynamic data for multi-component systems are extrapolated mostly from binary and ternary systems.

As mentioned above, in recent years increasing emphasis has been placed on enhancing the thermodynamic databases and consequently on improving the predictive capability of the CALPHAD scheme by coupling the CALPHAD methodology with *ab initio* density-functional theory databases [60]. As will be discussed in chapter 5, the resulting ab-inito/CALPHAD-calculated phase diagrams are in good agreement with the experimental phase diagrams. Hence, in the future, the approach of combining *ab initio* methods with the CALPHAD formalism, will become increasingly important for the design of TCP

phase-free nickel-based superalloys as more and more *ab initio* data for TCP phases, and in particular for the less common TCP phases, becomes available.

2.4 Summary

In this chapter we have briefly discussed the practical importance of nickel-based superalloys due to their superior creep and fatigue behaviour. Moreover, we have given an overview of the main features of TCP phases which form in nickel-based superalloys if high concentrations of refractory elements are present. TCP phases are associated with creep resistance degradation mediated by acting as crack initiation sites or simply by depleting the Ni-rich matrix of potent solid solution strengthening elements. Existing semi-empirical methods like PHACOMP and CALPHAD which have been used to investigate the formation of TCP phases are based on an understanding that the factors controlling the stability of TCP phases are primarily the valence electron concentration and size difference, as deduced from studies of binary, ternary and quaternary TCP phases. These models are valid tools for predicting the formation of TCP phases as long as alloys are considered with compositions that are close to those multi-component systems which are already well understood. Thus, these models are good at interpolating data, but less useful for predictions, for example, on the effect of new elements added to an alloy. These limitations may be partly due to the simplified physical basis which underlies these models.

The following chapter will cast light on the physical basis of TCP phase formation in terms of the influence of the two most important factors controlling TCP phase formation, namely the valence electron concentration and the atomic size difference (see Sec. 2.2.2). Furthermore, the occurrence of binary, ternary and multi-component TCP phases will be investigated by means of two-dimensional structure maps. This investigation will focus mainly on transition metal systems (with occasional references to aluminium) for three reasons. Firstly, as explained in Sec. 2.1.2, TCP phases in Ni-based superalloys

involve high concentrations of transition metals. Secondly, TCP phases are commonly found as intermetallic phases in binary and ternary alloys. This allows us to build up an understanding of TCP phase stability in multi-component systems starting from less complex systems. Finally, the theoretical investigation carried out in chapter 6 will explain the observed structural trends by means of simple models for non-magnetic transition metal systems.

Chapter 3

Two-dimensional structure map for TCP phases

Over the past decades a number of structure maps investigating the influence of several parameters on the formation of transition metal alloys have been published [65–68]. The main purpose of these maps is to separate experimental data into characteristic domains of different crystal structures so that their formation can eventually be understood with respect to the structure map parameters. These two- or three-dimensional maps employ a variety of experimental and semi-empirical parameters which are chosen such that the best separation of the investigated crystal structures on the maps is obtained. However, the success of the structure maps in grouping the crystal structures of transition metal compounds varies significantly and their application is mostly limited to only certain families of structure-types and specific stoichiometries.

In this chapter we propose a two-dimensional structure map which allows for the investigation of not only binary but also multi-component systems, without being restricted to a particular stoichiometry or structure-type. We focus on two-dimensional rather than three-dimensional structure maps for ease of applicability, choosing the two co-ordinates of valence electron concentration and size factor difference. In Sec. 3.1, we will justify our choice of co-ordinates, followed by Sec. 3.2 where we will discuss the experimental

data used for the construction and the validation of the structure map. In Sec. 3.3, we will discuss trends which are observed within the structure map using experimental data for binary alloys. Moreover, the relation between the domains demarcating different TCP structure-types will be explained. In Sec. 3.4 investigations of ternary phase diagrams and multi-component TCP phases in Ni-based superalloys will demonstrate that TCP phases, regardless of the number of constituents, are located in the same regions of the structure map that are favoured by the binary compounds of the same structure type.

3.1 Choice of structure map co-ordinates

The average electron concentration and the difference in atomic size are, as explained in Sec. 2.2.2, the most important factors for the formation of TCP phases regardless of the number of constituent elements [22]. As discussed in Sec. 2.3.1, the influence of the valence electron concentration on the stability of TCP phases was studied in great detail by Rideout and Beck [32–34] who effectively used a one-dimensional structure map with the average number of holes, $\bar{N}_h$, as its only axis in order to identify the preferred regions of TCP phase formation. The first two-dimensional structure map for TCP phases including a size factor was introduced by Watson and Bennett [42] who used the structure map to study the occurrence of TCP phases in binary transition metal alloy systems as a function of the average number of holes, $\bar{N}_h$, and the ratio of the equilibrium atomic volume of the A and B transition metal elements, $V_\mathrm{A}/V_\mathrm{B}$. Although they illustrated the importance of the atomic size for the Laves phases with respect to non-TCP phases, their two-dimensional structure map ($\bar{N}_h$, $V_\mathrm{A}/V_\mathrm{B}$) was limited to stoichiometric AB_2 TCP structure-types.

In order to overcome this limitation we propose a set of composition-dependent co-ordinates. However, instead of making use of the concept of electron holes as used by Rideout and Beck, we simply assign our co-ordinate to be given by the valence electron

concentration

$$\bar{N} = \sum_i c_i N_i, \tag{3.1}$$

where c_i is the concentration of the constituent element i. The ordinate is given by the average of the relative volume difference $\overline{\Delta V/V}$ which is defined by

$$\overline{\Delta V/V} = \sum_{i,j} c_i c_j |V_i - V_j|/[(V_i + V_j)/2], \tag{3.2}$$

where V_i is the atomic volume of the constituent element i. The equilibrium atomic volume of the chemical elements is obtained from their metallic radii for co-ordination number 12 at room temperature as given in [69]. Figure 3.1 shows the atomic volume for all transition metal elements. Watson and Bennett's ordinate V_i/V_j can be either greater than or less than unity depending on whether $V_i - V_j \lessgtr 0$. In contrast, our choice of co-odinate needs to depend on the magnitude of ΔV since the size factor contribution to the heat of formation, and hence phase stability, varies as $(\Delta V)^2$ to lowest order [70]. The inclusion of the prefactor $c_i c_j$ guarantees that the size factor $\overline{\Delta V/V} \to 0$ as either $c_i \to 0$ or $c_j \to 0$, as it must. Moreover, the composition dependence is needed not only for handling the χ phase in the binaries but also for the correct treatment of ternary and multi-component systems as will be seen in the following sections.

As pointed out in Sec. 2.2.2, theoretical studies showed that the electronegativity difference has only a minor effect on the stability of Laves phases. However, in order to justify the neglect of this parameter as a third co-ordinate in our structure map, in contrast to, for example, Villars et al. [68] in their phenomenological three-dimensional binary plots, it is important to study the influence of the electronegativity difference on the stability of all TCP phases. Hence, and in a similar fashion to the structure map $(\bar{N}, \overline{\Delta V/V})$ of binary TCP systems which is presented in this chapter, we have studied the grouping of TCP phases with other ordinates that involve the most common electronegativity scales, such as those of Pauling [71], Mulliken [72], Allen [73] and Martynov-Batsanov [74], and employed

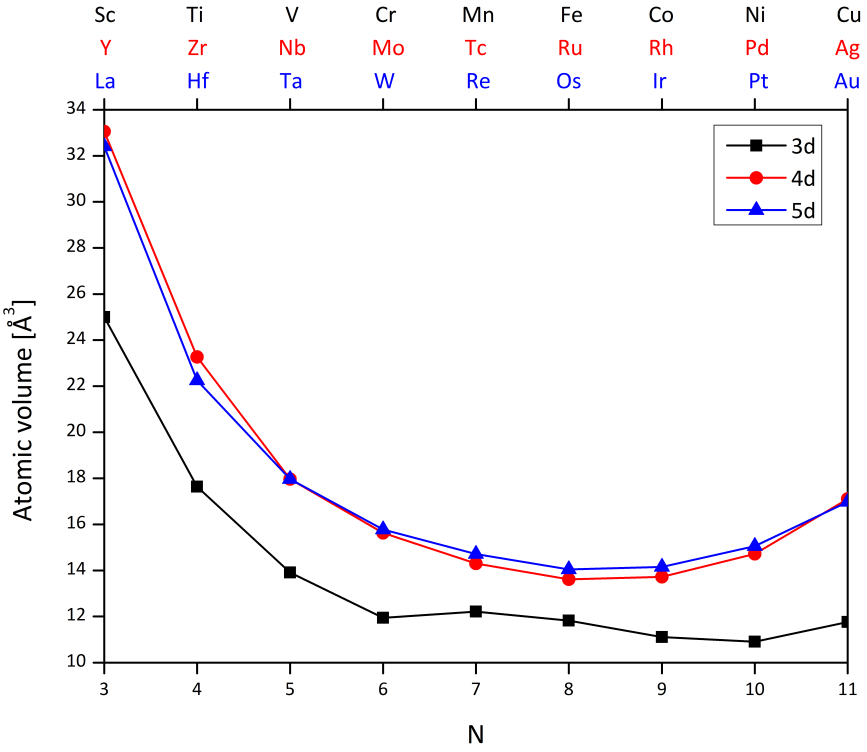

Figure 3.1: The equilibrium atomic volume of the chemical elements calculated from their metallic radii for the co-ordination number 12 at room temperature as given in [69]. The x-axis indicates the number of valence electrons N.

various kinds of composition-dependent and non-composition-dependent prefactors. Our investigations show that none of the studied ordinates involving the electronegativity difference successfully separate the experimental binary TCP phase data into characteristic domains. This supports previous observations that the electronegativity difference affects all TCP phases in a similar way and that this effect plays only a minor role. Note that a detailed discussion of our findings would go beyond the scope of this thesis.

3.2 Data on experimental TCP phases

3.2.1 Binary TCP phases

For the construction of the binary structure map in Sec. 3.3, we have investigated the compositions and homogeneity ranges of all stable TCP, fcc-, bcc- and hcp-based phases of

all binary transition metal systems except the noble metals of group XI and the rare earths La-Lu because they are, in general, not considered for the design of Ni-based superalloys. Since aluminium is one of the main components of nickel-based superalloys and is therefore found in small amounts in their TCP phases, we have also investigated all aluminium containing transition metal binary systems. These systems will be discussed separately in Sec. 3.3.3. Only the homogeneity ranges of stable phases observed experimentally up to the melting temperature are obtained from systematic studies of the data within Massalski [75], Sinha [22], Watson and Bennett [42] and Joubert [27, 76]. Cross-checks on the reliability of our database have also been carried out using the Linus Pauling File Database [77] and the Inorganic Crystal Structure Database [78]. Table 3.1 shows the investigated transition metal binary systems and their observed TCP phases. The table is arranged with respect to the two elements constituting the A_xB_{1-x} TCP phase designated as A and B which is defined by the preferred stoichiometries of the individual TCP phases i.e. A_3B for A15, A_2B for σ, A_6B_7 for μ, AB_2 for the Laves phases and A_5B_{24} and $A_{17}B_{12}$ for χ. Phases for which A and B elements cannot be identified i.e. systems that are found to be stable at compositions deviating significantly from the 'ideal' composition, are shown in both corresponding cells. Moreover, the R and δ phases do not have preferred stoichiometries because they are found only once in Mo-Fe and Mo-Ni, respectively. Therefore, R and δ are shown in both their corresponding cells. Note that in 1962, Waterstrat [79] found a second R phase which was later approved by Murray but whose existence has been questioned recently by Chen [80]. This phase is not listed in Tab. 3.1.

3.2.2 Ternary TCP phases

Table 3.2 lists 90 TCP phases forming in transition metal ternary systems. The stable TCP phases are discussed in Sec. 3.4.1 with respect to the corresponding valence electron concentration and relative volume difference. Most of the ternary systems were chosen

because their TCP phases either have widely-stretched stability regions, which can reach even to the boundaries of the binary system, or are located within the isothermal sections of the phase diagram and do not extend to any of the binary systems. We shall refer to the latter as true ternary TCP phases [81]. Hence, Tab. 3.2 contains a representative selection of isothermal sections with a total of 120 very differently shaped and positioned TCP phase stability ranges found within the 90 isothermal sections of phase diagrams at equilibrium temperatures ranging between 800°C and 1400°C. Table 3.2 comprises 45 σ phases (containing 3 true ternary phases), 13 χ phases and 20 μ phases. Four ternary phase diagrams contain the R phase (containing 3 true ternary phases), 5 contain A15 and 33 contain Laves phases with C14 (NiTiZr) being the only true ternary Laves phase. As mentioned previously, there are no P phases observed in binary compounds but Co-Mn-Mo and Cr-Mo-Ni form P phases. The only ternary system that forms the M phase is $Nb_{48}Ni_{39}Al_{13}$, which is not given in Tab. 3.2 because it contains a small amount of aluminium, namely 13 at.%. This M phase is the only aluminium containing ternary TCP phase studied in Sec. 3.4.1.

3.2.3 Multi-component TCP phases

Literature about the composition of multi-component TCP phases with more than three different constituents is rare, especially about TCP phases formed in nickel-based superalloys. The average equilibrium compositions of multi-component TCP phases are taken from [14, 17, 82, 83]. Some of the TCP phases which are observed in nickel-based superalloys contain up to 3% wt. aluminium.

		3d B elements						**4d B elements**						**5d B elements**					
		V	Cr	Mn	Fe	Co	Ni	Nb	Mo	Tc	Ru	Rh	Pd	Ta	W	Re	Os	Ir	Pt
3d A elements	Sc			C14	C14,C15, C36	C15	C15			χ	C14					χ,C14	C14	C15	
	Ti		C14,C15, C36	C14	C14	C15,C36				χ			A15					A15	A15
	V			σ	σ	σ	A15,σ					A15	A15			σ	A15	A15	A15
	Cr			σ	σ	σ					σ	A15					A15,σ	A15	A15
	Mn								σ										
	Fe								R										
	Co																		
	Ni								δ										
4d A elements	Y			C14,C15	C15	C15	C15			C14	C14	C15				C14	C15	C15	C15
	Zr	C15	C14,C15, C36	C14	C15	C15			C15	χ,C14	C14				C15	χ,C14		C15	
	Nb		C14,C15	C14	μ,C14	μ,C14, C15,C36	μ			χ		A15,σ				σ,χ	A15,σ, χ	A15,σ	A15,σ
	Mo				σ,μ, C14,R	σ,μ	δ									χ	A15	A15,σ	A15
	Tc		σ	σ	σ				A15,σ						σ				
	Ru																		
	Rh																		
	Pd																		
5d A elements	Hf	C15	C14,C15	C14,C36	C14,C15	C15			C15,C36	χ,C14					C15	χ,C14	C14		
	Ta	C15	C14,C15	C14	μ, C14	μ,C14, C15,C36	μ			χ		σ	σ			σ,χ	σ χ	σ	A15,σ
	W				μ,C14	μ					σ						σ	σ	
	Re	A15	σ	σ					σ						σ,χ				
	Os	A15												χ					
	Ir																		
	Pt																		

Table 3.1: The investigated transition metal binary systems with their observed TCP phases. The table is arranged with respect to the two elements constituting the A_xB_{1-x} TCP phase designated as A and B which are defined by the preferred stoichiometries of the individual TCP phases.

Co-Cr-Fe	σ	Cr-Hf-V	Laves	Ir-Ru-Zr	Laves
Co-Cr-Mo	σ,μ,**R**	Cr-Mn-Ni	σ	Mn-Ni-V	σ
Co-Cr-Ni	σ	Cr-Mo-Nb	Laves	Mo-Nb-Ni	μ
Co-Cr-Re	σ	Cr-Mo-Ni	$\boldsymbol{\sigma}$,**P**	Mo-Nb-Re	σ
Co-Cr-Ti	σ	Cr-Mo-Zr	Laves	Mo-Nb-Zr	Laves
Co-Cr-W	σ,μ,**R**	Cr-Nb-Ni	μ,Laves	Mo-Ni-Re	χ,σ
Co-Fe-Mo	σ,μ	Cr-Nb-Ti	Laves	Mo-Os-W	A15
Co-Fe-Re	σ	Cr-Ni-Re	σ	Mo-Re-Ru	χ,σ
Co-Fe-V	σ	Cr-Ni-W	$\boldsymbol{\sigma}$	Mo-Re-Ta	χ,σ
Co-Fe-W	μ	Cr-Re-W	σ	Mo-Re-V	χ,σ
Co-Mn-Mo	μ,**R**,**P**	Cr-Ta-Ti	Laves	Mo-Re-W	σ
Co-Mn-V	σ	Cr-Ta-V	Laves	Mo-Re-Zr	χ,σ
Co-Mo-Nb	μ,Laves	Cr-Ti-V	Laves	Mo-Rh-Ru	σ
Co-Mo-Ni	μ,Laves	Cr-Ti-Zr	Laves	Mo-Ru-Ta	σ
Co-Mo-W	μ	Cr-V-Zr	Laves	Mo-Ru-W	σ
Co-Mo-Zr	μ,Laves	Cr-W-Zr	Laves	Mo-Ti-Zr	Laves
Co-Nb-Ta	μ,Laves	Fe-Mn-Mo	σ,μ,R	Mo-W-Zr	Laves
Co-Nb-W	μ,Laves	Fe-Mn-V	σ	Nb-Ni-Re	χ
Co-Nb-Zr	Laves	Fe-Mo-Ni	μ	Nb-Re-V	χ
Co-Ni-Ta	μ,Laves	Fe-Mo-V	σ,μ	Nb-Re-W	χ,σ
Co-Ni-Ti	Laves	Fe-Nb-W	Laves	Nb-Re-Zr	χ,Laves
Co-Ni-V	σ	Fe-Ni-Re	σ	Ni-Re-Ta	μ
Co-Pt-Ta	A15,μ	Fe-Ni-V	σ	Ni-Re-V	σ
Co-Pt-V	A15	Fe-W-Nb	Laves	Ni-Re-Zr	χ
Cr-Fe-Mn	σ	Hf-Re-W	Laves	Ni-Ti-Zr	**Laves**
Cr-Fe-Mo	σ	Hf-Ta-V	Laves	Os-Ta-W	σ
Cr-Fe-Re	σ	Ir-Ni-Ta	σ,μ	Re-Ru-W	χ,σ
Cr-Fe-Ti	Laves	Ir-Pt-Ti	A15	Re-Ta-W	σ
Cr-Fe-V	σ	Ir-Re-W	σ	Re-V-W	χ,σ
Cr-Fe-W	σ,Laves	Ir-Ru-Ti	A15	Re-W-Ta	χ

Table 3.2: The investigated transition metal ternary systems with their observed TCP phases. Bold TCP phases are true ternary phases, i.e. those for which no binary TCP phase exists in any of the boundary systems.

3.3 Binary structure map

Figure 3.2 shows two binary structure maps. The structure map on the right-hand side employs the composition dependent ordinate as defined in Eq. (3.2) whereas the ordinate used for the structure map on the left-hand side is chosen to be independent with respect to the stoichiometry, due to the constant prefactor $c_i c_j = 1/4$. This constant prefactor results from using $c_i = c_j = 1/2$, however, any fixed value for c_i and $c_j = (1 - c_i)$ could be used because the relative topology of the different structural domains would not be affected by the choice. In both structure maps shown in Fig. 3.2 the homogeneity ranges which are obtained from the phase diagrams of the binary systems given in Sec. 3.2.1 are indicated by thick lines while the thin lines demarcate the domains in which the homogeneity ranges of a particular structure-type are located.

Figure 3.2 demonstrates that the relative locations and topologies of the TCP structural domains are identical in both structure maps for most of the TCP phases with the exception of the χ phase domains which are clearly very different. Whereas the χ phases in the right-hand figure are closely grouped and localised within the overlap region between the A15 phase domain, in the left-hand figure some χ phases are located near the lower-middle of the Laves domain next to the μ domain and away from the overlap region between the A15 phase domain where the other χ phases are positioned. Therefore, unlike in the right-hand figure, the left-hand figure of Fig. 3.2, with the composition-dependent size factor, allows for a clear definition of two groups with respect to the size factor: The first group with an atomic size factor $\overline{\Delta V/V}$ less than about 0.15 involves the structural domains of the A15, σ and χ phases. The second group comprises μ and the Laves domains with a relative volume difference $\overline{\Delta V/V}$ greater than about 0.15. Moreover, the R and δ phases are found at $\overline{\Delta V/V}$ values of around 0.15 i.e. in the region of overlap between these two groups. This indicates that the separation between the two groups is correlated with the classification of the TCP phases in terms of their elementary units as explained in Sec. 2.2.1. Recalling that the χ phase is not considered in terms of its elementary

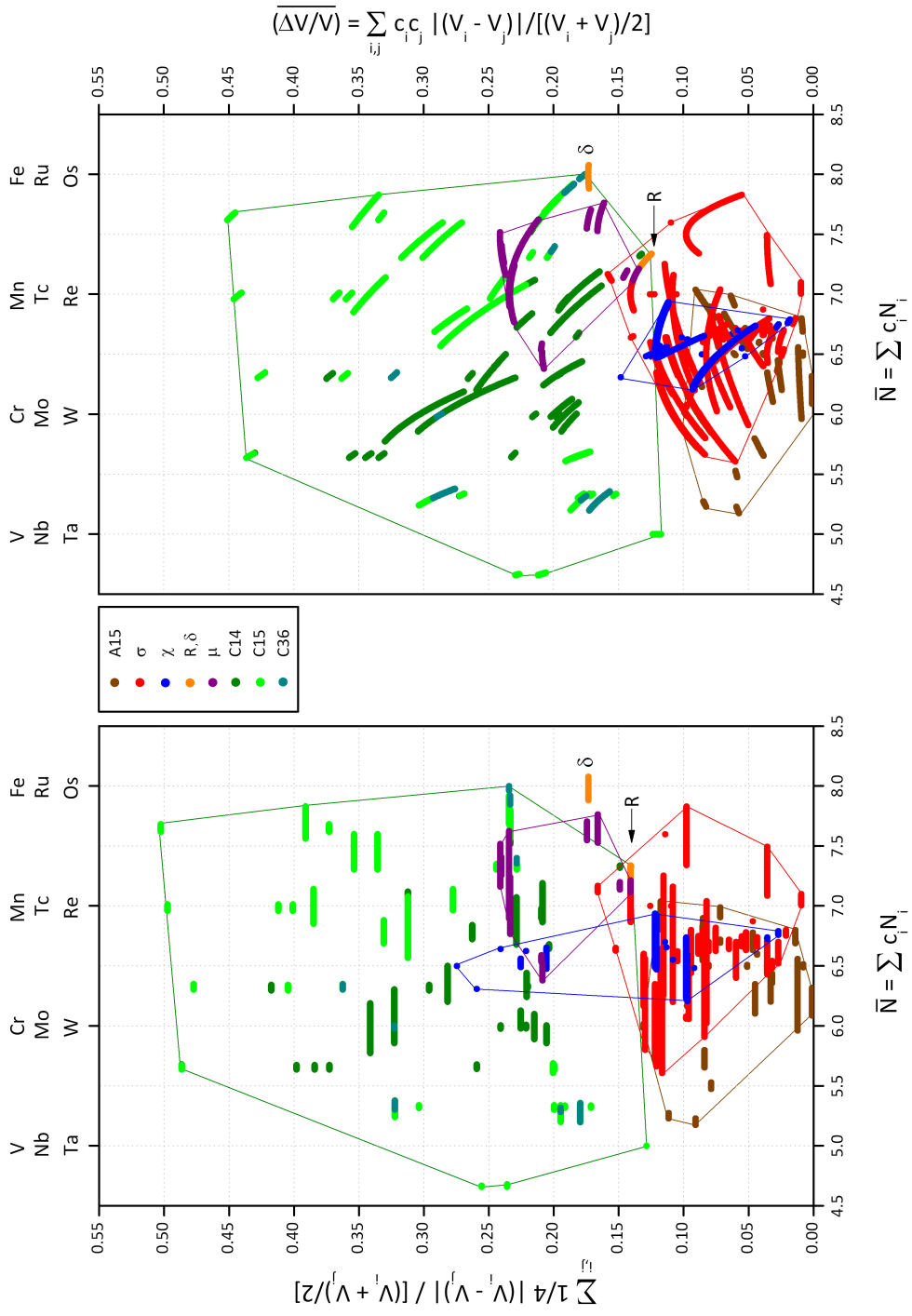

Figure 3.2: Structure maps of binary TCP phases with the different TCP domain boundaries marked by thin lines (A15 (brown), σ (red), χ (blue), μ (purple) and Laves (green)) using the experimental homogeneity ranges as a guide. The size factor ordinate is given by Eq. (3.2) with the left- and right-hand side maps being independent and dependent of stoichiometry, respectively. The co-ordinate in both maps corresponds to the valence electron concentration as given by Eq. (3.1).

units, the structural elementary units of the other two structure-types of the group with $\overline{\Delta V/V} \lesssim 0.15$, A15 and σ, are hexagonal antiprisms. Pentagonal antiprisms are structural elementary units of the structure-types of the group with $\overline{\Delta V/V} \gtrsim 0.15$ including the μ phase and the Laves phases. The P, R and δ phases, which have mixed hexagonal and pentagonal antiprisms, occur in the region of overlap between these two groups. Moreover, it shows that the f_{12} ordering in Tab. 2.2 also correlates with the division of the TCP phases into two groups with respect to the size factor because A15, σ and χ, i.e. the structure-types with $\overline{\Delta V/V} \lesssim 0.15$, and μ and the Laves phases, i.e. the structure-types with $\overline{\Delta V/V} \gtrsim 0.15$ have the lowest ($f_{12} \leqslant 0.41$) and the largest fractions ($f_{12} \leqslant 0.54$) of Z12 co-ordination polyhedra, respectively. The fractions of Z12 co-ordination polyhedra of the P, R and δ phases lie between the two groups ($0.43 \leqslant f_{12} \leqslant 0.51$) as observed within the structure map with respect to $\overline{\Delta V/V}$. This observation clearly indicates a direct relation between the topologies of the TCP structures and the location of the structural domains within the right-hand structure map. The positioning and spread of each TCP structural domain within the right-hand structure map will be discussed in greater detail in the following subsection.

3.3.1 Structural TCP domains of the binary structure map

A15 phase region

The A15 region is very unique with respect to the size factor for two reasons. Firstly, it has, of all TCP phases, not only the smallest lower size limit but also the smallest upper size limit with $\overline{\Delta V/V} \approx 0.00$ (V_3Rh) and $\overline{\Delta V/V} = 0.10$ (Nb_3Os), respectively. The fact that the A15 phase has the lowest upper size limit is not unexpected as its largest co-ordination polyhedra is only Z14 whereas the atoms in other TCP phases have access to larger co-ordination polyhedra. Secondly, many A15 phases have, unlike most other TCP phases, an atomic radius ratio of r_A/r_B which is less than one such that A15 phases exist in the range $r_A/r_B = 0.92$ (Cr-Pt) $- 1.09$ (Nb-Rh). With most composition ranges of the

23 investigated A15 compounds being relatively narrow and frequently confined to the 'ideal' (A_3B) composition, this shows that the general concept of the small icosahedral sites being occupied by B atoms and the larger polyhedra by A atoms, as discussed in Sec. 2.2.1, is less relevant for the A15 then for the other TCP structures. Only a few binary A15-type phases, like V-Ir with 61–76 at.% V, $Mo_{0.8}Pt_{0.2}$, $Tc_{0.6}Mo_{0.4}$, VOs, and $Re_{0.71}V_{0.29}$ are found to be stable at compositions deviating significantly from the 'ideal' composition. A15 structures are observed within a wide range of valence electron numbers, namely between 5.2 (Ti_4Pd) and 7.1 (Cr_3Pt), but showing a preferred formation between 6 to 6.5 electrons.

σ phase region

The σ phase is the most commonly observed non-Laves TCP phase as 44 binary alloys are listed in Tab. 3.1. σ phases cover a broad range of compositions from 10 at.% A (VMn) to 85 at.% A (TaIr) such that σ phases may exist for almost any A/B composition [27]. Nevertheless, most σ phases have stoichiometric compositions close to A_2B such that the σ domains in the left-hand and the right-hand panel of Fig. 3.2 look very similar. As compared to the A15 phase domain, the σ domain has a slightly larger size factor range with $\overline{\Delta V/V} \approx 0.01$ (Mn_2Mo) and $\overline{\Delta V/V} \approx 0.16$ ($Cr_{49}Fe_{51}$) being the lower and the upper bounds, respectively. Hence, the σ phases exist in a slightly different atomic radius ratio range $r_A/r_B = 0.96$ (Cr-Os) $- 1.12$ (Mo-Co) with 3 phases exhibiting an atomic radius ratio of r_A/r_B which is less than one. The broader extension of the σ phase domain with respect to the size factor reflects the fact that the constituent atoms can vary much more in size than for A15 because σ has 5 non-equivalent co-ordination polyhedra with the largest being Z15. However, the σ phases with size factors above 0.13, which are either located in the μ or the Laves phase region i.e. $\sigma(Mo_2Co)$, σ(MoFe), and $\sigma(MoMn_2)$, form at temperatures above 1200°C. This therefore highlights the importance of temperature on the stability of σ phases exhibiting large atomic size difference. Similar to the A15 phase region, the electron concentration range for the σ phase region from 5.6

to 7.8 electrons is fairly broad but most σ phases show a clear preference for formation at electron concentrations between 6 to 7 electrons. Figure 3.3 indicates how strongly the stability of σ phases can be affected by magnetism as it shows that all of the σ phases with electron concentrations above 7 electrons lies away from the other σ phases and involve mainly the three magnetic $3d$ transition elements Fe, Co and Ni. As will be discussed in Sec. 5.1.2, theoretical investigations have indeed demonstrated that magnetism of Fe and Co atoms increases the stability of the σ-phases. Fig. 3.3 also shows that the Mo-Fe and Mo-Co systems exhibit structural trends from $\sigma \rightarrow \mu \rightarrow$ R $\rightarrow$ C14 and $\sigma \rightarrow \mu \rightarrow DO_{19}$ (ordered hcp-type structure), respectively, as the average number of valence electrons increases.

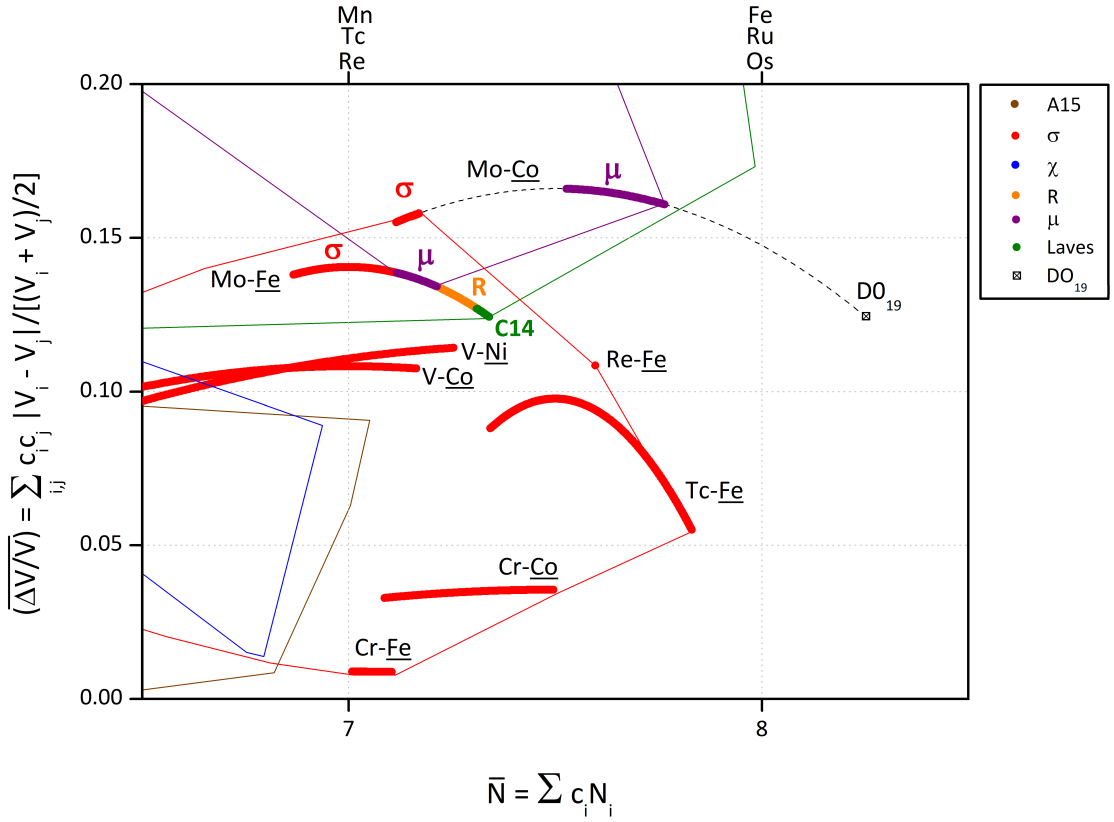

Figure 3.3: Structure map ($\bar{N}$,$\overline{\Delta V/V}$) of all the binary σ phases with $\bar{N} > 7$ and the other TCP phases of the Mo-Fe and Mo-Co systems. The different TCP domain boundaries are marked using the homogeneity ranges shown in Fig. 3.2.

χ phase region

In the left-hand of Fig. 3.2, as described above, it shows that without the concentration dependence of the size factor many χ phases lie within the Laves phase domain separated from the other χ phases located in the overlap region of the A15 and σ phase domains. The reason for this separation is that χ phases have compositions which cover a broad range ($x = 0.40 \ldots 0.88$), and are either close to A_5B_{24} (where the B atoms are 12 and 13 fold co-ordinated and the A atoms are 16 fold co-ordinated) or $A_{17}B_{12}$ (where the B atoms are 12 fold co-ordinated and the A atoms are 13 and 16 co-ordinated) [76]. The χ phases exist in the range $r_A/r_B = 1.02$ (Mo-Re) $- 1.18$ (Zr-Tc), however, the two different stoichiometries are preferred by χ phases with very different atomic radius ratios. χ phases which are located in the A15 and σ overlap region due to the small differences in atomic size ($1.02 \lesssim r_A/r_B \lesssim 1.06$) have compositions close to the $A_{17}B_{12}$ stoichiometry while most of the χ phases with compositions close to A_5B_{24}, such as Sc-Tc, Sc-Re, Zr-Tc, Hf-Tc, Hf-Re and Zr-Re, lie in the Laves phase region because they generally have larger differences in atomic size ($1.07 \lesssim r_A/r_B \lesssim 1.18$). Hence, in the right-hand panel of Fig. 3.2, where the concentration dependent size factor of Eq. (3.2) is used, it can be seen that the latter χ phases join the other χ phases in the overlap region of the A15 and σ phase domains to form a more compact χ domain as compared to the χ domain which is shown in the left-hand panel of Fig. 3.2. For example, Zr-Re exhibits the C14 Laves phase $ZrRe_2$ and the χ phase Zr_5Re_{24} which are both located in the left-hand panel of Fig. 3.2 near the lower-middle of the Laves domain because both have a composition independent size factor of 0.22. However, in the right-hand panel of Fig. 3.2, with the compositional-dependent prefactor included, the C14 phase, with $\overline{\Delta V/V} = 0.20$, remains roughly at the same position near the middle of the Laves domain while the χ phase, with $\overline{\Delta V/V} = 0.13$, has moved down amongst the A15 and σ phases. Figure 3.2 shows that the χ phase is only found in a very narrow electron concentration range between 6.3 and 6.8 electrons. This range is extended to 7.3 electrons if one considers the solid solutions

(αMn) as we will see in Sec. 3.3.3. The homogeneity ranges of individual χ phases can cover a broad range of compositions such as, for example, χ(Nb-Re) with Nb ranging from 12 to 38 at.% or χ(Ta-Re) with Ta ranging from 20 to 40 at.%.

R and δ phase regions

As discussed in Sec. 3.2.1, the R and δ phases are found only in Mo-Fe and Mo-Ni, respectively, so that no binary structural domains can be established for these two structure-types.

The only R phase is found in the Fe-Mo system in which, interestingly, σ, μ and C14 are also formed. The R phase in this binary system is stabilised as $Mo_{38}Fe_{62}$ over the small temperature range 1235°C to 1488°C. The C14 phase is found at a similar stoichiometry, namely $Mo_{33}Fe_{67}$, but is only stable up to 927°C. The high temperature σ(MoFe) phase is found between 1235°C and 1611°C whereas $\mu(Mo_{51}Fe_{79})$ is a low temperature phase which is stable up to 1370°C. As can be seen in the left-hand panel of Fig. 3.2 and in Fig. 3.3, Fe-Mo is, together with the homogeneity ranges of all four TCP phases, therefore located in the overlap region between the structural domains of the σ, μ and Laves phases. Depending on the temperature range, different structural trends with increasing valence electron concentration are observed. For example, for the small temperature ranges from 1235°C to 1370°C and 1370°C to 1488°C we observe $\sigma \rightarrow \mu \rightarrow$ R and R $\rightarrow \mu$, respectively. The latter trend and the trend $\mu \rightarrow$ C14, for temperatures up to 927°C, correlate with the overall ordering of R $\rightarrow \mu \rightarrow$ Laves as given by f_{12} in the final column of Tab. 2.2. Note that Waterstrat's [79] alleged R phase $TiMn_4$ would have the co-ordinates (6.4, 0.14) and would be, therefore, located in the overlap region between the σ and χ domains far from the $Mo_{38}Fe_{62}$ phase. This justifies our decision to exclude this R phase from our investigation.

The only δ phase has the composition $Mo_{49}Ni_{51}$ and is located at around 8 electrons, very close to the μ phase and Laves phase region.

μ phase region

We see from Tab. 3.1 that μ phases are formed in 10 binary A-B transition metal systems where A is a $4d$ or $5d$ transition element from group V or VI and B is a magnetic $3d$ element Fe, Co, or Ni [84]. The structure prototype of the μ phase is W_6Fe_7 in which the smaller Fe atoms have icosahedral co-ordination whereas two of the six larger W atoms are each surrounded by either 14, 15 or 16 neighbouring atoms. However, investigations of the homogeneity ranges by Joubert and Dupin [84] indicated that this 'ideal' composition, with the magnetic $3d$ element being the majority element, only exists in the systems Ta-Co, W-Co, and Mo-Co [84]. Hence, it was assumed that the μ phase is characterised by a large non-stoichiometry due, in particular, to the deviation from the ideal composition towards the A-rich side, as observed for Ta-Fe, Nb-Ni, Nb-Co, and Ta-Ni. In this respect, it is interesting to see that the A-poor μ phases are located below $\overline{\Delta V/V} \approx 0.20$ near the σ phase domain while the A-rich μ phases lie above this threshold near the lower-middle of the Laves domain. As can be seen in the right-hand panel in Fig. 3.2, the μ phase region extends over a size factor range of $0.13 \leq \overline{\Delta V/V} \leq 0.24$ and a valence electron range of $6.50 \leq \bar{N} \leq 7.75$. Therefore, the μ phase region is clearly located in the extensive Laves phase region high above those of the A15, σ, and χ phases indicating that the difference in atomic size is more crucial for the stability of the μ and Laves phases than for the A15, σ, and χ phases. However, although from the right-hand panel of Fig. 3.2 it can be seen that both phases have a very similar minimum size factor, we see from the differences in the size factor ranges of the two structure-types that the atomic size differences in the Laves phases can be much larger than those of the μ phase. This narrower size factor range of the μ phase can be explained by the differences in the size of the non-icosahedral co-ordination polyhedra, that is, because the Z16 of the Laves phases are larger than the Z14, Z15 and Z16 co-ordination polyhedra of the μ structure.

Laves phase region

As can be seen in the right-hand panel of Fig. 3.2, the Laves phase region is by far the largest region, stretching over a valence electron range between 4.66 (C15(HfV_2)) and 8 (C36($NbCo_3$)) electrons and a size factor range between 0.114 (C15(TaV_2)) and 0.446 (C15(YNi_2)). This means that atomic radius ratio r_A/r_B varies between $r_A/r_B = 1.08$ of TaV_2 and $r_A/r_B = 1.445$ of YNi_2, although the maximum space filling for the ideal AB_2 stoichiometry, where A atoms occupy the large 16-fold sites and the B atoms occupy the small 12-fold sites, is obtained for an ideal radius ratio $r_A/r_B = 1.225$. These significant deviations of the atomic radius ratios, for which there is clearly no correlation between the size ratio and the stable structure-type, indicate that the radii of the atoms in a Laves phase must differ from those of the elemental metals [85]. It was suggested [86] and later confirmed [87] that electron transfer causes the contraction or expansion of the atoms which results in a deviation from the ideal radius ratio. Hence, this might also explain the large homogeneity ranges that lead to significant variations in $\overline{\Delta V/V}$ as shown in the left-hand panel of Fig. 3.2. Although no correlation between the valence electron concentration and the stable structure-type can be obviously identified, this does not mean that C14, C15 and C35 are evenly distributed within the structural domain. In 1976 Johannes et al. [88] determined the correlation between crystal structure and the valence electron concentration in transition metal Laves phases. They found a tendency to form C15 $\rightarrow$ C14 $\rightarrow$ C15 $\rightarrow$ C36 as the valence electron concentration increases [85] and a simple *d*-band tight binding model was then used to rationalize this trend. However, Fig. 3.2 demonstrates that some Laves phases deviate from this trend mainly because the Laves phases appear to be restricted to a range of valence electron concentrations and radius ratios rather than to just a valence electron concentration range. The necessity to include both size and electronic factors in order to obtain a good qualitative agreement between a simple *d*-band tight binding model and an AB_2 structure map was demonstrated by Ohta and Pettifor [43].

3.3.2 Structural trends and predictability

In the previous section we have seen that the structural domains within the two groups exhibit significant overlap with each other. Importantly, for the group of phases with $\overline{\Delta V/V} \lesssim 0.15$, Fig. 3.2 shows that A15, σ and χ significantly overlap, in particular in the region between 6 and 7 electrons as this is the region where all three TCP phases are predominantly observed. In order to understand the reasons for the overlap between A15, σ and χ domains, we study the formation of the three TCP phases in a select set of non-magnetic $4d$ and $5d$ binary A_xB_{1-x} alloys which are chosen such that the binary systems are very similar with respect to the valence electron concentration and the metallic radii to their constituent elements. As shown in Fig. 3.4, we therefore consider binary systems where A is either Nb ($N_A = 5$) or Mo ($N_A = 6$) and B is from a group with 7, 8 or 9 valence electrons respectively. Hence, in total the following 6 sets of binary systems are compared:

- $N_B = 9$: ① Nb(Rh/Ir) and ② Mo(Rh/Ir),
- $N_B = 8$: ③ Nb(Ru/Os) and ④ Mo(Ru/Os) and
- $N_B = 7$: ⑤ Nb(Tc/Re) and ⑥ Mo(Tc/Re),

where the circled numbers label the different curves in Fig. 3.4.

Firstly, we study the formation of stable phases for the binary systems with $N_B = 9$ i.e. the Rh- and Ir-containing alloys. For curves ① we see in Fig. 3.4 that both binary systems, Nb-Rh and Nb-Ir, exhibit very similar parabola because Rh and Ir have very similar atomic radii of around 1.345 Å and 1.357 Å (see Fig. 3.1), respectively. Hence, both curves take almost the same structure map co-ordinates ($\bar{N}_{x=0.5} = 7, \overline{\Delta V/V}_{max} \approx 0.12$). Fig. 3.4 shows that both binary systems display with increasing valence electron concentration the same structural trend from A15 $\rightarrow \sigma \rightarrow L1_0 \rightarrow L1_2$, where $L1_0$ and $L1_2$ are ordered phases with respect to an underlying fcc lattice. Therefore, despite minor differences in the homogeneity ranges of their stable phases, Nb-Rh and Nb-Ir are very similar with respect

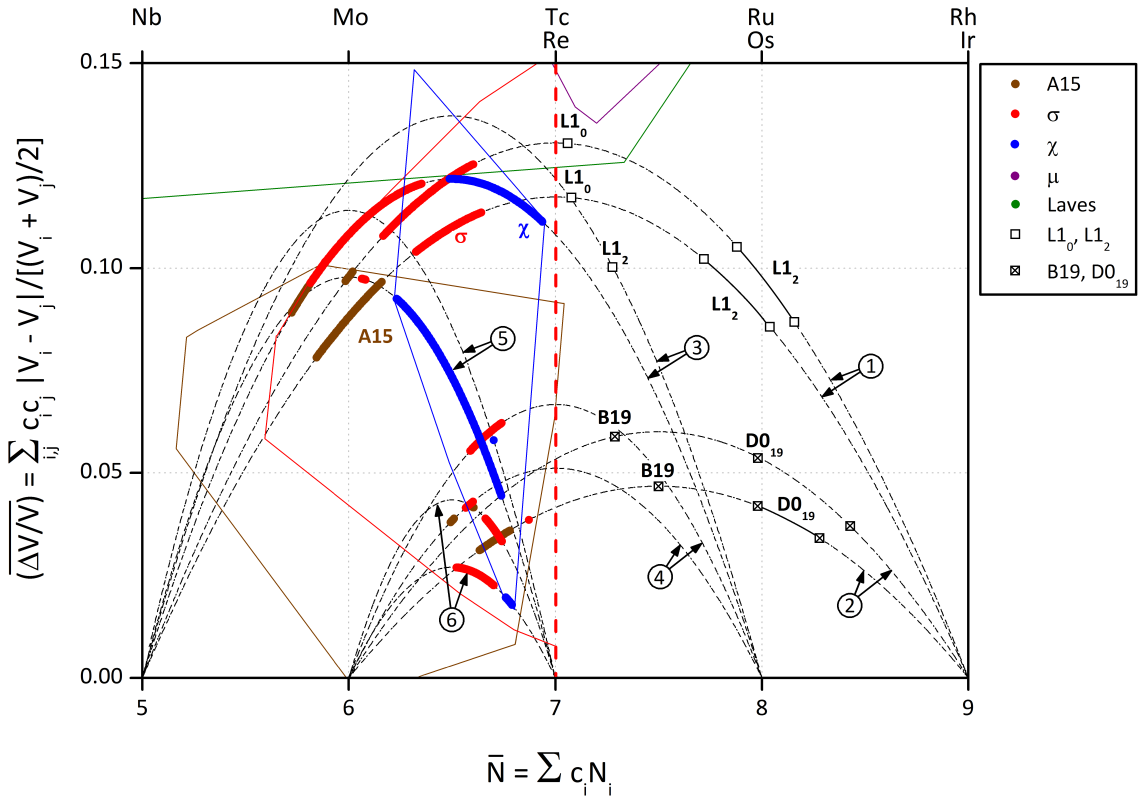

Figure 3.4: Structure map ($\bar{N}$,$\overline{\Delta V/V}$) of a selection of 4*d* and 5*d* binary phases containing Nb and Mo. The curves are labelled according to ① Nb(Rh/Ir), ② Mo(Rh/Ir), ③ Nb(Ru/Os), ④ Mo(Ru/Os), ⑤ Nb(Tc/Re) and ⑥ Mo(Tc/Re). The different TCP domain boundaries are taken from Fig. 3.2 with the dashed vertical red line from $\bar{N}$ representing the right-hand boundary of the *non-magnetic* σ phases (see Fig. 3.3).

to phase formation, which is what one would expect from almost identical binary systems. Replacing Nb by Mo, the maxima of the structure map co-ordinates of Mo-Rh and Mo-Ir parabola ② shift to ($\bar{N}_{x=0.5} = 7.5, \overline{\Delta V/V}_{max} \approx 0.05$). The drop in the maximum relative size factor is due to the smaller metallic radius of Mo (1.400 Å) which, compared to that of Nb (1.468 Å), is much closer to the metallic radii of Rh and Ir. However, although both binary systems display, again, almost identical parabolas, this time it can be seen that the two binary systems do not form the same phases. Namely, whereas stable B19 and $D0_{19}$ are found almost at the same valence electron concentration in both systems, only Mo-Ir forms additional TCP phases. With the σ phase being only just stable at

temperatures over 100°C, which is just below the melting temperature, Mo-Ir exhibits the trend A15 $\rightarrow \sigma \rightarrow$ B19 $\rightarrow$ D0$_{19}$ as $\bar{N}$ increases. Note that the location of B19 and D0$_{19}$ between 7 and 9 electrons, close to the non-magnetic hcp transition elements of group VII and VIII with $\overline{\Delta V/V} = 0$, is not surprising because they are ordered structures with respect to an underlying hcp lattice.

Next, we study the group of binary alloys with $N_B = 8$ i.e. the Ru- and Os-containing alloys. For the curves ③ Fig. 3.4 exhibits very different stable structure-types despite very similar parabola. Whereas Nb-Ru only forms the fcc-based L1$_0$ and L1$_2$ phases, the Nb-Os system shows the sequence A15 $\rightarrow \sigma \rightarrow \chi$. As shown in Tab. 3.1, Nb-Os is unique in this respect because it is the only binary systems that forms all three TCP phases. Hence, bearing in mind that Ru and Os have the same number of valence electrons and almost identical metallic radii, it is surprising that one systems forms all three TCP phases whereas the other system does not. This indicates that the stability of phases is very sensitive to small changes in the free energy. Replacing Nb by Mo, the Mo-Ru and Mo-Os curves ④ shift to the right with much lower amplitude. Whereas Mo-Ru displays only a stable σ phase, Mo-Os shows an A15 $\rightarrow \sigma$ sequence.

Finally, we consider the group of binary alloys with $N_B = 7$ i.e. the Tc- and Re-containing alloys shown by the curves ⑤ and ⑥ in Fig. 3.4. We see for the curves ⑤ that Nb-Tc forms a χ phase which is a line compound, whereas, the phase diagram of Nb-Re shows the common sequence $\sigma \rightarrow \chi$, with a narrow high temperature σ phase which is stable only above a temperature of 400°C and a very broad χ phase. The Mo-Tc and Mo-Re curves ⑥ which are located between 6 and 7 electrons have the smallest valence electron difference and the smallest size difference of all of the curves shown in Fig. 3.4. The Mo-Tc system shows the sequence A15 $\rightarrow \sigma$ (with $\bar{N}_\sigma < 6.74$), whereas the Mo-Re system displays the sequence $\sigma \rightarrow \chi$ (with $\bar{N}_\chi > 6.76$). Hence, all three TCP phases, A15, σ and χ, can be found within a small area of the structure map.

In summary, we observe in Fig. 3.4 that the fact that binary systems are very similar with respect to the size difference and the valence electron does not imply that they form

the same homogeneity ranges of TCP phases. Importantly, it demonstrates that not even the homogeneity range can vary between very similar binary systems and that they can display very different structure types too. As explained above, the curves ② and ③ show that the 4*d* Ru and Rh alloys Nb-Ru and Mo-Rh do not exhibit TCP phases, whereas the 5*d* Os and Ir alloys Nb-Os and Mo-Ir do display TCP phases. The absence of TCP phases in Nb-Ru can be possibly explained by the existence of energetically more favourable fcc-based $L1_0$ and $L1_2$ phases competing with the nearby TCP phases, whereas, the formation of TCP phases in Nb-Os results from the absence of energetically favourable fcc-based phases. Unfortunately, the structure map is not able to capture the subtle differences in the formation energies. Hence, these results show that the structure map can be used to predict the likely structure of a phase whose composition is known to fall within a given structural domain but that it cannot be used to predict the non-occurrence of phases. This lack of predictability is not exclusive to our structure map but is a general property of structure maps [89]. We will see in chapter 3.4.2 that this causes a major limitation for the usability of the NewPHACOMP method.

Although the homogeneity ranges of the fcc, hcp and bcc phases observed in the Nb- and Mo-containing binary systems, shown in Fig. 3.4, do not overlap with other phases, it is clear from our discussion above that the overlap of structural domains is not unique to TCP phases. This is demonstrated in Fig. 3.5 where only their average homogeneity ranges and the borders of the previously obtained TCP regions are shown in order to get a clear picture of the distribution of the fcc, hcp and bcc-like structures among TCP structures. Moreover, unlike the TCP structure maps of Fig. 3.2, Fig. 3.5 does not include binary systems involving the magnetic elements Mn, Fe, Co and Ni.

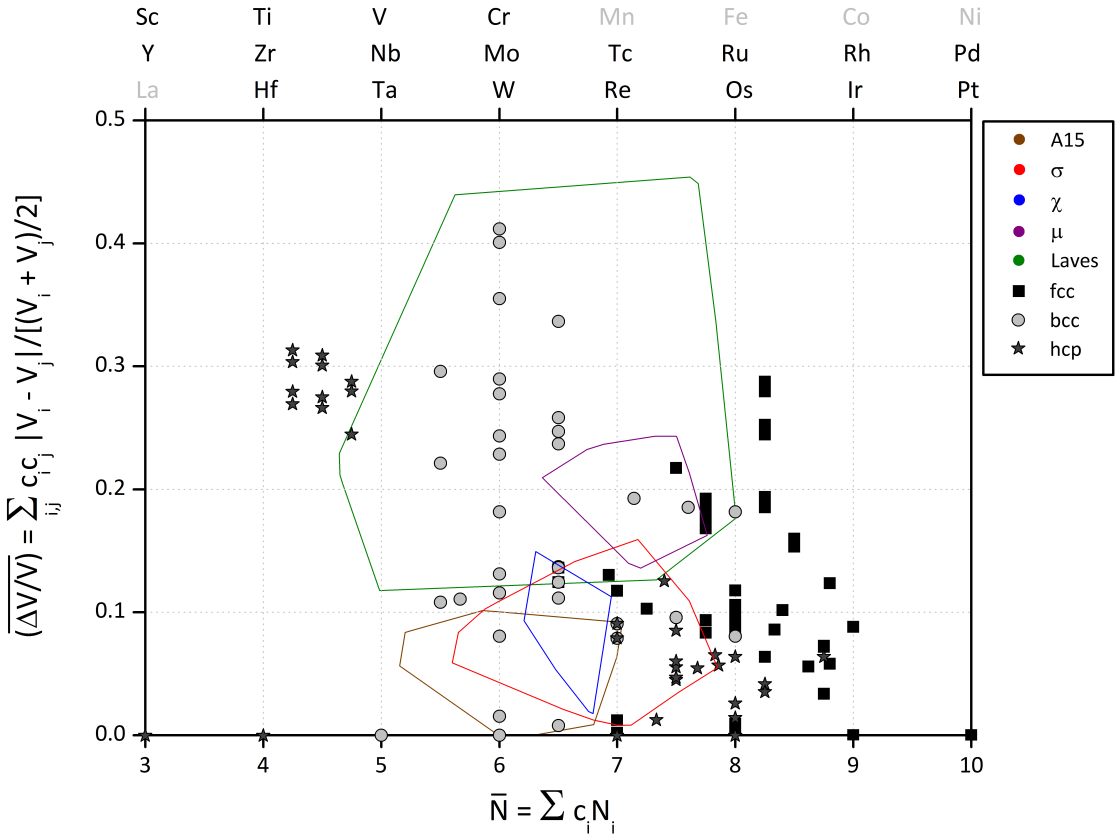

Figure 3.5: Structure map ($\bar{N}$,$\overline{\Delta V/V}$) of all the binary systems forming fcc, hcp and bcc. Data points of fcc- (squares), hcp-(stars) and bcc-(circles) like structures denote the average homogeneity ranges. The different TCP domain boundaries are marked using the homogeneity ranges shown in Fig. 3.2.

Fig. 3.5 indicates that the clustering of hcp phases between 3 to 4.8 electrons and bcc phases between 5 to 6.5 electrons is very similar to the observed structural trends across the elements. However, it is obvious that the identification of domains with little overlap is difficult at higher electron concentration between 6.5 to 8.0 electrons: as highlighted by Fig. 3.6, the fcc domain which is constructed from fcc elemental systems, Rh/Ir (9,0) and Pd/Pt(10,0), and the fcc binary systems is by far the biggest domain ranging from 6.9 to 10 electrons. Note that the low temperature phases at $\bar{N} = 6.5$, IrTi, RhTi, and RuTa, are normally listed as fcc-based $L1_0$ structures which transform to the bcc-based B2 structures by tetragonal distortions at higher temperatures. However, investigation into the c/a ratios for these three systems carried out by Watson [42] showed that their

values are closer to the cubic bcc rather than the cubic fcc structure. This means these $L1_0$ systems lie on distorted bcc lattices which is consistent with the other bcc phases at 6.5 electrons. Nevertheless, the fcc domain still fully encloses the hcp phase domain which ranges between 7 and 8.75 electrons. In addition, the fcc and hcp domains contain bcc phases which are all high temperature phases but since the structure map does not differentiate between low and high temperature phases we therefore obtain a noticeable overlap between all three basic structure domains.

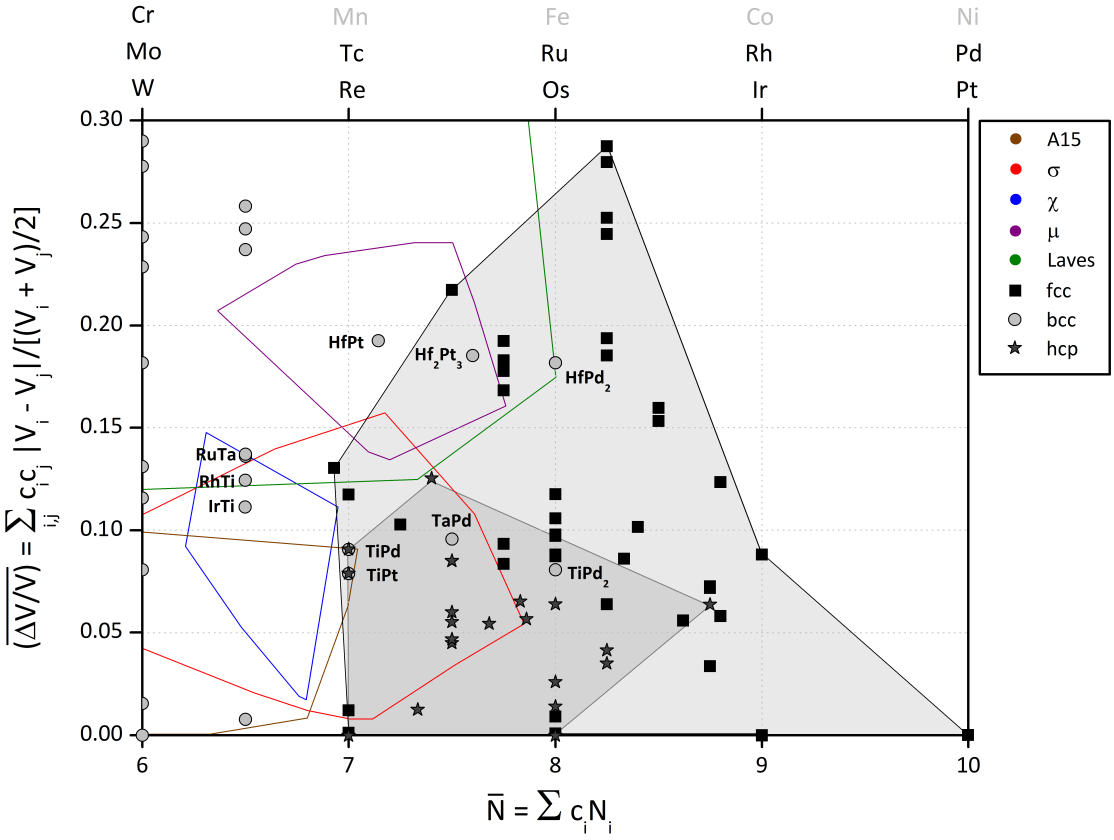

Figure 3.6: Structure map ($\bar{N}$,$\overline{\Delta V/V}$) of all the binary systems forming fcc, hcp and bcc structures. The data points of fcc- (squares), hcp-(stars) and bcc-(circles) like structures denote the average homogeneity ranges. The different TCP domain boundaries are marked using the homogeneity ranges shown in Fig. 3.2. The hcp and fcc domains, which are constructed from the corresponding elemental and binary systems, are highlighted by light and dark grey areas, respectively.

3.3.3 Further remarks

Aluminium-containing binary TCP phases

The binary structure map introduced above consists of stable binary phases made from transition metal elements. However, since aluminium is the second most important component in nickel-based superalloys, TCP phases in nickel-based superalloys often contain small amounts of aluminium. Thus, the use of structure maps for aluminium-containing TCP phases requires that we assign an effective valence and atomic volume to Al that is appropriate for these low concentrations. Traditionally, Al is treated as a transition metal element with its experimental metallic volume [69] of 1.43 Å^3 but with an effective valence of 3, corresponding to the actual number of sp-valence electrons, by PHACOMP or with an effective Md value of 1.9 by NewPHACOMP [49]. This latter Md value lies between those of Ti and V, Nb and Mo, and Ta and W respectively, suggesting that Al behaves in the presence of transition elements as though it had 4 to 6 *spd*-valence electrons. However, a recent study by Joubert [27] on aluminium-containing σ phases has found that Al behaves as if it has 9 or 10 valence electrons. By choosing $N_{\text{Al}} = 9$ we see in Fig. 3.7 that almost all experimentally observed binary TCP phases that contain aluminium are found within their structural domains which are constructed from the aluminium-free TCP phases. Only the two σ phases having the largest content of Al of more than 22%, Al-Nb and Al-Ta, are located slightly outside the σ domain. Hence, for our multi-component structure maps shown in the following sections we have chosen $N_{\text{Al}} = 9$ but we consider only TCP phases with small amounts of aluminium i.e. less than 15%.

Solid solutions of α-Mn

The α form of pure manganese, α-Mn, is isostructural with the χ phase. Theoretical studies on the magnetic properties of the different sites in pure α-Mn at 0 K show that Z16 sites have much larger magnetic moments than the smaller Z12 and Z13 sites [90].

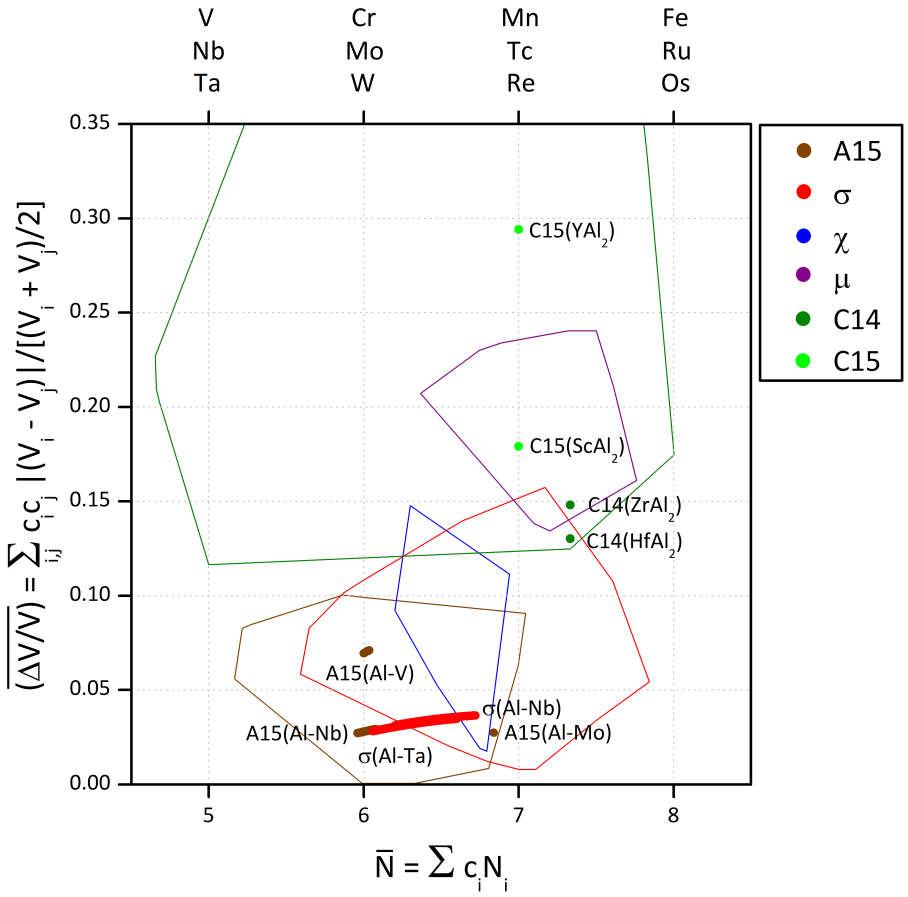

Figure 3.7: Structure map ($\bar{N}$,$\overline{\Delta V/V}$) of all Al-containing binary TCP phases. The different TCP domain boundaries are marked using the homogeneity ranges shown in Fig. 3.2.

An explanation for the stability of α-Mn is that Mn atoms with different magnetic and electronic configurations are effectively atoms of different sizes [91]. Experimental nearest-neighbour measurements support this [92]. As shown by the description of the σ phase domain, our structure map can indicate how much magnetism affects the stability of a phase if its location within the structure map deviates significantly from most of the other phases of same structure-type. Hence, in Fig. 3.8 we investigate α-Mn and its binary solutions forming in Mn-M (with M = Cr, Ti, V, Mo, Re, Ru, Fe, Ni) and Ni together with the χ phases, as shown in the left-hand panel of Fig. 3.2. Figure 3.8 shows that most α-Mn solid solutions form with $\bar{N} \leq 7$ and some curves even reach into the χ phase domain obtained from the χ binary compounds. Although it looks as

if the size factor difference is generally lower for the binary solutions with $\bar{N} > 7$, as compared to the other solutions, it is not clear how the size difference and the valence electron concentration affect the homogeneity range. However, neutron diffraction data of α-Mn with transition-metal impurities indicate that the crystal structure, i.e. the site occupancy, significantly depends on the type of transition-metal element added and its effect on the magnetic structure.

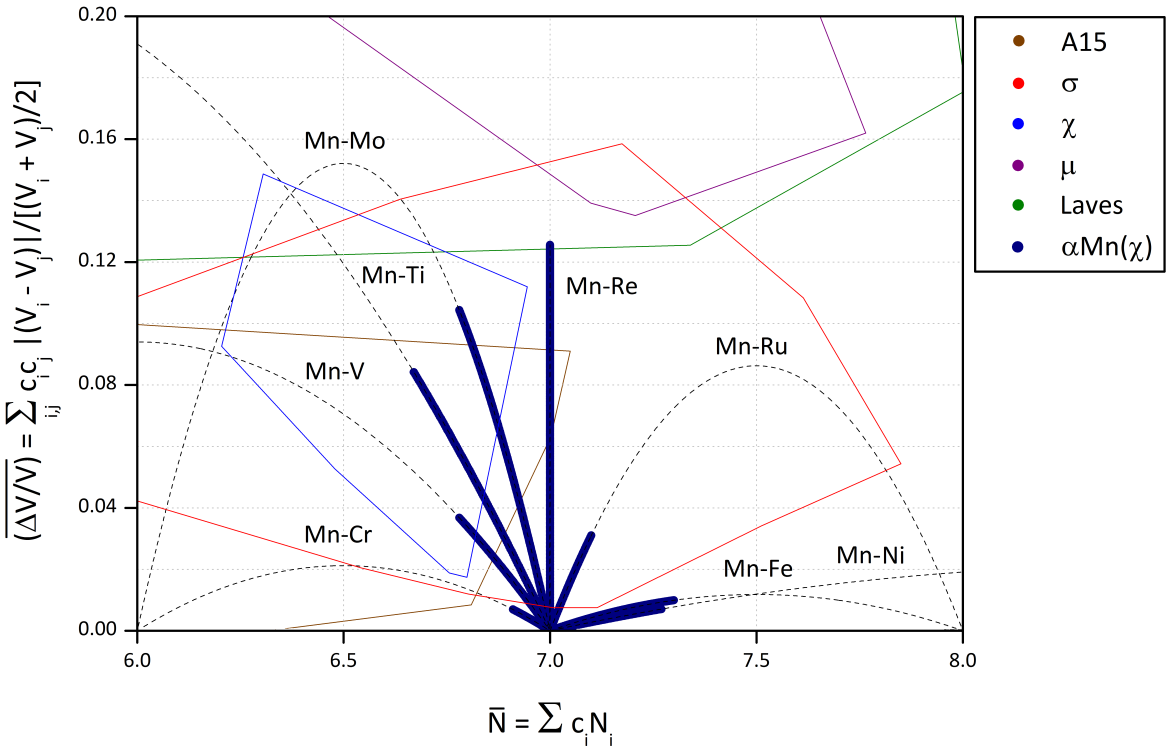

Figure 3.8: Structure map $(\bar{N}, \overline{\Delta V/V})$ of all the binary systems forming α-Mn (χ) solid solutions. Note that σ(Al-Ta) and σ(Al-Nb) lie on top of each other. The different TCP domain boundaries are marked using the homogeneity ranges shown in Fig. 3.2.

3.4 Multi-component systems

In this section we investigate the applicability of the two-dimensional structure map $(\bar{N}, \overline{\Delta V/V})$ introduced in the previous section to the ternary and multi-component sys-

tems given in Sec. 3.2. This will show whether the factors that are found to be responsible for the stability of TCP phases in binary systems also drive the stability of TCP phases in multi-component systems.

3.4.1 Ternary systems

Figures 3.9 and 3.10 show how the ternary TCP phases of isothermal sections, as listed in Tab. 3.2, are mapped onto the two dimensional structure map $(\bar{N}, \overline{\Delta V/V})$. Firstly, Fig. 3.9 shows the Co-containing ternary alloys, Co-Cr-Mo (left) and Co-Mn-Mo (right), where the upper image of each ternary system consists of an experimental isothermal phase diagram and the lower image consists of an $(\bar{N}, \overline{\Delta V/V})$ structure map. The isothermal sections show contour lines which mark areas of constant $\bar{N}$ (thin black lines) and constant $\overline{\Delta V/V}$ (coloured contoured areas) such that the relative final positions of the TCP phases in the structure map are indicated. It can be seen in Fig. 3.9 that both Co-containing ternary systems form σ, μ and R phases and that an additional P phase is found in Co-Mn-Mo. The R and P phases are true ternary phases which lie within the isothermal section between the σ and μ phases. Hence, the P and R phases must be located in the overlap region between σ and μ in the structure map. For the structure maps, we use light grey dots to indicate the possible areas bounded by the parabolas of the corresponding binary systems which can be covered by the TCP phases. As expected, we see that the R and P phases in Co-Cr-Mo and Co-Mn-Mo do indeed lie between σ and μ. A similar trend is observed for the Ni-containing ternary alloys, namely Ni-Cr-Mo and Ni-Mo-Re, involving the σ, δ, and P phases. Figure 3.10 shows that the P phase is formed between the σ phase and the δ phase and is therefore also found between those two phases in the structure map. Hence, one may conclude, from the mapping of the TCP phases of the four ternary systems, that with increasing $\bar{N}$ and $\overline{\Delta V/V}$ the following succession of co-existing TCP structure types exists: $\sigma \rightarrow \mathrm{P/R} \rightarrow \delta/\mu$. This means that there is a relation between the formation of R, δ and P together with σ and μ in the same ternary

system, as indicated by a structural classification in terms of their basic unit layers [30].

However, it can be seen from the grey areas shown in Figs. 3.9 and 3.10 that the transformations need not be single-valued which means that the mapping from the structure map to the phase diagram is not unique. Two crossings can be obtained for a constant $\bar{N}$ due to the parabolic behaviour of the size-factor contribution $\overline{\Delta V/V}$ as indicated by the overlapping grey areas. For example, in the Co-Cr-Mo phase diagram it can be seen that ($\bar{N} = 7.11$, $\overline{\Delta V/V} = 0.156$) corresponds to both a binary σ phase and a ternary R phase, so that (7.11, 0.156) falls in a very small region in the structure map where the σ and R domains overlap. This multi-valuedness, which is a general problem of any surjective mapping method, causes difficulties only for the mapping from the structure map back to the isothermal section. Hence, it reduces the structure map's ability to predict ternary TCP phases from the structural domains within the structure map but has no consequence on our study of the structural trends.

We pointed out in Sec. 3.2 that the only ternary system that forms the M phase is $Nb_{48}Ni_{39}Al_{13}$ [93]. The Al-Ni-Nb system is very interesting because not only are other TCP phases, such as A15, σ, μ and C14, formed but the two essential phases for nickel-based superalloys namely γ(Ni) and $\gamma'(Ni_3Al)$ (see Sec. 2.2) are also formed. We notice from the ternary phase diagram for 1140°C by Benjamin et al. [94] in Fig. 3.11 that the μ and M phases are positioned very close to one another on the ternary phase diagram. This is not surprising because of the close relation of their crystal structures, as was discussed in Sec. 2.2.1. By choosing $N_{Al} = 9$, as explained in Sec. 3.3.3, the M phase is located at a fairly constant valence electron concentration of 7.5 electrons. This is slightly higher than the valence electron concentration of $\mu(Nb_7Ni_6)$ which is located at around 7.25 electrons. Moreover, both phases have very similar stability ranges, with respect to the relative volume difference $\overline{\Delta V/V}$, as μ and M range between 0.18 to 0.25 and between 0.22 to 0.25, respectively. Hence, the M phase is placed above, but close to, the μ phase as shown in Fig. 3.11. According to the mapping of the TCP phases on the structure map, all TCP phases would lie within their corresponding binary domains as defined in

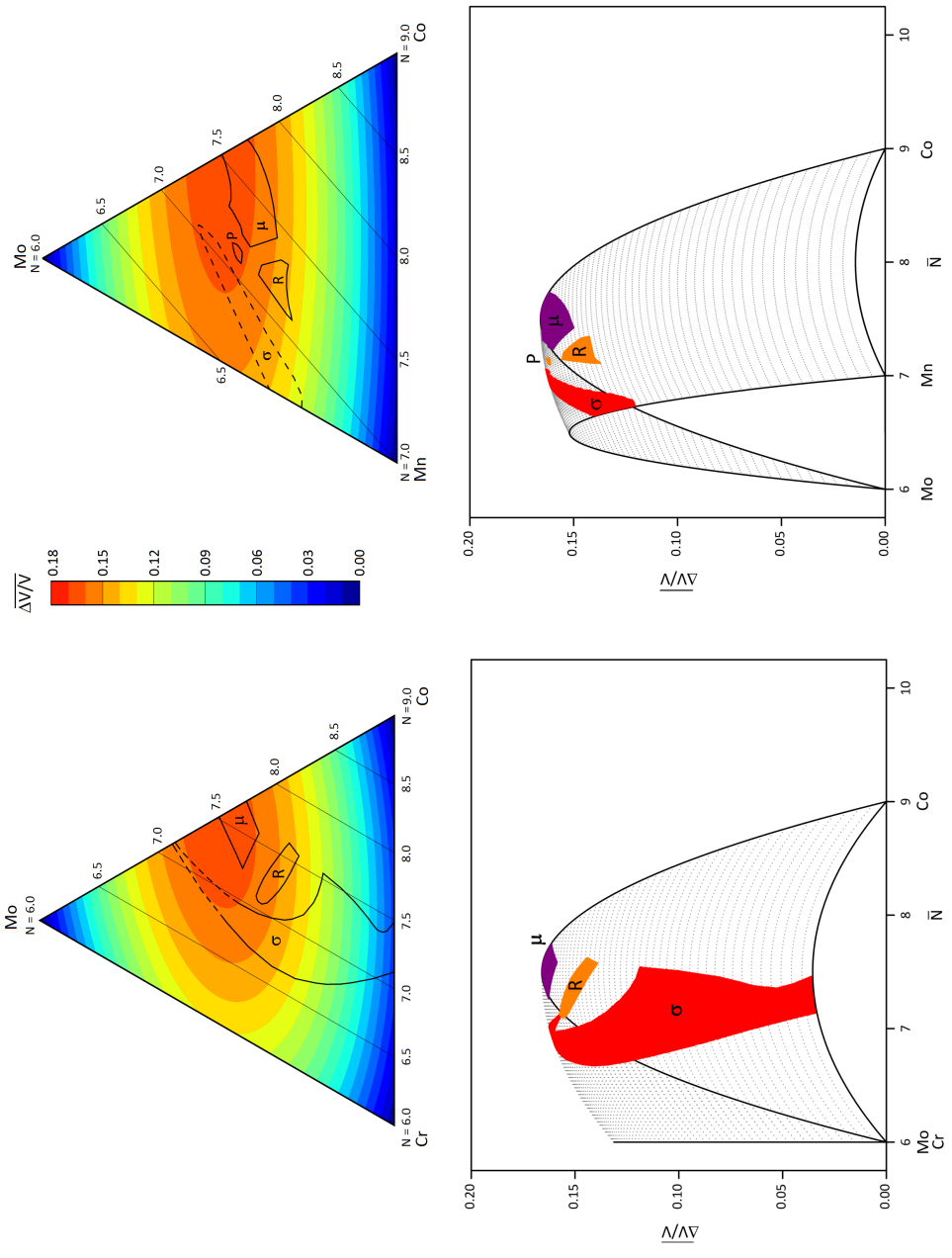

Figure 3.9: Isothermal sections of the Co-containing ternary alloys, Co-Cr-Mo and Co-Mn-Mo, at 1300°C and 1240 °C, respectively. Below each isothermal section is an $(\bar{N}, \overline{\Delta V/V})$ structure map on which the TCP phases of the corresponding ternary phase diagram are mapped.

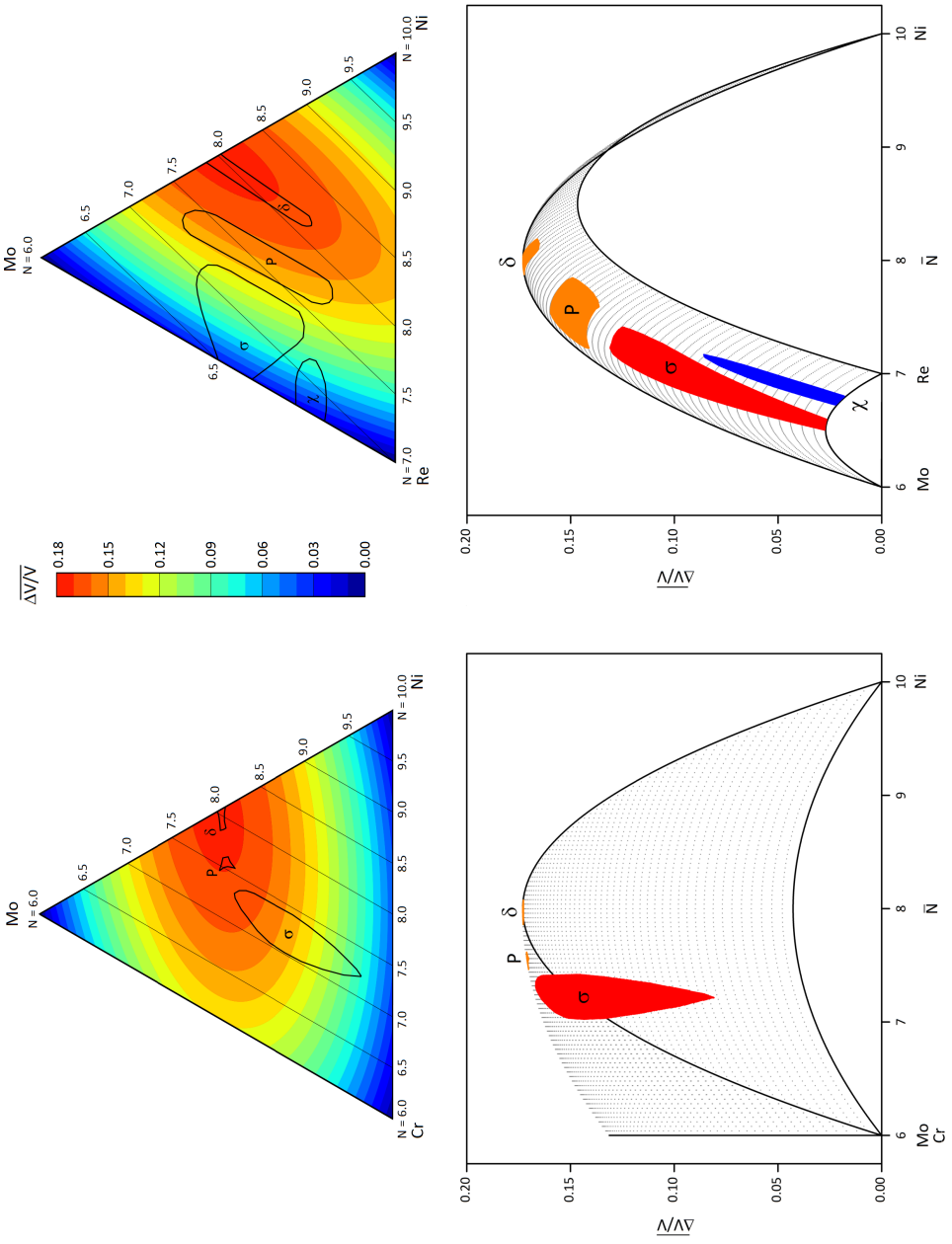

Figure 3.10: Isothermal sections of the Ni-containing ternary alloys, Cr-Mo-Ni and Mo-Ni-Re, at 1250°C and 1152°C, respectively. Below each isothermal section is an $(\bar{N}, \overline{\Delta V/V})$ structure map on which the TCP phases of the corresponding ternary phase diagram are mapped.

Sec. 3.3. This supports the previous observation that Al acts like a transition metal (see Sec. 3.3.3). Moreover, both non-TCP phases, γ and γ' (where γ' is located above γ), are found in the fcc region as shown in Fig. 3.6, as they must do.

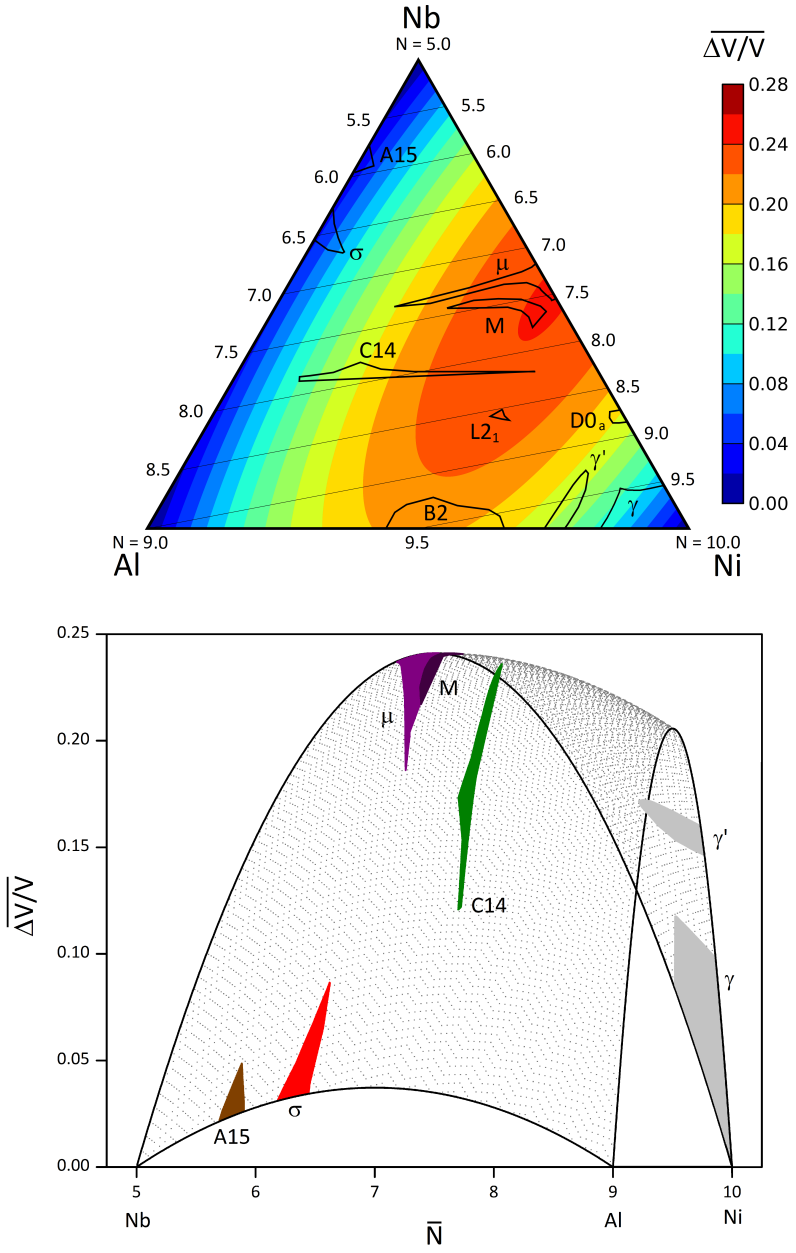

Figure 3.11: Isothermal sections of the Al-containing ternary alloy Al-Ni-Nb at 1140°C by Benjamin et al. [94]. Below the isothermal section is an $(\bar{N}, \overline{\Delta V/V})$ structure map on which all of the stable TCP phases of the ternary phase diagram, together with γ and γ', are mapped.

We see in Fig. 3.12 that all ternary TCP phases are clearly located in or close to the same regions of the structure maps that are favoured by the binary and ternary compounds of the same structure type as defined in Sec. 3.3. As a result of the unequal number of ternary TCP phases per structure type, the A15 and Laves domains are less well covered than σ, χ and μ. Nevertheless, other ternary TCP phase systems that are not given in Sec. 3.2.2 will fall in the appropriate domains within Fig. 3.12.

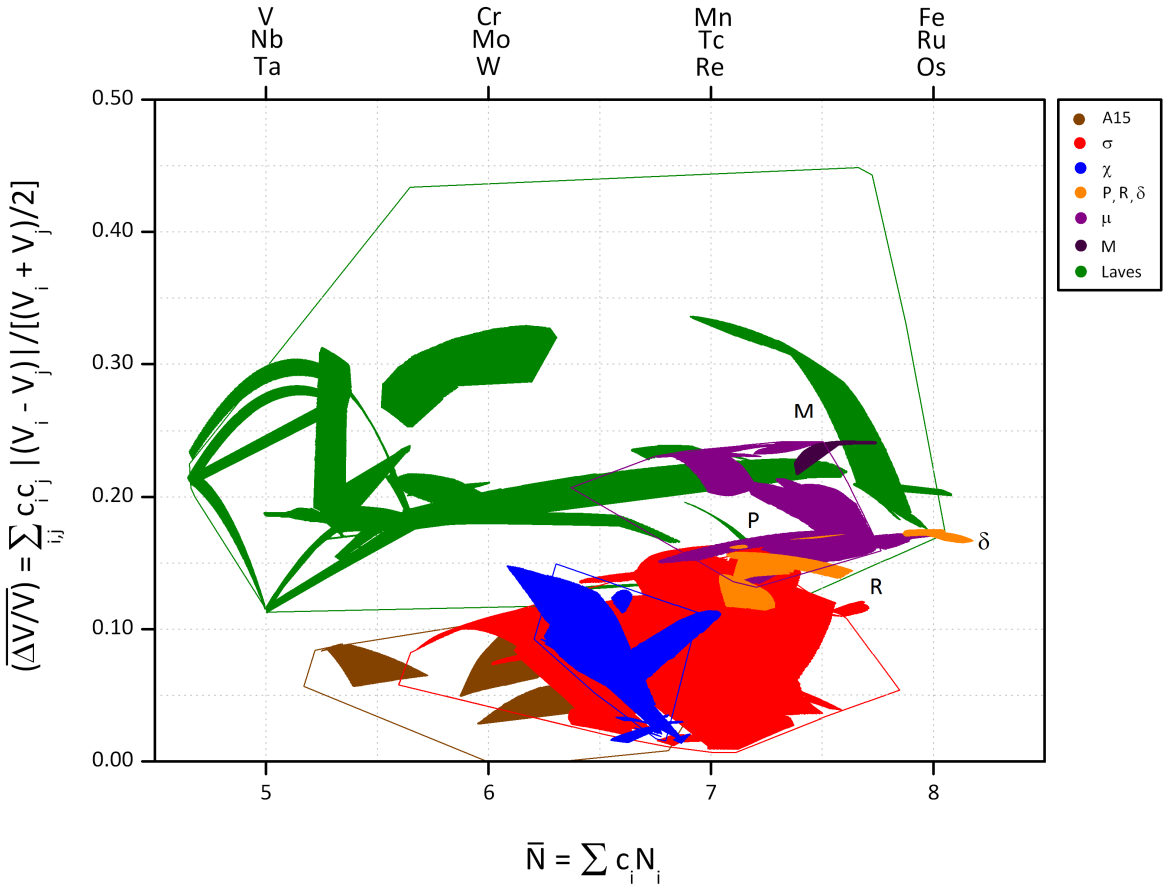

Figure 3.12: Structure map ($\bar{N}$,$\overline{\Delta V/V}$) of the ternary TCP phases given in Tab. 3.2. The values $\bar{N}$ and $\overline{\Delta V/V}$ of each alloy are calculated from the composition of the experimentally observed phases. The different TCP domain boundaries are derived from their homogeneity ranges as shown in Fig. 3.2 and Fig. 3.12.

3.4.2 TCP phases in Ni-based superalloys

Figure 3.13 demonstrates that all multi-component TCP phases are located in or close to the same regions of the structure maps that are favoured by the binary and ternary compounds of the same structure type. Moreover, it shows that the TCP phases which were studied by Rae et al. [14] are packed very closely next to the overlap region of the σ, P/R and μ phases with $\overline{\Delta V/V} \approx 0.150$ to 0.175 and $7.0 \leq \bar{N} \leq 7.5$. This is not surprising because within each of these nickel-based superalloys at least two TCP phases are formed, mostly the σ phase together with the P phase, with very similar compositions. However, studies of the relative position of the co-existing TCP phases in the structure map reveal that the size factor mostly follows the same sequence as for the ternary TCP phases, namely $\sigma \rightarrow \mathrm{P} \rightarrow \mu$ as $\overline{\Delta V/V}$ increases.

3.5 Summary

In this chapter we have introduced a new two-dimensional structure map ($\bar{N}$,$\overline{\Delta V/V}$) where $\bar{N}$ is the average electron concentration and $\overline{\Delta V/V}$ is a composition-dependent relative volume difference. This map separates the experimental data of the TCP phases of binary transition metal alloys into well-defined regions corresponding to different structure types such as A15, σ, χ, R, P, δ, μ, M and Laves. However, these regions can overlap not only with other TCP phase domains but also with domains of fcc, hcp and bcc-like structures. This means that the structure map can only indicate whether a TCP phase is likely to form but cannot actually predict its formation. However, two groups of TCP phase are identified with respect to the size factor. These are, firstly, the electron compounds, A15, σ and χ with $\overline{\Delta V/V} \leq 0.15$ and, secondly, the μ, M and Laves phases with $\overline{\Delta V/V} \geq 0.15$. The R, P and δ phases are located in the overlap region between these two groups. Detailed investigations of multi-component systems demonstrate that TCP phases, regardless of the number of constituents, are located in the same regions of the structure map that are favoured by the binary compounds of the same structure type. Moreover, the structure

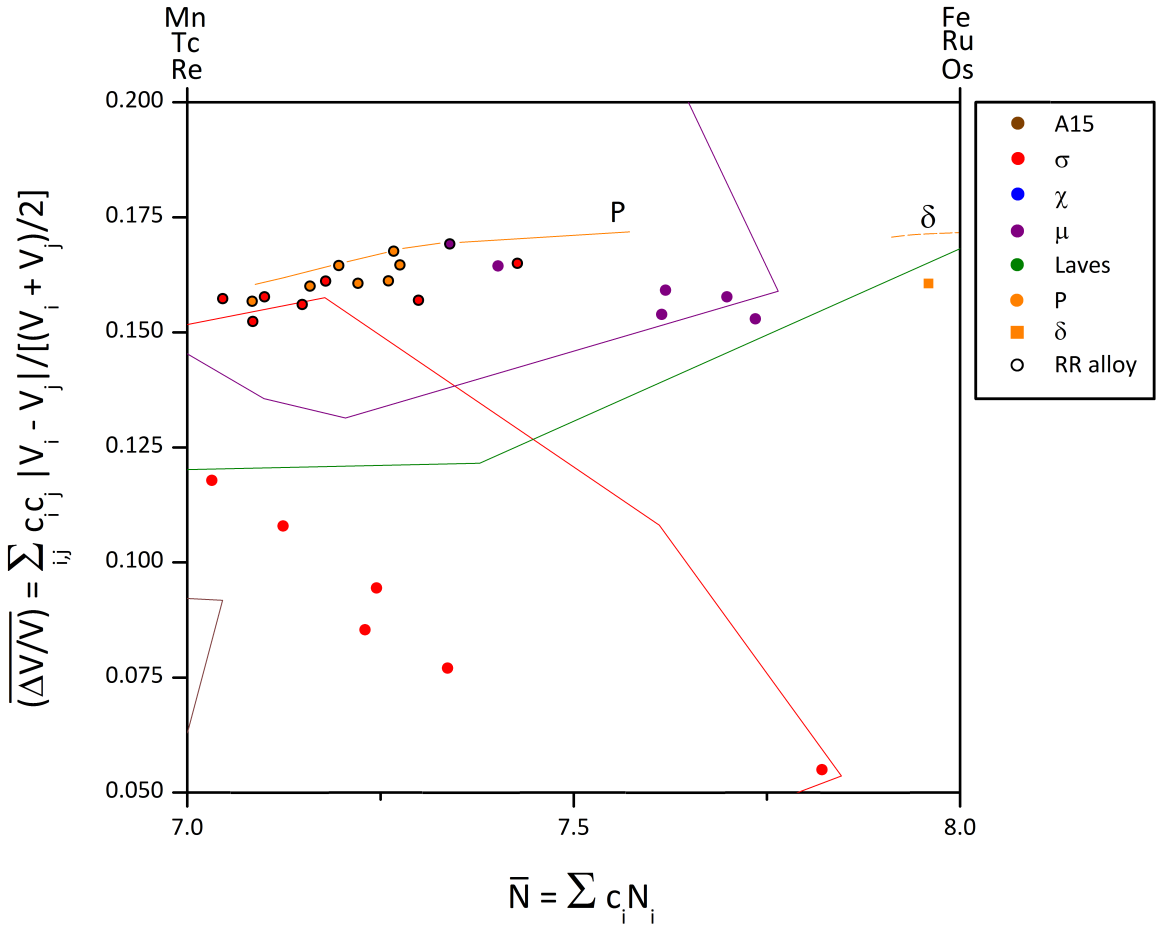

Figure 3.13: Structure map ($\bar{N}$,$\overline{\Delta V/V}$) of the TCP phases formed in Ni-based superalloys. The values $\bar{N}$ and $\overline{\Delta V/V}$ of each alloy are calculated from the composition of the experimentally observed phases. The domain boundaries of A15, σ, χ, μ, δ and the Laves phases are derived from their homogeneity ranges as shown in Fig. 3.2. The domain boundary of the R phase is estimated from the investigated ternary systems as shown in Fig. 3.12.

map is a useful tool for studying various aspects of TCP phase stability such as the influence of aluminium, the solid solutions of α-Mn and common structural trends like the succession of phases bcc $\rightarrow$ TCP(A15 $\rightarrow$ σ $\rightarrow$ χ) $\rightarrow$ hcp $\rightarrow$ fcc of alloys with $\overline{\Delta V/V} \leq 0.15$.

In the following chapter we will use the structure map together with CALPHAD computations to draw conclusions concerning the applicability of existing one-dimensional methods, like PHACOMP and NewPHACOMP, for the seven component Ni-Co-Cr-Ta-W-Re-Al system studied by Reed et al. [95].

Chapter 4

Application of the two-dimensional structure map to alloy design

The structure map introduced in the previous chapter let us identify regions where the formation of a specific TCP phase is likely, however, it was pointed out in Sec. 3.3.2 that structure maps cannot be used to predict the occurrence of phases. This lack of predictability should make structure maps such as the one-dimensional PHACOMP and NewPHACOMP method, or our two-dimensional map, poor TCP predictors. However, very recently, Reed et al. [95] used NewPHACOMP to predict the formation of TCP phases for the seven component Ni-Co-Cr-Ta-W-Re-Al system in an attempt to base the design of new nickel-based superalloys solely on theoretical analysis and computer models. Since our investigation of multi-component TCP phases in the previous chapter showed that TCP phases, regardless of the number of components, are located within the structure map regions that are favoured by the binary TCP phases, the structure map can be used to test if the TCP phase predictions of Reed et al., which are based on NewPHACOMP, are valid.

As discussed in Sec. 2.3.1, NewPHACOMP only indicates whether an alloy is likely to form TCP phases but it does not provide any information about the composition of the TCP phases. Equally, our structure map cannot be used to test whether NewPHACOMP

correctly predicts the formation of TCP phases without any specified compositions. Fortunately, the CALPHAD method which is described in detail in Sec. 2.3.2 can be used to calculate multiphase, multi-component equilibria and the compositions of all stable phases for any given temperature. Reed et al. also carried out CALPHAD calculations but instead of directly predicting whether the investigated systems are TCP phase prone or not, they used CALPHAD to calculate the γ/γ' lattice parameter misfit in order to prevent excessive coarsening of the γ' structure within their designed alloys. Before we can actually validate the predictability of the NewPHACOMP method, CALPHAD calculations will first be carried out in Sec. 4.1 to see whether the CALPHAD predicted TCP phases do lie in the correct respective regions of the structure map. The resulting CALPHAD data of correctly predicted TCP phases will then be used in Sec. 4.2 to study the robustness of NewPHACOMP to predict the formation of these phases.

4.1 CALPHAD predictions

Following the lead of Reed et al. [95], the Co concentration is taken to vary from 0 to 10 wt.% ($\approx$ 0.0-11.0 at.%), the Cr concentration from 4 to 12 wt.% ($\approx$ 4.3-14.7 at.%), the Ta concentration from 4 to 8 wt.% ($\approx$ 1.2-2.9 at.%), the W concentration from 0 to 8 wt.% ($\approx$ 0.0-2.8 at.%), the Re concentration from 0 to 5 wt.% ($\approx$ 0.0-1.7 at.%) and the Al concentration from 4 to 7 wt.% ($\approx$ 8.4-16.1 at.%) which leaves Ni to vary from 50 to 88 wt. % ($\approx$ 52.4 - 85.8 at.%). Reed et al. carried out the calculations at a resolution of 1 wt.% for all elements which gave a compositional dataset consisting of approximately 100,000 alloys. Our calculations are also carried out at a resolution of 1 wt. % for Re and Al but Co, Cr, Ta and W are varied with a resolution of 2 wt.% in order to reduce computational time. Hence, our dataset consists of 18,000 alloys which is sufficiently large for our purposes.

The CALPHAD software interface Thermo-Calc^{TM} together with the thermodynamic database for nickel-based superalloys, Thermo-Tech^{TM} TTNi database [96] version 6 was

used in order to obtain the compositions of all stable phases from the lowest Gibbs free energy state (see Sec. 2.3.2) for each individual alloy composition at various temperatures. According to its developers, the TTNi database can predict, in addition to the well studied γ and γ' phases, several TCP phases such as A15, σ, χ, R, P, δ, C14 and C15. The resulting composition of each thermodynamically stable phase was then used to calculate its corresponding valence electron concentration $\bar{N}$ and size factor $\overline{\Delta V/V}$, as defined in Eqs. 3.1 and 3.2, respectively.

The points ($\bar{N}$, $\overline{\Delta V/V}$) calculated from the compositions of the resulting thermodynamically stable phases at a service temperature of 900°C are shown in Fig. 4.1. The γ and γ' phases are predicted to be located in the fcc-based region and are each tightly grouped together. In addition, similar to the Al-Nb-Ni system in Sec. 3.4.1, it shows that in alloys where γ and γ' coexist, the γ phase is generally located below the γ' phase because of the higher Ni content of the γ phase. Importantly, as can be seen in Fig. 4.1, the thermodynamic database locates the σ phases in the expected region, between 6 and 7 electrons, but clearly incorrectly predicts the locations of the μ phase and the P phase, as they lie far outside the expected regions. This observation agrees well with Zhao and Henry's study [64] (see Sec. 2.3.2) which highlights the difficulties encountered in using the thermodynamic database for the prediction of less well known TCP phases such as the μ and P phases.

The calculations of Reed et al. for the γ/γ' equilibria were made at 900°C because it was assumed to be a common service temperature of turbines blades. However, TCP phases in Ni-based superalloys are usually found to form between 700 and 1100°C [11]. Hence, further CALPHAD calculations for 700°C, 1100°C and 1300°C were carried out and the data points ($\bar{N}$, $\overline{\Delta V/V}$) calculated from the compositions of the resulting thermodynamically stable TCP phases at these temperatures are shown in Fig. 4.2. These confirm our previous observation for 900°C, namely that μ and P phases are located outside their domains, whereas it seems that the σ phases are located well within their domain regardless of the temperature.

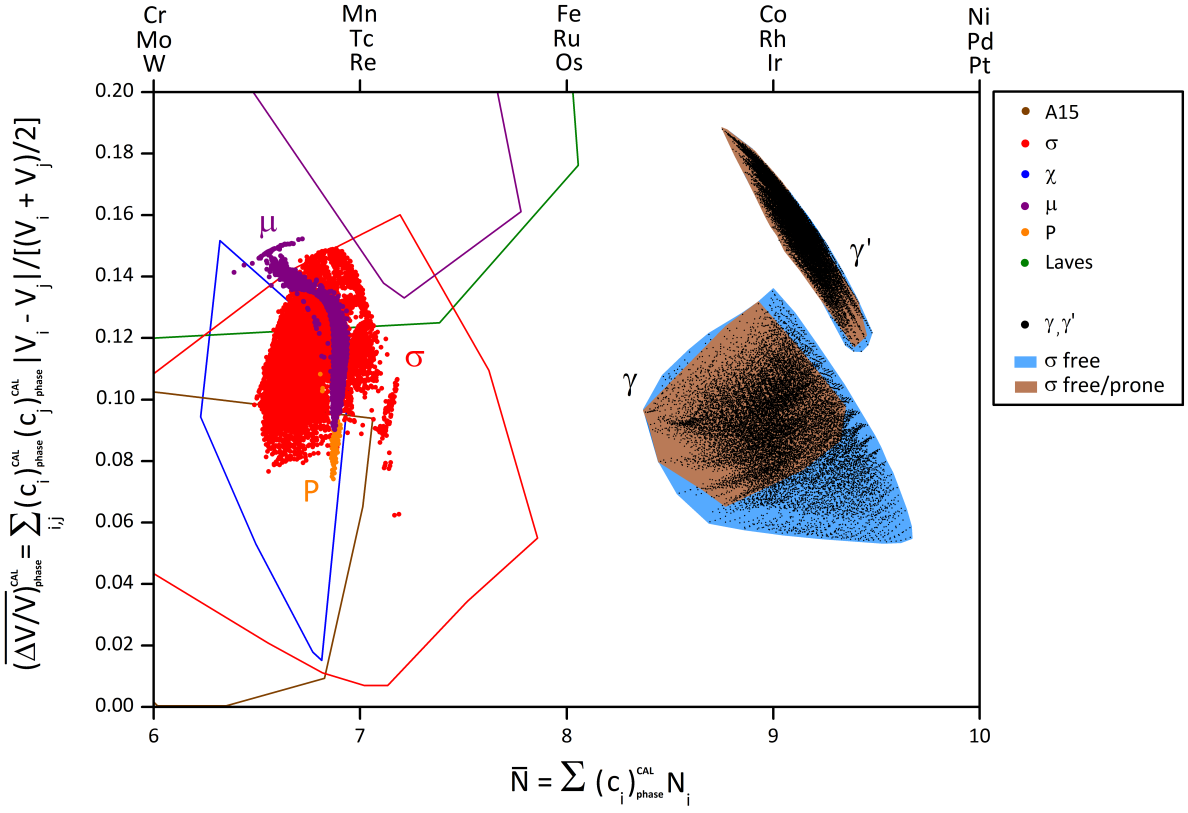

Figure 4.1: Structure map $(\bar{N}, \overline{\Delta V/V})^{CAL}_{phase}$ where the two co-ordinates are calculated from the CALPHAD-predicted compositions of the individual phases. The predicted $\gamma$and γ' domains with $\bar{N}$ and $\overline{\Delta V/V}$ are also included. They are coloured to show the blue σ free region where no σ phases are found and the brown σ free/prone region where some alloys are free from σ phases but others are not. The different TCP domain boundaries are taken from Fig. 3.2.

Since most σ phases seem to be fairly well predicted by the thermodynamic database, one can compare the composition of the 6758 σ-prone alloys with the composition of the 11242 σ-free alloys for 900°C and examine the influence of certain elements on the formation of TCP phases. Therefore, in the following two subsections we will discuss the effect of elements on σ formation and σ fraction.

4.1.1 Influence of alloying elements on σ phase formation

In Fig. 4.3 we show the content of Ni-Co-Cr-Mo-Al, averaged over a small region of the structure map in σ-free and σ-prone alloys. It confirms the common perception that W

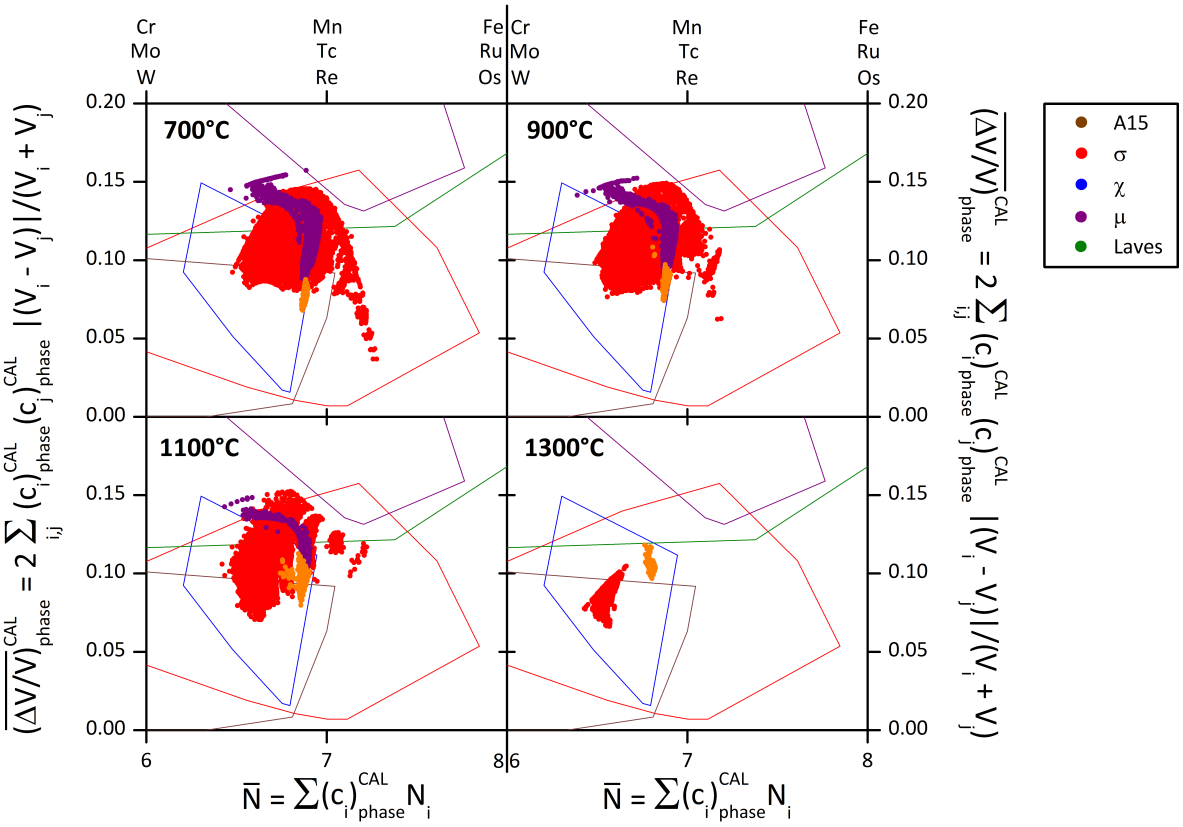

Figure 4.2: Structure map ($\bar{N}$,$\overline{\Delta V/V}$) of the CALPHAD predicted TCP phases at 700°C (upper left), 900°C (upper right), 1100°C (lower left) and 1300°C (lower right) where $\bar{N}$ and $\overline{\Delta V/V}$ are calculated from the compositions of the predicted phases. The different TCP domain boundaries are taken from Fig. 3.2.

and Re are the elements which most potently promote TCP phase formation. Unfortunately, as discussed in Sec. 2.1.1, W and Re are essential components of superalloys as they provide the necessary solution strengthening of the γ matrix which leads to higher resistance against creep formation [95]. Fig. 4.3 shows that the overall average W content of σ-free alloys is 3.40 wt.% which is significantly smaller than the overall average W content of σ-prone alloys of 4.99 wt.%. For rhenium we see an even larger difference as the σ-free and the σ-prone alloys contain 1.86 wt.% and 3.55 wt.%, respectively. In addition, Fig. 4.3 demonstrates that σ formation is far more likely for alloys with about 2.5 wt.% Re ($\approx$ 1 at.%). Interestingly, it shows that σ-prone alloys which do not contain Re (23 out of 2977 alloys) involve very high concentrations of W (above 7 wt.% on average). The opposite is observed for alloys without W, where a high content of Re seems to lead to

the formation of σ phases. However, the presence of small σ-free regions of $\bar{N} \approx 9.0$ and $\overline{\Delta V/V} \approx 0.15$ in the lower left-hand panel in Fig. 4.3 imply that σ phase formation is not guaranteed even if alloys contain significant amounts of Re.

4.1.2 Influence of alloying elements on σ phase fraction

In the previous subsection all σ-prone alloys were considered to be equal regardless of the actual amount of σ particles. The detrimental effects of TCP phases however depend to a large extent on the volume fractions of the precipitates [12]. The histogram in the upper panel of Fig. 4.4 displays the distribution of σ-prone alloys as a function of the atomic fraction of the predicted σ phases. The histogram shows that most predicted σ phases have relatively low fractions (75% of all σ phases have atomic fractions of less than 4 at.%) as compared to γ and γ' fractions. This is in agreement with the atomic fractions of the experimental σ phases which were studied in Sec. 3.4.2 which are not higher than 3 at.%. The middle panel of Fig. 4.4 shows the average content of Co, Ta, Re, Cr, W and Al of the total alloy as a function of the atomic fractions of the predicted σ phase. It confirms general experimental observations which indicate that additions of transition metals to the total alloy composition (i.e. replacing Al or Ni with Cr, Co, Re, W or Ta) increases the fraction of σ phases present. In addition, it was shown in the previous subsection that W and Re have the largest influence on the formation of σ phases. This is also confirmed by the lower panel of Fig. 4.4 which shows the average content of Co, Ta, Re, Cr, W and Al of the predicted σ phases as a function of their atomic fractions. For alloys with low σ fractions, we notice that Re, with more than 50 at.%, and W, with around 25 at.%, are the elements with the largest concentrations within the predicted σ phase, although the total contents of Re and W within these alloys are the lowest of all elements. Moreover, in the less likely case of having σ fractions above 4%, the lower panel of Fig. 4.4 shows a decrease in the content of Re and W as the σ phase increases. However, this does not contradict the previous argument about the potency of Re and W to form σ phases

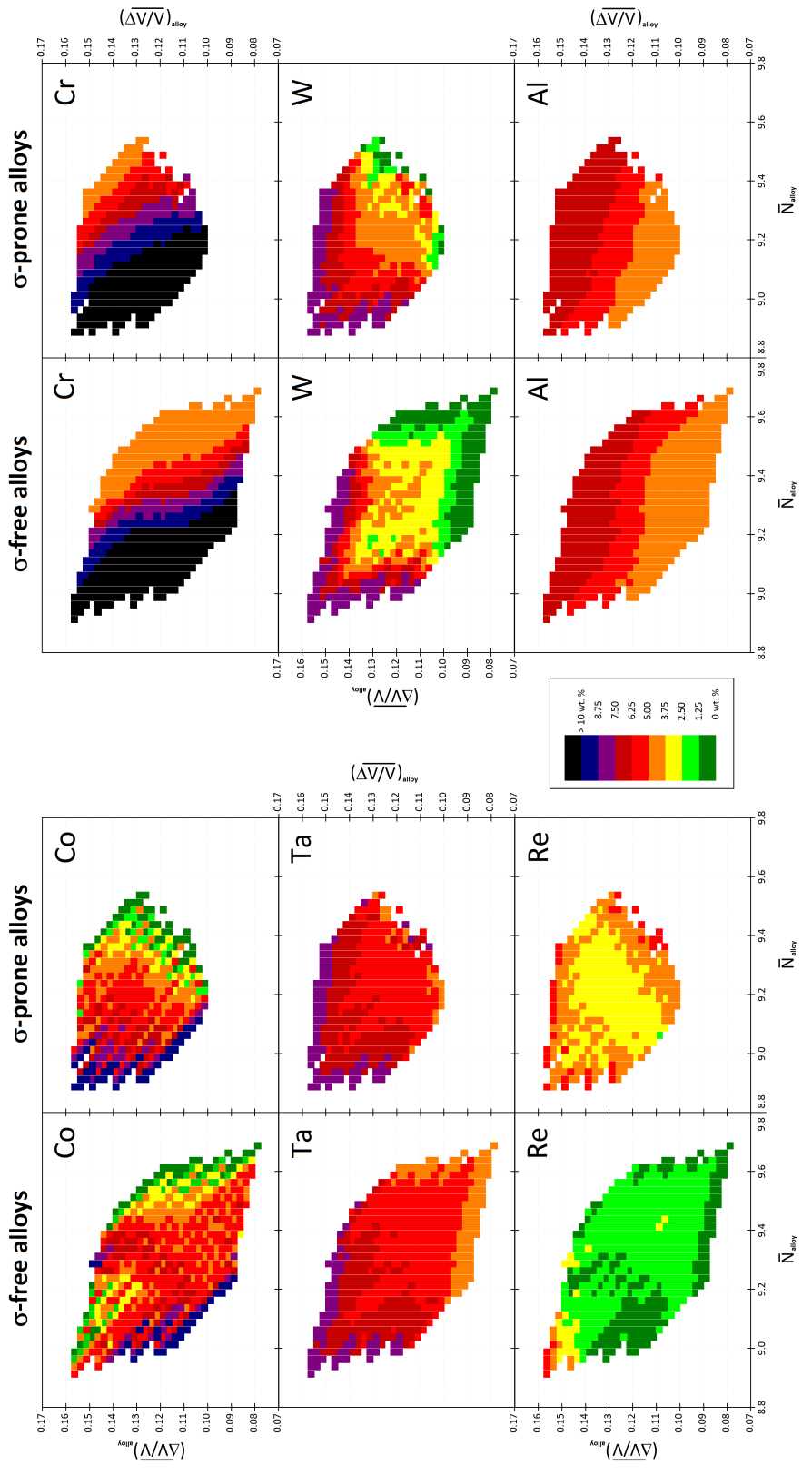

Figure 4.3: Structure maps ($\bar{N}$,$\overline{\Delta V/V}$) showing the average concentration of Co, Ta, Re, Cr, W and Al of CALPHAD-predicted σ-free and σ-prone Ni-Co-Cr-Ta-W-Re-Al alloys. The values, $\bar{N}$ and $\overline{\Delta V/V}$, are calculated from the total alloy compositions. The average interval lengths are 0.025 and 0.0025 for $\bar{N}$ and $\overline{\Delta V/V}$, respectively.

because as the σ phase fraction becomes larger more Re and W are located within the σ phases and not within the γ and γ' phases as is the case for smaller σ fractions. For example, only 23% of the total amount of Re is found within the σ phase for the alloys with predicted σ fractions of 1% as compared to an average overall Re content of 70% for the alloys with a predicted σ fraction of 10%.

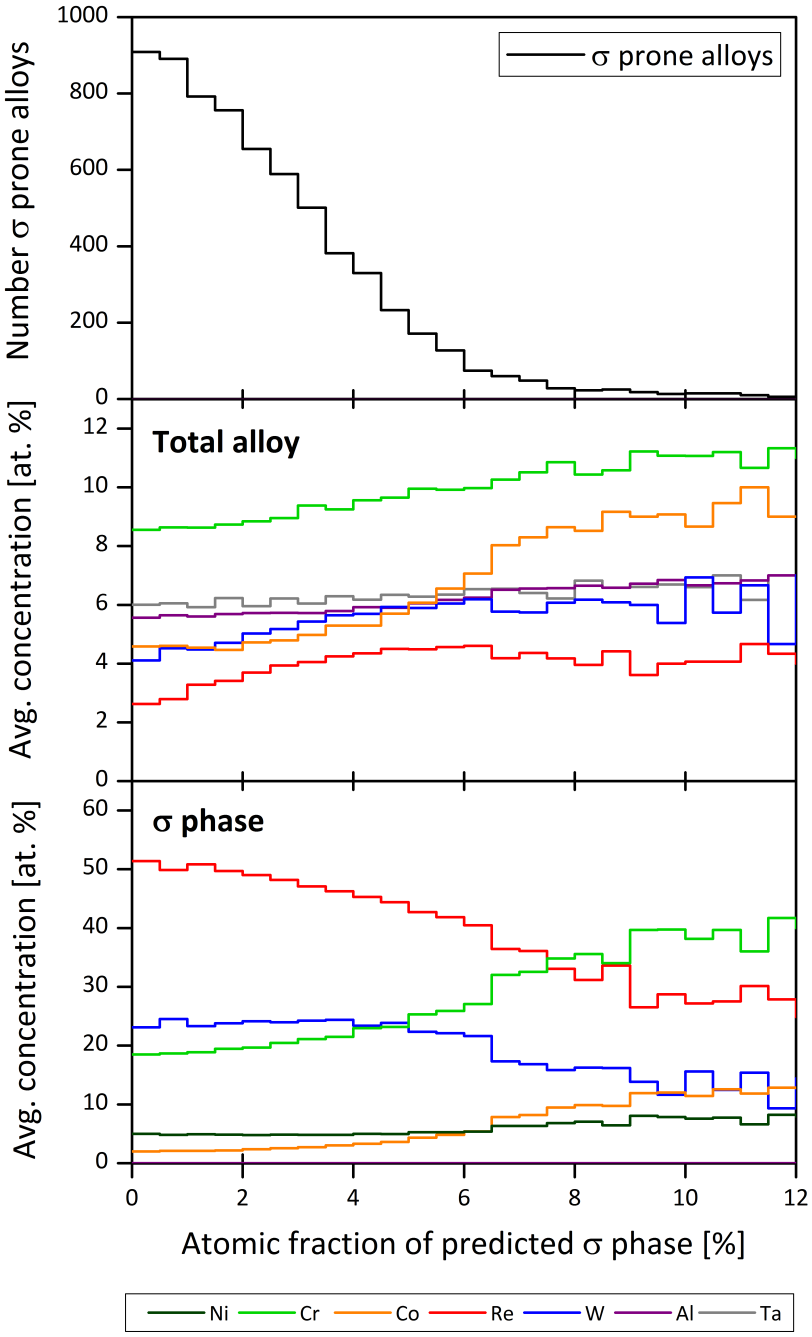

Figure 4.4: Upper panel: Frequency histogram showing the number of CALPHAD-predicted σ-prone alloys per bin versus the atomic fraction of the predicted σ phase. Middle panel: Average concentration of Co, Ta, Re, Cr, W and Al of the average alloy composition as a function of the atomic fraction of the predicted σ phase. Lower panel: Average concentration of Ni, Co, Ta, Re, Cr, W and Al of the CALPHAD-predicted σ phase as a function of the atomic fraction of the predicted σ phase.

4.2 NewPHACOMP predictions

The CALPHAD data on σ formation allows us to study the robustness of NewPHACOMP to predict the formation of σ phases by comparing σ-prone and σ-free alloys. As discussed in Sec. 2.3.1, this comparison can be carried out with respect to the Md values calculated from the total alloy or γ compositions. Thus, the two frequency histograms in Fig. 4.5 show the number of Ni-Co-Cr-Ta-W-Re-Al alloys per bin that are σ-prone or σ-free according to CALPHAD as a function of Md values which are calculated from total alloy compositions ($\bar{Md}_{alloy}$)and γ compositions ($\bar{Md}_{\gamma}$) for the upper histogram and lower histogram, respectively. However, the latter Md values are only calculated from the actual CALPHAD predicted γ phase if no TCP phases are predicted to be formed in the alloy because the PHACOMP method assumes that σ forms from within the γ phase (see Sec. 2.3.1). Hence, in the case of CALPHAD predicting TCP phases, the predicted TCP phase compositions must therefore be added to the γ composition in order to calculate $\bar{Md}_{\gamma+TCP}$.

Reed et al. calculated $\bar{Md}_{alloy}$ and chose a tolerance of $\bar{Md}_{alloy} < 0.961$ eV which is smaller than the Md_{alloy} value of CMSX-4 and CMSX-10, $\bar{Md}_{alloy}^{crit,CMSX-4/10}$. All of the alloys within this tolerance should therefore be more stable than CMSX-4 and CMSX-10 with respect to σ formation. However, Proctor [97] studied samples of CMSX-4 annealed at 1050 and 1150°C and found that, at these temperatures, CMSX-4 is a μ stable alloy, with small amounts of R present at 1150°C. Our CALPHAD calculations of CMSX-4, with the composition of CSMX-4 taken from [3], and calculations carried out by Saunders [98] show that CMSX-4 is correctly calculated to be μ dominant at higher temperatures with a small amount of P forming just below the TCP solvus temperature. The CMSX-4 calculations also predict the formation of a σ phase at lower temperatures. Thus, the threshold for the study of σ formation with respect to $\bar{Md}_{\gamma}$ is $\bar{Md}_{\gamma+TCP}^{crit,CMSX-4/10} = 0.941$ eV.

Besides the fact that this choice of threshold is questionable because CMSX-4 does not

seem to be entirely TCP-free, the use of a universal critical value for an investigation that covers a relatively large compositional space is also unusual. In practice, as explained in Sec. 2.3.1, a critical value would be estimated experimentally by trial-and-error testing for a family of alloys so that only alloys within a certain compositional space can be assumed to be TCP-free. Therefore, significant compositional changes as carried out in the Ni-Co-Cr-Ta-W-Re-Al system would need continuous adjustment of the critical value Md^{crit} values as has been shown, for example, by Caron in [53].

It is therefore not surprising that the thresholds $\bar{M}d_{alloy}^{CMSX-4/10}$ and $\bar{M}d_{\gamma}^{CMSX-4/10}$ significantly underestimate the risk of σ phase formation as shown in Fig. 4.5. Moreover, it is interesting to see that both ways of calculating the $\bar{M}d$ value do not vary significantly in their ability to predict σ phases because in the upper panel of this figure we see that 23% of all alloys with $\bar{M}d_{alloy} < 0.961$ and in the lower panel 24% of all alloys with $\bar{M}d_{\gamma/\gamma+TCP} < 0.941$ are predicted to be σ-prone. Figure 4.5 shows that thresholds of $\bar{M}d_{alloy}^{crit,free} = 0.905$ and $\bar{M}d_{\gamma/\gamma+TCP}^{crit,free} = 0.865$ define σ-free domains but these domains only contain 14% and 13% of all alloys for the upper and lower panel, respectively, while the remainder lie within the domain where alloys are either σ-free or σ-prone. Therefore, regardless of the way $\bar{M}d$ is calculated, Fig. 4.5 demonstrates a more fundamental problem of the NewPHACOMP-like approaches. That is, since the critical parameter cannot clearly differentiate between σ-free and σ-prone alloys, any reasonable choice of a threshold will rule out a significant amount of σ-free alloys (77% and 80% of all σ-free alloys for $\bar{M}d_{alloy}$ and $\bar{M}d_{\gamma}$, respectively) which may possibly have superior properties. This makes these methods unsuitable for the design of new nickel-based superalloys.

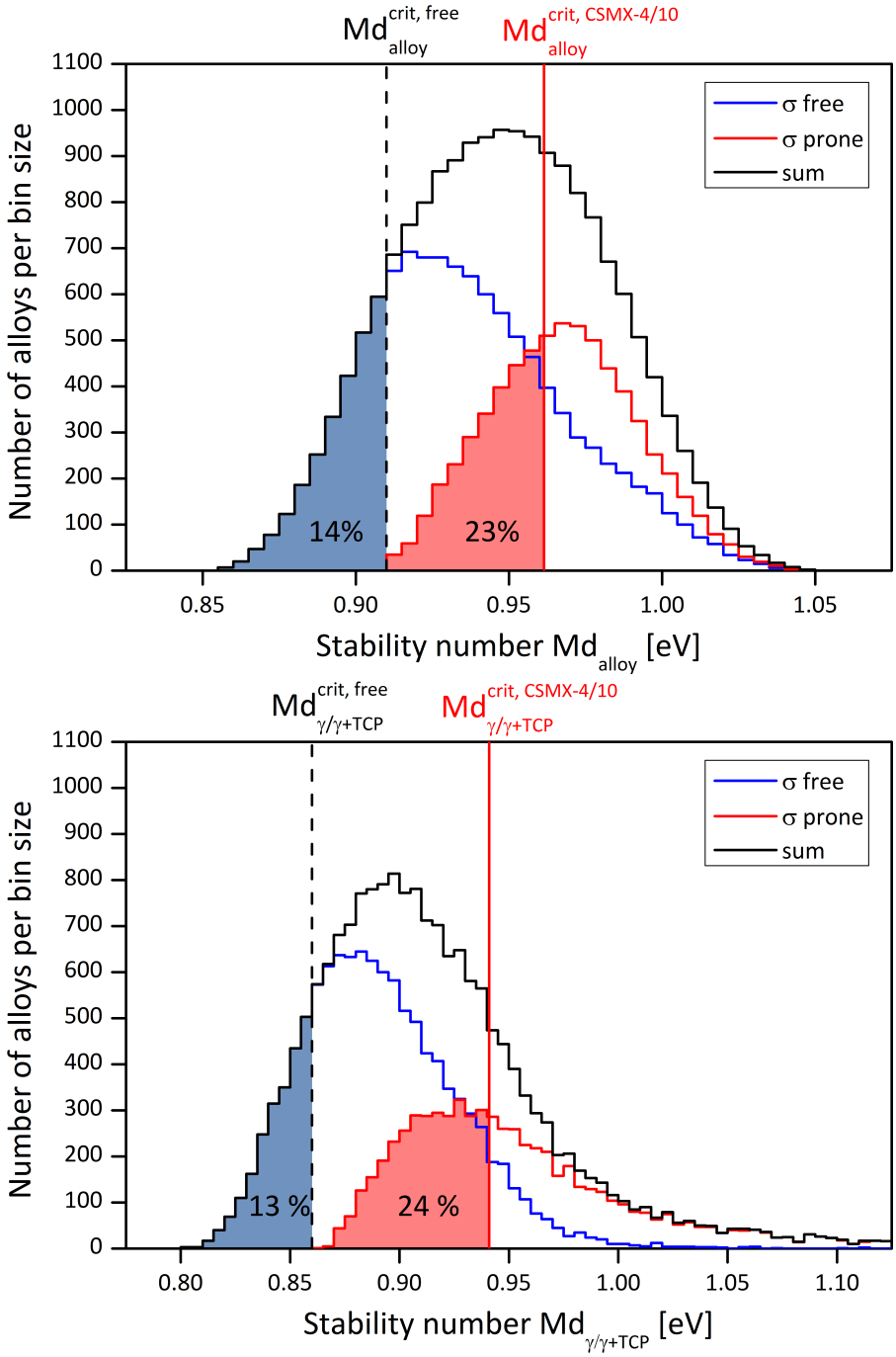

Figure 4.5: Frequency histogram showing the number of Ni-Co-Cr-Ta-W-Re-Al alloys per bin that are σ-prone or σ-free according to CALPHAD as a function of Md which is calculated from the composition of the alloy (upper panel) and the γ phase. The thick red lines indicate the critical Md value for CMSX-4/10 as suggested by Reed et al. [95] (upper panel) and the CALPHAD predicted value (lower panel). The red area corresponds to 23% and 24% of all alloys up to this threshold which NewPHACOMP wrongly predicts to be σ-free for the upper and lower panel, respectively. The dashed black line marks the alloy with lowest Md value that is predicted to be σ-prone. The alloys (i.e. 14% and 13% of all alloys for alloy and γ composition, respectively) below this threshold are σ-free.

4.2.1 Comparison with two-dimensional structure map predictions

Despite the fact that structure maps are not supposed to predict the formation of new phases (see Sec. 3.3.2), it is still interesting to know how well the structure map co-ordinates, $\bar{N}$ and $\overline{\Delta V/V}$, calculated from the total alloy composition (indicated by *alloy* as subscript) and from the composition of the CALPHAD calculated γ phase (indicated by γ as subscript) separate TCP-free from TCP-prone alloys in comparison to the $\bar{M}d$ value as discussed in the previous subsection. We see in the upper panel of Fig. 4.6 that the co-ordinates $(\bar{N}_{alloy}, \overline{\Delta V/V}_{alloy})$ demarcate a larger σ-free domain containing 22% of all alloys as compared to 14% for $\bar{M}d_{alloy}$ in the upper panel of Fig. 4.5. A similar trend is observed for the lower panels of Figs. 4.5, for $(\bar{N}_{\gamma}, \overline{\Delta V/V}_{\gamma})$, and 4.6, for $\bar{M}d_{\gamma}$, where the σ-free domain of the structure map is found to consist of 25% of all alloys as compared to 13% for the NewPHACOMP method. Although both sets of structure map co-ordinates perform better than NewPHACOMP, the overlap regions of σ-free and σ-prone are still too large for robust and reliable alloy design because too many σ-free alloys with potentially superior properties would be ruled out. Therefore, the two-dimensional structure map should only be used with caution as a design tool for new nickel-based superalloys.

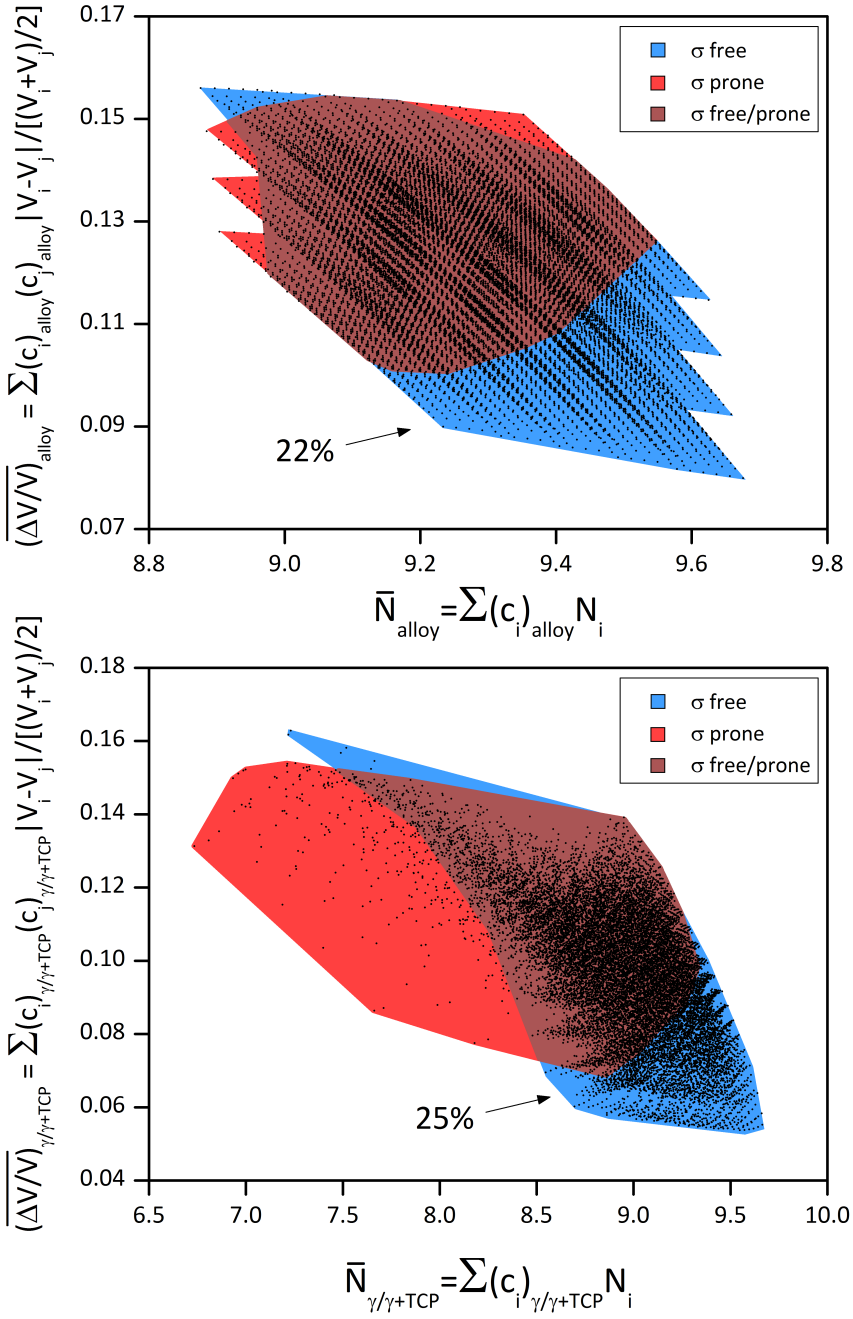

Figure 4.6: Upper panel: σ-stability map $(\bar{N}_{alloy}, \overline{\Delta V/V}_{alloy})$ alloy of CALPHAD-predicted Ni-Co-Cr-Ta-W-Re-Al alloys that are σ-free (blue region), σ-prone (red region), and σ-free/prone (brown region) where some alloys are free from σ phases but others are not. The blue σ-free region contains 22% of all alloys. Lower panel: σ-stability map $(\bar{N}_{\gamma}, \overline{\Delta V/V}_{\gamma})$ alloy of CALPHAD-predicted Ni-Co-Cr-Ta-W-Re-Al alloys that are σ-free (blue region), σ-prone (red region), and σ-free/prone (brown region) where some alloys are free from σ phases but others are not. The blue σ-free region contains 25% of all alloys.

4.3 Summary

In this chapter we have demonstrated that our structure map can be used to test the most commerically prominent methods used in the design of nickel-based superalloys in terms of their ability to predict correctly the susceptibility of nickel-based superalloys to TCP phase formation. CALPHAD calculations in the Ni-Cr-Co-Re-W-Al-Ta system apparently predict correctly the formation behaviour of σ phases, as these phases are found in the σ phase region in our structure map, but fails to correctly predict the formation behaviour of the μ and P phases. The study of $\bar{M}d$ values of all alloys for which the thermodynamic database predicts σ phases demonstrates that NewPHACOMP significantly underestimates the risk of σ formation for the recommended choice of critical values. Although the performance of the structure map in separating σ-free from σ-prone alloys was better than NewPHACOMP, we argue against the use of either NewPHACOMP or the two-dimensional structure map for the design of new nickel-based superalloys. Hence, as indicated in Sec. 2.3.2, future reliable predictions of TCP phase stability in nickel-based superalloys will require enhanced thermodynamic databases which incorporate *ab initio*-derived properties in order to overcome the lack of experimental data.

However, even with these enhanced thermodynamic databases, CALPHAD will only be a valid tool for predicting the formation of TCP phases as long as the alloys considered are those with compositions that are close to those multi-component systems which are already well understood and for which data already exists. This means that CALPHAD will still perform rather well when interpolating data, but will probably lead to incorrect results when extrapolated predictions have to be made, for example, on the effect of new elements added to an alloy. As pointed out in Sec. 2.3.2 this may be due to the lack of physical footing in the method.

In the following chapters we will present the results of electronic structure calculations carried out in order to cast light on various physical aspects of the stability of $4d$ and $5d$ transition metal TCP phases. In particular, we want to develop a physically sound

and simple explanation for the structural trends that have been discussed in chapter 3 by means of our two-dimensional structure map.

Chapter 5

TCP structural trends within DFT and TB model

We wish to gain a better understanding of the TCP phase structural trends that have been discussed in chapter 3, in particular the separation of A15, σ and χ from μ and Laves phases with increasing size factor difference $\overline{\Delta V/V}$ and the occasional trend from A15 $\rightarrow \sigma \rightarrow \chi$ with increasing valence electron concentration $\bar{N}$. Our approach to do this is to study the electronic structure of the TCP phases using a combination of electronic-structure methods from DFT via a TB model to analytic BOPs, where the latter is used to identify the structural origins causing the energetic differences between TCP structure-types.

Since our investigation of multi-component TCP phases showed that TCP phases, regardless of the number of components, are located within the structure map regions that are favoured by the binary TCP phases, simpler systems other than multi-component systems may be investigated in order to understand the origin of the TCP structural trends. Thus, in the first step of coarse graining the DFT electronic structure to TB, DFT calculations of elemental alloys and binary systems will be carried out and discussed in Sec. 5.1. The elemental DFT calculations allow us to study exclusively the influence of the valence electron concentration on the stability of TCP phases across the $4d$ and $5d$ transi-

tion metal series since elemental systems do not exhibit any size factor or electronegativity differences. Therefore, only the number of valence electrons will change as we move across a given series. The DFT calculations of the four binary alloys, Nb-Ru, Nb-Re, Mo-Ru and Mo-Re, for which the contributions from the size factor and electronegativity differences are expected to be small, are carried out to see whether the observed elemental DFT and experimental multi-component structural trends are reflected in the predicted heats of formation. Moreover, the heats of formation will shed light on the role of the relative volume difference on the stability of TCP phases.

In the next step, the elemental DFT results are approximated in terms of a physically and chemically intuitive description by a canonical TB d-band model. This TB model will involve simple expressions of dd bond integrals with the well-known ratio $dd\sigma : dd\pi : dd\delta = -6 : 4 : -1$ and only one adjustable parameter which determines the rate of decay of the bond integrals as a function of distance. We will show that this simple TB model reproduces the DFT structural energy difference curves provided the structural energy difference is used. This important theorem, which will be discussed in great detail in Sec. 5.2.1, will then be used to rationalize the influence of the relative size differences on the stability of individual TCP phases. These TB results will thus provide a valid basis for the application of BOP theory in the next chapter.

In the following sections the theoretical background, the relevant literature investigating TCP phase stability, and the results of our calculations will be discussed for the two electronic structure methods, DFT and TB. The interpretation of the structural trends by means of the analytic BOP theory, on the basis of the results presented in this chapter, will be discussed in the following chapter.

5.1 Density-Functional Theory

5.1.1 Methodology

DFT method

In quantum mechanics, the ground state of a many-body system like atoms, molecules and solids can be described by the time-independent non-relativistic Schrödinger equation for ions and electrons [99]

$$H|\psi\rangle = (T_e + T_i + V_{ee} + V_{eI} + V_{II})|\psi\rangle = U_{tot}|\psi\rangle. \tag{5.1}$$

The five contributions to the total energy are: the kinetic energy of ions T_i and electrons T_e and the Coulomb interactions between electrons (e) and ions (I), (V_{ee}, V_{eI} and V_{II}). The Born-Oppenheimer approximation assumes that the motion of ions can be neglected as compared to the motion of the electrons, therefore the total energy of the system is a function of the positions of the ions [100]. This enables one to consider the electron gas of the system to be in a time-independent external potential. In such a case, the many-body Hamiltonian for the electrons has three contributions: the kinetic energy, $\hat{T}_e$, the electron-electron interaction, $\hat{V}_{ee}$, and the electron-ion interaction, $\hat{V}_{eI}$, given by

$$\hat{T} = -\frac{1}{2}\sum_{i=1}^{N}\nabla_i^2, \tag{5.2}$$

$$\hat{V}_{ee} = \sum_{i=1}^{N}\sum_{I=1}^{M} V_{ion}(|\mathbf{r}_i - \mathbf{R}_I|), \tag{5.3}$$

$$\hat{V}_{eI} = \frac{1}{2}\sum_{i\neq j}^{N}\frac{1}{|\mathbf{r}_i - \mathbf{r}_j|}, \tag{5.4}$$

where $V_{ion}(r)$ is the external potential from the ions in the material (note that all equations are given in atomic units $e^2 = 1$). N and M are the numbers of electrons and ions, and $\mathbf{r}_i$ and $\mathbf{R}_I$ are their positions, respectively. Therefore, the many-body Schrödinger equation

takes the form

$$\hat{H}|\psi\rangle = (\hat{T}_e + \hat{V}_{ee} + \hat{V}_{eI})|\psi\rangle = U_{tot}|\psi\rangle, \tag{5.5}$$

where the wave function $|\psi\rangle$ depends on the co-ordinates of all N electrons. The total energy of the ground state $|\psi_0\rangle$ is obtained from the variational principle by minimizing the energy with respect to the electron wave function of the system $|\psi\rangle$

$$U^0_{tot} = \langle\psi_0|\hat{H}|\psi_0\rangle \leq \langle\psi|\hat{T} + \hat{V}_{ee} + \hat{V}_{eI}|\psi\rangle. \tag{5.6}$$

In 1964 [101], Hohenberg and Kohn proved that all properties of a many-electron system can be considered to be unique functionals, with the ground state density $\rho(\mathbf{r})$ their basic variable. Therefore, the individual terms in the expression for the total energy are written as

$$U_{tot}[\rho] = T_e[\rho] + V_{ee}[\rho] + V_{eI}[\rho], \tag{5.7}$$

where the interaction with the external potential can be written as

$$V_{eI}[\rho] = \int V_{ion}(\mathbf{r})\rho(\mathbf{r})d\mathbf{r} = \int \sum_{I=1}^{M} V_{ion}(|\mathbf{r} - \mathbf{R}_I|)d\mathbf{r}, \tag{5.8}$$

and the total energy of the ground state is given by

$$U^0_{tot} = U_{tot}[\rho_0] \leq U[\rho]. \tag{5.9}$$

Unfortunately, the kinetic energy $T[\rho]$ and the electron interaction energy $V_{ee}[\rho]$, though universal functionals of ρ, have an unknown functional form. Kohn and Sham [102] showed that the total energy functional for the interacting many-particle system can be transformed into a set of single-particle equations, called the Kohn-Sham equations

$$[-\frac{1}{2}\nabla^2 + V_{eff}(\mathbf{r})]\psi^{(n)} = E^{(n)}\psi^{(n)} \tag{5.10}$$

which have the same form as a Schrödinger equation for a set of non-interacting electrons moving in an effective potential V_{eff}. This effective one electron potential

$$V_{eff}(\mathbf{r}) = V_{ion} + V_H + V_{xc} \tag{5.11}$$

has contributions from the ion-electron interaction, while the electron-electron interaction is divided into the Hartree term, V_H, describing the electron-electron Coulomb repulsion and the exchange correlation potential, V_{xc} [103]. The latter is the functional derivative of the exchange and correlation energy U_{xc} with respect to the density,

$$V_{xc} = \frac{\partial U_{xc}[\rho]}{\partial \rho}. \tag{5.12}$$

In DFT, the Kohn-Sham equations are solved self-consistently and the ground state electron density is determined from the normalised one-electron wave functions, ψ_i, as

$$\rho(\mathbf{r}) = \sum_{n}^{N} |\psi^{(n)}|^2. \tag{5.13}$$

In DFT codes, the correct electron density which minimizes the total energy of the system is obtained in an iterative process, the so called self-consistent loop. Initially, trial wave functions are assigned which are used to calculate the electron density. New trial wave functions are then obtained by solving the Kohn-Sham equations and this procedure is repeated until convergence is achieved between input and output wave functions. The transformation of the equation describing the many-particle system into a set of one-electron Kohn-Sham equations is formally exact. However, the exchange-correlation functional is not known and therefore needs to be approximated by a closed function expression. During the first years after the initial development of density functional theory the local density approximation (LDA) was used exclusively to approximate U_{xc} [104]. In the LDA, it was assumed that the exchange-correlation energy at a given point is equivalent to the energy of a homogeneous electron gas having the same electron density,

$U_{xc}^{LDA}[\rho] = \int u_{xc}(\rho)\rho(\mathbf{r})d\mathbf{r}$. The exchange-correlation energy of the homogeneous electron gas has been calculated for different electron densities to parameterize an LDA exchange-correlation energy density as a function of the electron density. In the present day, the generalised gradient approximation (GGA), which additionally includes the charge density gradients in the expression of U_{xc} [105], is often used as an alternative to LDA.

Calculation setup

The self-consistent non-magnetic DFT calculations were carried out using the Vienna *ab initio* simulation package (VASP) [106–108]. The LDA to the exchange-correlation functional was used and p semi-core states were treated as valence states. In addition, the calculations were performed using pseudopotentials of the projector augmented wave (PAW) type. Integrations in reciprocal space used the linear tetrahedron method with Blöchl corrections [109] with a k-space density of 0.02 and the electronic wave functions were expanded in terms of plane waves up to a cutoff kinetic energy of 400 eV. In all calculations, this choice of parameters guaranteed that the convergence targets for energy differences and maximum forces of 1 meV and 1 meV/Å, respectively, were met. Structural optimizations with respect to unit cell and internal degrees of freedom were carried out. The results presented in the following subsection correspond to the structural stability at a temperature of 0 K (excluding the zero point vibrational energy).

5.1.2 Previous DFT studies on TCP phases

DFT calculations are now a common and important component of many materials research efforts [103–105]. One of the great achievements of DFT was its successful prediction of the structural stability of transition elements for unary, binary and ternary systems [110]. Moreover, DFT studies have provided important insights into TCP phase formation.

The first study on this topic by Cortella et al. [111] dealt with metastable phases of pure transition metals formed in undercooled systems. The calculated structural energy

differences between fcc, hcp, bcc and A15 structures for Hf, Ta and Re showed that the A15 phase is a possible candidate for these structures, as had been found before in strongly undercooled pure transition metal droplets like Ta [112]. In a more recent publication, Berne et al. [39] have extended the investigation to σ and χ phases, and studied the metastability for most $4d$ and $5d$ pure refractory element systems. One important result of this study is that there is strong competition between the bcc phase and TCP phases for valence electron per atom ratios ranging from 4.5 to 6.5, particularly for the A15 phase. This observation not only corresponds fairly well to the region of stable TCP binary systems observed experimentally (see the binary structure map in Sec. 3.3), but also helps to explain why metastable A15 structures have been found mainly for pure transition metals. Moreover, one particular band filling ratio, namely e/a = 6.7, has been shown to be of particular importance because at this point all competing phases show almost the same energy difference with respect to fcc. At this band filling, it is therefore assumed that, due to structural competition, TCP phases are more likely to form. Below this point, it was shown that the sequence of structures is ordered vertically with respect to their relative energies as bcc $\rightarrow$ A15 $\rightarrow \sigma \rightarrow \chi \rightarrow$ fcc $\rightarrow$ hcp, whereas the reverse ordering was observed for higher valence electron concentrations. Berne et al. argued that the change in the ordering of the energies can explain the band filling dependence of the structural trend bcc $\rightarrow$ A15 $\rightarrow \sigma \rightarrow \chi \rightarrow$ fcc/hcp as observed in various binary systems. Moreover, they related the ordering to the different percentages of icosahedral sites present (as shown in Tab. 2.2) because it was assumed that the icosahedral site is the most unimodal, with degenerate d levels as compared to the other co-ordination polyhedra whose d-level degeneracy would be partially broken. In chapter 6 we will investigate the density of states of individual co-ordination polyhedra in TCP phases with respect to the bimodality and compare the results with the values for the perfect Frank-Kasper co-ordination polyhedra to see whether this assumption is correct.

Sluiter and his collaborators also investigated the phase stability of binary systems and the composition dependence of the site occupancy in the non-magnetic σ phase systems

Fe-Cr [113], Re-W [21], Re-Ta [114], and Cr-Ru and Cr-Os [115] and in the μ phase system Ni-Nb [116]. Theoretical results were compared with results from X-ray and neutron scattering experiments indicating that the *ab initio* calculations were accurate. However, Hammerschmidt et al. [117] showed that where the heats of formation were positive, that entropic contributions must be important in the stabilization of many TCP phases.

As discussed in Sec. 2.3.2, in recent years increasing emphasis has been placed on an approach which uses a combination of *ab initio* calculations with CALPHAD. Korzhavyi et al. [118] combined these two methods to study the site occupancy and thermodynamic properties of the Fe-Cr, Co-Cr, Fe-V, and Fe-Mo binary σ-phases as a function of composition and temperature. They showed that magnetism plays an important role in the thermodynamics of σ-phases containing $3d$ transition elements like Fe and Co. Pavlù et al. [119], who carried out more accurate calculations on the formation energy and magnetism of σ phase in CrFe and CrCo systems, confirmed that the inclusion of magnetic ordering in σ phase calculations causes the decrease of the energy of formation and shifts the stability region towards the iron or cobalt sides. Hence, as pointed out in Sec. 3.3, magnetism seems indeed to be of significant importance for the stability of σ phases which are located above 7 electrons in our structure map, as is shown in Fig. 3.3. This is not surprising because, in the case of the elemental systems, Fe with N = 8 takes the bcc structure characteristic of groups V and VI and not the hcp structure of the non-magnetic isovalent group VIII elements Ru and Os [120]. More recently, Crivello et al. [121] combined DFT and CALPHAD to study the σ and χ phases in the Mo-Re and W-Re systems where the resulting binary CALPHAD-calculated phase diagrams were in good agreement with the experimental phase diagrams. Moreover, by successfully obtaining an *ab initio* ternary σ-phase diagram of the CrMoRe system, Crivello et al. [122] proved that the approach of combining *ab initio* calculations and the CALPHAD method is not limited to binary systems.

Hence, in the future, the approach of combining *ab initio* methods with the CALPHAD formalism, will become increasingly important for the design of TCP-free nickel-based

superalloys. However, for the less common TCP phases such as μ, M, P, R and δ, *ab initio* methods will need to overcome the greatest problem which is the limited system sizes which can be studied, due to the increasing computational cost. For example, Sluiter et al. [116,123] were only able to study σ and μ phases because other TCP phases such as the δ, P, or R phases have much larger unit cells and more non-equivalent sites. Hence, even for binary systems, as will be seen in the following Results section, it is computationally expensive to calculate all possible distributions of atoms for all possible stoichiometries which are needed for CALPHAD calculations.

5.1.3 Results

Elemental metals

The total energies of bcc, fcc and hcp, A15, χ, σ, μ and the Laves structures, C14, C15 and C36 were calculated for the $4d$ and $5d$ transition elements of groups III to XII, in order to study the influence of the valence electron concentration on the stability of TCP phases. These calculations were carried out by Thomas Hammerschmidt but were supplemented by calculations of R, P, M and δ by the author of this thesis. The latter calculations did not include the late transition elements of the groups XI and XII, firstly, because our structure maps in chapter 3 show that none of these structure-types are found within this valence electron range, and secondly, these calculations are computationally expensive because of the large unit cells involved.

In Tab. 5.1 we compare the DFT and experimental values of the cohesive energy and the equilibrium volume for the ground-state structures of the $4d$ and $5d$ transition metal series. The table shows that the DFT results for the cohesive energy are generally overestimated due to errors resulting from the LDA [124]. However, we are not interested in absolute values of the cohesive energies but rather in their differences, and the DFT overestimation of the cohesive energy only affects the absolute values of the normalised energy differences, not their ordering. In Figure 5.1 the relative structural energy differences,

with respect to the reference structure, fcc, and normalised by the fcc cohesive energy of the respective group VI element, are shown. It demonstrates that DFT correctly predicts the ground-state structures for both series such that the elemental structural trend from hcp $\rightarrow$ bcc $\rightarrow$ hcp $\rightarrow$ fcc across the non-magnetic $4d$ and $5d$ transition-metal series excluding La is observed in agreement with experiment as shown in Tab. 5.1. The only error in this trend is the predicted ground-state structure of La which experimentally is found to be dhcp [125] but here is predicted to be fcc instead. This is because the total energy of dhcp was simply not calculated in this work. If we had studied the last element in the lanthanide series, Lu, instead of first element, La, we would have found that DFT correctly predicts Lu to have a ground-structure of hcp [126].

	$4d$ Elements					$5d$ Elements				
		U[eV]		V[Å^3]			U[eV]		V[Å^3]	
N	Name	Exp	DFT	Exp	DFT	Name	Exp	DFT	Exp	DFT
3	Y(hcp)	4.37	5.01	33.06	29.95	La(dhcp)	4.47	-	32.41	-
4	Zr(hcp)	6.25	7.56	23.27	21.95	Hf(hcp)	6.44	7.71	22.25	20.81
5	Nb(bcc)	7.57	8.45	17.97	17.40	Ta(bcc)	8.10	9.73	17.97	17.28
6	Mo(bcc)	6.82	7.98	15.63	15.25	W(bcc)	8.90	10.04	15.78	15.53
7	Tc(hcp)	6.85	8.87	14.30	13.95	Re(hcp)	8.03	9.59	14.71	14.47
8	Ru(hcp)	6.74	8.80	13.61	13.27	Os(hcp)	8.17	10.33	14.04	13.77
9	Rh(fcc)	5.75	7.59	13.72	13.45	Ir(fcc)	6.94	9.41	14.16	13.92
10	Pd(fcc)	3.89	4.90	14.72	14.35	Pt(fcc)	5.84	7.04	15.06	14.90
11	Ag(fcc)	2.95	3.75	17.10	16.19	Au(fcc)	3.81	4.40	16.98	16.76

Table 5.1: Self-consistent ground-state properties of the $4d$ and $5d$ transition metals. V, the reference atomic volume, and U, the experimental cohesive energy, are taken from [127].

Importantly, Fig. 5.1 shows that the structural energy difference of the TCP phases are very similar for both series, in particular, it indicates that the energy difference of some TCP phases are close to the energy difference of the ground-state structures in the range between 4.5 and 7.5 electrons. In the right-hand panel of Fig. 5.1, we see for the $5d$ elements that σ and A15 are energetically the closest phases to the bcc ground states of Ta and W, respectively. These results support studies in which these structure were found

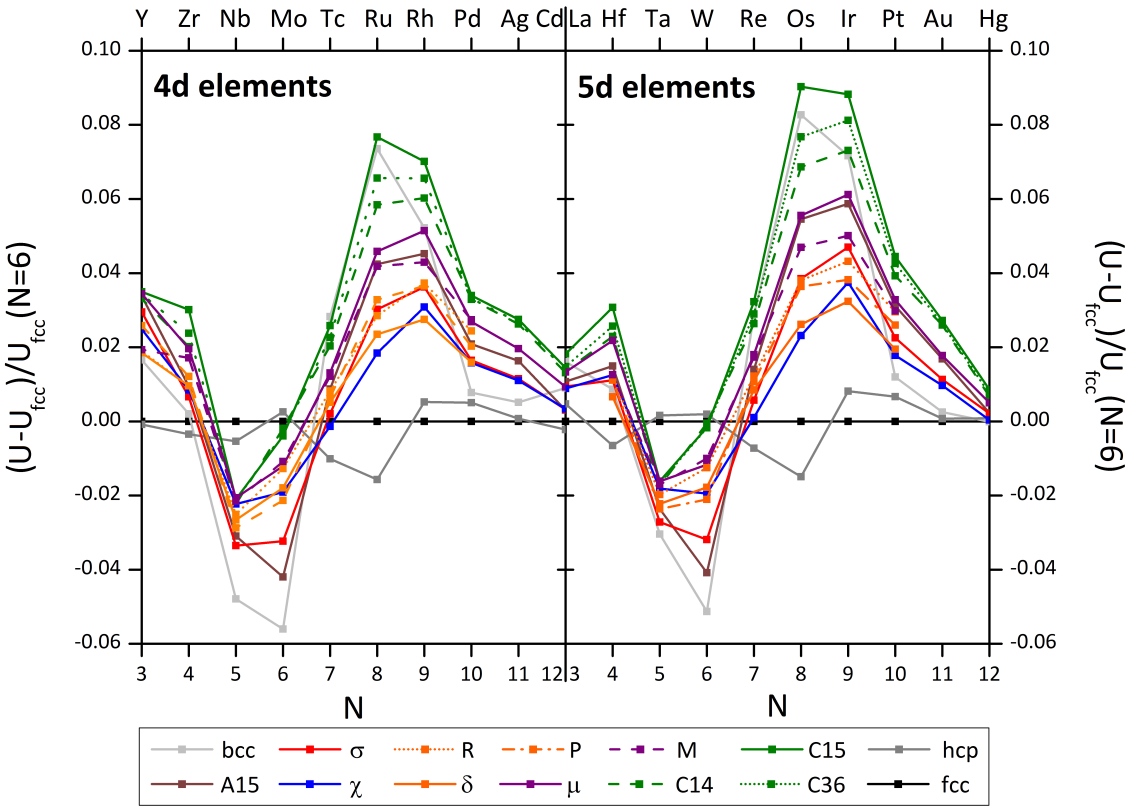

Figure 5.1: DFT structural energy differences with respect to fcc versus the number of valence *spd* electrons of 4*d* transition metals (left panel) and 5*d* transition metals (right panel).

experimentally to be the metastable phases closest in energy to the bcc ground states (see [128,129] for Ta and [130,131] for W). More crucially, we see that the lines of A15, σ and χ intersect with the lines of bcc and hcp between 6 and 7 electrons, i.e. between the stable phases bcc(Mo/W) and hcp(Tc/Re). Thus, as the electron concentration increases the following succession of phase formation is found to occur hcp $\rightarrow$ bcc $\rightarrow$ TCP(A15 $\rightarrow$ σ $\rightarrow$ χ) $\rightarrow$ hcp $\rightarrow$ fcc. However, A15, σ and χ are obviously not elemental ground-state structures because their low energies at partial valence are the result of the interpolation of the elemental structural energy differences between group VI and VII elements. Although we used a different exchangecorrelation functional and another integration method to that used by Berne et al. [39], it is clear that both studies exhibit similar results with respect to the stability of elemental 4*d* and 5*d* fcc, hcp, bcc, A15, σ and χ phases. However, our

additional calculations of the R, P, δ, μ, M and Laves phases shown in Fig. 5.1 demonstrate that the A15, σ and χ are the only 'stable' TCP phases between 6 and 7 electrons. Hence, since we study elemental systems with no differences in atomic size or in electronegativity, this means that the stabilization of the A15, σ and χ and destabilization of all other TCP phases is driven by the valence electron concentration. Moreover, in Fig. 5.1 for $N = 6.5$ we see the vertical sequence A15/σ/$\chi \rightarrow \delta$/P $\rightarrow R \rightarrow \mu$/M $\rightarrow$ Laves (C14, C15 and C36) with respect to their relative energies. Hence, the μ, M and Laves phases have the largest energy differences with respect to fcc while A15, σ and χ are the most stable TCP phases. The R, P and δ phases lie between the curves of the μ, M and Laves phases and the A15, σ and χ phases. This ranking with respect to relative energies is consistent with the location of the structural domains on the binary structure map (see Fig. 3.2). In particular, it shows that the only stable TCP phases for $\overline{\Delta V/V} < 0.1$ between 6 and 7 electrons are A15, σ and χ.

In accordance with Sec. 2.2.1, which explains the relationship between TCP phases with respect to their elementary units, the stacking sequence of their close-packed layers and their co-ordination polyhedra, we see in Fig. 5.1 that the structural energy differences of certain TCP phases are indeed very similar across the series. For example, it is not a surprise that the structural energy differences of the Laves phases are largely identical for almost the whole electron range, with larger differences being observed only between 7 to 9 electrons. Moreover, the energy difference curves of the R, P and δ phases in Fig. 5.1 track each other across the series as expected from Sec. 2.2.1. However, the δ phase between 8 and 9 electrons is significantly more stable than the R and P phases which agrees well with $\delta(Mo_{49}Ni_{51})$ being located at around 8 electrons. Furthermore, this can explain its position relative to the P phases in the nickel containing ternary systems as shown in Figs. 3.9 and 3.10. In addition, a similar trend is observed for the μ and M phases which are almost identical across the series except between 8 and 9 electrons where the M phase has lower energy differences than the μ phase. This result is in accordance with our observation in Fig. 3.11 in Sec. 3.4.1 where the M phase in Al-Nb-Ni is located

at a slightly larger valence electron concentration than the μ phase of the same system.

For the DFT total energy results discussed above, the structures were allowed to relax their unit cells and their internal degrees of freedom during the energy minimization process. As shown in Tab. 5.1, the resulting equilibrium volumes for the ground state structures are close to the experimental values. Figure 5.2 shows the differences in the DFT equilibrium volumes, with respect to the reference structure, fcc, and normalised by the fcc equilibrium volume of the respective group VI element. As with Fig. 5.1 for the energy differences, the trends for the volume differences of the $4d$ and $5d$ elements look, again, very much the same. Importantly, in the region where A15, σ and χ are stabilised and all other TCP phases are destabilised by the valence electron concentration, i.e. between 6 and 7 electrons, it can be seen that fcc, hcp, and bcc are more compact than any TCP phase. This is somehow surprising because one would assume that the equilibrium volumes of A15, σ, and χ would be at least close to the equilibrium volumes of the competing ground-state structures. However, it shows that, excluding those for La, TCP phases are in fact never found to be more compact than the ground-state structures. In particular, at around 6.5 electrons the relative equilibrium volumes follow the sequence fcc/hcp/bcc $\rightarrow$ A15/σ $\rightarrow$ χ $\rightarrow$ δ/P $\rightarrow$ R $\rightarrow$ μ/M $\rightarrow$ Laves (C14, C15 and C36) ordered from the most to the least compact structure. Figure 5.2 confirms our previous observation relating to the relative energy differences, namely that certain phases behave very similarly to each other with an increasing number of valence electrons.

In Fig. 5.3 we study how the atomic relaxation during energy minimization affect the internal co-ordinates of the structures for each element by comparing the average nearest-neighbour bond lengths of the unrelaxed and the relaxed structures. This shows that the structures with no internal degrees of freedom, namely fcc, bcc, A15 and C15, have a ratio of one, as they must. Importantly, we see in Fig. 5.3 that the other phases also exhibit relatively small changes of around $\pm 2\%$ in their average bond lengths. Hence, Fig. 5.3 demonstrates that the structures do not relax into different structure types during energy minimization.

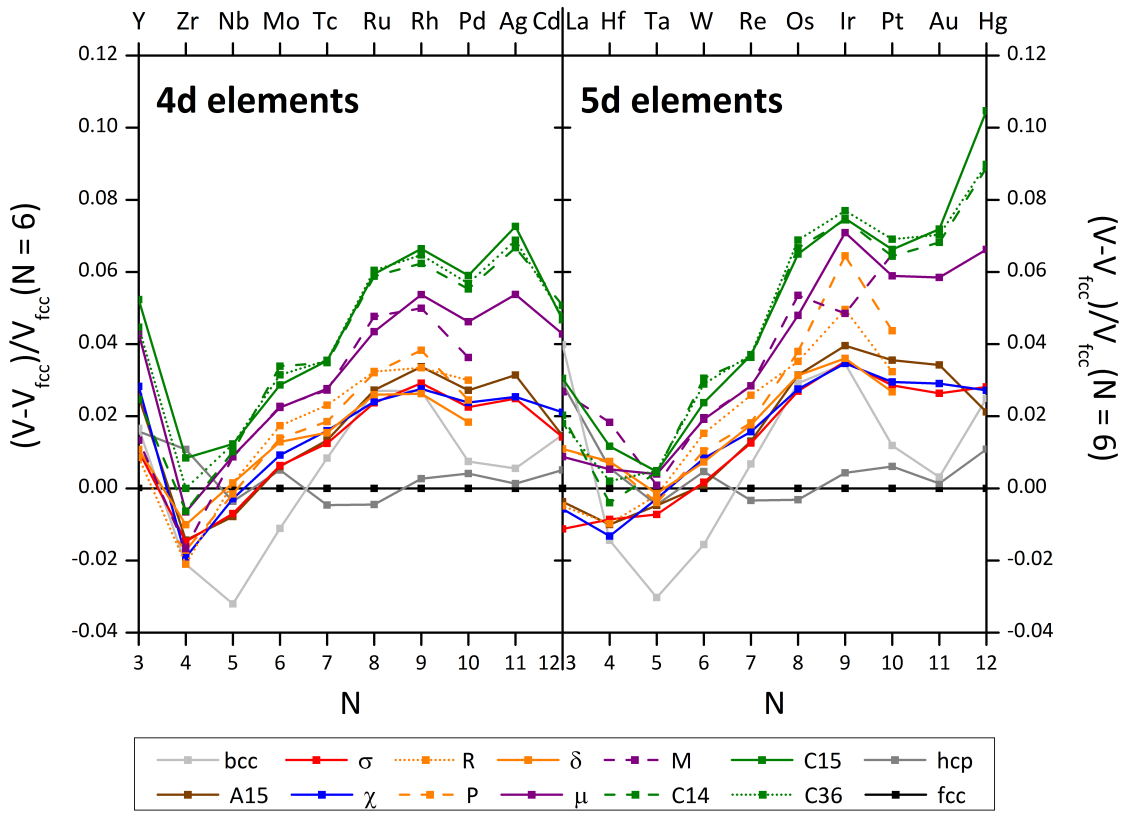

Figure 5.2: Normalised differences in the DFT equilibrium volumes with respect to fcc versus the number of valence *spd* electrons of 4*d* transition-metals (left panel) and 5*d* transition-metals (right panel).

Binary alloys

DFT calculations of elemental TCP phases have demonstrated in the previous subsection that, in the absence of size and electronegativity difference, the valence electron concentration stabilizes A15, σ and χ but destabilizes the other TCP phases such as R, P, δ, μ, M and the Laves phases. Moreover, it has been shown that DFT predicts the trend from A15 $\rightarrow$ σ $\rightarrow$ χ as the valence electron concentration increases, although A15, σ, and χ are not the most compact structures. Since these results have been obtained from linear interpolation of elemental structural energy difference, in this subsection we investigate whether this trend is also reflected by the heats of formation of binary systems with a relatively small size factor. Moreover, the study of multiple systems with different size factors will allow us to get a better understanding of how size difference, which is clearly

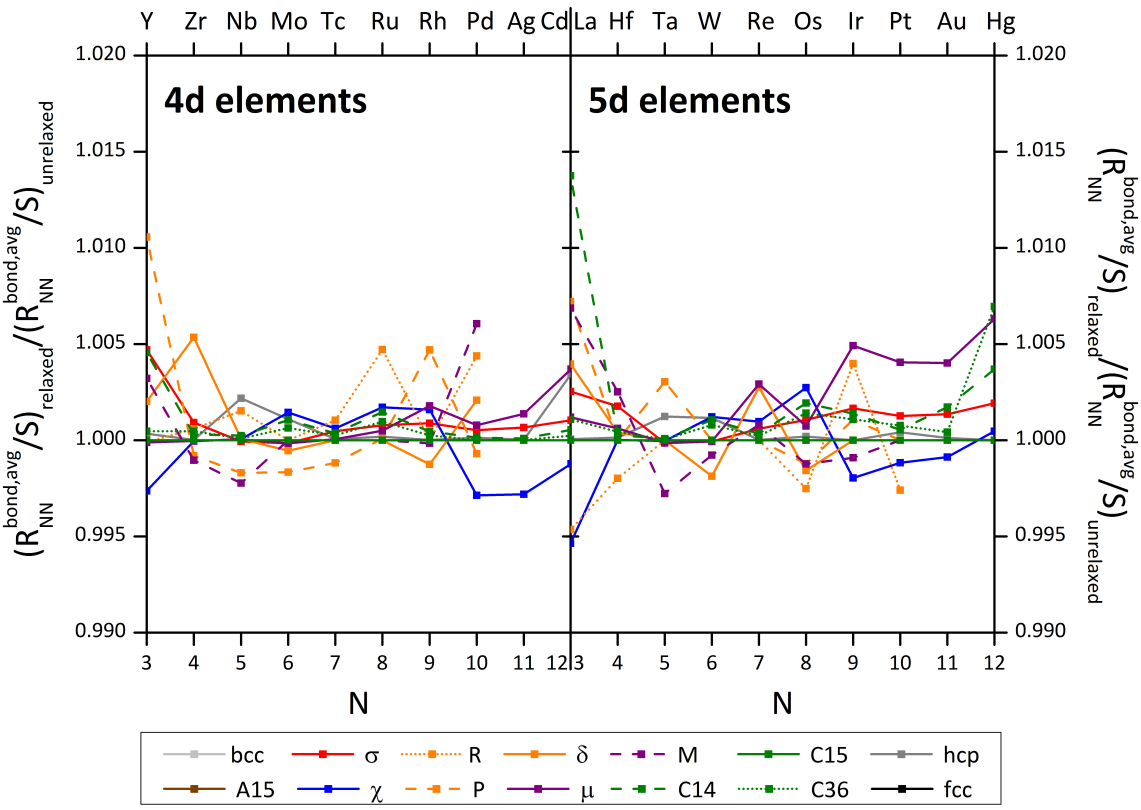

Figure 5.3: Average nearest neighbour bond lengths $(\bar{R}_{NNbond}/S)_{relaxed}$ of relaxed structure divided by $(\bar{R}_{NNbond}/S)_{unrelaxed}$ of the unrelaxed structure versus number of valence *spd* electrons of 4*d* transition-metals (left panel) and 5*d* transition-metals (right panel). S is the corresponding Wigner-Seitz radius.

important for the stability of the μ and Laves phases, affects the heats of formation and the equilibrium volumes of individual TCP phases.

As can be seen in Fig. 5.4, we investigate the heats of formation of four binary alloys which have previously been discussed with respect to the homogeneity ranges of their stable TCP phases by means of our structure map in Sec. 3.3.2. These binary alloys with the structure map co-ordinates $(\bar{N}_{x=0.5}, \overline{\Delta V/V}_{max})$ are Mo-Re (6.5, 0.03), Mo-Ru (7.0, 0.06), Nb-Re (6.0, 0.09), and Nb-Ru (6.5, 0.13). For each individual phase in each of the binary compound, a complete set of ordered configurations was obtained by distributing A or B atoms among the different sites and the total energy of each resulting configuration was calculated. For example, the σ phase possesses five non-equivalent sites which leads to $2^5 = 32$ different ordered configurations if the distribution of the

atoms is limited to its primitive unit cell. Hence, for each binary σ phase system 32 individual total energy calculations were carried out. From Tab. 2.2 we see that the P, R, δ and M phases have many non-equivalent sites (at least 10), thus, these phases are not included in this investigation as this would involve an intolerably large number of computationally expensive total energy calculations. Nevertheless, the total energies of all ordered configurations of the less complex systems A15, σ, χ, μ, and the Laves phases (C14, C15 and C36) were calculated. However, among the ordered complexes of each structure type, only the most stable ones, connected by straight line segments forming the convex hull, are shown in Fig. 5.4. All the total energy calculations of this subsection were carried out by Thomas Hammerschmidt within the EPSRC-funded 'Alloys by Design' project.

At first, we focus on the system with the smallest maximum size factor of $\overline{\Delta V/V}_{max} = 0.03$, namely Mo-Re, for which the heats of formation, together with the experimental homogeneity ranges of the stable σ and χ phases, are shown in the upper left-hand panel of Fig. 5.4. In Fig. 5.1 for the elemental case we found that the structures are ordered vertically with respect to their relative energies as bcc $\rightarrow$ A15 $\rightarrow \chi \rightarrow \mu \rightarrow$ Laves $\rightarrow$ fcc and hcp $\rightarrow$ fcc $\rightarrow \chi \rightarrow \sigma \rightarrow$ A15 $\rightarrow \mu \rightarrow$ Laves for Mo (6 electrons) and Re (7 electrons). In the binary system Mo-Re it shows that this change in the ordering of the energies with respect to the elemental A15, σ and χ phases leads to the predicted structural trend bcc $\rightarrow$ A15 $\rightarrow \sigma \rightarrow \chi \rightarrow$ hcp in terms of the minima of the convex hulls. However, none of the three TCP phases actually exhibit a configuration with a negative value of heat of formation, which would imply that the phases would be unstable at 0 K leading to decomposition into the pure elements. In this respect, our calculations do not agree with Crivello et al. [121] who found small negative heats of formation for the χ phase at around 18 at.% Mo. Nevertheless, both studies demonstrate that the location of the minima of the heats of formation of the σ and χ phases are in line with the experimental phase diagram, where σ and χ phases are observed over the ranges indicated in Fig. 5.1 at temperature intervals between 1125-2645°C and up to 2200°C, respectively [75].

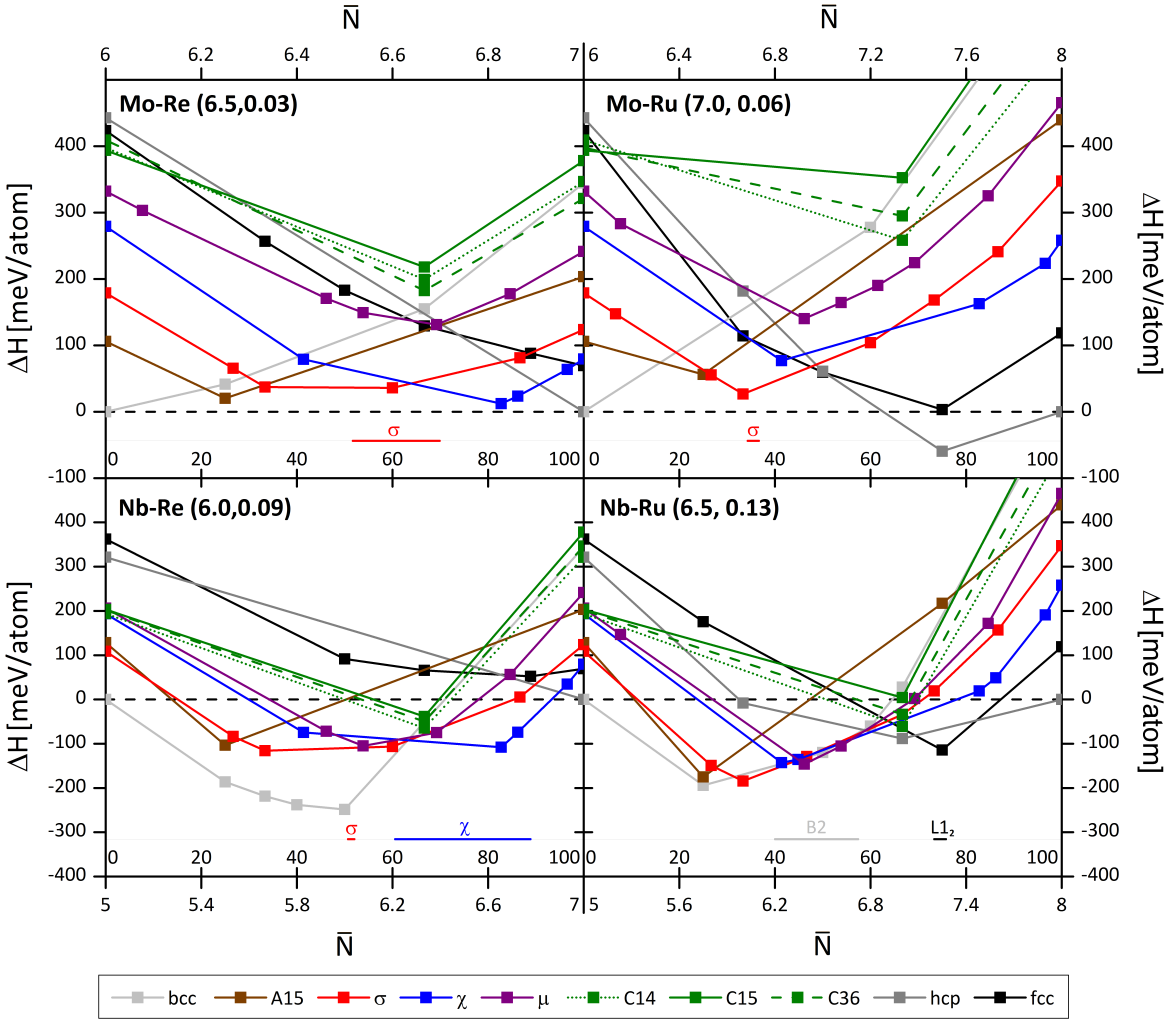

Figure 5.4: DFT heats of formation of fcc, hcp, bcc, A15, σ, χ, μ and Laves phases for Mo-Re (upper left), Mo-Ru (upper right), Nb-Re (bottom left) and Nb-Ru (bottom right). The structure map co-ordinates $(\bar{N}_{x=0.5}, \overline{\Delta V/V}_{max})$ are given in the upper left-hand corner of each alloy panel. The experimental ranges of σ, χ and $L1_2$ phases are indicated by red, blue and black bars respectively above the co-ordinate axes.

Moreover, with no stable A15 phase observed in the Mo-Re phase diagram, we assume that the entropic contributions to the free energy stabilize σ (and χ) but are apparently too small to stabilize the A15 phase. Importantly μ and the Laves phases have heats of formation that are greater than 125 meV/atom. Thus, in a binary system with a relatively small relative size difference such as Mo-Re, we observe the separation of the TCP phases into the two groups as was found by the DFT calculations on the elemental cases and by the two-dimensional structure map.

Next, we replace the 5*d* element Re (7 electrons) in Mo-Re by the larger 4*d* element Ru (8 electrons). The heats of formation of Mo-Ru with $\overline{\Delta V/V}_{max} = 0.06$ are shown in the top right-hand panel of Fig. 5.4. We see a similar trend from bcc $\rightarrow$ A15 $\rightarrow \sigma \rightarrow \chi \rightarrow$ hcp, as the valence electron concentration increases, although the TCP phases again have positive heats of formation. The only phase with negative heats of formation is the bcc phase with Ru ranging from 62 to 100 at.%. This agrees well with the experimentally observed solid solution range of bcc(Ru) at low temperatures. Moreover, the top right-hand panel of Fig. 5.4 shows that the narrow homogeneity range of $\sigma(Mo_{63}Ru_{37})$ which is stable between 1143-1915°C matches Mo_2Ru, the stoichiometry where the σ phase exhibits the lowest formation energy. As we explain in Sec.3.3.2, by replacing 4*d* Ru by 5*d* Os, which has the same number valence electrons but a smaller atomic radius, the sequence from A15 $\rightarrow \sigma$ in Mo-Os is observed in experiment.

By comparing Mo-Re with $\overline{\Delta V/V}_{max} = 0.03$ and Nb-Re with $\overline{\Delta V/V}_{max} = 0.03$, which are shown in the upper and lower left-hand panel of Fig. 5.4, respectively, it becomes evident that the heats of formation of all TCP phases are not affected equally by the change in the relative size difference. While the heats of formation of A15, σ and χ drop by around 125 meV/atom to negative values, it can be seen that the drop in the heats of formation of the μ and Laves phases are almost twice as large. Thus, the μ and Laves phases are found very close to the A15, σ and χ curves at around -100 meV/atom. Interestingly, since the A15, σ and χ phases exhibit the same drop in their heats of formation, the structural trend A15 $\rightarrow \sigma \rightarrow \chi$ is also observed in Nb-Re. Moreover, the concentration ranges of the most stable phases in Nb-Re, bcc, χ and hcp, agree with the experimental phase diagram where all phases are stable up to more than 2400°C [75]. The experimental phase diagram of Nb-Re also shows that the high temperature phase $\sigma(Nb_{45}Re_{55})$ forms over a temperature range from 2162-2565°C. Whereas the DFT predictions for the concentration range of the bcc, χ and hcp phases are in good agreement with the experimental phase diagram, we see almost identical heats of formation for σ and μ phases in the lower left-hand panel of Fig. 5.4. The entropic

contribution to the free energy of the σ phase must therefore be larger than that of the μ phase.

The last system shown in Fig. 5.4 is Nb-Ru has with $\overline{\Delta V/V}_{max} = 0.13$ the largest relative size difference of all the investigated systems. Hence, from previous findings for Nb-Re, which has a smaller size difference, it is not a surprise to see the μ and Laves phases competing with A15, σ and χ over a large concentration range. However, it is remarkable that neither of the TCP phases, not even A15, σ or χ phases, are found in the experimental Nb-Ru phase diagram. Instead the phase diagram exhibits the ordered $L1_2$ (fcc-based) alloy, $NbRu_3$, and B2 (bcc-based) alloy, NbRu. Interestingly, the experimental phase diagram of Nb-Os shows the full sequence from A15 $\rightarrow \sigma \rightarrow \chi$ [75] although Ru and Os have very similar atomic radii (see Fig. 3.1).

In Fig. 5.5 we study the relative equilibrium volumes of the 'ground state' stoichiometries for each structure type that are used for the construction of the convex hulls as shown in Fig. 5.4. The relative equilibrium volumes in Fig. 5.5 are given with respect to a concentration weighted volume of the components which is calculated according to Zen's law, i.e. $V(A_xB_{1-x}) = xV_A + (1-x)V_B$, where x is the concentration of element A and V_A and V_B are the ground state structures of the elements A and B, respectively. We see for all binary systems in Fig. 5.5 that all TCP phases have larger volumes than the competing fcc, hcp, and bcc structures, although it is shown in Fig. 5.4 that some TCP phases are the most stable phases. This result is consistent with our previous observation for the elemental case between 6 and 7 electrons, as shown in Fig. 5.2, where all TCP phases are less compact than the fcc, hcp, and bcc structures. For example, in the upper left-hand panel of Fig. 5.5 for Mo-Re with $\overline{\Delta V/V}_{max} = 0.03$ we see that the volumes of the binary phases are almost identical to the volumes of the elemental phases. Hence, the elemental trend from the most to the least compact structure fcc/hcp/bcc $\rightarrow$ A15/$\sigma \rightarrow \chi \rightarrow \delta$/P $\rightarrow R \rightarrow \mu$/M $\rightarrow$ Laves (C14, C15 and C36) is also shown by the TCP phases in Mo-Re. Although this sequence can also be found in the other binary alloys, Tab. 5.2 demonstrates that all TCP phases except the A15 are more

compact in systems with larger size differences. In particular, it shows that the effect of increasing atomic size difference is largest for Laves and μ phases but less important for the σ and χ phases.

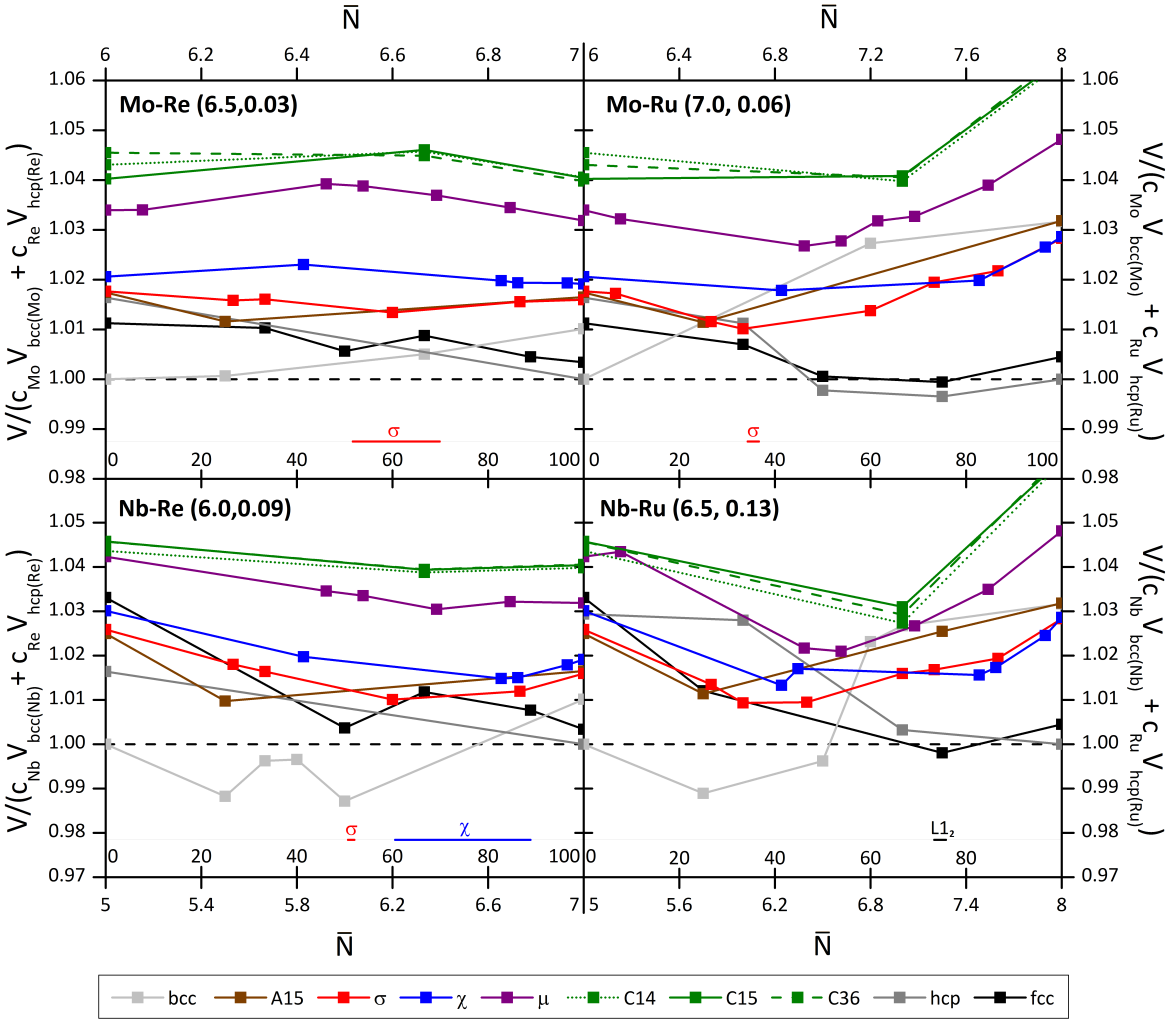

Figure 5.5: DFT minimum volumes of the convex hull of fcc, hcp, bcc, A15, σ, χ, μ and Laves phases (see Fig. 5.4) for Mo-Re (upper left), Mo-Ru (upper right), Nb-Re (bottom left) and Nb-Ru (bottom right) divided by the corresponding concentration weighted volume ($V(\mathrm{A}_x\mathrm{B}_{1-x}) = xV_\mathrm{A} + (1-x)V_\mathrm{B}$). The structure map co-ordinates ($\bar{N}_{x=0.5}, \overline{\Delta V/V}_{max}$) are given in the upper left-hand corner of each alloy panel. Experimental ranges of σ, χ and $\mathrm{L1}_2$ phases are indicated by red, blue and black bars, respectively, above the co-ordinate axes.

Alloy	Mo-Re	Nb-Re	Mo-Ru	Nb-Ru
$\overline{\Delta V/V}_{max}$	0.03	0.06	0.09	0.13
Structure	$\min(V)/V(A_xB_{1-x})$			
Laves	1.044	1.040	1.039	1.026
μ	1.037	1.027	1.033	1.021
χ	1.019	1.017	1.015	1.013
σ	1.013	1.010	1.010	1.009
A15	1.011	1.011	1.010	1.011

Table 5.2: DFT minimum volumes of A15, σ, χ, μ, and Laves phases in Mo-Re ($\overline{\Delta V/V}_{max} = 0.03$), Nb-Re ($\overline{\Delta V/V}_{max} = 0.06$), Mo-Ru ($\overline{\Delta V/V}_{max} = 0.09$) and Nb-Ru ($\overline{\Delta V/V}_{max} = 0.13$) divided by the corresponding concentration weighted volume ($V(\mathrm{A}_x\mathrm{B}_{1-x}) = xV_\mathrm{A} + (1-x)V_\mathrm{B}$).

5.1.4 Summary

In the first part of the DFT Results section, total energy DFT calculations for the elemental $4d$ and $5d$ transition metal series were reported. These results demonstrated that the valence electron concentration, in the absence of size and electronegativity difference, stabilizes the A15, σ and χ phases but destabilizes the other TCP phases between 6 and 7 electrons. Thus, we observe the separation of the TCP phases into the same two groups which were identified within the two-dimensional structure map in chapter 3. Moreover, our calculations have shown that DFT predicts the structural trend bcc $\rightarrow$ TCP(A15 $\rightarrow \sigma \rightarrow \chi$) $\rightarrow$ hcp which is experimentally found in many binary systems with small relative volume differences. However, the calculated equilibrium volumes have indicated that without any size difference neither the A15, σ, and χ phases nor any of the other TCP phases are more compact than ground-state structures. In the second part of our investigation we focused on the effect of size difference on the stability of TCP phases and have therefore studied the four binary systems Mo-Re, Mo-Ru, Nb-Re, and Nb-Ru, which differ in their relative volume differences. A comparison of the heats of formation has shown that while the μ and Laves phases are clearly less stable in binary systems with small relative volume differences than the A15, σ and χ phases, the μ and Laves phases become increasingly more stable and more compact than A15, σ and χ as

the relative size factor gets larger. Moreover, we have shown that the heats of formation of binary systems with small relative volume differences follow the commonly observed experimental TCP phase structural trend A15 $\rightarrow \sigma \rightarrow \chi$ as seen previously for the elemental transition metals. Therefore, since the structural trends of binary systems with small relative volume differences are similar to the structural trends of the elemental transition metals, we will investigate the structural trend of the elemental transition metals by coarse graining the electronic structure from DFT to the TB model in the next section. This resulting TB model will allow us to carry out a moment analysis within analytic BOP theory so that the structural origins causing the energetic differences between TCP structure-types can be identified.

5.2 Tight-binding

5.2.1 Methodology

TB model

A good starting point for a discussion is the first semi-empirical tight-binding method from Slater and Koster in 1954 [132, 133]. One of the key ideas of this approach is to write the eigenstates of the Hamiltonian in an atomic-like basis set. This idea was originally proposed by Bloch [134] who took advantage of the periodicity of solids and introduced the linear combination of atomic orbitals (LCAO) technique. This allows the Schrödinger equation to be solved in k-space rather than in real space, in order to find the electronic structure of extended systems. In addition to Bloch's LCAO method, Slater and Koster [135] replaced the exact many-body Hamiltonian operator with a parameterised matrix including bond integrals which describe the bonding between neighbouring atoms. Within the materials modelling community, over many years, TB models have been widely treated more as fitting and interpolation schemes rather than as quantitative calculation tools [136]. This was because the parameters of the bond integrals used for the fitting of

the band structures lacked physical foundations and the relationship to more fundamental theories like DFT was unclear.

As discussed by Finnis [132], deeper theoretical grounding to the TB method was provided by Sutton et al. [137] and Foulkes [136] who showed that DFT can be systematically simplified to the tight-binding bond model (TBBM). The justification of Sutton et al. for the functional form of the TB bond model is based on the approximation of Harris [138] and Foulkes [139] for the non-self-consistent approach to density functional theory. Harris and Foulkes found that the leading corrections to the total energy are of second order in the assumed charge density to the self-consistent approach. By neglecting this error and assuming that the charge density is the superposition of free-atom charge-densities, Sutton found that within well defined approximations, the Harris-Foulkes formulation of DFT can be expressed as a sum of single-electron eigenvalues (obtained by solving the Schrödinger equation in a minimal basis set with a tight-binding Hamiltonian) plus a sum of pair terms [140]. The TB binding energy per atom for an elemental non-magnetic transition metal may then be written as,

$$U = U_{rep} + U_{bond}, \tag{5.14}$$

where U_{rep} and U_{bond} are the repulsive energy and the attractive bond energy, respectively [132, 141]. For the description of the repulsive energy, U_{rep}, a simple pair potential that depends only on the distance between atoms and that implicitly includes the overlap repulsion, the electrostatic interaction between neutral atoms, an exchange-correlation contribution and any influences of the valence *sp* electrons is used [132, 137]. According to the Wolfsberg-Helmholz approximation [141] the pair potentials fall off with distance as the square of the bond integral, namely

$$U_{rep} = \frac{1}{2\mathfrak{N}} \sum_{i,j,i\neq j} \Phi(R_{ij}), \tag{5.15}$$

where

$$\Phi(R) = k[\beta(R)]^2, \tag{5.16}$$

with k a constant. The attractive bond energy U_{bond} is given by a sum of local bond contributions

$$U_{bond} = \frac{10}{\mathfrak{N}} \sum_{i}^{\mathfrak{N}} \int^{E_F} (E - E_i) n_i(E) dE, \tag{5.17}$$

where the prefactor 10 denotes the number of spin-orbitals per site (i.e. 2 for spin and 5 for the five d orbitals), $\mathfrak{N}$ denotes the number of atoms in the crystal, E_F and E_i are the Fermi energy and on-site atomic d level respectively. $n_i(E)$ is the average local density of states (LDOS) that is defined by

$$n_i(E) = \frac{1}{5} \sum_{\alpha=1}^{5} n_{i\alpha}(E). \tag{5.18}$$

For a periodic system, the energy eigenvalues, $E^{(n)}$, and eigenstates, $\psi^{(n)}$, which are needed for the computation of the LDOS can be obtained by solving the Schrödinger equation in k-space

$$\hat{H}\psi_{\mathbf{k}}^{(n)} = E^{(n)}(\mathbf{k})\psi_{\mathbf{k}}^{(n)}. \tag{5.19}$$

By using the definition of the wave function [132]

$$\psi_{\mathbf{k}}^{(n)}(\mathbf{r}) = \sum_{\mathbf{R}} \sum_{i\alpha} c^{i\alpha(n)} e^{i\mathbf{kR}} \phi_{i\alpha}(\mathbf{r} - \mathbf{R}_i - \mathbf{R}), \tag{5.20}$$

premultiplying Eq. (5.19) from the left with a direct basis vector $\phi_{j\beta}$ and integrating over the volume, the Schrödinger equation can be written as a matrix equation as follows

$$\sum_{i\alpha} H_{j\beta i\alpha}(\mathbf{k}) c^{i\alpha(n)}(\mathbf{k}) = E^{(n)}(\mathbf{k}) \sum_{i\alpha} S_{j\beta i\alpha}(\mathbf{k}) c^{i\alpha(n)}(\mathbf{k}). \tag{5.21}$$

This equation is then solved to obtain the eigenstates of the secular equation

$$\sum_{i\alpha} \left[H_{j\beta i\alpha}(\mathbf{k}) - E^{(n)}(\mathbf{k}) S_{j\beta i\alpha}(\mathbf{k}) \right] c^{i\alpha(n)}(\mathbf{k}) = 0, \tag{5.22}$$

with the hopping matrix elements taking the form

$$H_{j\beta i\alpha}(\mathbf{R}_j - \mathbf{R}_i) = \int_V \phi^*_{j\beta}(\mathbf{r} - \mathbf{R}_j) \hat{H} \phi_{i\alpha}(\mathbf{r} - \mathbf{R}_i) d\mathbf{r} \tag{5.23}$$

and the overlap matrix being given by

$$S_{j\beta i\alpha}(\mathbf{R}_j - \mathbf{R}_i) = \int_V \phi^*_{j\beta}(\mathbf{r} - \mathbf{R}_j) \phi_{i\alpha}(\mathbf{r} - \mathbf{R}_i) d\mathbf{r}. \tag{5.24}$$

In the TB approximation the real space matrix elements $S_{j\beta i\alpha}$ and $H_{j\beta i\alpha}$ are normally determined empirically by fitting experimentally observed molecular orbital energies. However, one important step towards a physically meaningful guideline for the fitting of the bond integrals was achieved through the application of scattering theory to the first principles band structure of transition metals [142–146] which is characterised by a fairly tightly bound and partially filled occupied *d*-band that overlaps and hybridizes with a broader, nearly-free-electron *sp*-band [147, 148]. It was shown that the TB *dd* bond integrals and hybridization matrix elements are determined in terms of the width and position of the *d* resonance [146]. Pettifor [149] and later Andersen [150] showed that these analytic expressions for the bond integrals can take the simple canonical form within the atomic-sphere approximation (ASA) [151], namely

$$\left.\begin{array}{l} dd\sigma \\ dd\pi \\ dd\delta \end{array}\right\} = \left.\begin{array}{r} -\ 6 \\ \ \ 4 \\ -\ 1 \end{array}\right\} \beta(R) \tag{5.25}$$

with

$$\beta(R) = C/R^n \tag{5.26}$$

and C a constant.

The original canonical theory gave $n = 5$, however, we allow the adjustment of the exponent n in order to obtain a better fit for the DFT results. Note that any choice of n with the right choice of cut-off radius leads to canonical d bands such that the shape of the density of states of a structure does not depend on the volume. Moreover, for each structure we use a global cut-off radius, r_{cut}, which sets the bond integrals to zero within the maximum gap in the distribution of ranked near-neighbour distances which defines the individual co-ordination polyhedra according to the method of Brunner and Schwarzenbach [152]. In order to achieve a physical interpretation of the origin of the DFT structural trends across the elemental transition metal series, we set all non-equivalent sites to have an identical on-site energy which is chosen as the energy reference, namely $E_i = H_{i\alpha i\alpha} = 0$ for all $i\alpha$. Furthermore, we neglect crystal field splitting effects such that $H_{i\alpha j\beta} = 0$ for $\beta \neq \alpha$. From Eq. (5.17) it follows that the bond energy is equivalent to the TB band energy for the elemental transition metal system

$$U_{bond} = \frac{10}{\mathfrak{N}} \sum_{i}^{\mathfrak{N}} \int^{E_F} E n_i(E) dE = U_{band}. \tag{5.27}$$

Additionally, all of our simulations are non-self-consistent and involve an orthogonal basis ($S_{i\alpha j\beta} = \delta_{ij}\delta_{\alpha\beta}$).

Structural energy difference theorem

To calculate the energy differences between two competing crystal structures, usually one first finds the electronic ground state for the two structures and then compares the binding energies at their equilibrium volumes. Although this way of calculating the energy difference would lead to correct results, it would not provide a simple physical explanation for the difference as the binding energy difference would need to be broken down into repulsive and bonding energy contributions at equilibrium bond lengths which already embody the delicate interplay between repulsive energy and bond energy [141]. Pettifor‘s

structural energy difference theorem [153] has proven to be a very useful tool for the comparison of crystal structures as it allows a more transparent physical interpretation of the observed structural trends. It states that if the binding energy is given as the sum of a bonding and repulsive contribution as in Eq. (5.14), then the energy difference ΔU, between two structures is given to first order by

$$\Delta U = [\Delta U_{bond}]_{\Delta U_{rep}=0} \,. \tag{5.28}$$

In practice, in order to obtain the difference in energy between two phases, we calculate the lattice constant for which the repulsive energy of the second structure is equal to the repulsive energy of the first structure, and then calculate the difference in the bond energies at the adjusted volumes. Hence, the structural energy difference theorem is a more general version of the common two-step process used for the study of ionic compounds where, in the volume preparation step, hard spheres are packed together until they touch and, in the second step, the electrostatic or Madelung energies are compared. As discussed above, we have chosen the repulsive contribution to fall off as the square of the TB hopping parameters such that the normalised second-order error is given according to [153] by $\delta^2/4$ where δ is the first order error normalised by U. Thus, the structural energy difference theorem is useful whenever the energy difference between two competing structure types is small compared to the total binding energy, as has been observed for the structural energy differences of the elemental fcc, hcp, bcc and TCP phases which have been discussed in the DFT section. In order to reproduce the DFT results we prepare the volumes of the different structures to guarantee the same repulsive energy such that differences in bond energies can be studied. Note that the differences in the bond energies had been used for many years as an expression for the binding energies [88,141,154]. However, instead of adjusting the volumes to obtain the same repulsive energies, as is done with the structural energy difference theorem, the comparisons of the bond energies were carried out at the same atomic volume. This procedure works well for the comparison

of structures with very similar atomic volumes but fails if structures with very dissimilar first nearest-neighbour bonds are studied. In the TB Results section we will demonstrate that this procedure does not therefore work for fcc, hcp and bcc and the TCP phases as they have very different equilibrium volumes for a particular element as discussed in Sec. 5.1.3. Moreover, we will show that the structural energy difference theorem will not only allow us to reproduce the elemental DFT structural energy differences within a simple TB description but can also be used to rationalize the influence of the relative size differences on the stability of individual binary TCP phases.

Calculation setup

All the necessary TB routines needed to solve the secular equation of Eq. (5.22) in k-space and for the computation of the LDOS using either the tetrahedron k-space technique with Blöchl corrections [109] or the Methfessel-Paxton method [155] were implemented into the Bond-Order Potential from Oxford (BOPfox) package. All calculations shown within the Results section were converged with respect to the k-space density.

5.2.2 Previous TB studies on TCP phases

Over the course of the last few decades, TB models have been successfully applied to metals [156, 157], semiconductors [158–160], fullerenes [161, 162] and ionic materials [163, 164]. Importantly, Pettifor [165] showed that simple d-band TB models can be used to explain the observed structural trends from hcp to bcc to hcp to fcc across the non-magnetic $4d$ and $5d$ transition metal series and demonstrated that the structural energy differences are given by the d-band energy differences only. This contradicted the Engel-Brewer hypothesis that the d-electrons play no role in the structural stability of transition metals. In 1976 Johannes et al. [88] demonstrated that a TB d-band model could also be used to predict the observed change within the Laves phases from cubic (C15) to hexagonal (C14) to cubic (C15) as the valence electron concentration increases [85]. In 1983 Turchi

et al. [166] were the first to study the electronic structure and phase stability of the A15 phase in pure transition metals and their alloys. They used a simple *d*-band model to compute the bond energy difference as a function of the valence electron concentration and they showed that there is strong competition between the bcc phase and the A15 phase for the valence electron range between 3.0 to 5.0 *d* electrons. Although this result seemed to agree with a metastable A15 β-W phase being observed within their predicted *d* electron range [131], their A15 phase was wrongly predicted to be more stable than bcc. As we will see in the Results section, this error was a consequence of comparing the bond energies at the same volume. In 1990 Ohta and Pettifor [43] studied the different roles played by size and electronic factors in stabilizing the transition metal Laves phases. They found that good qualitative agreement with the empirical AB_2 structure map [167] can be obtained provided that both size and electronic factors were included. The good agreement between TB and experiment resulted from the structural energy difference theorem which was introduced by Pettifor [167] a few years earlier. In 1991 Hoistad and Lee [168] used the structural energy difference theorem together with an *spd*-valent TB-like Hückel model to study the stability of the σ and χ phases with respect to fcc, hcp and bcc. They found that σ and χ compete with fcc, hcp and bcc in the range from 6 to 7 valence electrons which agrees with our structure map and also with our elemental DFT calculations.

5.2.3 Results

Elemental metals

In this section we discuss the parameters and approximations which were used within our simple TB model in order to reproduce the elemental structural trends predicted by DFT and shown in Fig. 5.1. In order to match the crossing between A15, σ and χ between 6 and 7 electrons, we use the fully-relaxed internal co-ordinates for the different structure-types as predicted by DFT. However, instead of changing the internal co-ordinates according

to the band filling, we use the same internal co-ordinates which were predicted for group VI W with $N = 6$ across the whole d band. Keeping the internal co-ordinates fixed is a valid approximation as Fig. 5.3 has indicated that the change in the internal co-ordinates are not very large across the elemental transition metal series. Moreover, since we use the structural energy difference theorem to calculate the energy differences it is necessary to adjust the lattice constants of the individual structures such that the structures give the same repulsive energy. Fortunately, the adjustment of the lattice constants does not involve the change in the individual cut-off radii because the structural energy difference theorem allows us to use a single cut-off radius for all structures, namely $R_{cut}/S = 1.30$ with S as the corresponding Wigner-Seitz radius, which restricts atomic interactions to the co-ordination polyhedra. The following TB structural energy difference plots will show the bond energy difference, since we will make use of the structural energy difference theorem, normalised by the cohesive energy of Mo/W as is shown for the $4d$ and $5d$ transition metal series in Fig. 5.1. As pointed out in the previous subsection, we have chosen the repulsive pair potentials to fall off with distance as the square of the bond integral as given in Eq. (5.26). It is trivial to show that, under this condition, for any choice of n the cohesive energy of a crystal structure amounts to one-half the magnitude of the bond energy at equilibrium. Therefore, the normalised TB structural energy differences are independent of the proportionality constants C of Eq. (5.26) and k of Eq. (5.16).

As pointed out in Sec. 5.2.1, for the TB dd bond integrals we use the simple canonical form which is given by Eq. (5.25) where the exponent n in Eq. (5.26) is our only free parameter. However, our goal is not to obtain a perfect fit between DFT and TB structural energy differences across the transition metal series but to achieve good qualitative agreement between the DFT elemental structural energy difference curves such that all of the important DFT trends are reproduced with our simple TB model. Hence, we study the structural energy difference curves for two values of n, namely $n = 5$, which is used in the original canonical scheme, and $n = 4$, which was found to be the volume dependence of the DFT d-band width of $V^{-4/3}$ in the middle of the $4d$ series [149]. Fig. 5.6 shows the

structural energy difference curves for $n = 5$ and $n = 4$ in the left- and right-hand panel, respectively. Importantly, it can be seen that both choices of the exponent n lead to good agreement with the curves in Fig. 5.1. However, it can also be seen that the crossing between the A15, σ and χ linearly interpolated DFT *spd* curves near the intersection between the bcc and hcp curves at around $N = 6.5$ (see Fig. 5.1) are better reproduced by the right-hand panel with $n = 4$. As compared to left-hand panel, with $n = 5$, it can be seen that the energy differences of A15, σ are slightly lower for $n = 4$ near the crossing of the bcc and hcp curves in the vicinity of $N_d = 5.0$. Hence, we have chosen $n = 4$ rather than $n = 5$ for this work.

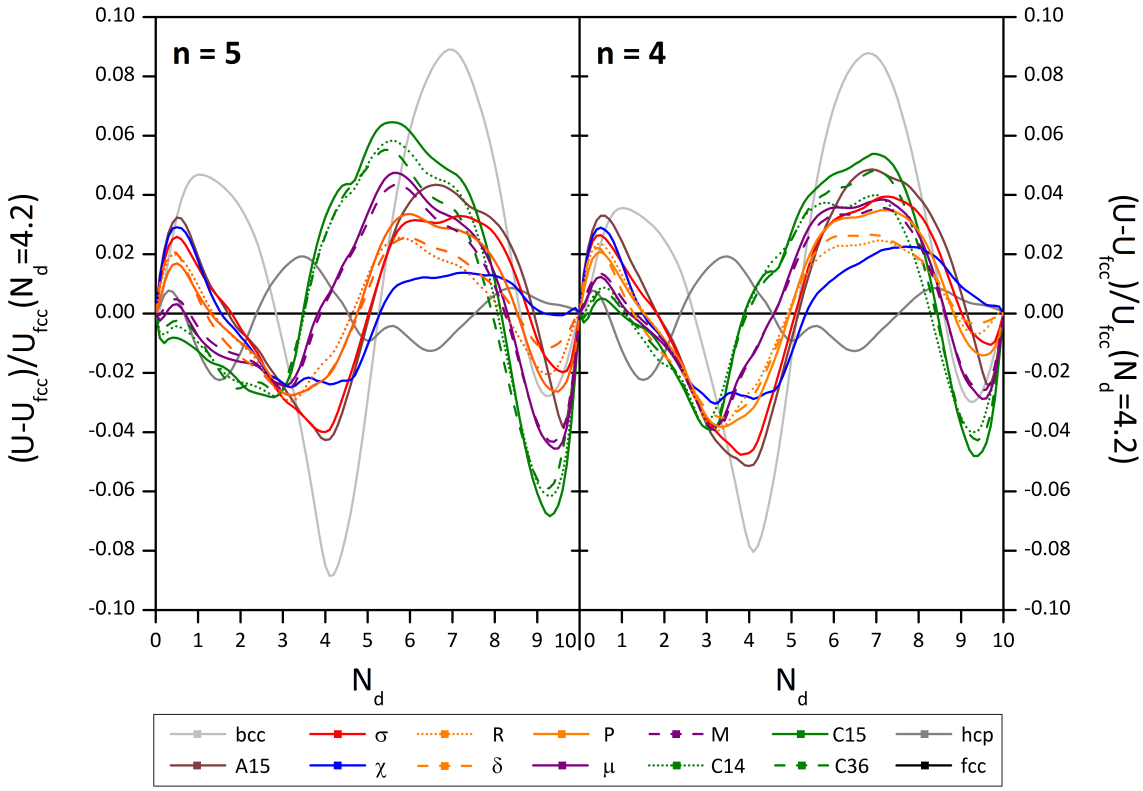

Figure 5.6: TB structural energy differences with respect to fcc versus the number of valence d electrons for bond integral exponent $n = 5$ (left panel) and $n = 4$ (right panel) using the structural energy difference theorem so that $\Delta U_{rep} = 0$.

Figure 5.7 shows a comparison of the two different approaches for calculating the structural energy differences for $n = 4$. In the left-hand panel the bond energy differences are

compared at fixed atomic volume, whereas in the right-hand panel the structural energy theorem is used to calculate the bond energy differences. Both approaches reproduce the DFT trends as in Fig. 5.1 for the fcc, bcc and hcp structures. It is not surprising that fixing the average between structure-types so that $\Delta V = 0$ leads to the right trend for fcc, bcc and hcp because it has been used successfully in the past for the comparison of the three common metallic structure-types [141,154]. Nevertheless, Fig. 5.7 demonstrates that this method fails to reproduce the structural trends for the TCP phases because of their very different nearest neighbour distances as compared to the fcc reference structure. For example, we find that the Laves structure-types are predicted to be the most stable phases everywhere for systems with small values of $\overline{\Delta V/V}$, contrary to our structure map. Moreover, in the case of $\Delta V = 0$, A15 is always more stable than bcc except near the band edges, a result which is in agreement with Turchi et al. [166] but in disagreement with the DFT results. Importantly, it can be seen that in the right-hand panel of Fig. 5.7 the structural energy difference theorem with ΔU_{rep} leads to TB curves that are in better agreement with the DFT results in Fig. 5.1 than that with $\Delta V = 0$ does.

Hence, the simple TB model with $n = 4$ together with the structural energy difference theorem gives the observed sequence hcp $\rightarrow$ bcc $\rightarrow$ TCP $\rightarrow$ hcp $\rightarrow$ fcc across the non-magnetic transition series. Unfortunately, as shown in the right-hand panel of Fig. 5.7, it fails to obtain the correct fcc crystal structure for the noble metal end of the series due to the neglect of *sp*-*d* hybridization. Furthermore, the predicted energy differences of the TCP phases between 2 to 3.5 *d* electrons are much lower than the energy difference of the competing fcc, hcp and bcc phases. This is not consistent with the DFT results and is probably due to the simplicity of the Wolfsberg-Helmholtz approximation for the repulsive contribution, which falls off as the square of the bond integrals. However, our interest lies in the region close to the crossing of the A15, σ and χ phases as our structure map demonstrates that this is a critical electron range for the occurrence of TCP phases in transition metal alloys. Hence, Fig. 5.8 shows a detailed comparison of the TB structural energy difference curves for $n = 4$ between $3 < N_d < 7$ (from the right-hand panel in

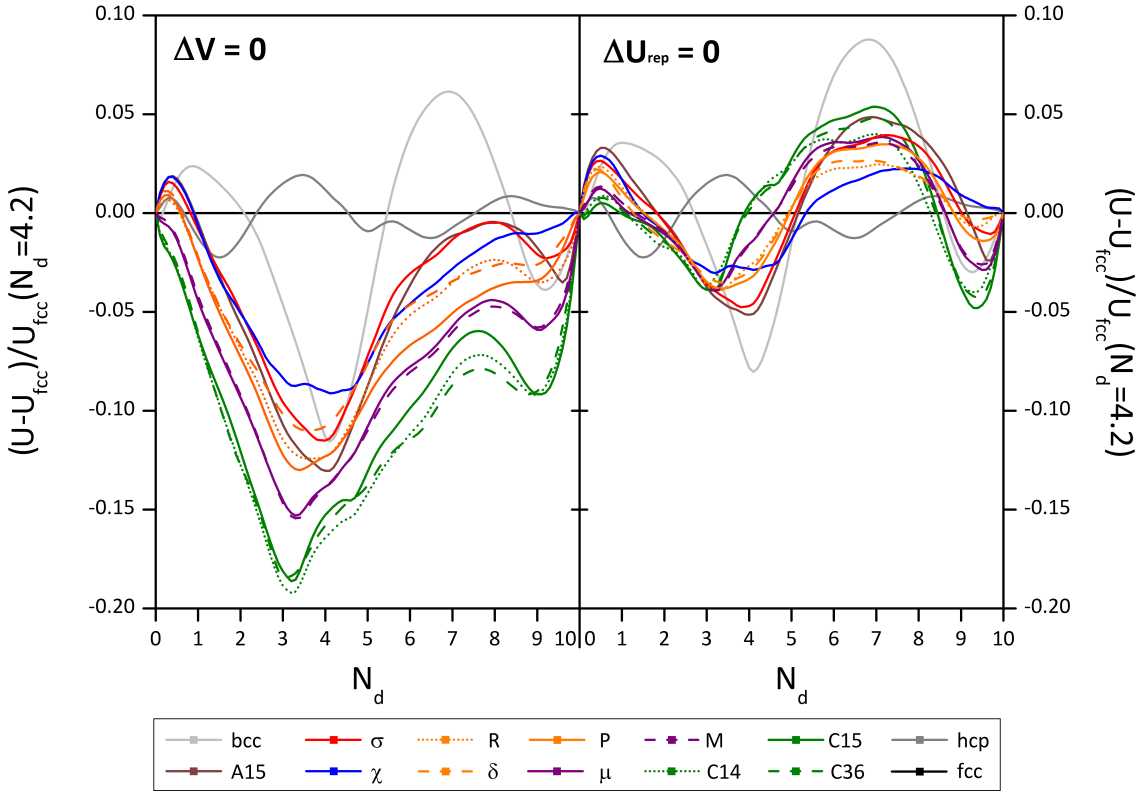

Figure 5.7: TB structural energy differences with respect to fcc for $n = 4$ versus the number of d electrons compared at the identical volumes (left panel) and the identical average repulsive energies using the structural energy difference theorem (right panel).

Fig. 5.7) and the DFT curves for the $5d$ transition metals between $4.5 < N_{spd} < 8.5$ (from the right-hand panel in Fig. 5.1). The agreement in this range is surprisingly good given the simplicity of the TB model and the small energy differences involved. In the right-hand panel of Fig. 5.8 we see that the crossing of the A15, σ and χ TCP curves with the bcc and hcp curves occurs at around $N_d = 5$ which corresponds to $N_{spd} = 6.5$ for the DFT results in the left-hand panel of Fig. 5.8. Note that W, whose cohesive energy is used for the normalization of the TB structural energy differences, lies approximately at a band filling of 4.2 d electrons as shown in the right-hand panel. This position of W has been estimated from the minimum in the energy difference between bcc and fcc and the crossing of the bcc and hcp curves.

Importantly, we see in both panels of Fig. 5.8 that the valence electron concentration

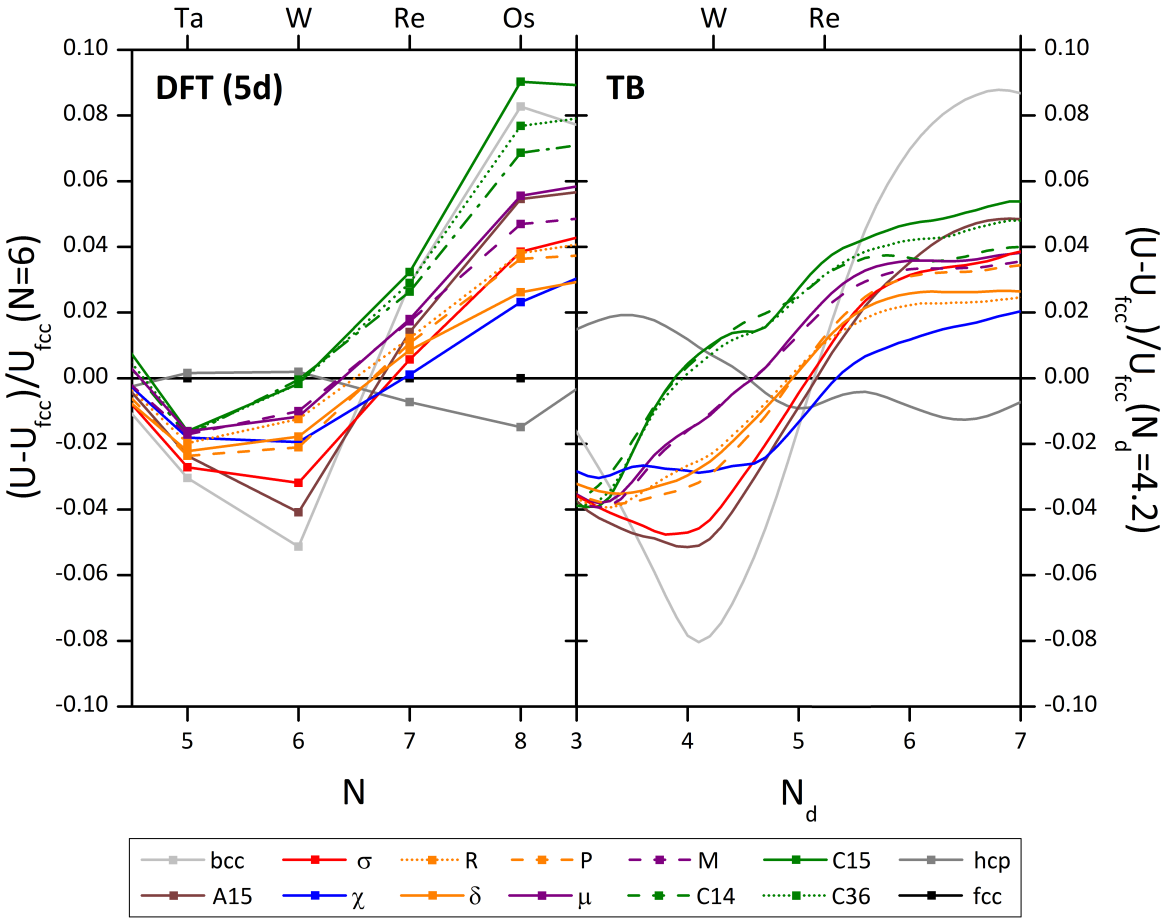

Figure 5.8: Left panel: DFT structural energy difference with respect to fcc versus the number of valence *spd* electrons N for 5*d* transition metals Ta, W, Re and Os. Right panel: TB bond energy difference with respect to fcc versus the number of valence d electrons N_d using the structural energy difference theorem. The position of N_d for W and Re on right-hand upper horizontal axis are estimated from the minimum of bcc curve and the crossing of the χ phase with fcc, namely approximately 4.2 and 5.2 respectively.

stabilizes the A15, σ and χ phases but destabilizes the other TCP phases between groups VI and VII. In particular, for 6.5 electrons or 5*d* electrons the following sequence of TCP structures is ordered vertically with respect to their relative energies: A15/σ/χ $\rightarrow$ δ/P $\rightarrow$ R $\rightarrow$ μ/M $\rightarrow$ Laves (C14, C15 and C36). As seen from our study of the DFT predicted heats of formation of binary TCP phases in Sec. 5.1.3, the difference in atomic size is crucial for the stability of the μ and Laves phases. In the following section, we will rationalize the importance of the relative size differences for these TCP phases by applying the structural energy difference theorem to binary systems.

Binary metals

In Sec. 5.1.3 the DFT predicted heats of formation of the four binary systems Mo-Re, Mo-Ru, Nb-Re and Nb-Ru, demonstrated the difference in the effect of size difference on the stability of individual TCP phases. In particular, we have seen that the change in the heats of formation as the relative size factor increases is larger for the μ and Laves phases than for the A15, σ and χ phases. Whereas the μ and Laves phases had positive heats of formation $\Delta H > 125$ meV/atom in the two Mo-containing alloys with $\overline{\Delta V/V}_{max} \leq 0.06$, we found that for the Nb-containing alloys with $\overline{\Delta V/V}_{max} \geq 0.09$ their heats of formation become negative and the phases therefore started to compete with the A15, σ and χ phases for the ground state. Moreover, Fig. 5.5 demonstrated that the μ and Laves phases become increasingly more stable but also that they become more closely packed as the size factor increases.

In order to understand the effect of size difference on the stability of individual TCP phases, we use our simple canonical TB model together with the structural energy difference theorem which allows us to estimate the volume change of A-B alloys as a function of the relative atomic size of the two constituent elements. Pettifor, together with Otha [43] and Podloucky [169], were the first to use this approach on *pd* and *dd* bonded binary systems. Following their lead, we write for bond integrals $\beta(R)$ for binary A-B alloys

$$\beta(R) \equiv \left.\begin{array}{l} \beta_{\mathrm{AA}}(R) \\ \beta_{\mathrm{BB}}(R) \\ \beta_{\mathrm{AB}}(R) \end{array}\right\} = \left.\begin{array}{l} (C_{\mathrm{A}}/R)^n \\ (C_{\mathrm{B}}/R)^n \\ (\beta_{\mathrm{AA}}(R)\beta_{\mathrm{BB}}(R))^{1/2} \end{array}\right\}, \tag{5.29}$$

where R is the internuclear separation and $\mathrm{C_A}$ and C_{B} are parameters which generally depend on the A and B constituents, respectively. The AB bond integral between the non-equivalent species A and B are given by the geometric mean of the respective integrals for each species [141]. By assuming that the repulsion falls off with distance as the square of the bond integral as in Eq. (5.16) we see from (5.15) that the repulsive energy per

atom is given by

$$U_{rep} = k\left[C_{\mathrm{A}}^{n}C_{\mathrm{B}}^{n}/\Omega^{2n/3}\right]\left[\alpha_{\mathrm{AB}} + \alpha_{\mathrm{AA}}\mathfrak{R}^{n} + \alpha_{\mathrm{BB}}\mathfrak{R}^{-n}\right], \tag{5.30}$$

where the coefficients α_{ij} are defined by

$$\alpha_{ij} = \mathfrak{N}^{-1}\sum(\Omega^{(1/3)}/R)^{2n} \tag{5.31}$$

with the sum extending over the relevant AA, BB or AB interactions on the lattice. These coefficients α_{ij} depend only on the structure and not on its volume. Ω is the unit cell volume per atom of the A-B alloy. It should not be confused with either the atomic volumes $\mathrm{V_A}$ and $\mathrm{V_B}$ of the elemental constituents, that define the relative volume difference in Eq. (3.2), or with the weighted volume of the components according to Zen's law (see Sec. 5.1.3). Thus, the repulsive energy in Eq. (5.30) is a function only of the relative size factor $\mathfrak{R}$ which is defined by

$$\mathfrak{R} = C_{\mathrm{A}}/C_{\mathrm{B}}. \tag{5.32}$$

If one assumes that the repulsive pair interaction is proportional to β^2, Eq. (5.16), Under the assumption of Eq. (5.16), it is trivial to show that if the equilibrium binding energies for the elemental systems A and B are given at internuclear distances $R_{\mathrm{AA}} = 2r_A$ and $R_{\mathrm{BB}} = 2r_{\mathrm{B}}$, respectively, then the relative size factor can be written as

$$r_{\mathrm{A}}/r_{\mathrm{B}} = C_{\mathrm{A}}/C_{\mathrm{B}} = \mathfrak{R}. \tag{5.33}$$

Hence, the relative size factor is a direct measure of the relative size of the A and B atoms, as is the relative volume difference $\overline{\Delta V/V}$ used for our structure map. With the elemental atomic volumes defined by $V_{\mathrm{A}} = (4\pi/3)r_{\mathrm{A}}^3$ and $V_{\mathrm{B}} = (4\pi/3)r_{\mathrm{B}}^3$, we see that both

size factors are related by

$$\overline{\Delta V/V} = c_{\mathrm{A}} c_{\mathrm{B}} |V_{\mathrm{A}} - V_{\mathrm{B}}|/(V_{\mathrm{A}} + V_{\mathrm{B}}) = c_{\mathrm{A}} c_{\mathrm{B}} |\mathfrak{R}^3 - 1|(\mathfrak{R}^3 + 1). \tag{5.34}$$

where c_{A} and c_{B}, the concentrations of element A and B, must not be confused with C_{A} and C_{B}, the constant prefactors in Eq. (5.29). Moreover, the relative volume difference takes a maximum value for $c_{\mathrm{A}} = c_{\mathrm{B}} = 0.5$ which is given to first order by

$$(\overline{\Delta V/V})_{max} = \frac{3}{2} |\Delta \mathfrak{R}|, \tag{5.35}$$

where $\Delta \mathfrak{R} = \mathfrak{R} - 1$. Two aspects differentiate the relative size factor $\mathfrak{R}$ from the relative volume difference $\overline{\Delta V/V}$. Firstly, the correct labeling of A and B atoms is important for the relative size factor, as this determines which atom is placed where within the TCP crystal structure, whereas the relative volume difference is independent of the labeling of the constituent elements. Secondly, $\overline{\Delta V/V}$ depends on the stoichiometry as discussed in Sec. 3, whereas $\mathfrak{R}$ is the same regardless of the composition of a phase. Hence, the composition-dependence of the repulsive energy in Eq. (5.30) is accounted for by the coefficients α_{ij}.

The heat of formation of a binary A-B compound at a specific stoichiometry can be evaluated from the binding energy of the A-B compound and the binding energies of the A and B elemental systems

$$\Delta H(c_{\mathrm{A}}, c_{\mathrm{B}}) = U_{\mathrm{AB}}(c_{\mathrm{A}}, c_{\mathrm{B}}) - (c_{\mathrm{A}} U_{\mathrm{A}} + c_{\mathrm{B}} U_{\mathrm{B}}). \tag{5.36}$$

Hence, we can calculate the differences in the heats of formation between two structures at the same stoichiometry by comparing their isostoichiometric binding energies. The structural energy difference between the two isostoichiometric structures can then be obtained from the structural energy difference theorem in two steps. First, the volumes of the two structures are prepared such that their repulsive energies are the same. In the

second step, the bond energies are compared for the prepared volumes. It follows from Eqs. (5.28) and (5.30) that the first-order change in prepared volume $\Delta\Omega$ is given by

$$\frac{\Delta\Omega}{\Omega} = \frac{3}{2n}\frac{\Delta\alpha_{\mathrm{A\ B}} + \mathfrak{R}^n\Delta\alpha_{\mathrm{A\ A}} + \mathfrak{R}^{-n}\Delta\alpha_{\mathrm{BB}}}{\alpha_{\mathrm{A\ B}} + \mathfrak{R}^n\alpha_{\mathrm{A\ A}} + \mathfrak{R}^{-n}\alpha_{\mathrm{BB}}}. \tag{5.37}$$

For $n = 5$ this agrees with Eq. (9) of Ohta and Pettifor [43] who studied the prepared volumes of the AB_2 transition metal compounds, C16 and the Laves phases, with respect to the $C11_b$ ($MoSi_2$) phase. We, on the other hand, use $n = 4$ as for the elemental metals. In the limits $r_{\mathrm{A}} \to 0$ (i.e. $\mathfrak{R} \to 0$) and $r_{\mathrm{B}} \to 0$ (i.e. $\mathfrak{R} \to \infty$) the fractional changes in prepared volume $\Delta\Omega/\Omega$ are $3\Delta\alpha_{BB}/8\alpha_{\mathrm{BB}}$ and $3\Delta\alpha_{\mathrm{AA}}/8\alpha_{\mathrm{AA}}$, respectively.

In Fig. 5.9 we see the fractional change in prepared volume difference as a function of the relative size factor $\mathfrak{R}$ for the phases that have been studied in the DFT binary section (see Sec. 5.1.3, namely, A15, σ, χ, μ and Laves structure-types). Each TCP phase is compared to an isostoichiometric bcc binary phase with the underlying lattice decorated to give the highest possible short-range order parameter. The highest short-range order is proportional to the total number of closest A-B neighbours [170]. The largest number of closest A-B interactions (i.e. the highest short range order) in bcc is achieved for a rapidly decaying repulsive potential such as $1/R^8$ when the minority atoms A in the bcc $A_xB_{(1-x)}$ alloy are separated by at least a for $1/4 \leq x \leq 1/2$ compositions and by at least $\sqrt{2}a$ for $0 < x \leq 1/4$, where a and $\sqrt{2}a$ are the second and third nearest neighbour distances in the bcc unit cell, respectively. The resulting reference bcc unit cells have 16, 24, 484, 104 and 24 atoms for A15(A_3B with A in Z14, B in Z12), σ (A_2B with A in Z14 and Z16, B in Z12), χ (A_5B_{24} with A in Z16, B in Z12 and Z13), μ (A_6B_7 with A in Z14, Z15, Z16, B in Z12) and the Laves phases (AB_2 with A in Z14 and Z16, B in Z12), respectively. The coefficients, α_{ij}, of the bcc reference structure together with the corresponding values for the TCP phases are given in Tab. 5.3. The bcc structure-type was chosen as the reference because it is the ground state structure of the group VI elements Mo and W and also the most compact structure as found from the elemental DFT calculations. Note that similar

conclusions can be drawn if hcp, the ground state structure of the group VII elements, is used as the reference structure instead of bcc.

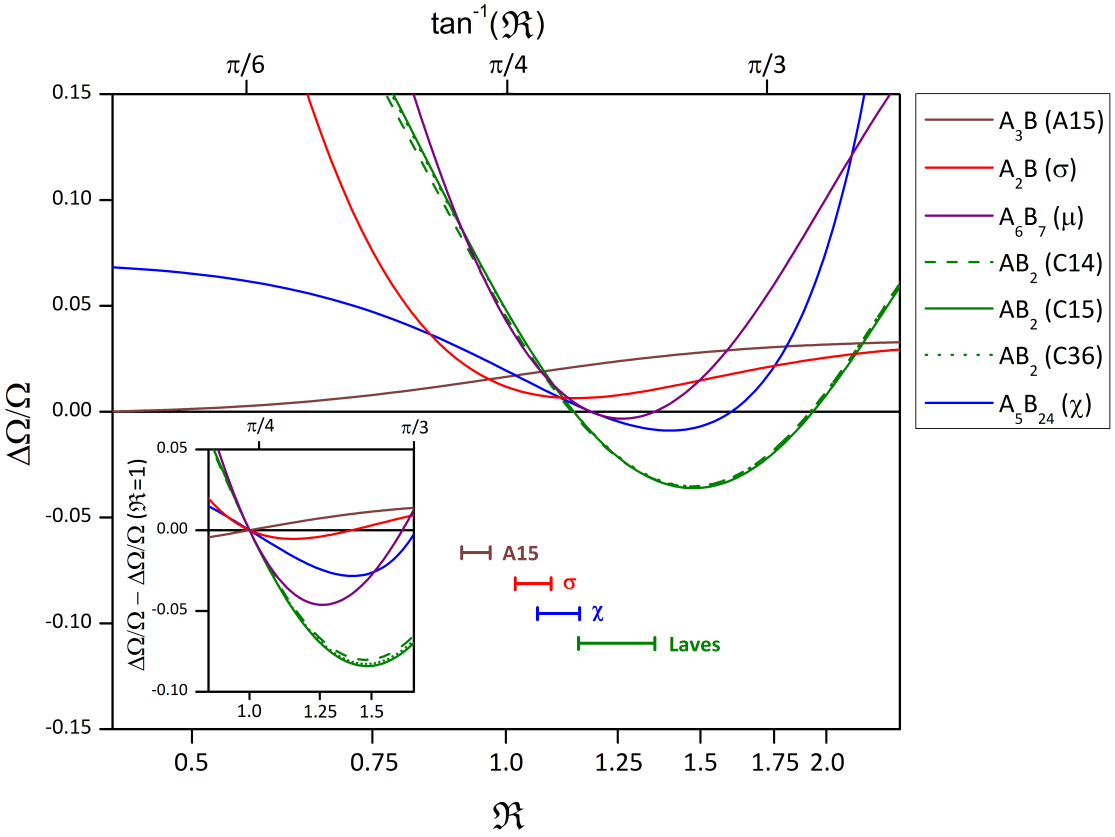

Figure 5.9: Fractional change in prepared volume $\Delta\Omega/\Omega$ with respect to the ordered isostoichiometric bcc structures versus the relative size factor $\mathfrak{R}$. Experimental binary TCP phases of $4d$ and $5d$ transition elements with $6 \leq \bar{N} \leq 7$ are observed within the ranges shown above the lower horizontal axis. In this range, binary μ phases (see Fig. 3.2) contain $3d$ transition elements.

Structure type	α_{AB}	α_{AA}	α_{BB}	Structure type	α_{AB}	α_{AA}	α_{BB}
A15(A_3B)	2.458	0.000	2.685	bcc(A_3B)	2.463	0.000	2.463
σ(A_2B)	2.574	1.959	0.549	bcc(A_2B)	2.970	1.800	0.157
μ(A_6B_7)	2.417	0.640	2.433	bcc(A_6B_7)	3.729	0.394	0.804
C14(AB_2)	1.932	0.226	3.359	bcc(AB_2)	2.970	0.157	1.800
C15(AB_2)	1.913	0.225	3.419	bcc(AB_2)	2.970	0.157	1.800
C36(AB_2)	1.922	0.226	3.403	bcc(AB_2)	2.970	0.157	1.800
χ(A_5B_{24})	1.299	0.047	3.835	bcc(A_5B_{24})	1.699	0.000	3.228

Table 5.3: The repulsive coefficients α_{ij}.

Figure 5.9 shows that the TCP structures are less compact than the corresponding

bcc structures for $r_{\mathrm{A}} \to 0$ (i.e. $\mathfrak{R} \to 0$) and $r_{\mathrm{B}} \to 0$ (i.e. $\mathfrak{R} \to \infty$). The fact that all TCP phases are less compact than bcc for $r_{\mathrm{A}} \to 0$ and $r_{\mathrm{B}} \to 0$ is due to $\Delta\alpha_{\mathrm{AA}} > 0$ and $\Delta\alpha_{\mathrm{BB}} > 0$, because they have either shorter nearest neighbour bond lengths or an increased number of like atoms within their co-ordination shells compared to that of the corresponding ordered bcc phases. In the case of the A15 phase $\Delta\Omega/\Omega$ converges to $(3/8)(\Delta\alpha_{\mathrm{AB}}/\alpha_{\mathrm{AB}})$ as $r_{\mathrm{A}} \to$ because $\alpha_{\mathrm{BB}} = 0$ for both structures at this stoichiometry as shown in Tab. 5.3. Since the nearest neighbour interactions are cut-off outside the co-ordination polyhedra at $R_{cut}/S = 1.30$, $\alpha_{\mathrm{BB}} = 0$ indicates that neither A15 nor its bcc reference structures have any short-range BB atom interactions within the first co-ordination shell for the A_3B stoichiometry. The minority B atom at the centre of icosahedral sites in A15 are completely surrounded by A atoms and the minority B atom in bcc has only neighbouring B atoms located beyond its 14-atom co-ordination polyhedron at third or higher nearest neighbours.

Importantly, it can be seen from Fig. 5.9 that for $\mathfrak{R} = 1$ all the TCP phases are less compact than their bcc reference structures which is consistent with the DFT predicted equilibrium volumes for pure Mo and W in Fig. 5.2. However, the prepared volumes of all the TCP phases except A15 decrease as $\mathfrak{R}$ increases up to around $\mathfrak{R} = 1.5$. The fact that the A15 phase becomes more compact as R decreases, unlike all of the other TCP phases, explains why most experimental binary A15 systems are found with $r_{\mathrm{A}}/r_{\mathrm{B}} < 1$ as indicated by the horizontal bar in Fig. 5.9. This shows that the general concept of the icosahedral Z12 sites being occupied by the smaller B atoms and the non-Z12 polyhedra by the larger A atoms (see Sec. 2.2.1) is not relevant for A15. This is consistent with the fact that the elemental second moment (or pairwise repulsive energy from Eq. (5.16) of the Z12 site in A15 is 6% smaller than that of the Z14 site, whereas in all of the other TCP phases the Z12 second moment is larger than that of the non-Z12 sites as, for example, in the C15 Laves phase where it is 85% larger. This anomaly is due to the value of the Z14 second moment in A15 being unexpectedly large as a result of two very close nearest neighbours that are evident in Fig. 2.5.

From the inset of Fig. 5.9 it can be seen that the change in the prepared volume, with respect to its value at $\mathfrak{R} = 1$, as $\mathfrak{R}$ increases is much larger for the Laves and μ phases as compared to the σ and χ phases. We expect from the inset of Fig. 5.9 that the larger the change in volume the more strongly the atoms will be bonded, and hence the more stabilised with respect to competing phases that they will become. This agrees well with our previous DFT study of the heats of formation of Mo-Re, Mo-Ru, Nb-Re, and Nb-Ru in Figs. 5.4 and 5.5 where μ and Laves phases were found to be more affected by the increase in the relative size difference than the A15, σ and χ phases as they exhibited larger changes in heats of formation and equilibrium volume. Thus, it shows that the structural energy difference theorem is a useful tool for rationalizing the influence of the relative size differences in binary TCP phases. In particular, it helps understand why the size factor is found to divide the TCP structure-types into two groups, namely A15, σ, and χ and μ and Laves, as shown in our two-dimensional structure map $(\bar{N}, \overline{\Delta V/V})$ in chapter 3.

5.2.4 Summary

In this section we have explained the coarse-graining from DFT to TB where the atomic-sphere approximation and simple TB bond integrals, with one adjustable parameter determining the rate of decay of the bond integrals with distance, lead to a simple canonical TB model which retains the quantum mechanical nature of bonding that is necessary to describe the structural stability of TCP phases. This simple TB model in combination with the structural energy difference theorem which states that the difference in structural energy is given to first order by the difference in the d bond energy alone if they are compared at the same average repulsive energy reproduce the observed elemental DFT structural trends. Thus, it correctly predicts the valence electron concentration to stabilize the A15, σ and χ phases in the vicinity between groups VI and VII, whereas all other TCP phases are destabilised. Importantly, our TB model displays at $N_d = 5$ the vertical

ordering amongst the TCP phases with respect to the DFT energy differences at $N = 6.5$ that agrees with the vertical ordering in the experimental structure map $(\bar{N}, \overline{\Delta V/V})$.

To understand the role of the relative volume difference on TCP phases which was highlighted in the DFT heats of formation of the binary alloys Nb-Re and Nb-Ru in chapter 5.1, we employed the structural energy difference theorem to predict the dependence of the binary alloy volume on the relative volume differences of the two elemental constituents. The relative volume difference was found to have a larger effect on the change in volume of μ and the Laves phases as compared to the other TCP phases. With increasing relative volume differences, the μ and Laves phases are expected to be increasingly stabilised with respect to other competing phases which is in line with the DFT heats of formation and the experimental structure maps.

In the following chapter we will further coarse-grain the d bond energy within the simple TB model by using analytic BOP theory to write the energy difference as a sum over moment contributions that can be linked directly to the topology of each site. Thus, with the moments retaining the important angular nature of the bonding, BOP theory will be used to unravel the link between structural stability and the local topology of the TCP phases.

Chapter 6

TCP structural trends within BOP theory

The analytic bond-order potentials for transition metals are real-space, semiempirical descriptions of the interactions between atoms, which are derived from the TB method. As an approximation to the TB method, analytic bond-order theory reduces the accuracy compared to the TB method but at the same time dramatically increases the computational efficiency making it possible to compute very large systems. In comparison to empirical potential models, BOPs have the advantage of increasing the level of accuracy in order to approximate TB results as closely as is necessary. Importantly, coarse graining from TB to BOP by expressing the TB LDOS in terms of its moments conserves the important angular nature of the bonding. Therefore, BOPs are the ideal choice for atomistic simulations in which quantum mechanical effects are significant but where the system size makes *ab initio* or tight-binding calculations impractical, for example large-scale molecular dynamic (MD) or kinetic Monte Carlo (kMC) simulations. Thus, as part of the bigger idea pursued by the 'Alloys by Design' project, that is to base the design of new nickel-based superalloys on theoretical analysis and computer models rather than empiricism and trial-and-error-based testing, BOPs will help to bridge the gap between the electronic and atomistic modelling hierarchies.

In this chapter, we will make use of the simplicity of the BOP formalism in order to provide a simple interpretation of the DFT and TB structural energy difference curves as discussed in the previous chapter. The findings of our investigation are important for two reasons. Firstly, the interpretation of the structural trends will lead to a deeper physical understanding of the differences between the individual TCP structures. Secondly, the requirements of inter-atomic potentials to correctly predict the differences between the individual TCP structures will be identified. Thus, the results are essential for the development of accurate yet still efficient analytic BOPs for possible use in future MD or kMC simulations which could address other important aspects of TCP stability such as structural transitions or TCP nucleation in nickel-based superalloys.

6.1 Methodology

6.1.1 Analytic BOP model

The analytic BOP method belongs to the family of moment methods which make use of the fact that the local density of states of an atom can be characterised by the position of its centre, its width and its shape, i.e. all properties which are related to the moments of the LDOS [171]. The mth moment of a given LDOS of atom i is defined by

$$\mu_{im} = \int E^m n_i(E) dE, \tag{6.1}$$

where $E_i = 0$ according to our non-self-consistent TB model. Therefore, the zeroth moment gives the normalization of the LDOS as $\mu_{i0} = 1$ from Eq. (5.18). The first moment μ_{i1} corresponds to the centre of gravity of the band, the second moment μ_{i2} is related to the mean square width, the third moment μ_{i3} gives a measure of how skewed the band is and the fourth moment μ_{i4} describes the unimodal versus bimodal character of the density of states. Hence, the more moments one calculates, the more information about the actual shape of the LDOS can be extracted. Moment methods such as analytic

BOPs use the moments of the LDOS in order to approximate the LDOS. However, from Eq. (6.1) we see that the LDOS would be needed first for the computation of the mth moment. Moment methods therefore make use of the powerful identity [171] that the mth moment of atom i can also be computed, without knowing the actual density of states, by summing over all self-returning hopping paths of length p that start and finish on atom i and orbital α. That is for an orthogonal basis,

$$\mu_{im} = \frac{1}{5} \sum_{\alpha} \sum_{\{j_k, \beta_k\}} H_{i\alpha, j_2\beta_2} H_{j_2\beta_2, j_3\beta_3} \ldots H_{j_m\beta_m, i\alpha}. \tag{6.2}$$

The first sum α runs over the five d orbitals on atom i. The second sum $\{j_k, \beta_k\}$ runs over all atomic sites and the five d orbitals at each site that can be reached within m self-returning hops from site i. Since the moments belong to the TB LDOS, $H_{i\alpha j\beta}$ are the same Hamiltonian matrix elements, involving the canonical hopping integrals of Eqs. (5.25) and (5.26) with $n = 4$, that are used to calculate the LDOS from the TB secular equation (see Sec. 5.2.1). The process of multiplying the pairsite Hamiltonian matrices for the calculation of the bonding path of length m can be interpreted as a process of hopping on the lattice along closed paths of length p, where $H_{i\alpha j\beta}$ describes the hop between orbital $\phi_{i\alpha}$ and orbital $\phi_{j\beta}$. In this sense, the first moment corresponds to a hop on a single site and the second moment includes the hops from site i to its nearest neighbours and, in order to close the path, the hop back to its own site. This shows that the number of moments used for the expression of the TB LDOS defines the number of shells taken into account. Therefore, the more moments calculated, the more information on the topology that is included and, consequently, the smaller the difference between the approximated TB DOS and its exact value. However, since the calculation of moments is computationally expensive, one tries to use as few moments as possible in order to make the potentials suitable for practical simulations. Once the moments of a density of states are known, there are several ways to reconstruct the LDOS and consequently calculate the bond energy [172].

The recursion method is an optimal method for building densities of states from moments by means of numerically calculating Green's functions. Haydock et al. [173] were the first to make use of the expression of the LDOS in terms of Green's function $G_{i\alpha i\alpha}$,

$$n_{i\alpha}(E) = -\frac{1}{\pi} \lim_{\epsilon \to 0^+} ImG_{i\alpha i\alpha}(E + i\epsilon) \tag{6.3}$$

with the Green's function $G_{i\alpha j\beta}(Z) = \langle i\alpha|(E - \hat{H})^{-1}|j\beta\rangle$ and $Z = E + i\epsilon$. Here, the local density of states requires only the diagonal element corresponding to the orbital of interest. Haydock [174] showed that the Green's function can be written explicitly by basis transformation and by incorporating the original tight-binding Hamiltonian into a new Hamiltonian for a one-dimensional semi-infinite chain. With the resulting tridiagonal Hamiltonian and by means of the Lanczos algorithm [175] for solving tridiagonal matrices, the Green's function of Eq. (6.3) is given by a continued fraction expansion,

$$G_{i\alpha i\alpha} = \cfrac{1}{E - a_0 - \cfrac{b_1^2}{E - a_1 - \cfrac{b_2^2}{E - a_2 - \cfrac{b_3^2}{\ddots}}}}. \tag{6.4}$$

Using the semi-infinite chain, it is straightforward to express the moments as a function of the recursion coefficients a_n and b_n^2. For the first four moments of the LDOS of atom i this reads:

$$\mu_{i1} = a_{i0} \tag{6.5}$$

$$\mu_{i2} = a_{i0}^2 + b_{i1}^2 \tag{6.6}$$

$$\mu_{i3} = a_{i0}^3 + a_{i0}b_{i1}^2 + a_{i1}b_{i1}^2 \tag{6.7}$$

$$\mu_{i4} = a_{i0}^4 + 2a_{i0}a_{i1}b_{i1}^2 + a_{i0}^2b_{i1}^2 + b_{i1}^2b_{i2}^2 + b_{i1}^4. \tag{6.8}$$

It follows from Eqs. (6.3) and (6.4) that for $b_{i2}^2 = 0$ the LDOS is totally bimodal. In general the bimodality of a LDOS is discussed by means of the dimensional shape parameter, s, which is defined as

$$s_i = (b_{i2}/b_{i1})^2 = (\mu_{i4}/\mu_{i2}^2) - (\mu_{i3}^2/\mu_{i2}^3) - 1. \tag{6.9}$$

The LDOS shows bimodal behaviour for $s < 1$ but unimodal behaviour for $s > 1$. We will see later that the shape factor will help us to understand the differences between A15, σ, χ and μ and the Laves phases. However, we will also point out that higher moments are also crucial for understanding the stability of TCP phases. For a finite number of calculated moments, it is only possible to calculate exact recursion coefficients up to $a_{(m_{max}+1)/2}$ and $b^2_{(m_{max}+1)/2}$ with m_{max} being the number of calculated moments. In order to take into account the remaining coefficients, it is common to truncate the continued fraction expansion by taking $a_m = a_\infty$ and $b_m = b_\infty$ for $n > (m_{max} + 1)/2$. a_∞ and b_∞ are the asymptotic values of a_m and b_m as $n \to \infty$ along the chain. a_∞ is defined by the centre of the band, $(E_{top} + E_{bottom})/2$, and $4b_\infty$ is given by its width, $(E_{top} - E_{bottom})$. Note that for an asymmetric DOS the centre of the band is not the same as the centre of gravity μ_{i1} since from Eq. (6.2) $\mu_{i1} = H_{i\alpha,i\alpha} = E_i = 0$ for all i. The use of a_∞ and b_∞ for higher terms leads to an analytic expression in the form of a square root of the eigenvalue dependence for the terminator [176]. The assumption that the continued fraction can be so simply truncated is only applicable for connected bands (ones without any band gaps) where the exact continued fraction coefficients converge towards asymptotic limits a_∞, b_∞ [177]. A detailed study of the convergence of the recursion coefficients for a DOS with band gaps carried out by Turchi et al. [178] led to improved terminators. Unfortunately, analytic expressions for the terminator of the continued fraction do not help with the problem that the poles of the resultant continued fraction cannot be obtained analytically. This has proved to be the computational bottleneck for force calculations where the density

matrix element, $\rho_{i\alpha j\beta}$, can also be written in terms of the Green's function element:

$$G_{i\alpha j\beta} = \frac{1}{2}(G_{++} - G_{--}). \tag{6.10}$$

In the recursion method, bonding and anti-bonding Green's function elements, ($G_{\pm\pm}$), of bonding (+) and anti-bonding states (−), $|\pm\rangle = (|i\alpha\rangle \pm |j\beta\rangle)/\sqrt{2}$ are used to find $G_{i\alpha j\beta}$. This approach, which is known as the inter-site method, has proved to converge very poorly for the intersite calculation of the bond energy [179].

In the late 1980s, pioneering work to improve the convergence of the inter-site method was undertaken by Pettifor [180] who introduced BOP theory. Together with his co-workers Aoki and Horsfield, they derived atom-based exact many-atom expansions for the bond order Θ [89, 181, 182] which allowed the decomposition of the bond energy of atom i into terms of individual bond energies associated with neighbouring atoms j, namely $\Theta_{ij}H_{ji}$. This powerful $\mathcal{O}(N)$ method was used successfully by Vitek and his collaborators to model the influence of the dislocation cores on the mechanical response of certain bcc, fcc and hcp transition-metals and their alloys [183]. Unfortunately, the calculation of the bond order still involved numerical integration of response functions [172] (hence the name numerical bond-order potentials) which made them less applicable for very demanding molecular dynamics.

More recently, Drautz and Pettifor [172] developed new BOPs for transition metals with analytic expressions for the response functions, bond energy and forces, hence, the name analytic bond-order potentials. The starting point of this approach is the semi-elliptic LDOS as this is not a bad first approximation for a transition metal d band [154, 172, 180, 184, 185]. Within the Green's function method the semi-infinite chain has only constant values $a_m = a_\infty = a_0$, $b_m = b_\infty = b_1$ for $m \geq 0$ which leads to $n_0(E) = n_0(\epsilon)/(2b_\infty)$ with the normalised LDOS taking the semi-elliptic form

$$n_0(\epsilon) = \frac{2}{\pi}\sqrt{1-\epsilon^2}, \tag{6.11}$$

where ϵ is a normalised energy given by $\epsilon = (E - a_\infty)/(2b_\infty)$. We see that this represents a band of states between $\epsilon = \pm 1$ or $E = a_\infty \pm 2b_\infty$. Drautz and Pettifor suggested the addition of a correction term, $\delta n(\epsilon)$, to the semi-elliptic DOS in order to obtain the actual density of states $n_i(\epsilon)$ of atom i such that

$$n_i(\epsilon) = n_0(\epsilon) + \delta n_i(\epsilon), \tag{6.12}$$

where $n_0(\epsilon)$ is in theory site independent since for a continuous band of states all sites are characterised by the same band edges. Then, the modification $\delta n(\epsilon)$ can be expanded in terms of Chebyshev polynomials of the second kind $P_m(\epsilon)$ [186]. By means of the orthogonality relation with respect to the weight function $2/\pi\sqrt{1-\epsilon^2}$,

$$\frac{2}{\pi}\int_{-1}^{1}\sqrt{1-\epsilon^2}P_l(\epsilon)P_m(\epsilon)d\epsilon = \delta_{lm}, \tag{6.13}$$

the density of states may be written as

$$n_i(\epsilon) = \frac{2}{\pi}\sqrt{1-\epsilon^2}\sum_{m=0}\sigma_{im}P_m(\epsilon). \tag{6.14}$$

The expansion coefficients σ_{im} with $m > 0$ are given by

$$\sigma_{im} = \sum_{l=0}^{m} p_{ml}\hat{\mu}_{il} \tag{6.15}$$

with the normalised moments

$$\hat{\mu}_{im} = \frac{1}{(2b_\infty)^m}\sum_{l=0}^{m}\binom{m}{l}(-1)^l a_\infty^l \mu_{i(m-l)} \tag{6.16}$$

and p_{mn} is the coefficient of $P_m(\epsilon)$ [172]. Since σ_{im} is a function of both the moments and the asymptotic recursion coefficients, a_∞ and b_∞, the expansion coefficient can also be

expressed in terms of the Lanczos recursion coefficients as described above. For example,

$$\sigma_{i1} = \gamma_{i0}, \tag{6.17}$$

$$\sigma_{i2} = \delta_{i1} + \gamma_{i0}^2, \tag{6.18}$$

$$\sigma_{i3} = \gamma_{i1} + \delta_{i1}(\gamma_{i1} + 2\gamma_{i0}) + \gamma_{i0}^3, \tag{6.19}$$

$$\text{and} \quad \sigma_{i4} = \left\{ \begin{array}{l} \delta_{i2} + [\delta_{i1}(\delta_{i1} + \delta_{i2}) + \gamma_{i1}(2\gamma_{i0} + \gamma_{i1})] + \\ \delta_{i1}(3\gamma_{i0}^2 + \gamma_{i1}^2) + \gamma_{i0}(\gamma_{i0}^3 + 2\gamma_{i1}\delta_{i1}^2) \end{array} \right\}, \tag{6.20}$$

with γ_{im} and δ_{im} defined by

$$\gamma_{im} = (a_{im} - a_\infty)/b_\infty, \tag{6.21}$$

$$\text{and} \quad \delta_{im} = (b_{im}^2 - b_\infty^2)/b_\infty^2. \tag{6.22}$$

As expected, we see for $a_{im} = a_\infty$ and $b_{i(m+1)} = a_\infty$ that all expansion coefficients with $m \geq 0$ are zero such that only the semi-elliptic DOS from Eq. (6.14) remains. The average DOS of a crystal structure can be obtained from the individual LDOS given by Eq. (6.14) by summing over the unit cell, namely

$$n(\epsilon) = \frac{2}{\pi}\sqrt{1-\epsilon^2}\sum_{m=0}\sigma_m P_m(\epsilon), \tag{6.23}$$

where the average expansion coefficient is given by

$$\sigma_m = \sum_\nu w_\nu \sigma_{\nu m}, \tag{6.24}$$

where ν labels the different non-equivalent sites in the unit cell and w_ν gives their weight or fraction. For example, the σ phase has the five non-equivalent sites A, B, C, D, E in the 30 atom unit cell with $w_{\rm A} = 2/30$ for the 2 atoms in the Z12 A sites, $w_{\rm B} = 4/30$ for the 4 atoms in the Z15 B sites, $w_{\rm C} = 8/30$ for the 8 atoms in the Z12 C sites, $w_{\rm D} = 8/30$ for the 8 atoms in the Z12 D sites and $w_{\rm E} = 8/30$ for the 8 atoms in the Z14 E sites.

By integrating Eq. (5.17) after substituting the derived expression of $n_i(\epsilon)$, the analytic form of the bond energy becomes

$$U_{bond}^{max}[\phi_F(N_d)] = 10b_\infty \sum_{m=0}^{m_{max}} \hat{\hat{\chi}}_m(\phi_F, \gamma_0)\sigma_m, \tag{6.25}$$

where m_{max} is the maximum number of calculated moments used for the series expansion. Hence, the mth moment contribution, where m represents the index of summation, consists of a product of the expansion coefficient σ_m and the response function $\hat{\hat{\chi}}_m$. As described above, the expansion coefficients are related to the topology of the crystal structure, whereas, the response function is effectively structure-independent and gives rise to the valence-dependent behaviour across the transition metal series of the individual moment contributions. The mth response function $\hat{\hat{\chi}}_m$ in Eq. (6.25) is given by

$$\hat{\hat{\chi}}_m(\phi_F, \gamma_0) = \hat{\chi}_m(\phi_F) - \gamma_0\hat{\chi}_{m+1}(\phi_F) + \hat{\chi}_{m+2}(\phi_F), \tag{6.26}$$

where $\hat{\chi}_0(\phi_F) = 0$ and

$$\hat{\chi}_1(\phi_F) = 1 - \phi_F/\pi + [\sin(2\phi_F)]/2\pi. \tag{6.27}$$

$\hat{\chi}_m$ are the normalised response functions from the original BOP paper by Pettifor [180] which take, for $m \geq 2$, the simple analytic form

$$\hat{\chi}_m(\phi_F) = \frac{1}{\pi}\left\{\frac{\sin[(m+1)\phi_F]}{(m+1)} - \frac{\sin[(m-1)\phi_F]}{(m-1)}\right\}, \tag{6.28}$$

where the Fermi phase, ϕ_F, of a structure with the Fermi level, E_F, corresponding to the band filling, N_d, is given by

$$\phi_F = \cos^{-1}\epsilon_F = \cos^{-1}[(E_F - a_\infty)/(2b_\infty)]. \tag{6.29}$$

The Fermi level and hence the Fermi phase are found iteratively by solving

$$N_d(\phi_F) = 10 \sum_{m=0}^{m_{max}} \sigma_m \hat{\chi}_{m+1}(\phi_F), \tag{6.30}$$

for a given band filling, N_d.

6.1.2 Structural energy differences

In the TB section we have shown that the structural energy difference theorem in Eq. (5.28) allows us to obtain the energy differences $\Delta U = (U^{II} - U^{I})$ between two different structure-types I and II by calculating the difference in their bond energy $(U^{II}_{bond} - U^{I}_{bond})$ after preparing their volumes such that their repulsive energies are the same. It follows from Eq. (6.25) that within analytic BOP theory this difference in bond energy is given by

$$U^{II}_{bond}[\phi^{II}_F(N_d)] - U^{I}_{bond}[\phi^{I}_F(N_d)] = 10 b_\infty \sum_{m=0}^{m_{max}} \{\hat{\hat{\chi}}_m[\phi^{II}_F, \gamma_0]\sigma^{II}_m - \hat{\hat{\chi}}_m[\phi^{I}_F, \gamma_0]\sigma^{I}_m\}. \tag{6.31}$$

We see that the individual bond energies are dependent on γ_0 and ϕ_F which will, in general, not be identical for the two different structure-types. Hence, the two structure-types have different response functions such that the difference in the mth moment contribution between the two structure-types does result solely from the difference in σ_m i.e. the difference in the topology. This makes it difficult to develop simple insights into the origin of the structural trends that are predicted by DFT and TB in the previous sections. To overcome this problem we apply the following approximations.

Firstly, we assume that the different structure-types, I and II, have the same asymptotic recursion coefficients, $(a^{II}_\infty, b^{II}_\infty) = (a^{I}_\infty, b^{I}_\infty) = (a^{TCP}_\infty, b^{TCP}_\infty)$, where $(a^{TCP}_\infty, b^{TCP}_\infty)$ are fitted to the upper and lower bounds, respectively, of the band edges of all the structures investigated in the TB calculations of Sec. 5.2.3 (see Tab. 6.1). It follows from Eq. (6.21) that $\gamma_0 = -(a^{TCP}_\infty / b^{TCP}_\infty)$ as $a_0 = 0$. We will see in Fig. 6.5 in this Results section that

this is an excellent assumption for the individual TCP phase densities of states.

Structure	$E_{bottom}/(W^{fcc}/2)$	$E_{top}/(W^{fcc}/2)$	$a_\infty/(W^{fcc}/2)$	$b_\infty/(W^{fcc}/2)$
fcc	-1.180	0.820	-0.180	0.500
hcp	-1.161	0.789	-0.186	0.488
C14	-1.221	0.960	-0.131	0.545
C15	-1.324	0.947	-0.188	0.567
C36	-1.267	0.957	-0.155	0.556
M	-1.152	0.918	-0.117	0.517
μ	-1.214	0.977	-0.118	0.548
R	-0.983	0.761	-0.111	0.436
δ	-0.969	0.762	-0.103	0.433
P	-1.119	0.922	-0.099	0.510
χ	-0.959	0.747	-0.106	0.426
σ	-1.067	0.887	-0.090	0.489
A15	-0.974	0.912	-0.031	0.472
bcc	-1.275	0.852	-0.211	0.532
TCP	-1.324	0.960	-0.182	0.571

Table 6.1: The upper and lower bounds of the band edges of the TB density of states of all investigated structures. E_{bottom}^{TCP} and E_{top}^{TCP} in the last row are determined by the minimum of the lower (E_{bottom}^{C14}) and the maximum of the upper (E_{top}^{C15}) bounds, respectively, of the band edges. The centre of the band, $(E_{top}+E_{bottom})/2$, is given by a_∞ and the width of the band, $(E_{top}-E_{bottom})$, by $4b_\infty$. All values are normalised by $W^{fcc}/2$.

Secondly, we solve the problem of a possible difference in the Fermi phase by using the first-order expression [187] for the difference in the energy of two bands with identical band filling N_d that is exact to first order in $\Delta E_F = E_F^{II} - E_F^I$. It is given by

$$\left\{U_{band}^{II}[\phi_F^{II}(N_d)] - U_{band}^{I}[\phi_F^{I}(N_d)]\right\}^{(1)} = \int^{E_F^I} (E - E_F^I)\Delta n(E) dE, \tag{6.32}$$

where $\Delta n(E) = n^{II}(E) - n^I(E)$. It follows from Eq. (5.27) that the band energy is equivalent to the bond energy for our non-self-consistent elemental TB calculations in Sec. 5.2. Hence, the left-hand side and right-hand side of Eq. (6.32) can be written as

$$\left\{U_{bond}^{II}[\phi_F^{II}(N_d)] - U_{bond}^{I}[\phi_F^{I}(N_d)]\right\}^{(1)} = \left\{U_{bond}^{II}[\phi_F^{I}(N_d)] - U_{bond}^{I}[\phi_F^{I}(N_d)]\right\} - E_F^I \Delta N_d(E_F^I). \tag{6.33}$$

Substituting in Eqs. (6.25) and (6.30) we have

$$\{U_{bond}^{II}[\phi_F^{II}(N_d)] - U_{bond}^{I}[\phi_F^{I}(N_d)]\}^{(1)} = 10b_\infty \sum_{m=2}^{m_{max}} \hat{\hat{\chi}}_m^{(1)}[\phi_F^{I}(N_d)]\Delta\sigma_m, \tag{6.34}$$

where $\Delta\sigma_m = \sigma_m^{II} - \sigma_m^{I}$. Hence the first two terms in the summation vanish since both $\Delta\sigma_0$ and $\Delta\sigma_1$ are zero. The first-order response function for $m \geq 2$ is given by

$$\hat{\hat{\chi}}_m^{(1)}(\phi_F) = \hat{\chi}_m(\phi_F) - 2\cos\phi_F\hat{\chi}_{m+1}(\phi_F) + \hat{\chi}_{m+2}(\phi_F). \tag{6.35}$$

Comparing Eq. (6.35) to Eq. (6.26) it can be seen that the first-order response function $\hat{\hat{\chi}}_m^{(1)}$ corresponds to the specific case of the response function $\hat{\hat{\chi}}_m(\phi_F, \gamma_0 = 2\cos\phi_F)$ where $2\cos\phi_F = (E_F - a_\infty)/b_\infty$. Substituting in Eq. (6.28) $\hat{\hat{\chi}}_m^{(1)}$ can be written as

$$\hat{\hat{\chi}}_m^{(1)}(\phi_F) = \frac{1}{\pi}\left\{\frac{2\sin[(m+1)\phi_F]}{m(m+2)} - \frac{\sin[(m+3)\phi_F]}{(m+2)(m+3)} - \frac{\sin[(m-1)\phi_F]}{m(m-1)}\right\}. \tag{6.36}$$

This first-order response function was first derived by Turchi and Ducastelle [154]. In Fig. 6.1 we see the first-order response functions $\hat{\hat{\chi}}_m^{(1)}$ of Eq. (6.36) with $2 \leq m \leq 6$ and the normalised response functions $\hat{\chi}_m$ the of Eq. (6.28) also with $2 \leq m \leq 6$ in the right-hand and left-hand panels, respectively. Figure 6.1 demonstrates the crucial oscillatory behaviour of the response functions across the transition metal series. In particular, it can be seen that the response functions of higher moments oscillate more rapidly than the response functions of lower moments. It can also be seen that the mth response functions, $\hat{\chi}_m$ and $\hat{\hat{\chi}}_m$ have m nodes (if the end points are included). However, Fig. 6.1 demonstrates that the absolute values of the global maxima of both sets of response functions become smaller as m increases. It follows from Eq. (6.28) that the absolute values of the normalised response functions show a $1/m$ dependence as shown in the left-hand panel, whereas, the first-order response functions shown in the right-hand panel decay much quicker, namely with $1/m^2$ which follows from Eq. (6.36). Thus, the difference in the lower moments between two structure-types contribute more, in general,

to the total energy difference than the more rapidly oscillating higher moments. Hence, in order to understand the band filling dependence of structural energy differences, it can be sufficient to understand the origin in the differences of lower moments.

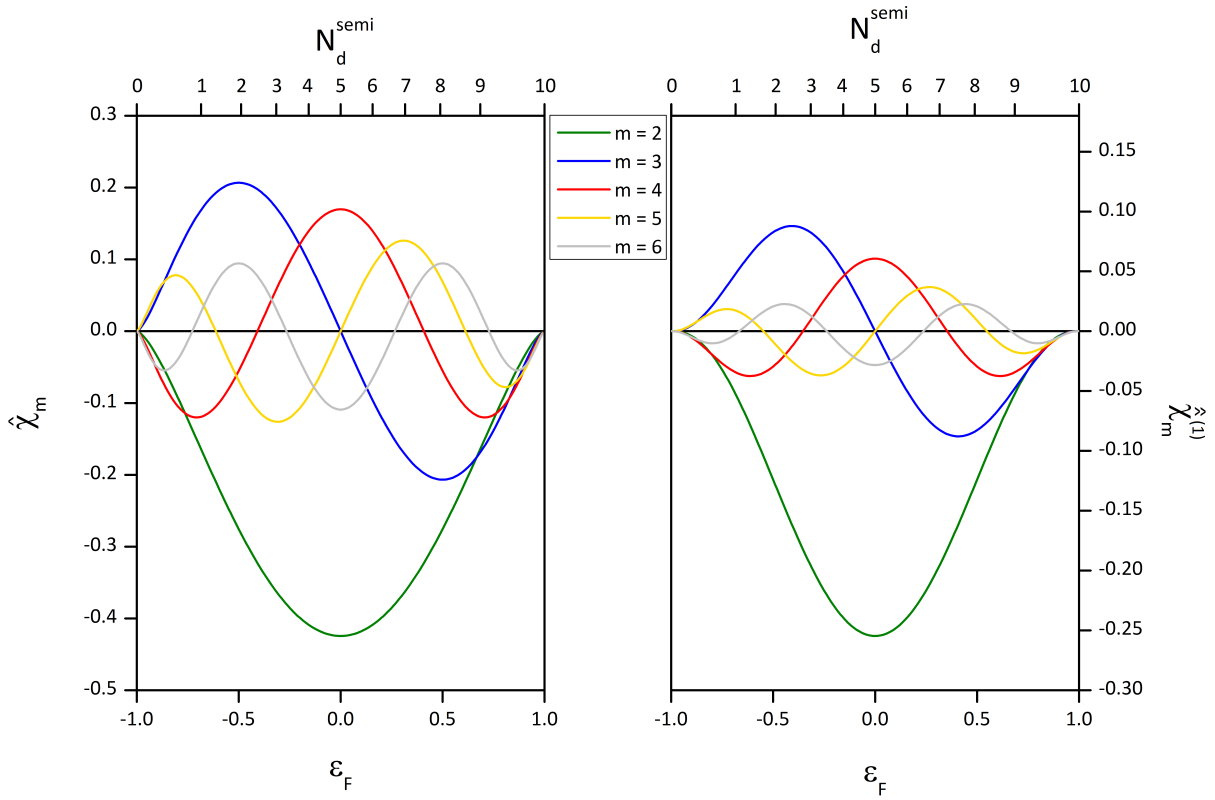

Figure 6.1: Reduced response functions $\hat{\chi}_m$ (left panel) and first-order response functions $\hat{\chi}_m^{(1)}$ (right panel) as a function of the normalised Fermi energy ϵ_F as defined by Eq. (6.29). The upper horizontal axis in both panels shows the band filling of the semi-elliptic density of states N_d^{semi} as a function of ϵ_F.

Finally, we can further simplify the bond energy difference in Eq. (6.34) if we let the repulsive potential within our TB model fall off with distance as the square of the bond integrals, $\Phi(R) = k[\beta(R)]^2$, as in Eq. (5.16). Hence, the requirement of the structural energy difference theorem of having the same repulsive energy such that $\Delta U_{rep} = 0$ is achieved by adjusting the volumes such that $\Delta\mu_2 = 0$. For the choice of a common $(a_\infty^{TCP}, b_\infty^{TCP})$ for all the different structure-types as described above, we therefore see from Eq. (6.18) that $\Delta\sigma_2 = 0$. Hence, the second-moment contribution in Eq. (6.34), with the dominant $\hat{\chi}_2$ response function which gives rise to the parabolic behaviour of

the experimental cohesive energy across the $4d$ and $5d$ transition metal series [141], is not included within the sum. Thus, given that the third-moment contribution is the first-moment contribution which may differ between two stucture-types, the first-order structural difference can be written as

$$\{U^{II}_{bond}[\phi^{II}_F(N_d)] - U^{I}_{bond}[\phi^{I}_F(N_d)]\}^{(1)} = 10 b_\infty \sum_{m=3}^{m_{max}} \hat{\chi}^{(1)}_m[\phi^{I}_F(N_d)]\Delta\sigma_m. \tag{6.37}$$

The simplification of $\Delta\mu_2 = 0$ together with the first-order approximation to the energy difference allow a direct physical interpretation of the structural trends between the TCP and other close-packed phases as was found earlier by DFT and TB. This will be discussed further in the Result section.

6.2 Previous moment method studies on TCP phases

In 1971, Ducastelle and Cyrot-Lackmann [188] were the first to investigate the phase stability of fcc, bcc and hcp structures as a function of the d-band filling with moment methods in order to understand the origin of their structural trends across the transition-metal series. Due to difficulties with the bcc phase, they focused mainly on the relative stability of fcc and hcp and found that the difference in the cohesive energy arises from the difference in the fourth moment of fcc and hcp. Additionally, Masuda and coworkers [189,190] showed that a fourth-moment model is sufficient to predict the fcc-bcc structural energy difference, but higher moments are needed to obtain the correct hcp-fcc energy difference. In 1985, Turchi and Ducastelle [154] derived the linearised Green's function method (LGM) to study the origin of the structural trends of fcc, hcp, bcc, A15 and Laves phases. The LGM is based on the first-order Dyson equation for the on-site Green's function where the mth expansion coefficient σ_m depends only linearly on γ_{im} and δ_{im} provided common asymptotic values are assumed (see Eqs (6.17) - (6.20)). However, the linear contributions only lead to good results for the calculation of the energy difference

between structure-types which have a similar DOS. Hence, Turchi and Ducastelle used a numerical reference DOS constructed from the average Lanczos recursion coefficients of the investigated structure-types instead of the analytic semi-elliptic DOS which was used for the first-order response functions. Their study showed that all close-packed structures differ from their fifth moment μ_5 onwards, and not, as previously shown for fcc and bcc, from their fourth moment μ_4. However, the discrepancy between Turchi and Ducastelle's results and previous studies regarding the difference between fcc and bcc may have resulted from the choice of bond integrals and the fact that the structure-types were examined at constant volume (see [191]). In 1988, Moriarty [192] derived an analytical expression for the fourth-moment contribution of a planar ring as a function of the bond angle which is plotted in Fig. 6.2 (right). Moriarty showed that the difference in bond angles for the four-membered ring contribution gives rise to the difference between the bcc and fcc structures. As shown in Fig. 6.2 (left), the bcc and fcc planar rings have bond angles of 70.5° (109.5°) and 90°, respectively. As a consequence, the contribution to the fourth moment is negative for bcc and positive for fcc which finally results in $\mu_4^{bcc} < \mu_4^{fcc}$. Hence, the bimodal shape parameter, s, in Eq. (6.9) of bcc is smaller than that of fcc which means that the density of states of bcc is more bimodal than fcc making fcc less stable than bcc for half-full d-bands, as is observed experimentally. Philips and Carlsson [193] also showed that the dominant interaction favouring the formation of TCP phases with respect to fcc for approximately half-full d-bands - they investigated the structural stability of bcc, A15, σ, χ and Laves phases - is the same four-body angular interaction that favours bcc at this band filling. Unfortunately, the study did not include higher moment contributions because it was aimed at finding the lowest-order interaction that stabilizes the TCP phases as a class. Therefore, no information was given about the interactions that differentiate TCP phases among each other. Moreover, Legrand [156, 157], in 1985, showed that six moments are sufficiently accurate to obtain convergence of the stacking-fault energy in hcp. Later Aoki and Pettifor [182, 194] demonstrated that the competition between the fcc and hcp close-packed lattices is determined by the sixth-moment contribution. However, unlike the

four-membered ring term describing the difference between fcc and bcc, no single hopping path could be identified that is solely responsible for the difference between fcc and hcp.

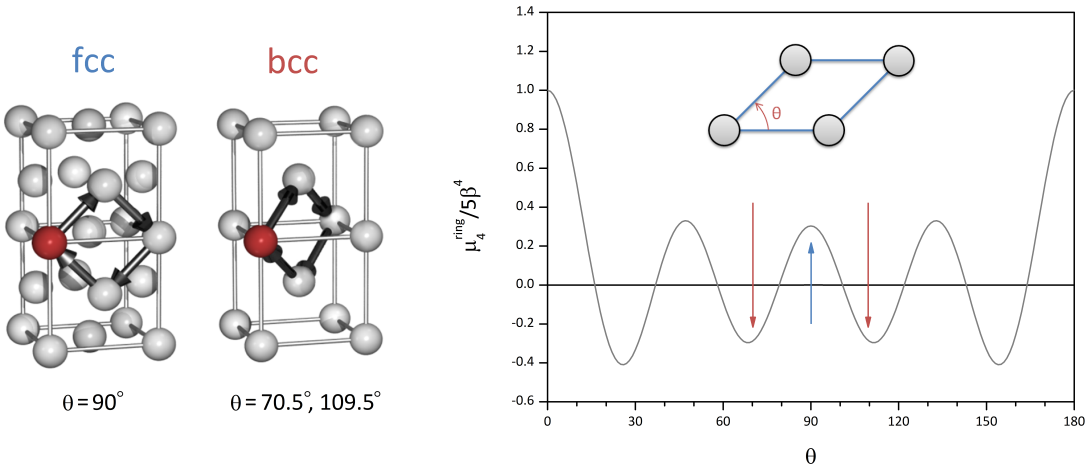

Figure 6.2: The four-membered ring contribution in the fcc and bcc lattices respectively (left) and its contribution to the fourth moment of a d-band as a function of the bond angle Θ (right). The arrows indicate the negative contribution (red) and the positive contribution (green) of bcc and fcc, respectively [141].

6.3 Results

6.3.1 Structural energy differences

In Fig. 6.3 we investigate the convergence of the 'exact' BOP and the first-order BOP energy difference expansion with respect to the upper bounds, m_{max}, of their summations in Eqs. (6.31) and (6.37), respectively. We see that the 'exact' BOP energy difference curves in the left-hand panel converge gradually with increasing number of moments to the 'exact' TB energy difference curves which is shown in the bottom right-hand panel. Moreover, the right-hand panels of Fig. 6.3 demonstrate an equally good convergence with respect to m_{max} for the first-order BOP energy difference curves. The good agreement between both BOP curves for $m_{max} = 10$ and their corresponding TB curves indicate how well the analytic BOP method reproduces the TB results even though we use the

common asymptotic values $(a_\infty^{\mathrm{TCP}}, b_\infty^{\mathrm{TCP}})$ for all the given structure-types instead of their unique values $(a_\infty^{\mathrm{TB}}, b_\infty^{\mathrm{TB}})$ which are given in the two right-hand columns of Tab. 6.1. However, the use of the common asymptotic values $(a_\infty^{\mathrm{TCP}}, b_\infty^{\mathrm{TCP}})$ can lead to problems with the convergence of both BOP expansions if m_{max} becomes large. This is because the expansion coefficients σ_m only vanish if the correct asymptotic values $(a_\infty^{\mathrm{TB}}, b_\infty^{\mathrm{TB}})$ are used. For example, by using $a_\infty = a_0$ and $b_\infty = b_1$ which produced excellent results for the study of the energy difference between fcc, bcc and hcp for $m_{max} \leq 8$ [172], the σ_m values of all structure-types would not converge to zero but instead would oscillate between $\pm\infty$ as m_{max} tends to infinity. Fortunately, we have chosen $(a_\infty^{\mathrm{TCP}}, b_\infty^{\mathrm{TCP}})$ to be close to the TB values $(a_\infty^{\mathrm{TB}}, b_\infty^{\mathrm{TB}})$ and we have seen already that the maxima of the response functions decrease rapidly with increasing m such that we can expect the convergence error to be small even for large m_{max}. Hence, in this section we do not need to be concerned about the convergence of the BOP energy difference curves for large values of m_{max} because our interest lies in the origin of the structural trends that are driven by the small values of m_{max} in Fig. 6.3.

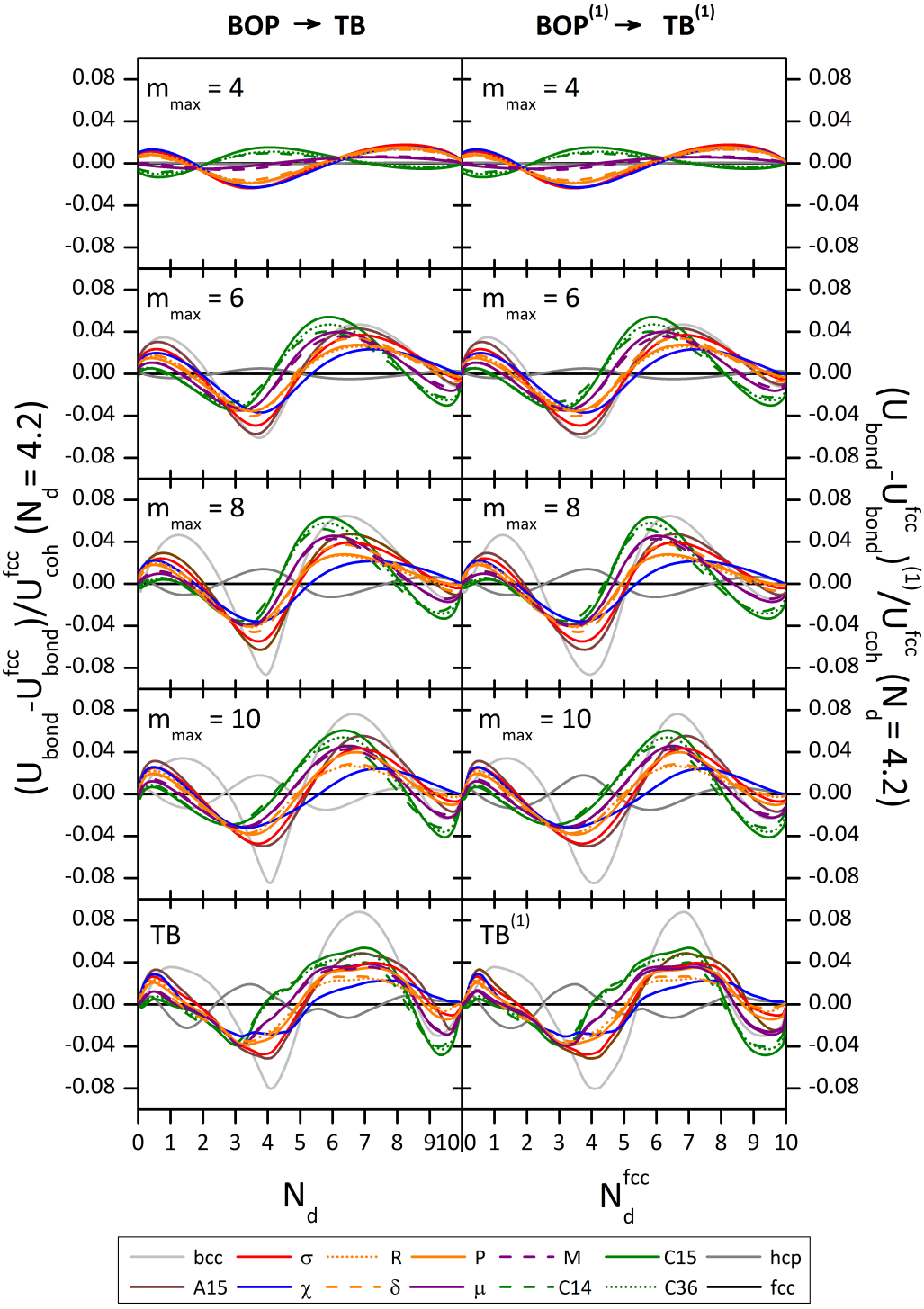

Figure 6.3: Left panel: The convergence of the structural energy differences for the exact BOP expansion with respect to the maximum number of moments m_{max}. The bottom panel gives TB reference structural energy differences as shown in right panel of Fig. 5.7. All energy differences are given with respect to fcc and are plotted against the number of d electrons. Right panel: The convergence of the structural energy differences for the first-order BOP expansion with respect to the maximum number of moments m_{max}. The bottom panel gives first-order TB reference structural energy differences. All energy differences are given with respect to fcc and are plotted against number of d electrons in fcc.

Figure 6.4 explicitly shows the convergence of the difference between the BOP and the TB normalised structural energy difference curves with an increase in the number of moments. This figure confirms that the errors that remain for $m_{max} = 10$ are indeed very small as it shows a maximum error of 1.8 % for (C15-fcc) energy difference curves at around 4 electrons in the two bottom panels. We also see that the remaining errors are not constant across the d band but rapidly oscillate around zero. The oscillation of the error for $m_{max} = 10$ can be understood from the corresponding density of states as shown in Fig. 6.5. Importantly, this figure demonstrates that away from the band edges the common asymptotic values $(a_\infty^{\mathrm{TCP}}, b_\infty^{\mathrm{TCP}})$ are indeed an excellent assumption for the individual TCP phase densities of states because it appears that there is almost no difference between the individual DOS whether the common values, $(a_\infty^{\mathrm{TCP}}, b_\infty^{\mathrm{TCP}})$, or the unique values, $(a_\infty^{\mathrm{TB}}, b_\infty^{\mathrm{TB}})$, are used. Although, the BOP does an excellent job of reproducing the TB DOS for either set of asymptotic values, Fig. 6.5 shows that BOP with $m_{max} = 10$ is not able to reproduce the fine structure of some TB DOS, such as the Laves phase DOS, which results in the small errors seen in Fig. 6.4.

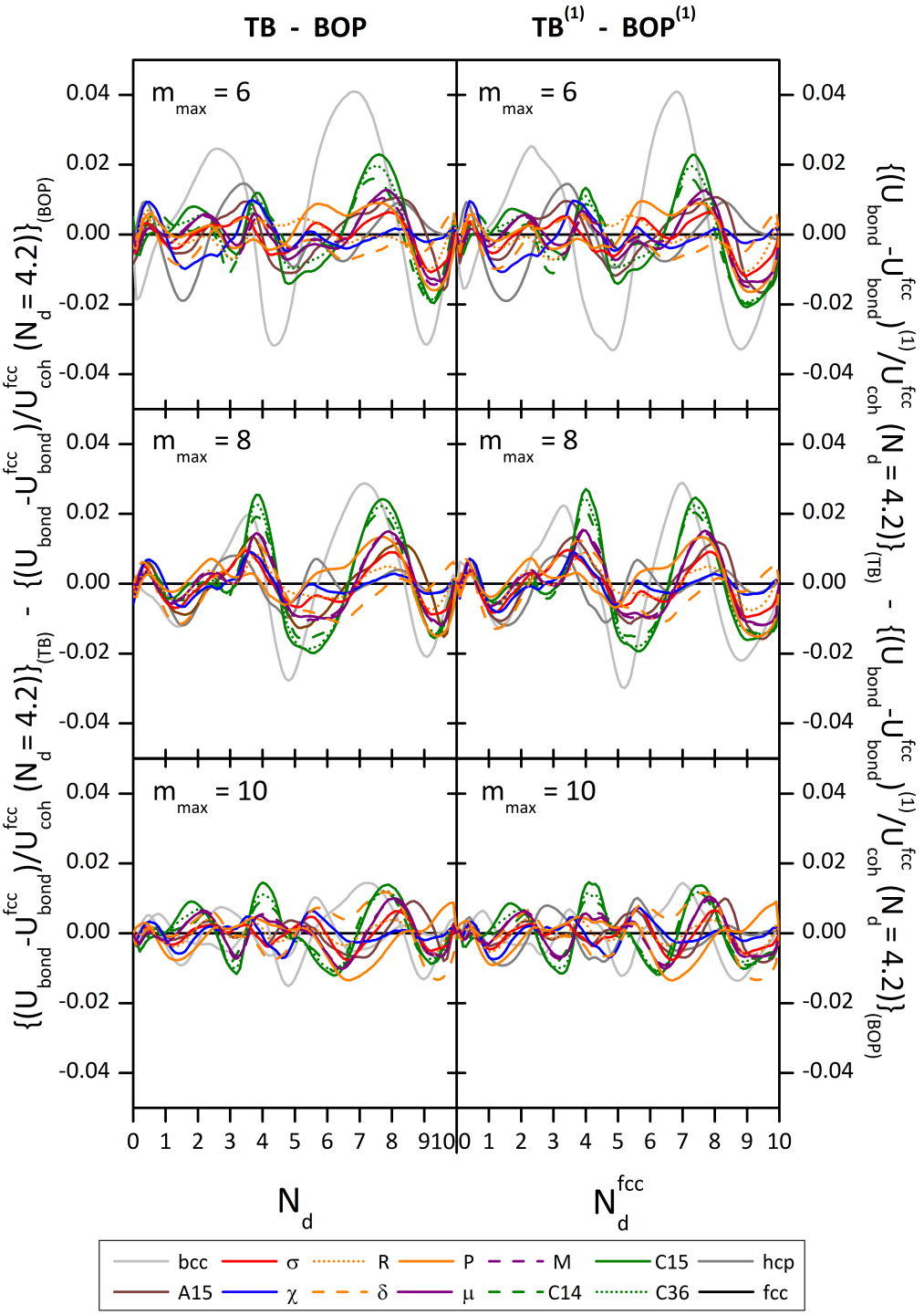

Figure 6.4: Left panel: Errors in exact BOP structural energy difference curves for $m_{max} = 6, 8, 10$ with respect to the exact TB result shown in the bottom left panel of Fig. 6.3. The errors are plotted against the number of d electrons. Right panel: Errors in first-order BOP structural energy difference curves for $m_{max} = 6, 8, 10$ with respect to the first-order TB result shown in the bottom right panel of Fig. 6.3. The errors are plotted against the number of d electrons in fcc.

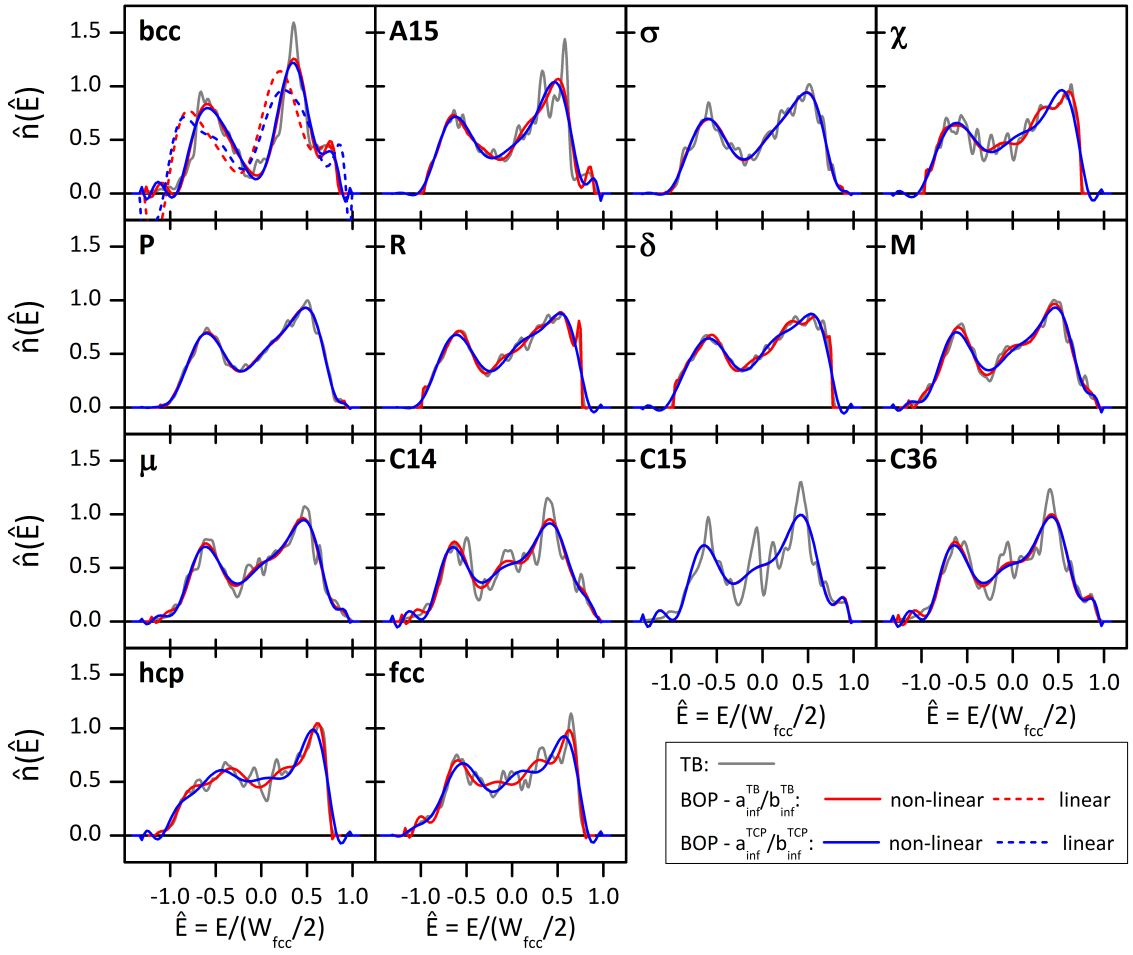

Figure 6.5: Density of states of all relevant structures normalised with respect to the band width of fcc for TB (grey solid), non-linear (red solid) and linear (red dashed) BOP with common asymptotic values $(a_\infty^{\mathrm{TCP}}, b_\infty^{\mathrm{TCP}})$, and non-linear (red solid) and linear (red dashed) BOP with the asymptotic values $(a_\infty^{\mathrm{TB}}, b_\infty^{\mathrm{TB}})$. All BOP densities of states are computed for m_{max}. The TB densities of states are calculated with the Methfessel-Paxton method [155] in order to smooth occasionally spiky density of states as are obtained with the tetrahedron method.

However, the fact that BOP does not pick up fine details of the TB DOS for a relatively small number of moments is not exclusive to BOP. It is a well-known problem of moment methods [195] in general and is evidenced in Fig. 6.6 where the continued fraction and BOP densities of states of the C15 phase are computed for increasing m_{max} values. Note that we plot the DOS for odd values of m_{max} as $(2n+1)$ moments are needed to obtain the recursion coefficients for the nth level within the continued fraction. We see in Fig. 6.6 that the densities of states of both moment methods gradually converge to the TB reference DOS. For example, the two main peaks at around $\hat{E} = -0.75$ and $\hat{E} = 0.5$ are captured by both methods for $m_{max} \leq 11$. Importantly, we notice for $m_{max} \geq 11$ that the moment methods with increasing m_{max} pick up the rapid oscillation of the TB DOS in the middle of the band, the region where we find the maximum error in Fig. 6.4. Although the moment methods with $m_{max} = 21$ still fail to reproduce the fine structure of the C15 TB DOS in every detail, the maximum error in the BOP structural energy difference is, at 0.3%, much smaller compared to 1.8% for $m_{max} = 10$ as shown in the bottom left panel of Fig. 6.4. Fig. 6.6 illustrates that whereas the continued fraction and BOP curves are very different for small m_{max} values, for example, for m_{max} the two main peaks are better predicted by the continued fraction as compared to BOP, they become very close for larger m_{max} values. This can be explained by the different ways in which the expansions are truncated. In the case of the continued fraction we terminate the continued fraction with the square-root terminator by taking $a_n = a_\infty$ and $b_n = b_\infty$ for $(2n+1) \geq m_{max}$ whereas the expansion coefficients σ_m with $m \geq m_{max}$ are set to zero within BOP. In the upper left panel of Fig. 6.6 we show that a terminator for BOP similar to the square-root terminator of the continued fraction (by taking $a_n = a_\infty$ and $b_n = b_\infty$ for $(2n+1) \geq m_{max}$) leads to a better prediction of the two main peaks and to a positive DOS at the band edges. However, using this terminator makes it more difficult to develop simple insights into the origin of the structural trends.

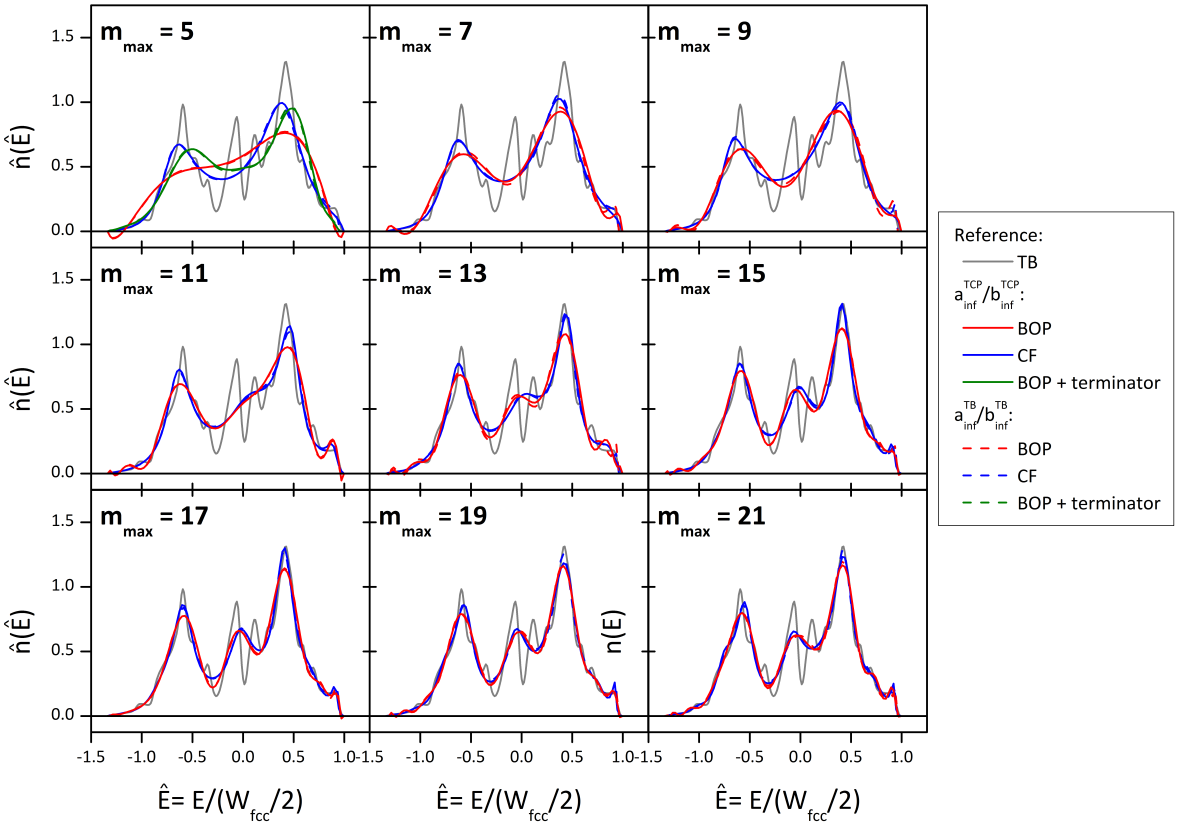

Figure 6.6: Density of states of the C15 phase normalised with respect to the band width of fcc as a function of m_{max}. The densities of states of BOP (red line), continued fraction (blue line), and BOP with terminator (green line) are calculated with common asymptotic values $(a_\infty^{\mathrm{TCP}}, b_\infty^{\mathrm{TCP}})$ (solid lines) and $(a_\infty^{C15}, b_\infty^{C15})$ of Tab. 6.1 (dashed lines). TB density of states (grey solid) are calculated using the Methfessel-Paxton method [155] in order to smooth occasionally spiky density of states as are obtained with tetrahedron method.

As an aside the top left-hand panel of Fig. 6.5 shows that the linear approximation to the expansion coefficients leads, for the bcc DOS, to very different results as compared to the non-linear expansion coefficients. We notice a sizeable shift in the bonding and anti-bonding peaks in the bcc DOS to lower energies because the DOS is strongly negative at the lower band edge. In Fig. 6.7, where the first-order TB structural energy difference curves in the right-hand panel are compared to the first-order BOP curves for $m_{max} = 10$ with linearised expansion coefficients in the left-hand panel, we see that the sizeable difference in the bcc DOS leads to a shift of the minimum of the (bcc-fcc) BOP structural energy difference curve from around $N_d = 4.1$ (non-linear) to $N_d = 3.4$ (linear) (as shown

in Fig. 4. of [172]). Moreover, Fig. 6.7 shows that the TCP curves experience a larger shift to lower band filling than bcc. Thus, the crossing of A15, σ and χ curves at around $N_d = 5.1$ in the right-hand panel is found lower, at around $N_d = 4.2$, in the left-hand panel such that the three TCP curves no longer intersect with the fcc and bcc curves at the same band filling. Hence, it demonstrates that the non-linear contributions are crucial for the correct prediction of the TB structural energy difference curves as shown in Fig. 6.3. However, it is surprising that the overall agreement between the left-hand and right-hand panels in Fig. 6.7 is not too bad considering that the linear BOP and TB DOS curves in Fig. 6.5 display major differences.

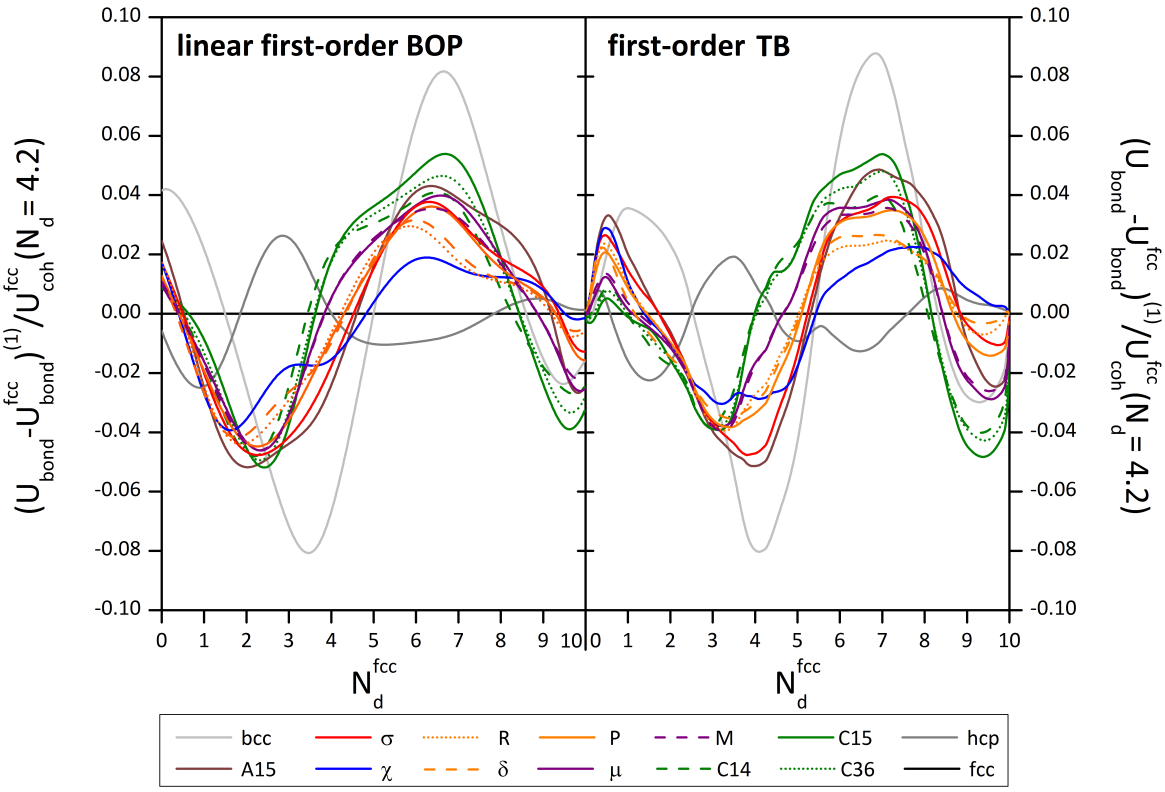

Figure 6.7: Left panel: The linear first-order BOP structural energy differences for $m_{max} = 10$ with respect to fcc versus the number of valence d electrons. Right panel: The first-order TB structural energy differences with respect to fcc versus the number of valence d electrons shown in the bottom right panel of Fig. 6.3.

In order to separate the errors of the moment expansion due to the errors resulting from the first-order expression in Eq. (6.32), we study the latter for the TB case in Fig.

6.8. To achieve a sensible and consistent normalization for the panels in this figure, we divide all ordinates by $\mathrm{W}^{fcc}/2$ as compared $U_{coh}^{fcc}(N_d = 4.2)$ in Figs. 6.3 and 6.4. For our TB model $[U_{coh}^{fcc}(N_d = 4.2)]/[W^{fcc}/2] = 1.07$. In the bottom panel of this figure we see the normalised difference between the 'exact' TB structural energy differences (i.e. bond energies compared at the same N_d) and the first-order TB structural energy differences (i.e. bond energies compared at the same Fermi level E_F, which corresponds to the band filling N_d^{fcc} of the fcc reference structure) as a function of N_d^{fcc}. It shows that the errors are all positive with the (bcc-fcc) curve exhibiting the largest error in the middle of the band. The main contribution to the errors can be found in Eq. (6.32) in which the neglected second-order error is given by

$$\left\{(U_{bond}^{II} - U_{bond}^{I}) - (U_{bond}^{II} - U_{bond}^{I})^{(1)}\right\}^{(2)} = \frac{1}{2} n^{I}(E_F^{I})(\Delta E_F)^2, \tag{6.38}$$

where $\Delta E_F = E_F^{II} - E_F^{I}$. The original expression of Sutton et al. [137] of the second-order error was derived for the difference in the band energy but since the on-site energies are zero in our non-self-consistent TB model the expression holds for the bond energies. The middle panel of Fig. 6.8 shows the band-filling variation in the normalised second-order error from the right-hand side of Eq. (6.38) calculated from ΔE_F which are shown in the panel above. We notice that the errors made by using the first-order expression in the lower panel are well described by the second-order error in the middle panel with minor differences resulting from neglected higher-order terms. Hence, the large error for (bcc-fcc) for half-full bands in the lower panel can be explained by the difference in the Fermi level of the two structure-types in the upper panel. The difference in the Fermi level of fcc and bcc can be understood from their corresponding TB DOS in Fig. 6.5 as it shows that bcc has, unlike any of the other structure-types studied, a deep pseudogap in the middle of the band.

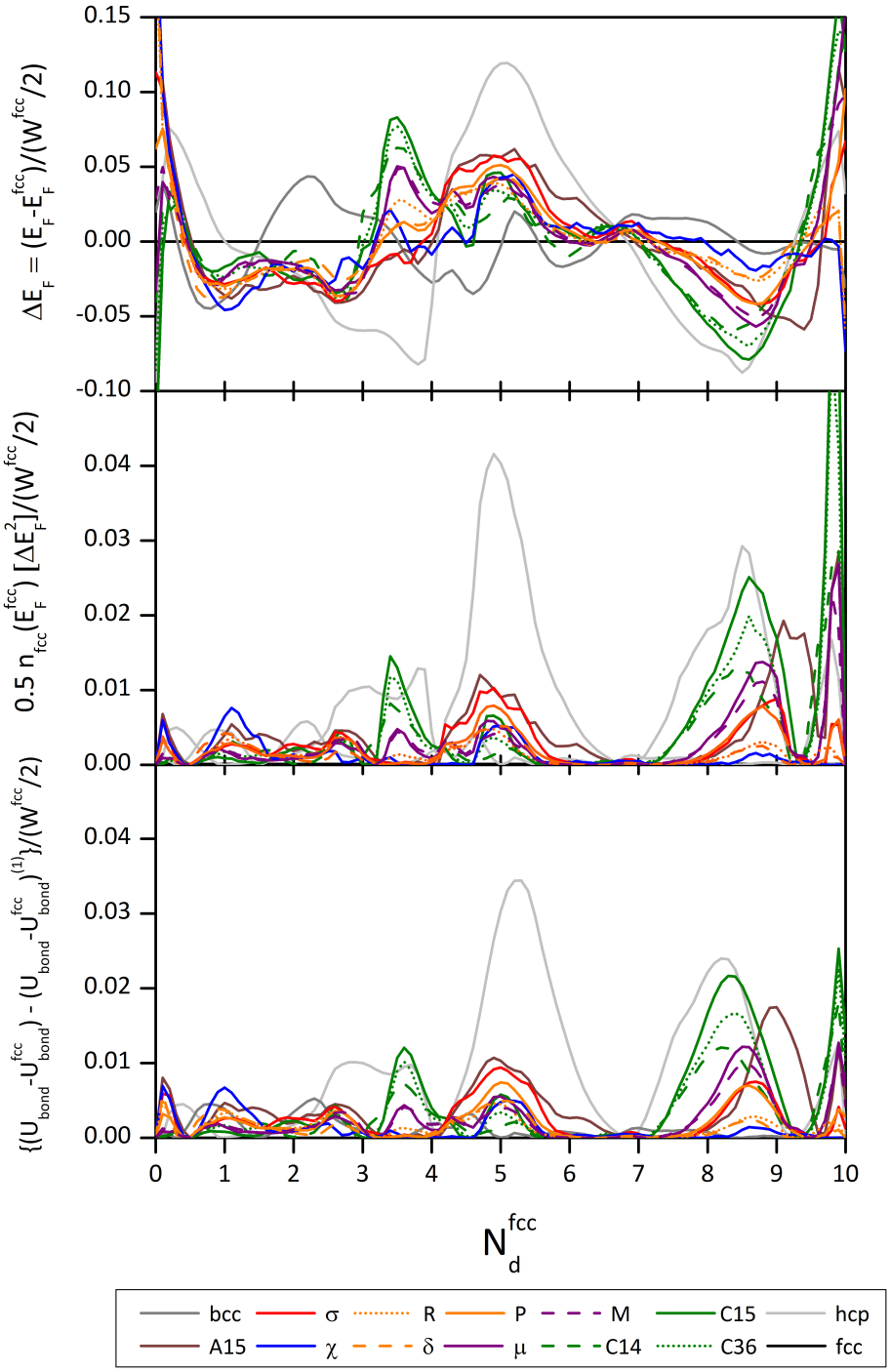

Figure 6.8: Upper panel: The normalised values of ΔE_F with respect to fcc for different structure-types as a function of the number of d electrons in fcc. Middle panel: The normalised second-order error from the right-hand side of Eq. (6.38) as a function of the number of d electrons in fcc. Lower panel: The errors made by using the first-order TB expression obtained by comparing 'exact' with first-order TB structural energy difference curves in the lowest left-hand and right-hand panels of Fig. 6.3.

6.3.2 Interpretation of the origin of the structural trends

Grouping of TCP structure-types

In the previous section we have seen in Fig. 6.3 that excellent agreement between the first-order BOP curves and the first-order TB curves is achieved for $m_{max} = 10$. In particular, the first-order BOP curves reproduced the vertical sequence of stability for $N_d = 5$ from $A15/\sigma/\chi \rightarrow \delta/\mathrm{P}/\mathrm{R} \rightarrow \mu/\mathrm{M} \rightarrow$ Laves (C14, C15 and C36) which explains the separation of the A15, σ and χ phases from the μ, M and Laves phases as found in our empirical structure map $(\bar{N}, \overline{\Delta V/V})$. Importantly, the top panels of Fig. 6.3 show that the division of the TCP structure-types into two groups is already displayed for first-order BOP curves with $m_{max} = 4$. Note that the BOP structural energy difference curves which include up to the third-moment, or σ_3 contribution, are not shown in Fig. 6.3 because all structure-types have similar third moments such that resulting differences in the energy contributions are small compared to the much larger differences in the fourth moment energy contribution. Hence, with $\Delta\mu_3 \approx 0$ and $\Delta\mu_2 = 0$ due to the structural energy difference theorem, we can approximate $\Delta\sigma_4$ in Eq. (6.20) by

$$\Delta\sigma_4 \approx (1 - \delta_1)\Delta\delta_2 = c\Delta(b_2/b_1)^2 \tag{6.39}$$

with $c = (b_1/b_\infty)^4$, which takes $c = 0.543$ in our model. Hence, the difference in the expansion coefficient σ_4 is proportional to $\Delta(b_2/b_1)^2$, the difference in the bimodal shape parameter $s = (b_2/b_1)^2$ of the average DOS. Similar to the observations for the difference between fcc and bcc as discussed in Sec. 6.2, we can therefore expect that the most stable structure-type for half-full d-bands is the structure-type with the smallest bimodal shape parameter (see in Eq. (6.9)) and consequently with the most bimodal DOS. In the first two columns of Tab. 6.2 we list $\Delta\sigma_4$ and $\Delta(b_2/b_1)^2$ for the individual TCP structure-types. Note that the errors made by using the approximation for $\Delta\sigma_4$ in Eq. (6.39) are not larger than 0.005. Importantly, it can be seen that the following sequence of TCP

structures is ordered with respect to $\Delta\sigma_4$ and $\Delta(b_2/b_1)^2$ as (A15/σ/χ) $\rightarrow$ (δ/R/P) $\rightarrow$ (M/μ) $\rightarrow$ (C14, C15 and C36) with A15/σ/χ and Laves (C14, C15 and C36) being the most and least bimodal TCP structure-types, respectively. This sequence is identical to the vertical ordering of the relative energies at $N = 6.5$ for DFT in the left-hand panel and $N_d = 5.0$ for TB in the right-hand panel of Fig. 5.8. Hence, the difference in the bimodality of the DOS explains the separation between the A15, σ and χ structural group and the μ and the Laves structural group that we found earlier within the two-dimensional structure map.

	First and second shells		First shell only	
	$\Delta\sigma_4$	$\Delta(b_2/b_1)^2$	$\Delta\sigma_4$	$\Delta(b_2/b_1)^2$
A15	0.000	0.000	0.000	0.000
σ	-0.002	0.004	-0.003	0.002
χ	-0.001	-0.002	-0.009	-0.017
δ	0.012	0.032	0.006	0.019
R	0.014	0.029	0.009	0.019
P	0.021	0.047	0.013	0.031
M	0.054	0.107	0.036	0.074
μ	0.063	0.125	0.042	0.086
C14	0.096	0.181	0.066	0.125
C15	0.099	0.191	0.067	0.132
C36	0.112	0.216	0.075	0.148

Table 6.2: Differences in TCP expansion coefficients σ_4 and bimodal shape parameters $(b_2/b_1)^2$ with respect to those of A15, where σ_4 and $(b_2/b_1)^2$ are for the average DOS for the individual TCP structure-types. The sums of first and second shell contributions are given in the second and third columns, first shell only contributions are given in the last two columns.

As we have seen in the case of energy difference between bcc and fcc in Sec. 6.2, moment methods allow a direct interpretation of structural trends in terms of the behaviour of the moments, which can be related to the local topology of the structure-types. As a first step towards the identification of the important moment contributions or hopping paths that give rise to the differences in the bimodality of the individual TCP structure-types, we study the influence of the fourth-moment contribution from within the first shell (i.e. we exclude self-returning fourth-moment hops out to the second shell and back

to the central atom). The corresponding $\Delta\sigma_4$ and $\Delta(b_2/b_1)^2$ values are listed in the last two columns of Tab. 6.2. It shows that the first shell only values, $\Delta\sigma_4$ and $\Delta(b_2/b_1)^2$, lead to the same ordering amongst the TCP structure-types as found for the first and second shell values in the first two columns of Tab. 6.2. However, the neglect of second shell contributions changes the relative stability of the TCP phases with respect to the fcc, hcp and bcc structure-types. This is illustrated in Fig. 6.9 where the first-order BOP structural energy difference curves that include only contributions to σ_4 from the first co-ordination shell (middle panel) are compared to the curves shown in the top right panel of Fig. 6.3 in which all contributions are considered (left panel). The middle panel of Fig. 6.9 shows that fcc and hcp are the most stable structures for half-full bands when the second shell contributions to σ_4 are not included. This result is expected for bcc as the distinctive planar four-membered ring contributions to the fourth moment involves hops to and from atoms of the second co-ordination shell as shown in Fig. 6.2. Moreover, we see from the right panel of Fig. 6.9, which shows the structural energy difference curves that include only the four-membered ring contributions, how important the ring terms are for stabilizing bcc and TCP phases with respect to fcc at half-full bands. This confirms Philips and Carlsson's [193] observation that the bimodal behaviour of the bcc and the TCP DOS results from a four-atom ring contribution with energetically favourable local minima near the structure's observed bond angles of 70° or 110°.

The fact that the structural ordering amongst the TCP phases persist for first shell only $\Delta\sigma_4$ values illustrates that the energetic differences between TCP structure-types must be related to the difference in fourth-moment hopping contributions confined within the individual co-ordination polyhedra. Our search for distinctive hopping paths is limited to the study of the A15 and C15 co-ordination polyhedra because A15 and C15 are, in the absence of higher moments, the most and least bimodal structure-types, respectively. Moreover, both structure-types are very simple as they have only two non-equivalent sites each and they are free of internal degrees of freedom such that the bond angles and bond lengths are unaffected by an energy minimization process. In Tab. 6.3 the

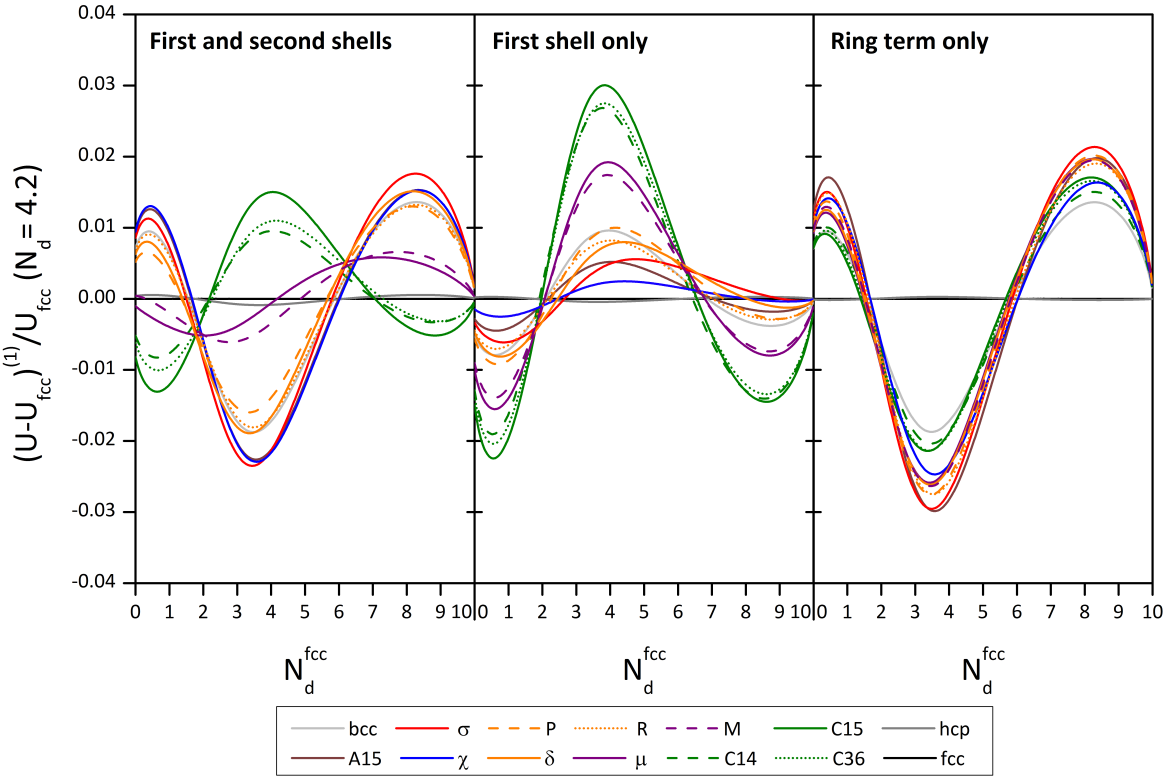

Figure 6.9: Left panel: The first-order BOP structural energy difference curves for $m_{max} = 4$ in the upper right-hand panel of Fig. 6.3. Middle panel: The first-order BOP structural energy difference curves for $m_{max} = 4$ excluding all second shell contributions to σ_4. Right panel: The first-order BOP structural energy difference curves for $m_{max} = 4$ which only include contributions from four-hop three-body paths that include second shell atoms.

co-ordination polyhedra Z12, Z14 and Z16 found in A15 and C15 are compared to the perfect corresponding Frank-Kasper polyhedra. Note that bond lengths of the individual co-ordination polyhedra are such that μ_2 are the same for all polyhedra. In the first two rows Tab. 6.3 we list the individual neighbour distances and bond angles from the central site of all co-ordination polyhedra. The third row gives the corresponding values of $(b_2/b_1)^2$ where the fourth-moment contributions are limited to the hopping paths involving the central atom and the atoms of its first co-ordination shell.

First shell	Z12			Z14		Z16	
	FK	A15	C15	FK	A15	FK	C15
Neighbours (distance)	12 (R_{icos})	12 (R_{icos})	6 (0.946 R_{icos}) 6 (1.109 R_{icos})	14 (1.020 R_{icos})	2 (0.901 R_{icos}) 4 (1.008 R_{icos}) 8 (1.104 R_{icos})	16 (1.037 R_{icos})	12 (1.027 R_{icos}) 4 (1.072 R_{icos})
Bond angles from centre	63.43°	53.13° 66.42°	60.00° 62.96° 64.76°	54.74° 66.84°	48.19° 56.79° 63.43°	50.48° 58.52°	50.48° 58.52°
$(b_2/b_1)^2$	0.178	0.223	0.297	0.221	0.220	0.189	0.201
$(b_2/b_1)^2/(b_2/b_1)^2_{icos}$	1.000	1.250	1.670	1.242	1.236	1.060	1.124

Table 6.3: Number of neighbours, neighbour distances, bond angles from centre, shape factors and normalised shape factors of Z12, Z14 and Z16 co-ordination polyhedra found within the A15 and C15 structure-types and perfect Frank-Kasper (FK) polyhedra. The neighbour distances are given with respect to the nearest-neighbour distance of an icosahedron, R_{icos}.

Contrary to previous statements in the literature [39], Tab. 6.3 shows that the icosahedron has the smallest shape parameter $(b_2/b_1)^2$ and it is therefore the most bimodal co-ordination polyhedra (not only in comparison to co-ordination polyhedra listed in Tab. 6.3 but compared to all co-ordination polyhedra found in TCP phases). Berne et al. [39] assumed that the icosahedral site has the most unimodal DOS as a result of the degenerate d-levels while the point group symmetries of the other co-ordination polyhedra have less degenerate d-levels and are therefore less unimodal. Moreover, it was believed that the effective deviations from the point group symmetry of the icosahedron are small for the distorted icosahedral building units in TCP phases such that they have little influence on the degeneracy of the d-levels. Hence, it was assumed that the distorted Z12 co-ordination polyhedra are as unimodal as the icosahedron. Tab. 6.3 clearly demonstrates that the packing of the TCP phases demands severe distortions of the polyhedra such that their topology can be very different from the perfect Frank-Kasper polyhedra. However, Tab. 6.3 indicates that the degree of distortion of the icosahedral environment and consequently the change in the bimodality depends on whether the Z12 polyhedra is found within the A15 or the C15 phase. The bimodal shape parameter $(b_2/b_1)^2$ shows that both Z12 co-ordination polyhedra are less bimodal than the icosahedron as $(b_2/b_1)^2/(b_2/b_1)^2_{icos} > 1$ but the increase of the shape parameter in C15 of 67% is much larger than that of A15 of 25%.

This difference in bimodality of the icosahedral sites with respect to the perfect icosahedron can be related directly to the different four-hop paths within the first shell that contribute to $(b_2/b_1)^2$. In Tab. 6.4 we show the normalised fourth-moment contributions μ_4/μ_2^2 for the icosahedron and the icosahedral sites in A15 and C15. In order to allow a better identification of the difference in the four-hop contributions we divide the fourth-moment paths into three types according to the number of atoms and the bond angles. The first group of paths consist of the self-returning paths which include only hops to the nearest neighbours and back, as can be seen from the schematic drawings next to Tab. 6.4. The second group is comprised of the four-hop three-body contributions where

we distinguish between paths with a general bond angle θ (group 2.2) and the special case $\theta = 180°$ (group 2.1). The last group is comprised of the four-membered ring path. Schematic drawings of the three types are depicted in the figure next to Tab. 6.4. Note that any of the depicted atoms in the figure could in general be the central site as follows from Eq. (6.2) that the calculation of the moment contributions is invariant under cyclic permutations of atoms. However, since we restrict hops to the first shell, the atom in the middle of the $\theta = 180°$ three-body path (group 2.1) must be the central site of the co-ordination polyhedra.

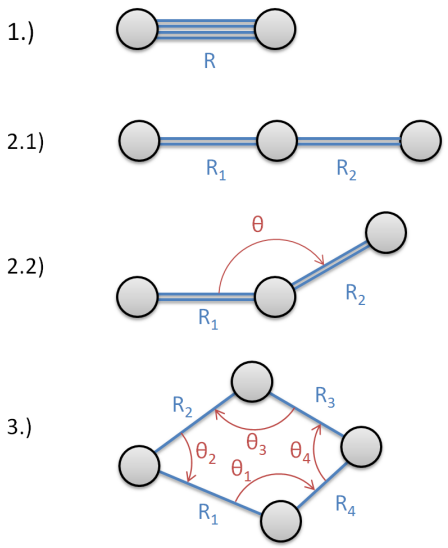

Path	Icosahedron	A15	C15
1	0.154	0.154	**0.203**
2.1	0.846	0.849	0.229
2.2	0.251	**0.317**	0.917
	1.097	1.166	**1.146**
3	-0.014	-0.033	-0.001
Sum	1.237	1.287	1.348

Table 6.4: Normalised fourth-moment contributions μ_4/μ_2^2 of Z12 co-ordination polyhedra found within the A15 and C15 structure-types and icosahedron. Classification of fourth-moment contributions are according to the number of atoms as shown in the left figure: Two-body contribution (group 1), two-body contribution (group 2) with the general bond angle θ (group 2.1) and $\theta = 180°$ (group 2.1) and three-body contribution.

Tab. 6.4 shows that the difference in the four-hop three-body contributions gives rise to the 15% increase of the shape factor of the A15 structure with respect to the shape factor of the icosahedron. In particular, we notice that the three-body contributions with general bond angles, θ, are different whereas the contributions with $\theta = 180°$ are almost identical. It shows that the difference in the contributions for the general case can be associated with different bond lengths between the atoms surrounding the central site.

Whereas the 12 atoms surrounding the central site in the perfect icosahedron have the same distance as each other, the bond lengths between shell atoms around the icosahedral A15 site are either $1.095R_{icos}$ or $0.894R_{icos}$. We find that paths that involve the latter, much shorter distance have a sizeable effect on the fourth-moment contribution. The three-body path as shown in the upper panel of Fig. 6.10 with the bond lengths $R_1 = R_{icos}$ and $R_2 = 0.894R_{icos}$ is of particular significance. The bond lengths of the corresponding path in the perfect icosahedron are $R_1 = R_{icos}$ and $R_2 = 1.051R_{icos}$. The bond angles of this path are very similar in both co-ordination polyhedra such that the bond angle difference has almost no influence on the difference in size of the contribution as is shown in the bottom panel of Fig. 6.10. On the assumption that the bond angles are identical, it follows from Eq. (5.26) and $\beta(R) \propto 1/(R_1^2 R_2^2)$ from Eq. (5.26) that the contribution of this path in A15 is approximately $(1.051^8)/(0.946^8) = 3.649$ larger than the corresponding path in the perfect icosahedron. Hence, this explains why the icosahedral site in A15 has a larger fourth moment than the icosahedron and therefore why we see this difference in bimodality, as it is related directly to the different four-hop paths that contribute to $(b_2/b_1)^2$.

Table 6.3 demonstrates that the shape parameter within the first-shell approximation is 67% larger for the icosahedral site in C15 than in the perfect Frank-Kasper polyhedron. This can again be understood by the more detailed breakdown of the different hopping contributions in Tab. 6.4. It shows that the fourth-moment contributions of the two- and three-atom paths are significantly larger for the icosahedral site in C15 than in A15 and the perfect Frank-Kasper polyhedron. As for the icosahedral site in A15, the large fourth-moment contributions of the two- and three-atom paths in C15 can be traced back directly to the difference in the bond lengths, in particular, to the splitting of the 12 nearest neighbour atoms into 6 atoms at $0.946R_{icos}$ and a further 6 atoms at $1.109R_{icos}$ respectively. The shorter distance has a particularly large impact on the contributions of the two-atom paths, β^4, because they involve four times the hopping integral, $\beta(0.946R_{icos})$, between the central atom and a particular neighbouring atom.

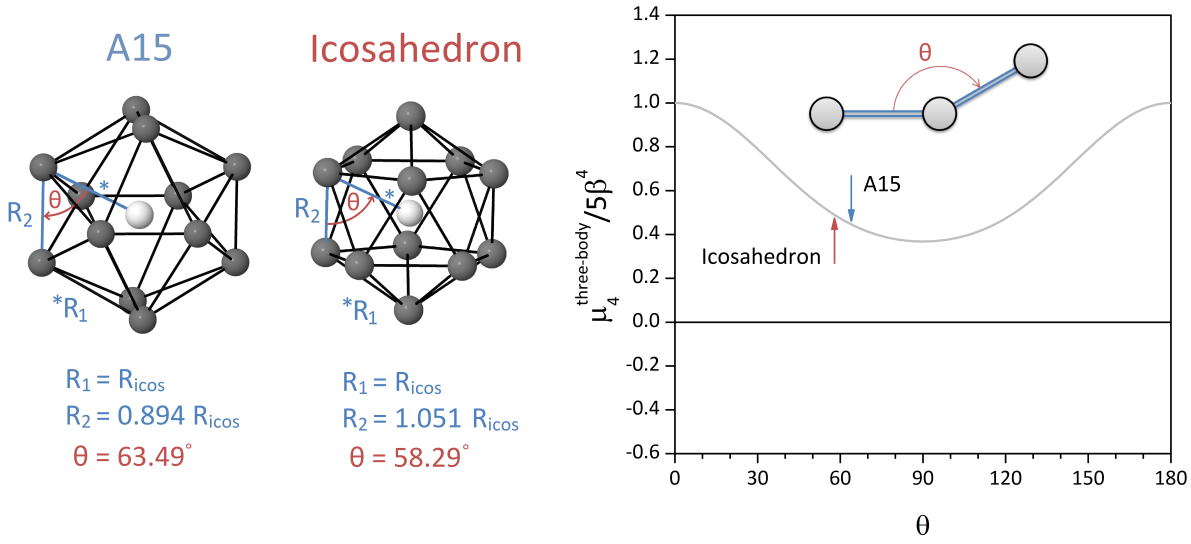

Figure 6.10: Four-hop three-body contribution in the icosahedral A15 site and the icosahedron (left) and its fourth-moment contribution as a function of the bond angle Θ (right). The arrows indicate the bond angles of 58.29° and 63.49° in A15 and icosahedron, respectively.

From Eq. (5.26) with $\beta(R) \propto 1/R^4$ it follows that this β^4 contribution to the closer atoms at $0.946R_{icos}$ is $1/0.946^{16} = 2.431$ larger than the corresponding path in the perfect icosahedron. Moreover, the left-hand panel of Fig. 6.11 with the shell atoms at $0.946R_{icos}$ and $1.109R_{icos}$ being coloured in blue and red, respectively, shows that the closer atoms are again split into two groups of three where their blue neighbours are separated by the bond length $0.946R_{icos}$. Hence, it is not surprising that the four-hop three-atom path with bond lengths of $0.946R_{icos}$, as shown in middle panel of Fig. 6.11, accounts for 58% of the overall three-body fourth-moment contribution as given in Tab. 6.4. The second largest contribution to the the three-body fourth-moment contribution, of 38%, comes from the self-returning paths that involve hops between the central atom and its close neighbouring atoms at $0.946R_{icos}$ (blue atoms) and hops to and from the atoms which are further away at $1.109R_{icos}$ (red atoms) as shown in the right-panel of Fig. 6.11. Thus, it can be seen that the short distance $0.946R_{icos}$ which is found between the central atom and 6 of its neighbouring atoms and also between its neighbouring atoms lead the much

larger two- and three-body fourth-moment contributions, and therefore explains the 67% increase in the shape parameter as compared to the perfect Frank-Kasper polyhedron. As an aside it shows in Tab. 6.4 that the change in the bond lengths has almost no effect on the four-hop four-body contributions. This is for two reasons, the first being that four-membered contributions can be positive or negative as has been demonstrated by the bond-angle dependence of the fourth-moment contribution of the planar ring in Fig. 6.2. Note that none of the icosahedral sites in A15, C15 or the perfect Frank-Kasper polyhedron have planar rings but the four-body fourth-moment contributions depend on all four bond angles θ_i as shown in Fig. 6.4. Secondly, it shows that the bond angles within the first shell are such that the fourth-moment contributions are generally much smaller than the three-membered contributions in Tab. 6.4.

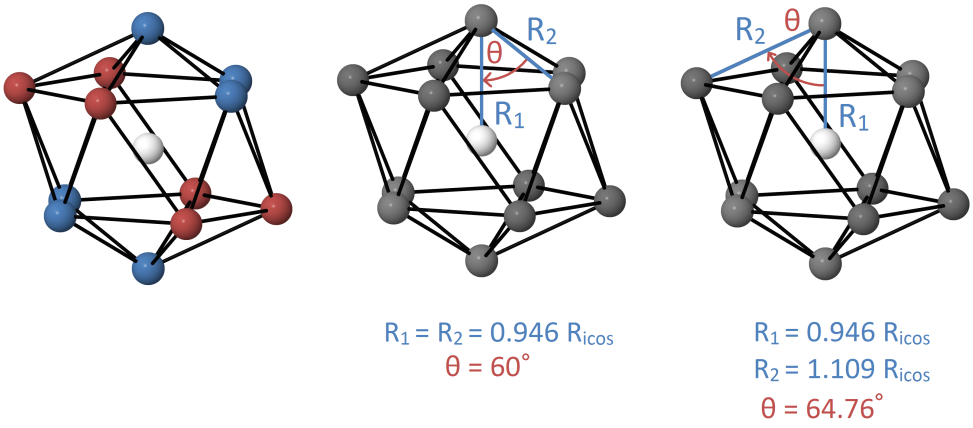

Figure 6.11: Left figure: The icosahedral site in C15 with the shell atoms being $0.946R_{icos}$ (blue) and $1.109R_{icos}$ (red) apart from the central atom (white). Middle and right figures: Examples of the four-hop three-body contribution in the icosahedral C15 site.

Structural trend from A15 to σ to χ

The second interesting trend that was revealed by our structure map in chapter 3 is the structural trend within a given binary alloy system from A15 $\rightarrow$ σ $\rightarrow$ χ as the valence electron concentration increases. This structural trend is reflected in the DFT heats of formation and is also predicted by unary DFT and TB calculations in the previous sections. As shown in the left-hand panel of Fig. 5.8, in the DFT calculations the trend

is obtained by linearly interpolated structural energy difference curves for the elements of groups VI and VII. In the right-hand panel of Fig. 5.8, the present TB model has difficulties in predicting the subtle structural energy differences between the A15 and σ phases at around $N_d = 5$. Hence, a more sophisticated TB model with specially fitted bond integral parameters and less crude assumptions regarding the decay of the repulsion will be needed in order to predict the structural competition between A15, σ and χ in a given binary system. However, Fig. 6.3 shows that a reasonable parametrization up to at least the sixth moment would be required within analytic BOP to separate the A15, σ and χ phases as they are almost indistinguishable at $m_{max} = 4$. This again contradicts the idea of Berne et al. that the structural trend A15 $\rightarrow \sigma \rightarrow \chi$ can be related to the percentages of icosahedral site due to the unimodal DOS as the difference in bimodality would have been picked up within the fourth-moment contribution. Importantly, the need for up to the sixth moment shows that second-moment models such as Finnis-Sinclair [196] or fourth-moment models such as Phillips and Carlsson [193] are *not* sufficient to make these subtle predictions within the TCP structure-types. Note that parameters of fifth-moment TB models could be fitted such that they would give sensible results, however, the physical footing of the parametrization would need to be questioned.

Like the previous moment analysis for the difference in σ_4, the differences in σ_6 for the A15, σ and χ phases are computed and an attempt made to identify the individual interference paths which give rise to the differences in order to explain the origins of the structural trend from A15 $\rightarrow \sigma \rightarrow \chi$. Considering previous failed attempts to identify specific sixth-hop paths that cause the small (fcc-hcp) energy difference and the fact that the crystal structures are much more complex than for fcc and hcp, it is not completely unsuspected that we are unable to distinguish a single, simple hopping path that drives this trend.

6.4 Summary

In this chapter, analytic BOP theory together with the TB bond integrals from chapter 5.2 was used to show that the exact BOP structural energy difference curves converge to the TB structural energy difference curves as the number of moments in the BOP expansion is increased. As well as comparing the bond energy at the same number of electrons we used the first-order expression which allows a comparison of the bond energies at the same Fermi energy instead. The errors made by using the first-order expression were shown to be well understood by the neglected second-order error. Moreover, the oscillatory nature of the remaining difference between the well converged BOP curves that include up to the tenth moment and TB curves was discussed briefly by comparing the corresponding TB and BOP densities of states. For example, the fine structure of the C15 TB DOS were shown to be picked up by the high-order Chebyshev polynomials in the BOP expansion. Importantly, the BOP densities of states demonstrated that the results with our choice of common asymptotic values $(a_\infty^{\mathrm{TCP}}, b_\infty^{\mathrm{TCP}})$ are close to the results obtained with the asymptotic values $(a_\infty^{\mathrm{TB}}, b_\infty^{\mathrm{TB}})$. This valid approximation together with the first-order approximation allowed a simple interpretation of the TB structural energy difference curves with respect to analytic response functions and the differences in the moments of the DOS.

A moment analysis demonstrated that the fourth-moment contribution due to differences in the bimodality of the corresponding DOS separates the A15, σ and χ from the μ and Laves phases in agreement with the experimental structure map. By focusing on the difference between the A15 (most bimodal) and C15 (least bimodal) structure-types, it was shown that this behaviour results from crystal packing as this leads to different distortions in their co-ordination shells compared to the perfect Frank-Kasper co-ordination polyhedra. In particular, the differences in the bimodal shape factor of the icosahedral sites in the A15 and C15 phases with respect to the perfect icosahedron indicated the importance of the distortions of icosahedral sites for overall difference in the bimodality

between A15 and C15. A detailed breakdown of the individual fourth-moment contributions lead to the conclusion that the minor increase in the bimodal shape factor of the A15 icosahedron can be explained by its three-body fourth-moment contributions that involve hops between first-shell atoms that are separated by a relatively small bond length. Moreover, the C15 icosahedron's large bimodal shape factor was shown to be directly related to the fact that half of the neighbouring atoms of the C15 polyhedron are located much closer to the central atom as compared to the equidistantly distributed neighbours of the A15 phase and icosahedron. Finally, second-moment or fourth-moment interatomic potentials were shown not to be sufficient to predict the structural transitions within the TCP phases as it was demonstrated that the subtle trend from A15 $\rightarrow \sigma \rightarrow \chi$ requires at least the sixth moment. Unfortunately, we were not able to identify a single, simple hopping path that drives this trends was found to be impossible due to the complexity of the crystal structures.

Chapter 7

Summary and conclusion

The precipitation of topologically close-packed (TCP) phases during the lifetime of a jet engine seriously degrades the mechanical properties of the nickel-based superalloy turbine blades not only because of their brittle nature but also because they deplete the Ni-rich matrix of potent solid solution strengthening elements. Over the past decades several detrimental TCP phases have been observed in nickel-based superalloys and it has been shown that the same factors that control the stability of TCP phases of binary and ternary TCP phases also control the formation of multi-component TCP phases. Existing models, like the phase computation methods PHACOMP and NewPHACOMP, are based on this knowledge regarding the factors controlling TCP phase stability. In general most methods do quite well in interpolating data, but, once predictions have to be made, for example, on the effect of new elements added to an alloy, they may give inadequate results due to the lack of a physical footing of the method. Thus, no reliable tool exists for the prediction or prevention of TCP phase formation which moves systematic alloy design towards an approach with a strong emphasis on theoretical analysis and computer models, and a disregard for empiricism and trial-and-error-based methods. A general understanding of the factors controlling the stability of TCP phases can provide useful information about the formation, and consequently the prevention, of TCP phases in nickel-based superalloys. In this thesis the influence of electronic and size factors on the

stability of TCP phases was studied by a phenomenological two-dimensional structure map complemented by analytic bond-order potentials (BOPs) providing valuable insights into the origin of the observed structural trends.

Firstly, in chapter 3 a novel two-dimensional structure map ($\bar{N}$, $\overline{\Delta V/V}$) where $\bar{N}$ is the average electron concentration and $\overline{\Delta V/V}$ is a composition dependent size-factor difference was introduced. This map allowed a detailed investigation of the occurrence of experimental TCP phases in binary, ternary and multi-component transition metal alloys which revealed two interesting structural trends within the experimental data. Firstly, the size factor was found to divide the TCP structure-types into two groups, namely A15, σ, and χ for $\overline{\Delta V/V} \lesssim 0.15$ and μ, M and Laves for $\overline{\Delta V/V} \gtrsim 0.15$ with R, P and δ in the overlap region between these two groups. Thus, within alloys having a small size factor difference, the valence electron concentration stabilizes A15, σ and χ but destabilizes the other TCP phases. Secondly, increasing the valence electron concentration within binary alloy systems from the first group was occasionally found to drive a structural trend from A15 $\rightarrow \sigma \rightarrow \chi$.

Detailed investigations of multi-component systems demonstrated that TCP phases, regardless of the number of constituents, are located in the same regions of the structure map that are favoured by the binary compounds of the same structure type. This result is important for two reasons. Firstly, it proves that the factors that control the stability of TCP phases of binary and ternary TCP phases also control the formation of multi-component TCP phases. Secondly, it allows the testing of the robustness of commercial methods to predict TCP phase formation in nickel-based superalloys by means of the structure map. Thus, in chapter 4, the structure map was used in combination with CALPHAD computations on the Ni-Co-Cr-Ta-W-Re-Al system to compare the one-parameter method NewPHACOMP with the structure map co-ordinates $\bar{N}$ and $\overline{\Delta V/V}$ in terms of their capability to predict σ phase formation. With both methods being unable to separate σ-free from σ-prone alloys and CALPHAD's database failing to correctly predict μ and P phases, future reliable predictions of TCP phase stability in nickel-based super-

alloys will rely on the CALPHAD method with reliable first-principles thermodynamic databases.

Insights into the microscopic origin of the structural trends that were discussed using the empirical structure map were obtained by first coarse graining the electronic structure from DFT to the TB model and then carrying out a moment analysis within analytic BOP theory. The coarse-graining of the electronic structure from DFT through TB to bond-order potentials started with DFT calculations of the structural energy differences across the elemental $4d$ and $5d$ transition metal series, with no size or electronegativity differences, and DFT calculations of the heats of formation of the four binary alloys Mo-Re, Mo-Ru, Nb-Re and Nb-Ru, which all exhibit relatively small but important size differences. The elemental DFT calculations were used to provide the quantitative benchmark for the study of the energy differences between the various structure-types as a function of the valence electron concentration. The elemental results demonstrated that, in the absence of size and electronegativity differences, the valence electron concentration stabilizes the A15, σ and χ phases but destabilizes the other TCP phases such as R, P, δ, μ, M and the Laves phases. Thus, the linear interpolation of elemental DFT structural energy differences led to the trend from hcp $\rightarrow$ bcc $\rightarrow$ TCP(A15 $\rightarrow \sigma \rightarrow \chi$) $\rightarrow$ hcp $\rightarrow$ fcc as the valence electron increases which is in good agreement with experimental trends found for binary systems having small size factor differences. The binary DFT calculations then showed that this trend is also reflected in the heats of formation of binary systems that are characterised by relatively small differences in the size factor. However, as the size factor differences become larger, μ and Laves phases (and probably R, P, δ and M phases) become increasingly more stable and more compact than A15, σ and χ phases, explaining the separation of the two structure-type groups in the structure map. The elemental DFT structural energy difference curves with the predicted structural trends were reproduced by a simple canonical TB model with one adjustable parameter in conjunction with the structural energy difference theorem. The latter theorem proved to be extremely useful for rationalizing the influence of the relative size differences in binary TCP phases in

particular for μ and Laves phases as indicated by the DFT binary calculations and the experimental structure map.

The TB bond integrals that reproduced the elemental DFT trends were then used within analytic BOP theory to provide a simple interpretation of the elemental structural energy difference curves by relating the energy differences to the differences in the local topology of the structure-types using the moments of the local TB density of states. A first-order expression for comparing the difference in the bond energy at the same Fermi level was derived which allowed a discussion of the individual difference in the moments with respect to analytic response functions and the differences in the moments of the DOS. Structural energy difference calculations using this first-order approximation and the exact BOP expansions converged to the TB reference results as the number of moments in their expansions was increased. In the course of this convergence test, individual moment contributions were identified to be responsible for the two observed structural trends. Firstly, the division between the A15, σ, χ and the μ, C14, C15, C36 Laves phases in the experimental structure map was found to be driven by the fourth-moment contribution due to the bimodality of the corresponding DOS. The analysis of the individual moment contributions of the most bimodal, A15, and least bimodal, C15, structures led to the conclusion that the difference in bimodality originates from the amount of distortion in their co-ordination shells resulting from crystal packing. Secondly, at least the sixth moment is required to reproduce the subtle trend from A15 $\rightarrow$ σ $\rightarrow$ χ and, as such, neither second-moment nor fourth-moment interatomic potentials are sufficient to predict the structural transitions within the TCP phases. Unfortunately, the complexity of the TCP crystal structures makes it impossible to identify a single simple hopping path that drives this trends.

In conclusion, our two-fold approach of employing a phenomenological two-dimensional structure map and electronic structure calculations has proved to be very powerful in explaining the influence of the two most important factors controlling TCP phase formation, namely the valence electron concentration and the atomic size difference. Analytic bond-

order theory was found to be particularly useful for unraveling the link between structural stability and the local topology of the TCP phases. In the future, BOPs which are suitable for large-scale atomistic simulations due to their analytic forces will play a crucial part in understanding phase stability and in modelling interfaces of co-existing phases in superalloys. However, such investigations would need to involve more sophisticated BOPs than those presented in this work. The information gained from this thesis will be essential for the parametrization of these BOPs.

Bibliography

[1] D. G. Pettifor. Computer-aided materials design: Bridging the gaps between physics, chemistry and engineering. *Physics Education*, 32(3):164–168, 1997.

[2] C. T. Sims and W. C. Hagel. *The superalloys*. John Wiley & Sons, Inc., New York, 1973.

[3] R. C. Reed. *The superalloys: Fundamentals and applications*. Cambridge University Press, Cambridge, 2006.

[4] Michael Cervenka. The Rolls-Royce Trent Engine. http://www.msm.cam.ac.uk/phase-trans/mphil/Trent1/index.htm, November 2000.

[5] P. Caron and T. Khan. Evolution of Ni-based superalloys for single crystal gas turbine blade applications. *Aerospace Science And Technology*, 3(8):513–523, 1999.

[6] J. R. Davis, editor. *Heat-resistant materials*. ASM International, 1997.

[7] R. C. Reed, A. C. Yeh, S. Tin, S. S. Babu, and M. K. Miller. Identification of the partitioning characteristics of ruthenium in single crystal superalloys using atom probe tomography. *Scripta Materialia*, 51(4):327 – 331, 2004.

[8] T. Murakumo, T. Kobayashi, Y. Koizumi, and H. Harada. Creep behaviour of Ni-base single-crystal superalloys with various γ' volume fraction. *Acta Materialia*, 52(12):3737–3744, 2004.

[9] A. Volek, F. Pyczak, R.F. Singer, and H. Mughrabi. Partitioning of Re between γ and γ' phase in nickel-base superalloys. *Scripta Materialia*, 52(2):141–145, 2005.

[10] G. S. Hillier. *The defect energies and deformation mechanisms of single crystal superalloys*. PhD thesis, University of Cambridge, 1984.

[11] M. Durand-Charre. *The microstructure of superalloys*. Gordon and Breach Science, Amsterdam, 1997.

[12] M. J. Donachie. *Superalloys: A technical guide*. ASM International, 2002.

[13] L. R. Liu. Formation of carbides and their effects on stress rupture of a Ni-base single crystal superalloy. *Materials science and engineering C*, 361(1-2):191–197, 2003.

[14] C. M. F. Rae and R. C. Reed. The precipitation of topologically close-packed phases in rhenium-containing superalloys. *Acta Materialia*, 49(19):4113–4125, 2001.

[15] R. C. Reed, N. Matan, D. C. Cox, M. A. Rist, and C. M. F. Rae. Creep of CMSX-4 superalloy single crystals: Effects of rafting at high temperature. *Acta Materialia*, 47(12):3367–3381, 1999.

[16] R. C. Reed, D. C. Cox, and C. M. F. Rae. Damage accumulation during creep deformation of a single crystal superalloy at 1150°C. *Materials Science and Engineering A*, 448(1-2):88–96, 2007.

[17] J. X. Yang, Q. Zheng, X. F. Sun, H. R. Guan, and Z. Q. Hu. Topologically close-packed phase precipitation in nickel-base superalloy during thermal exposure. *Materials Science and Engineering A*, 465:100–108, 2007.

[18] C. T. Sims. *Superalloys 2*, chapter 8, pages 217–237. John Wiley & Sons, Inc., New York, 1987.

[19] M. Simonetti and P. Caron. Role and behaviour of μ phase during deformation of a nickel-base single crystal superalloy. *Materials Science and Engineering A*, A254:1–12, 1998.

[20] L. Z. He, Q. Zheng, X. F. Sun, H. R. Guan, Z. Q. Hu, A. K. Tieu, C. Lu, and H. T. Zhu. Effect of carbides on the creep properties of a Ni-base superalloy M963. *Materials Science and Engineering A*, 397(1-2):297–304, 2005.

[21] C. Berne, M. Sluiter, Y. Kawazoe, T. Hansen, and A. Pasturel. Site occupancy in the Re-W σ phase. *Physical Review B*, 64:144103–1–7, 2001.

[22] A. K. Sinha. Topologically close-packed structures of transition metal alloys. *Progress in Material Science*, 15:81–185, 1972.

[23] F. C. Frank and J. S. Kasper. Complex alloy structures regarded as sphere packings. 1. Definition and basic principles. *Acta Crystallographica*, 11:184–190, 1958.

[24] F. C. Frank and J. S. Kasper. Complex alloy structures regarded as sphere packings. 2. Analysis and classification of representative structures. *Acta Crystallographica*, 12(7):483–499, 1959.

[25] H. J. Beattie and W. C. Hagel. Compositional control of phases precipitating in complex austenitic alloys. *Transactions of the Metallurgical Society of AIME*, 233:277–287, 1965.

[26] J. S. Kasper and R. M. Waterstrat. Ordering of atoms in the σ phase. *Acta Crystallographica*, 9(3):289–295, Mar 1956.

[27] J. M. Joubert. Crystal chemistry and CALPHAD modeling of the σ phase. *Progress in Materials Science*, 53(3):528–583, March 2008.

[28] D. P. Shoemaker and C. B. Shoemaker. *Developments in the structural chemistry of alloy phases*, pages 107–139. Plenum Press, New York, 1969.

[29] S. Andersson. Structures related to the β-tungsten or Cr_3Si structure type. *Journal of Solid State Chemistry*, 23, 1-2:191–204, 1978.

[30] K. H. Kuo, H. Q. Ye, and X. Li. Tetrahedrally close-packed phases in superalloys: New phases and domain structures observed by high-resolution electron microscopy. *Journal of Materials Science*, 21:2597–2622, 1986.

[31] A. H. Sully and T. J. Heal. An electron compound in alloys of transition metals. *Research*, 1:288, 1948.

[32] S. P. Rideout, W. D. Manly, E. L. Kamen, B. S. Lement, and P. A. Beck. Intermediate phases in ternary alloy systems of transition elements. *Transactions of the Metallurgical Society of AIME*, 191:872–876, 1951.

[33] D. K. Das, S. P. Rideout, and P. A. Beck. Intermediate phases in the Mo-Fe-Co, Mo-Fe-Ni, and Mo-Ni-Co ternary systems. *Transactions of the Metallurgical Society of AIME*, 194:1071–1075, 1952.

[34] S. P. Rideout and P. A. Beck. Survey of portions of the Cr-Co-Ni-Mo quaternary systems at 1200°C. *National Advisory Committee for Aeronautics, Report*, 1122:1–39, 1953.

[35] L. Pauling. The nature of the interatomic forces in metals. *Physical Review*, 54:899–904, 1938.

[36] W. Hume-Rothery, H. M. Irwing, and R. J. P. Williams. The valencies of the transition elements in the metallic state. *Proceedings Of The Royal Society Of London Series A-Mathematical And Physical Sciences*, 208(1095):431–443, 1951.

[37] P. Greenfield and P. A. Beck. Intermediate phases in binary systems of certain transition elements. *Transactions of the Metallurgical Society of AIME*, 206(2):265–276, 1956.

[38] C. W. Haworth and W. Hume-Rothery. A note on transtion metal alloys. *Philosophical Magazine*, 3:33:1013–1019, 1958.

[39] C. Berne, A. Pasturel, M. H. F. Sluiter, and B. Vinet. Ab initio study of metastability in refractory metal based systems. *Physical Review Letters*, 83:1621–1623, 1999.

[40] F. Laves. Über den Einfluss geometrischer Faktoren auf die stöichiometrische Formel metallischer Verbindungen, gezeigt an der Kristallstruktur des KNa_2. *Zeitschrift für anorganische und allgemeine Chemie*, 250:110–120, 1942.

[41] P. Duwez and S. R. Bean. X-ray study of the σ phase in various alloy systems. *Proceedings of the ASTM*, 50, 1950.

[42] R. E. Watson and L. H. Bennett. Transition-metal alloy formation - the occurrence of topologically close-packed phases - part I. *Acta Metallurgica*, 32(4):477–489, 1984.

[43] Y. Ohta and D. G. Pettifor. Size versus electronic factors in transition metal Laves phase stability. *Journal of Physics C*, 2:8189–8194, 1990.

[44] S. T. Wlodek. The structure of IN-100. *Transactions of the American Society for Metals*, 57:110–119, 1964.

[45] L. R. Woodyatt, C. T. Sims, and H. J. Beattie. Prediction of σ-type phase occurence from compositions in austenitc superalloys. *Transactions of the Metallurgical Society of AIME*, 236–4:519–527, 1966.

[46] W. J. Boesch and J. S. Slaney. Preventing σ phase embrittlement in nickel-based superalloys. *Metal Progress*, 86:109–111, 1964.

[47] H. J. Murphy, C. T. Sims, and A. M. Beltran. PHACOMP revisited. *Journal of Metals*, 20(11):46–53, 1968.

[48] U. R. Kattner. The thermodynamic modeling of multicomponent phase equilibria. *Journal Of The Minerals Metals & Materials Society (TMS)*, 49(12):14–19, December 1997.

[49] M. Morinaga, M. Yukawa, H. Adachi, and H. Ezaki. NewPHACOMP and its applications to alloy design. In *Superalloys 1984*, pages 523–532. The Minerals, Metals & Materials Society (TMS), Warrendale, PA, 1984.

[50] N. Saunders, R. W. Cahn, M. McLean, M. Rappaz, and D. G. Pettifor. Phase diagram calculations for high-temperature structural materials. *Philosophical Transactions: Physical Sciences and Engineering*, 351(1697):543–561, 1995.

[51] N. Yukawa, M. Morinaga, Y. Murata, H. Ezaki, and S. Inoue. High performance single crystal superalloys developed by the d-electron concept. In *Superalloys 1988*, 1988.

[52] J. S. Zhang, K. Matsugi, Y. Murata, M. Morinaga, and N. Yukawa. Evaluation of the phase stability of modified IN738LC alloys with NewPHACOMP. *Journal of Materials Science Letters*, 11:446–448, 1992.

[53] P. Caron. High γ' solvus new generation nickel-based superalloys for single crystal turbine blade applications. In *Superalloys*, pages 737–746. The Minerals, Metals & Materials Society (TMS), Warrendale, PA, 2000.

[54] J. C. Slater and K. H. Johnson. Self-consistent-field $X - \alpha$ cluster method for polyatomic molecules and solids. *Physical Review B*, 5–3:844–853, 1972.

[55] Y. Murata, S. Miyazaki, M. Morinaga, and R. Hashizume. Hot corrosion resistant and high strength nickel-based single crystal and directionally-solified superalloys developed by the d-electrons concept. In *Superalloys 1996*, pages 61–70. The Minerals, Metals & Materials Society, 1996.

[56] K. Matsugi, Y. Murata, M. Morinaga, and N. Yukawa. Realistic advancement for nickel-based single crystal superalloys by the d-electrons concept. In *Superalloys 1992*, 1992.

[57] F. R. N. Nabarro and F. de Villiers. *The physics of creep: Creep and creep-resistant alloys*. Taylor & Francis Ltd., London, 1995.

[58] L. Kaufman and M. Cohen. The martensitic transformation in the iron-nickel system. *Journal of Metals*, 206:1393–1401, 1956.

[59] P. E. A. Turchi. Ab intio and CALPHAD thermodynamics of materials. *3rd International Conference on "Computational Modeling and Simulation of Materials", Acireale, Italy*, 2004.

[60] P. E. A. Turchi, I. A. Abrikosov, B. Burton, S. G. Fries, G. Grimvall, L. Kaufman, P. Korzhavyi, V. R. Manga, M. Ohno, A. Pisch, A. Scott, and W. Zhang. Interface between quantum-mechanical-based approaches, experiments, and CALPHAD methodology. *Computer Coupling of Phase Diagrams and Thermochemistry*, 31:4–27, 2007.

[61] C. Wolverton, X. Y. Yan, R. Vijayaraghavan, and V. Ozolins. Incorporating first-principles energetics in computational thermodynamics approaches. *Acta Materialia*, 50(9):2187–2197, 2002.

[62] N. Saunders and A. P. Miodownik. *CALPHAD calculation of phase diagrams a comprehensive guide*. Elsevier Science Ltd, Oxford, UK, 1998.

[63] T. Saito, editor. *Computational Materials Design*. Springer, Berlin, 1999.

[64] J.C. Zhao and M.F. Henry. CALPHAD–Is it ready for superalloy design? *Advanced Engineering Materials*, 4(7):501–508, 2002.

[65] E. S. Machlin and B. Loh. Structural stability of transition-metal binary compounds. *Physical Review Letters*, 45(20):1642–1644, Nov 1980.

[66] D. G. Pettifor. A chemical scale for crystal-structure maps. *Solid State Communications*, 51(1):31–34, 1984.

[67] D. G. Pettifor. Structure maps for pseudobinary and ternary phases. *Materials Science and Technology*, 4–8:675–691, 1988.

[68] P. Villars and K. Girgis. Regularities in binary intermetallic compounds. *Zeitschrift für Metallkunde*, 73–7:455–462, 1982.

[69] N. Greenwood and A. Earnshaw. *Chemistry of the Elements (2^{nd} Edition)*. Elsevier, 2002.

[70] J. A. Alonso and L. A. Girifalco. Electronegativity scale for metals. *Physical Review B*, 19(8):3889–3895, 1979.

[71] L. Pauling. The nature of the chemical bond. IV. The energy of single bonds and the relative electronegtativity of atoms. *Journal of the American Chemical Society*, 54(9):3570–3582, 1932.

[72] R. S. Mulliken. A new electroaffinity scale; Together with data on valence states and on valence ionization potentials and electron affinities. *Journal of Chemical Physics*, 2(11):782–793, 1934.

[73] L. C. Allen. Electronegativity is the average one-electron energy of the valence-shell electrons in ground-state free atoms. *Journal of the American Chemical Society*, 111(25):9003–9014, 1989.

[74] A. I. Martynov and S. S. Batsanov. A new method for determination of the electronegativity of atoms. *Russian Journal of Organic Chemistry*, 25:3171–3175, 1980.

[75] T. B. Massalski. *Binary alloy phase diagrams*. ASM International, 1990.

[76] J. M. Joubert and M. Phejar. Crystal chemistry and CALPHAD modelling of the χ phase. *Progress in Material Science*, 54(7):945 – 980, 2009.

[77] P. Villars, M. Berndt, K. Brandenburg, K. Cenzual, J. Daam, F. Hulliger, T. B. Massalski, H. Okamoto, K. Osaki, A. Prince, H. Putz, and S. Iwata. The Pauling file, Binaries edition. *Journal of Alloys and Compounds*, 367:293 – 297, 2004.

[78] D. A. Fletcher, R. F. McMeeking, and D. Parkin. The United Kingdom chemical database service. *Journal of Chemical Information and Computer Sciences*, 36(4):746–749, 1996.

[79] R. M. Waterstrat. Investigation of vanadium-manganese alloy system. *Transactions of the Metallurgical Society of AIME*, 224:240–&, 1962.

[80] L. Y. Chen, C. H. Li, K. Wang, H. Q. Dong, X. G. Lu, and W. Z. Ding. Thermodynamic modeling of Ti-Cr-Mn ternary system. *CALPHAD*, 33(4):658–663, 2009.

[81] F. Stein, A. Palm, and G. Sauthoff. Structure and stability of Laves phases part II - Structure type variations in binary and ternary systems. *Intermetallics*, 13(10):1056–1074, 2005.

[82] A. C. Yeh, A. Sato, T. Kobayashi, and H. Harada. On the creep and phase stability of advanced Ni-base single crystal superalloys. *Materials Science and Engineering A*, 490(1-2):445–451, 2008.

[83] M. V. Acharya and G. E. Fuchs. The effect of stress on the microstructural stability of CMSX-10 single crystal Ni-base superalloys. *Scripta Materialia*, 54(1):61–64, 2006.

[84] J. M. Joubert and N. Dupin. Mixed site occupancies in the μ phase. *Intermetallics*, 12(12):1373–1380, December 2004.

[85] F. Stein, M. Palm, and G. Sauthoff. Structure and stability of Laves phases part I - Critical assessment of factors controlling Laves phase stability. *Intermetallics*, 12(7-9):713–720, 2004.

[86] A. E. Dwight. Factors controlling the occurrence of Laves phases and AB_5 compounds among transition elements. *Transactions of the American Society for Metals*, 53:479–500, 1961.

[87] J. Hafner. *The structure of binary compounds*, chapter 3. Quantum theory of structure: sp-bonded systems, pages 147–286. North–Holland, Elsevier Science Publisher B. V., 1989.

[88] R. L. Johannes, R. Haydock, and V. Heine. Phase stability in transition-metal Laves phases. *Physical Review Letters*, 36:372–376, 1976.

[89] D. G. Pettifor. Electron theory in materials modelling. *Acta Materialia*, 51(19):5649–5673, 2003.

[90] D. Hobbs, J. Hafner, and D. Spisak. Understanding the complex metallic element Mn. I. Crystalline and noncollinear magnetic structure of α-Mn. *Physical Review B*, 68–1:014407–014425, 2003.

[91] A. C. Lawson, A. C. Larson, M. C. Aronson, S. Johnson, Z. Fisk, P. C. Canfield, J. D. Thompson, and R. B. Von Dreele. Magnetic and crystallographic order in α-manganese. *Journal of Applied Physics*, 76(10):7049–7051, 1994.

[92] J. S. Kasper and B. W. Roberts. Antiferromagnetic structure of α-manganese and a magnetic structure study of β-manganese. *Physical Review*, 101(2):537–544, 1956.

[93] C. B. Shoemaker and D. P. Shoemaker. The crystal structure of the M phase, Nb-Ni-Al. *Acta Crystallographica*, 23:231–238, 1969.

[94] J. S. Benjamin, B. C. Giessen, and N. J. Graut. Intermediate Phases in the Ternary System Nb(Cb)-Ni-Al at 1140 °C. *Transactions of the Metallurgical Society of AIME*, 236:224226, 1966.

[95] R. C. Reed, T. Tao, and N. Warnken. Alloys-by-design: Application to nickel-based single crystal superalloys. *Acta Materialia*, 57(19):5898–5913, 2009.

[96] N. Saunders. The application of CALPHAD calculations to Ni-based superalloys. In R. D. Kissinger, D. J. Deye, D. L. Anton, M. V. Nathal, T. M. Pollock, and D. A. Woodford, editors, *Superalloys*, page 101. The Minerals, Metals & Materials Society (TMS), Warrendale, PA, 1996.

[97] C. S. Proctor. *Formation and effects of Intermetallics in the rhenium-containing nickel-based superalloy CMSX-4*. PhD thesis, University of Cambridge, 1993.

[98] N. Saunders, M. Fahrmann, and C. J. Small. The application of CALPHAD calculations to Ni-based superalloys. In K. A. Green, T. M. Pollock, and R. D. Kissinger, editors, *Superalloys*, pages 803–812. The Minerals, Metals & Materials Society (TMS), Warrendale, PA, 2000.

[99] N. W. Ashcroft and N. D. Mermin. *Solid state physics*. Harcourt Brace College Publishers, San Diego, 1976.

[100] M. Born and R. Oppenheimer. Zur Quantumtheorie der Molekülen. *Annalen der Physik*, (84):457–484, 1927.

[101] P. Hohenberg and W. Kohn. Inhomogeneous electron gas. *Physical Review*, 136(3B):B864–B871, 1964.

[102] W. Kohn and L. J. Sham. Self-consistent equations including exchange and correlation effects. *Physical Review*, 140(4A):A1133–A1138, 1965.

[103] R. M. Martin. *Electronic structure: Basic theory and practical methods*. Cambridge University Press, Cambridge, 2004.

[104] W. Koch and M. C. Holthausen. *A chemists guide to density functional theory*. Wiley-VCH, Weinheim, 2001.

[105] Z. H. Barber, editor. *Introduction to materials modelling*. Maney Publishing, London, 2005.

[106] G. Kresse and J. Hafner. Ab initio molecular dynamics for liquid metals. *Physical Review B*, 47(1):558–561, Jan 1993.

[107] G. Kresse and J. Furthmüller. Efficiency of ab-initio total energy calculations for metals and semiconductors using a plane-wave basis set. *Computational Materials Science*, 6(1):15 – 50, 1996.

[108] G. Kresse and J. Furthmüller. Efficient iterative schemes for ab initio total-energy calculations using a plane-wave basis set. *Physical Review B*, 54(16):11169–11186, 1996.

[109] P. E. Blöchl, O. Jepsen, and O. K. Andersen. Improved tetrahedron method for brillouin-zone integrations. *Physical Review B*, 49-23:16223–16233, 1993.

[110] A. E. Mattsson, P. A. Schultz, M. P. Desjarlais, T. R. Mattsson, and K. Leung. Designing meaningful density functional theory calculations in materials science. *Modelling and Simulation in Materials Science and Engineering*, 13(1):R1–R31, 2005.

[111] L. Cortella, B. Vinet, P. J. Desré, A. Pasturel, A. T. Paxton, and M. van Schilfgaarde. Evidences of transitory metastable phases in refractory metals solidified from highly undercooled liquids in a drop tube. *Physical Review Letters*, 70(10):1469–1472, 1993.

[112] B. Vinet, L. Cortella, J. J. Favier, and P. Desre. Highly undercooled W and Re drops in an ultrahigh-vacuum drop tube. *Applied Physics Letters*, 58(1):97–99, 1991.

[113] M. H. F. Sluiter, K. Esfarjani, and Y. Kawazoe. Site occupation reversal in the Fe-Cr σ phase. *Physical Review Letters*, 75(17):3142–3145, 1995.

[114] C. Berne, M. Sluiter, and A. Pasturel. Theoretical approach of phase selection in refractory metals and alloys. *Journal of Alloys and Compounds*, 334:27–33, 2002.

[115] M. H. F. Sluiter and A. Pasturel. Site occupation in the Cr-Ru and Cr-Os σ phases. *Physical Review B*, 80(13):134122–134131, 2009.

[116] M. H. F. Sluiter, A. Pasturel, and Y. Kawazoe. Site occupation in the Ni-Nb μ phase. *Physical Review B*, 67(17):174203, 2003.

[117] T. Hammerschmidt, B. Seiser, R. Drautz, and D. G. Pettifor. Modeling topologically close-packed phases in superalloys: Valence-dependent bond-order potentials based on ab-initio calculations. In *Superalloys*. The Minerals, Metals & Materials Society (TMS), Warrendale, PA, 2008.

[118] P. A. Sundman B. Korzhavyi, M. Selleby, and B. Johansson. Atomic, electronic, and magnetic structure of iron-based σ-phases. In M.J. Mills, H. Clemens, C-L. Fu, and H. Inui, editors, *Integrative and Interdisciplinary Aspects of Intermetallics, Materials Research Society Symposium Proceedings*, volume 842, pages S4.10.1–6. MRS, Warrendale, 2005.

[119] J. Pavlu, J. Vrestál, and M. Sob. Ab initio study of formation energy and magnetism of sigma phase in Cr-Fe and Cr-Co systems. *Intermetallics*, 18(2):212–220, 2010.

[120] H. Hasegawa and D. G. Pettifor. Microscopic theory of the temperature-pressure phase of iron. *Physical Review Letters*, 50:130–133, 1983.

[121] J. C. Crivello and J. M. Joubert. First principles calculation of the σ and χ phases in the Mo-Re and W-Re systems. *Journal of Physics C*, 22–3:1–7, 2010.

[122] J. C. Crivello, M. Palumbo, T. Abe, and J. M. Joubert. Ab initio ternary σ-phase diagram: The Cr-Mo-Re system. *CALPHAD*, 34(4):487–494, 2010.

[123] M. H. F. Sluiter, A. Pasturel, and Y. Kawazoe. Prediction of site preference and phase stability of transition metal based frank-kasper phases in the science of complex alloy phases. *EPD Congress 2005, TMS (The Minerals, Metal and Materials Society), Warrendale, PA, USA*, pages 409–436, 2005.

[124] E. G. Moroni, G. Kresse, J. Hafner, and J. Furthmüller. Ultrasoft pseudopotentials applied to magnetic Fe, Co, and Ni: From atoms to solids. *Physical Review B*, 56(24):15629–15646, 1997.

[125] J. C. Duthie and D. G. Pettifor. Correlation between d-band occupancy and crystal structure in the rare earths. *Physical Review Letters*, 38(10):564–567, 1977.

[126] T. Qin. *Binding-energy relations and equations of state for non-magnetic transition metals*. PhD thesis, University of Oxford, 2008.

[127] C. Kittel. *Introduction to solid state physics*. John Wiley & Sons, Inc., Singapore, 2003.

[128] P. T. Moseley and C. J. Seabrook. The crystal structure of β-tantalum. *Acta Crystallographica Section B*, 29(5):1170–1171, May 1973.

[129] A. Arakcheeva, G. Chapuis, and V. Grinevitch. The self-hosting structure of β-Ta. *Acta Crystallographica Section B*, 58(1):1–7, 2002.

[130] W. G. Burgers and J. A. M. van Liempt. Zum Verhalten des Thoroxyds in Wolframglühdrähten. *Zeitschrift für anorganische und allgemeine Chemie*, 193(1):144–160, 1930.

[131] H. Hartmann, F. Ebert, and O. Bretschneider. Elektrolysen in Phosphatschmelzen. I. Die elektrolytische Gewinnung von α- und β-Wolfram. *Zeitschrift für anorganische und allgemeine Chemie*, 198(1):116–140, 1931.

[132] M. W. Finnis. *Interatomic forces in condensed matter*. Oxford University Press, Oxford, 2003.

[133] D. A. Papaconstantopoulos and M. J. Mehl. The Slater-Koster tight-binding method: A computationally efficient and accurate approach. *Journal of Physics C*, 15:413–440, 2003.

[134] F. Bloch. Über die Quantenmechanik der Elektronen in Kristallgittern. *Zeitschrift für Physik A*, 52(52):555–600, 1928.

[135] J. C. Slater and G. F. Koster. Simplified linear combination of atomic orbitals method for the periodic potential problem. *Physical Review*, 94–6:1498–1524, 1954.

[136] W. M. C. Foulkes and R. Haydock. Tight-binding models and density-functional theory. *Physical Review B*, 39-17:12520–12536, 1988.

[137] A. P. Sutton, M. W. Finnis, D. G. Pettifor, and Y. Ohta. The tight-binding bond model. *Journal of Physics C*, 21:35–66, 1988.

[138] J. Harris. Simplified method for calculating the energy of weakly interacting fragments. *Physical Review B*, 31:1770 – 1779, 1985.

[139] W. M. C. Foulkes. *Shakespeare and the Victorian stage*. PhD thesis, University of Cambridge, 1987.

[140] C. M. Goringe, D. R. Bowler, and E. Hernandez. Tight-binding modelling of materials. *Reports on progress in physics*, 60:1447–1512, 1997.

[141] D. G. Pettifor. *Bonding and Structure of Molecules and Solids*. Oxford University Press, 1995.

[142] J. M. Ziman. The T matrix, the K matrix, d bands and l-dependent pseudopotentials in the theory of metals. *Proceedings of the Physical Society*, 86(2):337, 1965.

[143] V. Heine. s-d interaction in transition metals. *Physical Review*, 153(3):673–682, 1967.

[144] J. Hubbard. The approximate calculation of electronic band structure. *Proceedings of the Physical Society*, 92(4):921, 1967.

[145] R. L. Jacobs. The theory of transition metal band structures. *Journal of Physics C*, 1(2):492, 1968.

[146] D. G. Pettifor. An energy-independent method of band-structure calculation for transition metals. *Journal of Physics C*, 2(6):1051, 1969.

[147] L. Hodges, H. Ehrenreich, and N. D. Lang. Interpolation scheme for band structure of noble and transition metals: Ferromagnetism and neutron diffraction in Ni. *Physical Review*, 152(2):505–526, 1966.

[148] F. M. Müller. Combined interpolation scheme for transition and noble metals. *Physical Review*, 153(3):659–669, 1967.

[149] D. G. Pettifor. Theory of energy bands and related properties of 4d transition metals. i. band parameters and their volume dependence. *Journal of Physics F*, 7(4):613, 1977.

[150] O. K. Andersen, W. Klose, and H. Nohl. Electronic structure of chevrel-phase high-critical-field superconductors. *Physical Review B*, 17(3):1209–1237, Feb 1978.

[151] O. K. Andersen. Simple approach to the band-structure problem. *Solid State Communications*, 13(2):133–136, 1973.

[152] G. O. Brunner and D. Schwarzenbach. Zur Abgrenzung der Koordinationssphäre und Ermittlung der Koordinationszahl in Kristallstrukturen. *Zeitschrift für Kristallographie*, 133:127–133, 1971.

[153] D. G. Pettifor and R. Podloucky. The structures of binary compounds: 2. Theory of the pd-bonded AB compounds. *Journal of Physics C*, 19:315–330, 1986.

[154] P. E. A. Turchi and F. Ducastelle. *Recursion Method and Its Applications*, pages 104–119. Springer, New York, 1985.

[155] M. Methfessel and A. T. Paxton. High-precision sampling for Brillouin-zone integration in metals. *Physical Review B*, 40(6):3616–3621, 1989.

[156] B. Legrand. Relation between the electronic-structure and ease of gliding in hexagonal close-packed metals. *Philosophical Magazine B*, 49(2):171–184, 1984.

[157] B. Legrand. Core structure of the screw dislocations 1/3[1120] in titanium. *Philosophical Magazine A*, 52(1):83–97, 1985.

[158] P. B. Allen, J. Q. Broughton, and A. K. Mc Mahan. Transferable nonorthogonal tight-binding parameters for silicon. *Physical Review B*, 34(2):859–862, 1986.

[159] P. B. Allen and J. Q. Broughton. Electrical-conductivity and electronic-properties of liquid silicon. *Journal of Physical Chemistry*, 91(19):4964–4970, 1987.

[160] A. P. Horsfield and P. Clancy. A tight-binding molecular-dynamics simulation of the melting and solidification of silicon. *Modelling And Simulation In Materials Science And Engineering*, 2(2):277–294, March 1994.

[161] M. Menon and K. R. Subbaswamy. Universal parameter tight-binding molecular-dynamics - application to C-60. *Physical Review Letters*, 67(25):3487–3490, 1991.

[162] M. Menon and K. R. Subbaswamy. Nonorthogonal tight-binding molecular-dynamics study of silicon clusters. *Physical Review B*, 47(19):12754–12759, 1993.

[163] S. Russo and C. Noguera. Acido-basic properties of simple oxide surfaces.1. Magnesium-oxide. *Surface Science*, 262(1-2):245–258, 1992.

[164] J. Goniakowski, S. Bouetterusso, and C. Noguera. Acido-basic properties of simple oxide surfaces .3. Systematics of H+ and OH- adsorption. *Surface Science*, 284(3):315–327, 1993.

[165] D. G. Pettifor. Theory of the crystal structures of transition metals. *Journal of Physics C*, 3(2):367–377, 1970.

[166] P. E. A. Turchi, G. Tregila, and F. Ducastelle. Electronic-structure and phase-stability of A15 transition-metals and alloys. *Journal of Physics F*, 13(12):2543–2567, 1983.

[167] D. G. Pettifor. The structures of binary compounds. i. Phenomenological structure maps. *Journal of Physics C*, 19(3):285, 1986.

[168] L. M. Hoistad and S. Lee. The Hume-Rothery electron concentration rules and second moment scaling. *Journal of the American Chemical Society*, 113(22):8216–8220, 1991.

[169] D. G. Pettifor and R. Podloucky. Microscopic theory of the structural stability of pd-bonded AB compounds. *Physical Review Letters*, 53(11):1080–1083, 1984.

[170] D. Feng and G. Jin. *Introduction to condensed matter physics*. World Scientific, Singapore, 2005.

[171] A. P. Horsfield, A. M. Bratkovsky, M. Fearn, D. G. Pettifor, and M. Aoki. Bond-order potentials: Theory and implementation. *Physical Review B*, 53(19):12694–12712, 1996.

[172] R. Drautz and D. G. Pettifor. Valence-dependent analytic bond-oder potential for transition metals. *Physical Review B*, 74:174117–1–14, 2006.

[173] R. Haydock, V. Heine, M. J. Kelly, and J. B. Pendry. Electronic density of states at transition-metal surfaces. *Physical Review Letters*, 29(13):868–871, 1972.

[174] R. Haydock. The recursive solution of the Schrödinger equation. *Computer Physics Communications*, 20:11–16, 1980.

[175] C. Lanczos. An iteration method for the solution of the eigenvalue problem of linear differential and integral operators. *Journal of Research of the National Bureau of Standards*, 45(4):255–282, 1950.

[176] R. Haydock, V. Heine, and M. J. Kelly. Electronic structure based on the local atomic environment for tight-binding bands. *Journal of Physics C*, 8(16):2591–2605, 1975.

[177] N. R. Beer. *The electronic structure of transition metal alloys.* PhD thesis, University of London, 1985.

[178] P. E. A. Turchi, F. Ducastelle, and G. Treglia. Band gaps and asymptotic behaviour of continued fraction coefficients. *Journal of Physics C*, 15(13):2891–2924, 1982.

[179] S. Glanville, A. T. Paxton, and M. W. Finnis. A comparison of methods for calculating tight-binding bond energies. *Journal of Physics F*, 18(4):693–718, 1988.

[180] D. G. Pettifor. New many-body potential for the bond order. *Physical Review Letters*, 63(22):2480–2483, 1989.

[181] A. P. Horsfield, A. M. Bratkovsky, D. G. Pettifor, and M. Aoki. Bond-order potential and cluster recursion for the description of chemical bonds: Efficient real-space methods for tight-binding molecular dynamics. *Physical Review B*, 53(3):1656–1666, 1996.

[182] M. Aoki. Rapidly convergent bond order expansion for atomistic simulations. *Physical Review Letters*, 71(23):3842–3845, 1993.

[183] M. Aoki, D. Nguyen-Manh, D. G. Pettifor, and V. Vitek. Atom-based bond-order potentials for modelling mechanical properties of metals. *Progress In Materials Science*, 52(2-3):154–195, 2007.

[184] R. Haydock. *Solid State Physics*, page 215. Academic, New York, 1980.

[185] R. N. Silver, H. Roeder, A. F. Voter, and J. D. Kress. Kernel polynomial approximations for densities of states and spectral functions. *Journal of Computational Physics*, 124(1):115 – 130, 1996.

[186] M. Abramowitz and I. A. Stegun. *Handbook of Mathematical Functions with Formulas, Graphs, and Mathematical Tables.* Dover, New York, 1964.

[187] F Ducastelle. Private communication with D. G. Pettifor (1970).

[188] F. Ducastelle and F. Cyrot-Lackmann. Moments developments: II. Application to the crystalline structures and the stacking fault energies of transition metals. *Journal of Physics and Chemistry of Solids*, 32(1):285–301, 1971.

[189] K. Masuda and A. Sato. Electronic theory for screw dislocation motion in dilute bcc transition meta alloys. *Philosophical Magazine A*, 44–4:799–814, 1981.

[190] K. Masuda, R. Yamamoto, and M. Doyama. Application of tight-binding type electronic theory to lattice defect problems in transition metals. *Journal of Physics F*, 13:1407–1413, 1983.

[191] P. E. A. Turchi. *Structure electronique et stabilite des alliages de metaux de transition: Effects de structure cristalline et d'ordre configurationnel.* PhD thesis, Universite Pierre et Marie Curie, 1984.

[192] J. A. Moriarty. Density-functional formulation of the generalized pseudopotential theory. III. Transition-metal interatomic potentials. *Physical Review B*, 38(5):3199–3231, 1988.

[193] R. Phillips and A. E. Carlsson. Universal statilizing mechanism for transition-metal polytetrahedrally packed phases. *Physical Review B*, 42-6:3345–3350, 1990.

[194] M. Aoki and D. G. Pettifor. Directional bonding in atomistic simulations. *Materials Science and Engineering A*, 176:19–24, 1994.

[195] N. R. Beer and D. G. Pettifor. *The Electronic Structure of Complex Systems*, volume 20, page 769. Plenum Press, New York, 1984.

[196] M. W. Finnis and J. E. Sinclair. A simple empirical N-body potential for transition metals. *Philosophical Magazine A*, 50:45–55, 1984.